Subsystems for all-optical coherent quantum-noise cancellation

Von der Fakultät für Mathematik und Physik
der Gottfried Wilhelm Leibniz Universität Hannover
zur Erlangung des Grades

Doktor der Naturwissenschaften
Dr. rer. nat.

genehmigte Dissertation
von

Daniel Steinmeyer, M. Sc.

2019

Kurzdarstellung

Wird ein System vermessen, so es dadurch immer auch gestört – und zwar umso stärker, je stärker und genauer die Messung ist. Bei schwachen kontinuierlichen Messungen führt der Kompromiss zwischen Messgenauigkeit und Störung des Systems zu einer optimalen Messempfindlichkeit, die bei optomechanischen Messungen wie der Gravitationswellendetektion unter dem Namen *Standardquantenlimit* (SQL) firmiert. Sie entspricht der Verwendung einer optimalen optischen Leistung, bei der Schrotrauschen und Strahlungsdruckrauschen zu gleichen Teilen zur Messunsicherheit beitragen. Durch kohärente Quantenrauschunterdrückung (coherent quantum-noise cancellation, CQNC) sollen mittels eines Oszillators mit effektiver negativer Masse das Strahlungsdruckrauschen reduziert und das SQL überwunden werden. In einer optischen Umsetzung von CQNC wird die effektive negative Masse mit einem verstimmtem optischen Resonator realisiert, der mit einem Strahlteiler und einem optisch-parametrischen Prozess an das einfallende Lichtfeld gekoppelt ist.[1] Der Resonator muss in Bezug auf Resonanzfrequenz, Zerfallsdauer und Kopplungsstärken auf das zu vermessende System angepasst werden.[2]

In der vorliegenden Arbeit werden CQNC und eine mögliche optische Realisierung theoretisch und experimentell untersucht. Ein besonderer Fokus liegt dabei auf der Strahlteiler- und der parametrischen Interaktion. Zwei potentielle Aufbauten werden theoretisch miteinander verglichen und kritische Parameter ermittelt. Zur Verfügung stehende optomechanische Elemente wurden charakterisiert und als für CQNC geeignet befunden.

Die Kopplungsstärke der optisch-parametrischen Interaktion, g_{DC}, wird auf experimentell messbare Parameter zurückgeführt. Messungen von zwei-Moden-gequetschtem Licht zeigten eine Reduktion des Vakuumrauschens um mehr als 2.3 dB. Mit diesen Messungen wurde die Kopplungsstärke zu $g_{DC} \approx 2\pi \times 200$ kHz bei 100 mW Pumpleistung bestimmt und liegt damit im erwünschten Rahmen. Zwei weitere Messmethodiken bestätigten dieses Resultat.

Mit einer Strahlteilerinteraktion gekoppelte optische Resonatoren werden theoretisch und experimentell untersucht. Eine Strahlteilerkopplung der Stärke g_{BS} wurde mit einer Wellenplatte realisiert. Eine Vereinfachung des experimentellen Aufbaus ermöglichte die Stabilisierung der gekoppelten Resonatoren. Messungen bestätigen die theoretischen Vorhersagen exakt. Die beobachtete Modenaufspaltung ergab eine Kopplungsstärke $g_{BS} \approx 2\pi \times 235$ kHz, die im

---

[1] M. Tsang and C. Caves, *Phys. Rev. Lett.* **105** (2010), 123601.

[2] M. H. Wimmer, D. Steinmeyer, K. Hammerer, and M. Heurs, *Phys. Rev. A* **89** (2014), 053836.

aktualisierten erwünschten Parameterbereich liegt.

CQNC wird von optischen Verlusten und einer begrenzten Messstärke limitiert sein. Die Umsetzung einer aktualisierten Liste an Parametern, beruhend auf den durchgeführten Experimenten, sollte eine Reduktion des Strahlungsdruckrauschens von bis zu 4.8 dB ermöglichen.

ABSTRACT

Quantum mechanics dictates that a measurement always disturb the measured system. In weak continuous measurements, the trade-off between measurement precision and back-action onto the system yields an optimal measurement sensitivity, which is known as the Standard Quantum Limit (SQL) in opto-mechanical measurements, such as gravitational-wave detection. It corresponds to finding the optimal optical power in a compromise between quantum shot noise and quantum radiation-pressure noise. Coherent quantum-noise cancellation (CQNC) aims at overcoming the SQL and reducing back-action noise via the introduction of an effective negative-mass oscillator. In an all-optical set-up, this oscillator is realised by a detuned optical resonator coupled to incoming light with a beam-splitter and a down-conversion interaction[1] and needs to be matched to the measured system in resonance frequency, damping and coupling strengths.[2]

This thesis explores the nature of CQNC and a potential all-optical realisation in theory and experiment, with a particular emphasis on the beam-splitter and the down-conversion interaction. Two possible set-ups are compared theoretically and critical parameters determined. Available opto-mechanical devices were characterised and confirmed to be suitable for CQNC.

The down-conversion coupling strength g_{DC} is linked to experimentally obtainable parameters. More than 2.3 dB reduction in uncertainty of two-mode squeezed light were observed. The squeezing measurements yielded $g_{DC} \approx 2\pi \times 200\,\mathrm{kHz}$ at 100 mW pump power, which is well within the initially required range and is in agreement with results from two other measurement methods.

Optical resonators coupled via a beam-splitter interaction are studied theoretically and experimentally. In this work, the beam-splitter interaction of strength g_{BS} was realised by a wave plate. A simplified experiment design enabled stabilisation of the coupled resonators. Our experimental observations accurately confirmed our theoretical predictions. The observed mode splitting yielded $g_{BS} \approx 2\pi \times 235\,\mathrm{kHz}$, within the updated requirements.

Losses and a limited measurement strength will be the limiting factors for CQNC. The updated set of parameters, backed by the conducted experiments, paves the way towards a reduction of radiation-pressure noise of up to 4.8 dB.

KEYWORDS: coherent quantum-noise cancellation, standard quantum limit, two-mode squeezed light, coupled optical resonators

---

[1] M. Tsang and C. Caves, *Phys. Rev. Lett.* **105** (2010), 123601.
[2] M. H. Wimmer, D. Steinmeyer, K. Hammerer, and M. Heurs, *Phys. Rev. A* **89** (2014), 053836.

Contents

FIGURES

TABLES

Introduction

They do.
　　— C. Caves

Radiation pressure has long been known as the force which a light field exerts onto an object. As early as 1619, Kepler suspected radiation pressure to be the cause of the comet's tail pointing away from sun.[1] A quantitative description of the effect was provided by Maxwell 250 years later.[2] In 1972, Rai Weiss lsited radiation-pressure noise among the main noise sources limiting the sensitivity of potential interferometric gravitational-wave detectors.[3] Fluctuating light power causes a fluctuating radiation pressure on the object. Where the position of an object is to be measured, this may result in additional fluctuations of the object's position, rendering its measurement imprecise. The masking of the 'true' position is called *noise*.

In 1980, Carlton Caves confirmed that not only classical fluctuations in light power give rise to radiation-pressure noise in gravitational-wave detectors, but that also quantum-mechanical fluctuations inherent to the quantum nature of light contribute.[4] What here shows as radiation-pressure noise is actually a far more general effect stemming from the quantum-mechanical description of a measurement. In quantum mechanics, a measurement is always bidirectional. In order to obtain information about a system, there has to be some interaction between the system and an observer. This measurement interaction will lead to a disturbance of the system. If not only the current state of a system is of interest, but also its evolution in time, this becomes a problem. For the class of

---

[1] For a history of radiation pressure and opto-mechanical interactions, see, e.g., M. Aspelmeyer, T. J. Kippenberg and F. Marquardt, 'Cavity optomechanics', *Rev. Mod. Phys.* **86** (2014), 1391–1452, Sec. I.

[2] J. C. Maxwell, *A Treatise on Electricity and Magnetism*, Oxford: Clarendon, 1873, §792 [= p. 391 in Vol. II of that work].

[3] R. Weiss, 'Electromagnetically coupled broadband gravitational wave antenna', *Q. Prog. Rep. Research Lab. Electronics, Massachusetts Inst. Technol.* **105** (1972), 54, p. 63.

[4] C. M. Caves, 'Quantum-mechanical radiation-pressure fluctuations in an interferometer', *Phys. Rev. Lett.* **45** (1980), 75–79.

weak continuous measurements,[5] a trade-off has to be found, taking into account measurement imprecision, which is lower with stronger measurements, and *back-action*, which disturbs the system and future measurements.

In interferometric measurements, light is used to estimate changes in forces or positions by monitoring a moveable object. Even if all technical noises have been mitigated, the quantum nature of light sets a limit to the possible measurement sensitivity. The weaker the light field is, the smaller is the signal and the less precise the measurement. If the light field is too weak, inherent fluctuations called *shot noise* limit the measurement, corresponding to the above-mentioned imprecision noise. On the other hand, if the field becomes too strong, the radiation-pressure effects, caused by the reflection of light off the moveable object, become visible. Radiation-pressure noise will limit the measurement, corresponding to the above-mentioned back-action noise. There is a trade-off between shot noise and radiation-pressure noise, leading to an optimal measurement strength. The obtained sensitivity is called *Standard Quantum Limit* (SQL). Changing the optical power from this optimal spot causes either shot noise or radiation-pressure noise to dominate and the sensitivity to decrease.

Gravitational-wave detectors are but one among a variety of opto-mechanical measurement apparatuses potentially affected by these effects. To date, they have been the most sensitive devices and are about to be limited by the trade-off between radiation-pressure noise and shot noise, between measurement imprecision and back-action.[6] But also in micro-opto-mechanical set-ups, radiation-pressure noise has been observed[7] and will, at some point, be limiting the measurement sensitivity.

However, the Standard Quantum Limit is not the ultimate limit. Several ideas exist of how to circumvent the SQL. Interest in techniques to overcome the SQL with quantum-mechanical tricks has been fuelled in the gravitational-wave community.[8] One of those tricks will be studied in the course of this

---

[5]See, e.g. A. A. Clerk et al., 'Introduction to quantum noise, measurement, and amplification', *Rev. Mod. Phys.* **82** (2010), 1155–1208.

[6]J. Aasi et al., 'Advanced LIGO', *Class. Quantum Gravity* **32** (2015), 074001.

[7]T. P. Purdy, R. W. Peterson and C. A. Regal, 'Observation of Radiation Pressure Shot Noise on a Macroscopic Object', *Science* **339** (2013), 801–804.

[8]V. B. Braginsky, Y. I. Vorontsov and K. S. Thorne, 'Quantum Nondemolition Measurements', *Science* **209** (1980), 547–557; C. M. Caves et al., 'On the measurement of a weak classical force coupled to a quantum-mechanical oscillator. I. Issues of principle', *Rev. Mod. Phys.* **52** (1980), 341–392.

thesis. It is known under the name *coherent quantum-noise cancellation*[9] and introduces an effective negative-mass serving as a reference against which the position of the device under test is to be measured. The idea is as follows. Whenever light is reflected off a mechanical object, this object is pushed away. An object with a *negative* mass, on the contrary, is attracted by such a push. Fluctuations in radiation pressure affect both objects oppositely. Sending light first onto one, and then onto the other object, the pushes by radiation pressure should cancel. Ever more measurement power could be used to obtain increased measurement sensitivities, not any more limited by back-action on the system.

In an all-optical set-up, as studied in this thesis, the effective negative-mass will be realised by a detuned optical resonator, as suggested by Tsang and Caves.[10] This *ancilla* cavity will be coupled to the incoming light via a beam-splitter interaction and a down-conversion interaction as to mimic the radiation-pressure interaction. An experiment showing back-action noise cancellation with all-optical CQNC consists of three subsystems. A positive-mass oscillator subject to radiation pressure and introducing radiation-pressure noise, and a beam-splitter interaction and a down-conversion interaction, together realising the coupling to a detuned ancilla cavity, which is the effective negative-mass oscillator. Combining the systems in a suitable parameter range should show radiation-pressure cancellation.[11]

This thesis aims at a better understanding of all-optical CQNC with respect to several aspects. Different set-ups are conceivable. The positive- and the negative-mass oscillator could be part of the same surrounding resonator as in the *integrated* set-up, or they are traversed by the light field one after the other as in the *cascaded* set-up. Advantages and disadvantages of the two set-ups have to be understood. Of particular interest are the limiting deviations from ideally required parameters. In an experiment, the underlying processes and effects have to be fully understood, especially the three subsystem – opto-mechanics, down-conversion interaction, beam-splitter interaction – and their limitations. It will be interesting see to what extent the required parameters can actually be realised in an experiment. A particular emphasis will lie on the beam-splitter coupling and down-conversion coupling.

---

[9] M. Tsang and C. M. Caves, 'Coherent quantum-noise cancellation for optomechanical sensors', *Phys. Rev. Lett.* **105** (2010), 123601.

[10] Tsang and Caves (2010).

[11] M. H. Wimmer, D. Steinmeyer, K. Hammerer and M. Heurs, 'Coherent cancellation of backaction noise in optomechanical force measurements', *Phys. Rev. A* **89** (2014), 053836.

STRUCTURE OF THE THESIS. Chapter 1 serves as an extended introduction. The basis for the following chapters will be laid by introducing light fields, interferometers and optical resonators. Opto-mechanical measurements leading to the Standard Quantum Limit will be formalised, and the state of the art regarding measurements below the Standard Quantum Limit will be presented.

Chapter 2 is devoted to coherent quantum-noise cancellation, particularly its all-optical realisation. After explaining how CQNC can be understood to work, the effects of CQNC are calculated for two different set-ups. Calculations for the integrated set-up[12] are compared to those for a cascaded set-up. The chapter concludes with motivating design decisions regarding a concrete experimental implementation, and with a set of experimentally feasible parameters for which the possible reduction in radiation-pressure noise is calculated.[13]

In Chapters 3 to 5, the three subsystems required to experimentally demonstrate CQNC are studied. Chapter 3 deals with the opto-mechanics needed to create radiation-pressure noise. Photonic-crystal membrane and Bragg mirrors are characterised in a Michelson interferometer.

Chapter 4 contains the two-mode squeezing part of CQNC. Calculations are presented in order to first clarify differences and similarities between single-mode and two-mode squeezing and then connect the down-conversion formalism with CQNC's formalism and an eventual experiment. From this, different ways of measuring the down-conversion coupling strength are devised and conducted.

In Chapter 5, the beam-splitter interaction is studied. It contains a theoretical description of coupled optical resonators, seen first as coupled harmonic oscillators in a Hamiltonian formalism and then coupled with a wave plate in a transfer-matrix approach. An experiment to study the theoretical predictions and to measure the down-conversion coupling is designed and conducted.

The thesis concludes with a summation of the findings. The set of experimentally feasible parameters determining all-optical CQNC is updated with the knowledge gained in the course of this work, resulting in reductions of quantum noise which should be in reach. Studying the different systems not only determined the next steps but also opened up further opportunities, which will finally be summarised.

---

[12]Wimmer, Steinmeyer, Hammerer and Heurs (2014).
[13]Wimmer, Steinmeyer, Hammerer and Heurs (2014).

Notes on notation. Different fields use different conventions. Within this thesis, quite different fields are touched. Rather than inventing a consistent and unambiguous notation, I will mostly stick to conventions used in the respective field. This entails some ambiguities when it comes to using symbols as place holders for physical quantities. Some of symbols are overloaded – r can be the complex amplitude reflectivity or the squeezing parameter, x can be a spatial coordinate or the pump parameter, R can be the power reflectivity, a resistance, or a radius of curvature, and so forth. In all cases, the respective meaning should be clear from context.

A lot of physical quantities in this thesis are rates and can thus be expressed in units of frequency (hertz) or in units of angular frequency (radians per second). The dimension usually used is that of an angular frequency. Experimentally, however, it is more convenient to talk in hertz, which is why sometimes the implicit factor of 2π is omitted.

As in the corresponding publication,[14] the operators, particularly the force in the calculations for CQNC in Secs. 2.3 and 2.4, are dimensionless. To obtain a force spectral density in units of N^2/Hz, multiply with $\hbar m \gamma_m \omega_m$.

All operators are denoted with a hat, $\hat{o}$, vectors are written in boldface (additionally, the unit vectors denoted $\hat{\mathbf{e}}$ also wear hats). The symbols for fields and their operators are usually chosen such that light fields and cavity modes are named a and c. b is used for the mechanical mode, the pump field or the local oscillator.

A core element of CQNC is the effective negative-mass oscillator. In this thesis, for brevity, the 'effective' is sometimes omitted, without wanting to imply that the mass is actually negative.

Works referenced in the preceding chapter

Aasi, J. et al., 'Advanced LIGO', *Class. Quantum Gravity* **32** (2015), 074001, DOI: 10.1088/0264-9381/32/7/074001.

Aspelmeyer, M., T. J. Kippenberg and F. Marquardt, 'Cavity optomechanics', *Rev. Mod. Phys.* **86** (2014), 1391–1452, DOI: 10.1103/RevModPhys.86.1391, arXiv: 1303.0733.

Braginsky, V. B., Y. I. Vorontsov and K. S. Thorne, 'Quantum Nondemolition Measurements', *Science* **209** (1980), 547–557, DOI: 10.1126/science.209.4456.547.

Caves, C. M., 'Quantum-mechanical radiation-pressure fluctuations in an interferometer', *Phys. Rev. Lett.* **45** (1980), 75–79, DOI: 10.1103/PhysRevLett.45.75.

---

[14]Wimmer, Steinmeyer, Hammerer and Heurs (2014).

Caves, C. M., K. S. Thorne, R. W. Drever, V. D. Sandberg and M. Zimmermann, 'On the measurement of a weak classical force coupled to a quantum-mechanical oscillator. I. Issues of principle', *Rev. Mod. Phys.* **52** (1980), 341–392, DOI: `10.1103/RevModPhys.52.341`.

Clerk, A. A., M. H. Devoret, S. M. Girvin, F. Marquardt and R. J. Schoelkopf, 'Introduction to quantum noise, measurement, and amplification', *Rev. Mod. Phys.* **82** (2010), 1155–1208, DOI: `10.1103/RevModPhys.82.1155`.

Maxwell, J. C., *A Treatise on Electricity and Magnetism*, Oxford: Clarendon, 1873, URL: `https://gallica.bnf.fr/ark:/12148/bpt6k95176j/`.

Purdy, T. P., R. W. Peterson and C. A. Regal, 'Observation of Radiation Pressure Shot Noise on a Macroscopic Object', *Science* **339** (2013), 801–804, DOI: `10.1126/science.1231282`.

Tsang, M. and C. M. Caves, 'Coherent quantum-noise cancellation for optomechanical sensors', *Phys. Rev. Lett.* **105** (2010), 123601, DOI: `10.1103/PhysRevLett.105.123601`, arXiv: `1006.1005`.

Weiss, R., 'Electromagnetically coupled broadband gravitational wave antenna', *Q. Prog. Rep. Research Lab. Electronics, Massachusetts Inst. Technol.* **105** (1972), 54, URL: `https://dcc.ligo.org/public/0038/P720002/001/P720002-00.pdf`.

Wimmer, M. H., D. Steinmeyer, K. Hammerer and M. Heurs, 'Coherent cancellation of backaction noise in optomechanical force measurements', *Phys. Rev. A* **89** (2014), 053836, DOI: `10.1103/PhysRevA.89.053836`, arXiv: `1403.2992`.

1

Measurements with Light

This chapter lays the foundations for what follows in Secs. 2 to 5. It starts with the classical and quantum-mechanical description of light. For distance measurements, light is used in interferometers and optical resonators, which are introduced in Sec. 1.2.1. Measurements with light often involve monitoring of a moving mechanical device. The formalism of such a measurement, which leads to the Standard Quantum Limit, is given in Sec. 1.3, followed by an overview of techniques to surpass the Standard Quantum Limit.

1.1 Light

Already the simple picture of plane waves as in Sec. 1.1.1 contains most of the important terms for describing light. A more realistic, and in fact for this thesis sufficient, description within the paraxial approximation of light is given in Sec. 1.1.2, where the term *mode* is defined. The second half of this section, Secs. 1.1.3 and 1.1.4, discusses a quantum-mechanical description of electromagnetic modes and formalises losses of a mode as mixing the mode with vacuum.

1.1.1 Plane waves, quadratures

One family of periodic solutions of Maxwell's equations in free space[15] are plane waves taking two arguments, position $\mathbf{r}$ and time t, and four parameters, amplitude A, phase ϕ_0, angular frequency ω, and wave vector $\mathbf{k}$.

$$E(\mathbf{r}, t) = A\cos(\omega t - \mathbf{k}\mathbf{r} + \phi_0). \quad (1.1)$$

Equally, $E(\mathbf{r}, t)$ can be written as
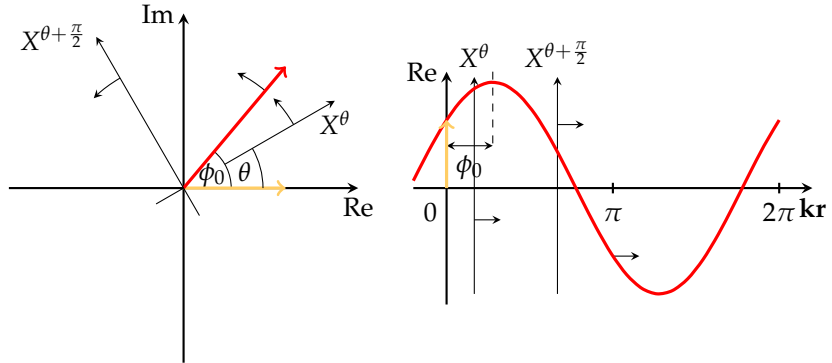
FIGURE 1.1: Left: Phasor picture of an electromagnetic field vector at time $t = 0$ and position $\mathbf{r} = 0$. Instantaneous electromagnetic field strength $E(\mathbf{r}, t)$ (yellow) and complex electromagnetic field $ae^{i(\omega t - \mathbf{kr})}$ (red). Right: Electromagnetic field strength $E(\mathbf{r}, t)$ at time $t = 0$ in space (red) and at $t = 0, \mathbf{r} = 0$ (yellow). Thin arrows indicate movement in time. Additional axes are co-moving quadrature coordinate system as in Fig. 1.2.
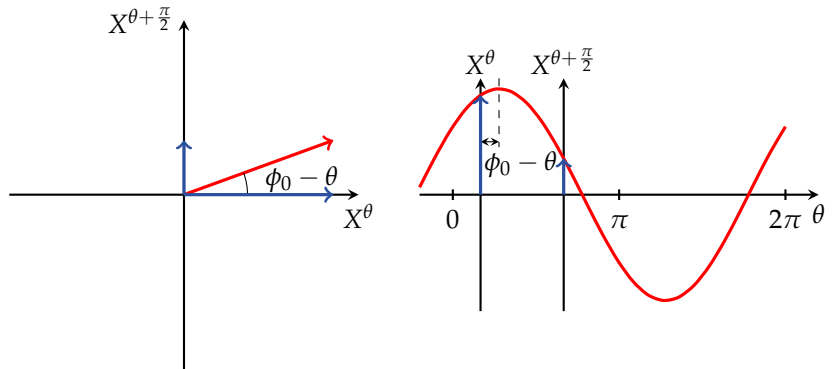
FIGURE 1.2: Phasor picture of electromagnetic quadratures in co-moving coordinate system. Left: Complex amplitude a (red) and projection of complex amplitude a onto quadrature axes (blue). Right: Projection of complex amplitude a on quadrature axis over quadrature θ (red) and projections onto quadrature axes θ and $\theta + \frac{\pi}{2}$ for fixed θ (blue).

$$E(\mathbf{r},t) = A\cos(\omega t - \mathbf{kr} + \phi_0)$$
$$= A\left(\cos(\omega t - \mathbf{kr})\cos\phi_0 + \cos(\omega t - \mathbf{kr} + \tfrac{\pi}{2})\sin\phi_0\right)$$
$$= X_1\cos(\omega t - \mathbf{kr}) - X_2\sin(\omega t - \mathbf{kr}) \tag{1.2}$$

where X_1 and X_2 are called field *quadratures* and defined as

$$X_1 = A\cos\phi_0, \qquad X_2 = A\sin\phi_0. \tag{1.3}$$

Amplitude and phase as well as the two quadratures can be used to parametrise the electromagnetic field. The first quadrature is often called amplitude quadrature as it is equal to the amplitude A in the limit of small phases ϕ_0. The second quadrature is called phase quadrature as it is proportional to phase ϕ_0 in the limit of small ϕ_0. They are, however, *not* the same as amplitude and phase:[16]

$$A = \sqrt{X_1^2 + X_2^2}, \qquad \phi_0 = \arctan\frac{X_2}{X_1}. \tag{1.4}$$

The field $E(\mathbf{r},t)$ is also often written in complex notation as to simplify calculations,

$$E(\mathbf{r},t) = \operatorname{Re} Ae^{i(\omega t - \mathbf{kr} + \phi_0)}, \tag{1.5}$$

sometimes with implicitly taking the real part. The complex part of the equation can be depicted in a complex plane as in Fig. 1.1, where the argument of the exponential, $\omega t - \mathbf{kr} + \phi_0$, defines the angle between the real axis and the line of length A leaving from the origin. This line is called *phasor*.

It is convenient to define a complex amplitude a,

$$a = Ae^{i\phi_0}. \tag{1.6}$$

Then,

$$E(t) = \operatorname{Re} ae^{i(\omega t - \mathbf{kr})} = \tfrac{1}{2}\left(ae^{i(\omega t - \mathbf{kr})} + a^*e^{-i(\omega t - \mathbf{kr})}\right)$$
$$= \tfrac{1}{2}(a + a^*)\cos(\omega t - \mathbf{kr}) + \tfrac{1}{2}i(a - a^*)\sin(\omega t - \mathbf{kr}). \tag{1.7}$$

Compare this with Eq. 1.2 and see that[17]

$$X_1 = \frac{a + a^*}{2}, \qquad X_2 = \frac{a - a^*}{2i}. \tag{1.8}$$

---

[15]Cf. Appendix A.1.

[16]This becomes particularly relevant in the quantum-mechanical description, see Sec. 1.1.3.

[17]One could also define the field, or rather the complex amplitude, as $E(t) = ae^{i(\omega t - \mathbf{kr})} + $ c.c., as does, e.g., R. W. Boyd, *Nonlinear Optics*, Amsterdam et al.: Acad. Press, 2008, Eq. 1.2.1. Then, $X_1 = a + a^*$ and $X_2 = -i(a - a^*)$. Cf. also Sec. 1.1.3, Eq. 1.31.

The same can be derived from

$$\text{Re}\, a = A \cos \phi_0 = X_1, \ \text{Im}\, a = A \sin \phi_0 = X_2 \ \Rightarrow a = X_1 + i X_2. \qquad (1.9)$$

The notion of quadratures can be generalised to arbitrary angles θ,

$$
\begin{aligned}
X^\theta &= X_1 \cos \theta + X_2 \sin \theta \\
&= \tfrac{1}{2} \left(a e^{-i\theta} + a^* e^{i\theta} \right) \\
&= A \cos \phi_0 - \theta, \qquad\qquad\qquad (1.10)
\end{aligned}
$$

$$X^{\theta + \frac{\pi}{2}} = A \sin \phi_0 - \theta, \qquad\qquad\qquad (1.11)$$

with θ called *quadrature angle*.

In the above representation of an electromagnetic field, a constant set of parameters was assumed, particularly only a single frequency ω. In reality, no field is truly *monochromatic*, as a finite lifetime of an electromagnetic wave results in a superposition of waves with in theory infinitely many different frequencies and in a finite linewidth. Often, particularly in the experimental configurations presented in the following and in the classical limit, the single-frequency approximation is nevertheless justified – except for modulated fields.

Time-dependent amplitude, phase and/or frequency changes, usually deliberately imprinted onto the light field and of a sinusoidal form, are called *modulations*. Of special interest are phase and amplitude modulations, which can be expressed as

$$A = A(t) = A(1 + m \cos \Omega t), \qquad\qquad (1.12)$$

$$\phi = \phi(t) = m \cos \Omega t, \qquad\qquad (1.13)$$

respectively, where Ω is the modulation frequency and m is the modulation index and is in practice very small. The electric field then becomes (setting $\mathbf{r} = 0$, $\phi_0 = 0$)

$$
\begin{aligned}
E_{\text{AM}} &= A \left(\cos \omega t + m \cos \omega t \cos \Omega t \right) \\
&= A \left(\cos \omega t + \tfrac{m}{2} \cos(\omega + \Omega)t + \tfrac{m}{2} \cos(\omega - \Omega)t \right), \qquad (1.14)
\end{aligned}
$$

$$E_{\text{PM}} = A \cos(\omega t + m \cos \Omega t). \qquad\qquad (1.15)$$

Amplitude-modulated light can thus be seen as a superposition of waves of three different frequencies, cf. Eq. 1.14 and Fig. 1.3. The mathematics of phase
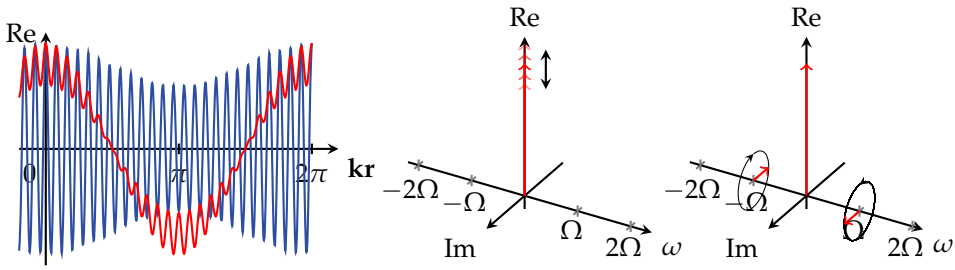
FIGURE 1.3: Amplitude modulation. Left: Strength of modulated field as in Eq. 1.14 with small modulation indices $m = 0.2$ and modulation frequency Ω much bigger (red) and much smaller (blue) than carrier frequency ω. Centre and right: Phasors in coordinate system rotating with carrier frequency ω. Centre: Phasor of modulated field. The arrow indicates the change of amplitude in time. Right: Phasor from central figure decomposed in phasors for carrier and side-bands at time $t = \pi/2\Omega$. Black arrows indicate movement in time. Adding up the phasors results again in the phasor shown in the centre. Note the difference in phase relation between side-bands at $\pm\Omega$ compared to Fig. 1.4.
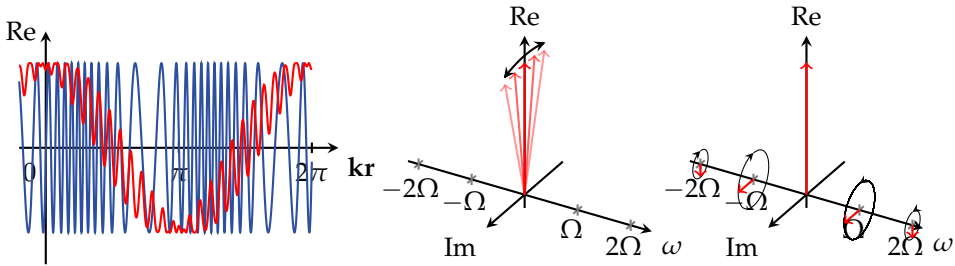
FIGURE 1.4: Phase modulation. Left: Strength of modulated field as in Eq. 1.15 with small modulation index $m = 0.4$ and a modulation frequency Ω much bigger than carrier frequency ω (red) and large modulation index $m = 10$ and a modulation frequency Ω much smaller than carrier frequency ω (blue). Centre and right: Phasors in coordinate system rotating with carrier frequency ω. Centre: Phasor of modulated field. The arrow indicates the change of phase in time. Right: Phasor from central figure decomposed in phasors for carrier and side-bands at time $t = 0$. Black arrows indicate movement in time. Adding up the phasors results again in the phasor shown in the centre. Note the difference in phase relation between side-bands at $\pm\Omega$ compared to Fig. 1.3.

modulation is slightly more involved, but Eq. 1.15 can be expanded into a sum of Bessel functions of the first kind using the Jacobi-Anger identity.[18] Technically, phase-modulated light has side-bands at every multiple of the modulation frequency. In practice and for small modulation indices m, an expansion up to a low order suffices. Expanding the phase-modulated field up to second order in m leads to

$$E_{\mathrm{PM}} = A \left[\left(1 - \frac{m^2}{4} \right) \cos \omega t - \frac{m}{2} \left(\sin(\omega - \Omega)t + \sin(\omega + \Omega)t \right) \right.$$
$$\left. - \frac{m^2}{8} \left(\cos(\omega - 2\Omega)t + \cos(\omega + 2\Omega)t \right) \right] + \mathcal{O}(m^3) \qquad (1.16)$$

with side-bands at $\pm\Omega$ and $\pm2\Omega$, see Fig. 1.4.[19]

It is not possible to measure the phase of an electromagnetic wave directly, a phase is only ever defined with regard to some reference. In a setting involving several waves, one of the phases can be chosen arbitrarily and is often set to zero, with all other phases being defined with respect to this reference. Neither can frequency or instantaneous field strength of an electromagnetic wave in the optical domain directly be measured, changes with rates of hundreds of terahertz are just to fast. Instead, the energy of a field deposited in a photodetector per unit time, its power P, is measured. The power as the number of incoming photons per time at a certain frequency is first converted into current by the photodiode, and then into voltage by a transimpedance amplifier.

The energy of an electromagnetic field is the volume integral over the energy density, which in free is space proportional to the square of electric and magnetic field strengths, such that[20]

$$H \propto \int \mathrm{d}V \left(\epsilon_0 \mathbf{E}^2(\mathbf{r}, t) + \frac{1}{\mu_0} \mathbf{B}^2(\mathbf{r}, t) \right). \qquad (1.17)$$

Under certain boundary conditions, e.g. restricting the field to a certain volume, the integration over the volume can be performed. With time-dependent constants $q(t)$ and $p(t) \propto \dot{q}(t)$, the energy, or Hamiltonian, of

---

[18]M. Abramowitz and I. A. Stegun, eds., *Handbook of Mathematical Functions: With Formulas, Graphs, and Mathematical Tables*, New York: Dover, 1972, p. 361, 9.1.44.

[19]Of course, one can also do all this in complex notation as do, e.g., C. Bond, D. Brown, A. Freise and K. A. Strain, 'Interferometer techniques for gravitational-wave detection', *Living Rev. Relativ.* **19** (2016), 1–221, Sec. 3.

[20]Cf., e.g., C. C. Gerry and P. L. Knight, *Introductory Quantum Optics*, Cambridge et al.: Cambridge University Press, 2005, Eq. 2.7.

a classical electromagnetic field with frequency ω can be written as[21]

$$H \propto \left(p^2 + \omega^2 q^2 \right). \tag{1.18}$$

As Eq. 1.18 looks like the Hamiltonian of an ordinary harmonic oscillator, the oscillating electromagnetic field can actually be understood as a harmonic oscillator. This is important for the quantisation of the electromagnetic field in Sec. 1.1.3 and for the interpretation of the approach used in Sec. 5.

The power as the energy transfer per time is defined via the intensity and the Poynting vector. The intensity $I(\mathbf{r}, t)$ is the magnitude of the time-averaged Poynting vector and for the fields in this thesis connected to the electric field strength via $|E|^2$. The power which flows through an area is the integral of the intensity over that area,[22]

$$I(\mathbf{r}, t) \propto |E|^2, \qquad P = \int \mathrm{d}A \, I(\mathbf{r}, t). \tag{1.19}$$

In practical applications, the electromagnetic fields do not have an infinite spatial extension as is assumed in the plane-wave description, see the following Sec. 1.1.2. Using normalised mode functions to describe their spatial extension, the power becomes proportional to $|E|^2$ as well. The exact conversion factors are often neglected and the measured quantities usually normalised – the output of a photodetector has units of volts anyway.

1.1.2 Modes of an electromagnetic field

The infinite spatial extension of wave in the previous chapter is in reality not true. Usually true, instead, is that the envelope of an electromagnetic wave does not vary much over one period of oscillation. This is the so-called *paraxial approximation* and leads to a family of solutions in free space, called Gaussian beams or Gaussian *modes*, see Appendix A.1.2. Modes are those solutions of a problem which do not, by themselves, change their shape over time, e.g. transform into other modes.

The field strength of Gaussian modes perpendicular to their axis of propagation follows a normal distribution as shown in Fig. 1.6. Position z_0 and beam waist w_0 at $z = z_0$ fully determine a Gaussian beam and its scaling at other

---

[21]Gerry and Knight (2005), Eq. 2.8.
[22]B. E. A. Saleh and M. C. Teich, *Fundamentals of Photonics*, 2nd, Hoboken, NJ: Wiley, 2007, Sec. 5.1.
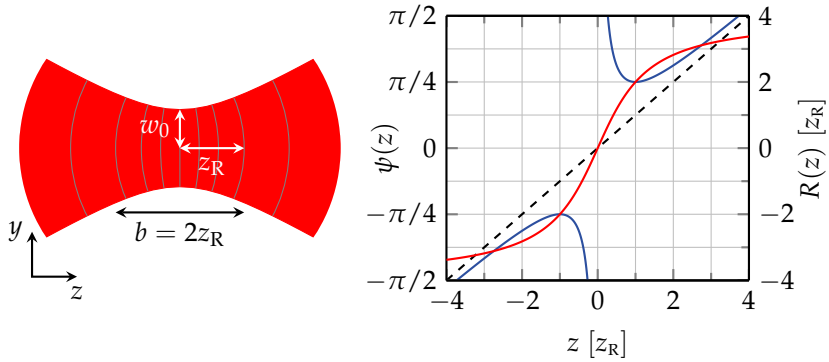
Figure 1.5: Gaussian beam. Left: Divergence of beam around the beam waist w_0 with the direction of propagation along the z-axis. Curved lines indicate points of equal phase. Right: Phase front's radius of curvature $R(z)$ (blue) and Gouy phase $\psi(z)$ (red) for a fundamental mode around the waist $z = 0$. The radius of curvature is minimal at the Rayleigh range $z = z_R$. The Gouy phase accumulated between $\pm z_R$ is equal to $\pi/2$.

positions in space. The beam waist is defined as the distance from the beam's axis of propagation where the field amplitude has decreased to $1/e$ of the maximum amplitude. From beam waist and position, other parameters (see Fig. 1.5) such as Rayleigh range z_R, waist $w(z)$, radius of curvature of the beam's phase front $R(z)$, and Gouy phase $\psi(z)$ can be determined (in the following, $z_0 = 0$):[23]

$$z_R = \frac{\pi w_0^2}{\lambda}, \tag{1.20a}$$

$$w(z) = w_0 \sqrt{1 + \left(\frac{z}{z_R}\right)}, \tag{1.20b}$$

$$R(z) = z \left[1 + \left(\frac{z_R}{z}\right)^2\right], \tag{1.20c}$$

$$\psi(z) = \arctan\frac{z}{z_R}. \tag{1.20d}$$

Equivalently, and more easily, Gaussian beams are parametrised by a single

---

[23]Cf., e.g., A. E. Siegman, *Lasers*, Sausalito, CA: University Science Books, 1986, Sec. 17.1.

$u(x,y)$

y

x

TEM$_{00}$

HG$_{01}$

HG$_{10}$

HG$_{11}$

HG$_{20}$

HG$_{20}$ + HG$_{02}$
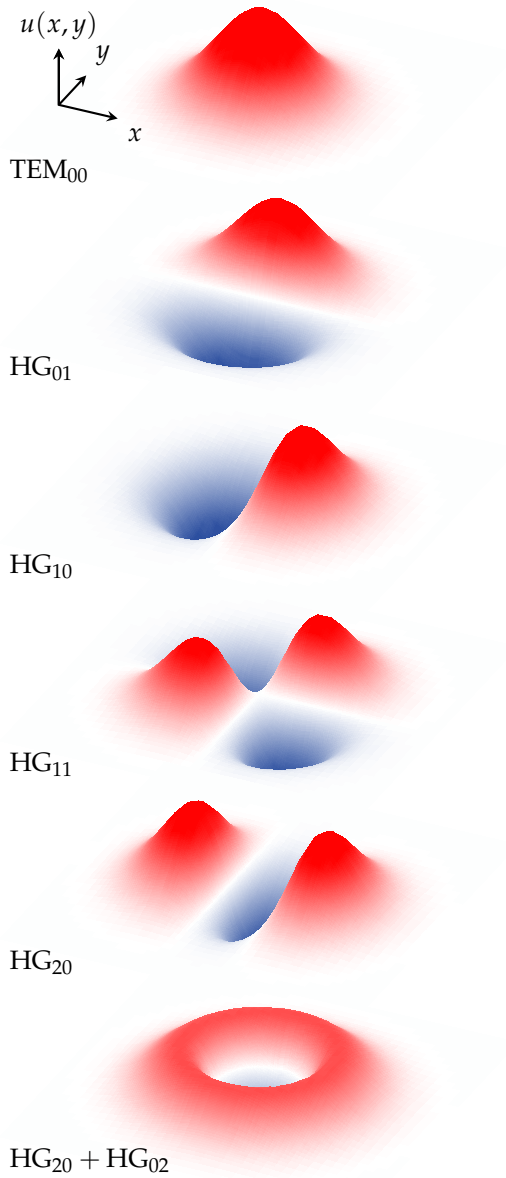
FIGURE 1.6: Transverse electromagnetic modes. Field amplitudes in a plane perpendicular to the wave's direction of propagation along the z-axis, plotted for the fundamental and some higher-order modes from Eq. 1.28. Note the radial symmetry resulting from the addition of modes HG$_{02}$ and HG$_{20}$ with the same phase.

complex beam parameter q comprising both, waist size and waist position,

$$q(z) = z + iz_R, \tag{1.21a}$$

$$\frac{1}{q(z)} = \frac{1}{R(z)} - i\frac{\lambda}{\pi w(z)^2}. \tag{1.21b}$$

The solutions to the paraxial wave equation consist of the fundamental TEM_{00} mode and higher-order modes, see Fig. 1.6. They form a complete orthogonal basis. In this approximation, each light beam can be described as a superposition of these modes. The most-commonly used higher-order modes are Hermite-Gaussian modes. They are convenient to describe beams with rectangular symmetry, which are regularly encountered in the experiment. Another set are Laguerre-Gauss modes with a cylindrical symmetry. Any Hermite-Gaussian mode can be written as a combination of Laguerre-Gaussian modes and vice versa.[24] An important aspect of higher-order modes is that the Gouy phase is a multiple of a TEM_{00}'s Gouy phase,

$$\psi_N(z) = (N+1)\psi(z), \quad \text{where } N = \begin{cases} m+n & \text{Hermite-Gauss modes,} \\ 2p+|l| & \text{Laguerre-Gauss modes,} \end{cases} \tag{1.22}$$

with m, n mode numbers of higher-order Hermite-Gaussian, and p, l mode numbers of higher-order Laguerre-Gaussian modes. The beams encountered in this work are rarely completely radially symmetric due to non-normal incidence on optical elements. Hermite-Gaussian modes are used for their description, see also Sec. 1.2.2. Non-normal incidence on focussing elements results in astigmatic beams. These beams are elliptical and have different waists in x- and y-direction and thus different Gouy phases for these directions. The Gouy phase of mode $HG_{m,n}$ can be written as[25]

$$\psi_{m,n}(z) = m\psi_x(z) + n\psi_y(z) + \frac{\psi_x(z) + \psi_y(z)}{2}. \tag{1.23}$$

The transformation of Gaussian beams by optical elements such as lenses and transmitting or reflecting surfaces can be described with $ABCD$-matrices

---

[24]The transformation is given by Eq. A3 in E. Abramochkin and V. Volostnikov, 'Beam transformations and nontransformed beams', *Opt. Commun.* **83** (1991), 123–135.

[25]Complications arise for odd-numbered modes under a non-normal angle of incidence on the optical element – then, an additional phase shift of π has to be included, see C. Mathis et al., 'Resonances and instabilities in a bidirectional ring laser', *Phys. D Nonlinear Phenom.* **96** (1996), 242–250.

of said elements via

$$q' = \frac{Aq + B}{Cq + D},\tag{1.24}$$

where q and q' are the complex beam parameters of incoming and outgoing beam as in Eq. 1.21.

Used in this thesis are *ABCD*-matrices M_n for a flat interface between materials with refractive indices n_{in} and n_{out}, M_{curved} for a curved mirror with radius of curvature R, and M_{prop} for propagation along a distance L,[26]

$$M = \begin{pmatrix} A & B \\ C & D \end{pmatrix},\tag{1.25a}$$

$$M_{prop}(L) = \begin{pmatrix} 1 & L \\ 0 & 1 \end{pmatrix},\tag{1.25b}$$

$$M_{curved}(R, \theta) = \begin{pmatrix} 1 & 0 \\ -2/R_{eff} & 1 \end{pmatrix},\tag{1.25c}$$

$$M_n(n_{in}, n_{out}) = \begin{pmatrix} 1 & 0 \\ 0 & n_{in}/n_{out} \end{pmatrix},\tag{1.25d}$$

with the effective radius of curvature $R_{eff} = R \cos \theta$ for incidence under an angle θ in the plane of incidence and $R_{eff} = R/\cos \theta$ perpendicular to the plane of incidence.

With this model, it is possible to calculate the Gouy phase shift accumulated by a beam traversing several optical elements, which change its complex parameter q_0.[27] The Gouy phase is connected to the matrix entries via[28]

$$\psi = \text{sgn } B \arccos \frac{A + D}{2}.\tag{1.26}$$

Conversely, one can calculate the characteristics of the elements from measuring the Gouy phase shift and this way characterise the optical system, see Appendix C.

The paraxial approximation is valid up to divergences of 30°,[29] roughly corresponding to beam waists of the order of, or bigger than, the beam's

---

[26]H. Kogelnik and T. Li, 'Laser Beams and Resonators', *Proc. IEEE* **54** (1966), 1312–1329; Siegman (1986), Secs. 15, 20.2.

[27]M. F. Erden and H. M. Ozaktas, 'Accumulated Gouy phase shift in Gaussian beam propagation through first-order optical systems', *J. Opt. Soc. Am. A* **14** (2008), 2190.

[28]K. Arai, *On the accumulated round-trip Gouy phase shift for a general optical cavity*, tech. rep., LIGO-T1300189, 2013, URL: https://dcc.ligo.org/LIGO-T1300189/public, Eq. 28.

[29]Siegman (1986), Sec. 16.1, p. 630.

wavelength, which is fulfilled in the experiments presented in this thesis. Additionally, Gaussian modes are solutions of a specific optical system such as an optical cavity, another reason for their widespread use.[30]

The full (monochromatic) electric vector field for one spatial mode in the Hermite-Gauss basis can thus be described as[31]

$$\mathbf{E}(t, \mathbf{r}) = \hat{\mathbf{e}}\, A\, u(\mathbf{r}) \cos(\omega t - \mathbf{k}\mathbf{r} + \phi_0), \tag{1.27}$$

$$u(\mathbf{r}) = \frac{w_0}{w(z)} H_m\left(\frac{\sqrt{2}x}{w(z)}\right) H_n\left(\frac{\sqrt{2}y}{w(z)}\right) e^{-\frac{x^2+y^2}{w(z)^2}} e^{-ik\frac{x^2+y^2}{2R(z)}} e^{i\psi(z)}, \tag{1.28}$$

with A the electric field strength amplitude at $\mathbf{r} = 0$ for a TEM$_{00}$ beam and $u(\mathbf{r})$ the mode shape, here in the Hermite-Gauss basis. A new vector was introduced in Eq. 1.28: $\hat{\mathbf{e}}$ indicates the *polarisation* of the light field, the direction in which it is oscillating. As the polarisation does not change in free space either, it represents another characteristic of a mode. The terms in $u(\mathbf{r})$ denote the decrease in field strength along z due to divergence, the spatial shape in x- and y-direction (H_m and H_n) scaled to account for the divergence, the Gaussian-shaped envelope perpendicular to the direction of propagation, also scaled, the phase due to curvature of the wave front, and the Gouy phase, an additional phase-shift of Gaussian beams compared to plane waves.

Modes can thus differ in their

- frequency ω (equivalently, wavelength λ, or magnitude of wave vector k, $k = |\mathbf{k}| = 2\pi/\lambda = \omega/c$);

- direction of propagation $\mathbf{k}/|\mathbf{k}|$;

- longitudinal and transversal mode shape $u(\mathbf{r})$;

- polarisation $\hat{\mathbf{e}}$.

Bachor and Ralph additionally list phase and amplitude to completely define a mode.[32] Often not mentioned is the temporal extension of a mode. Modes can also differ because they exist at different points in time.

---

[30] This is only true in the limit of negligible losses, cf. Siegman (1986)

[31] In more general terms, a field is a superposition of (in principle an infinite number of) components of different frequencies and a superposition of components of different mode shapes. The latter is important especially if the basis is changed from the beam's eigenbasis to, e.g., the basis of a cavity or of a second beam.

[32] H.-A. Bachor and T. C. Ralph, *A Guide to Experiments in Quantum Optics*, Weinheim: Wiley, 2004, Tab. 2.2. See also R. Schnabel, 'Squeezed states of light and their applications in laser interferometers', *Phys. Rep.* **684** (2017), 1–51, Sec. 2.1.

1.1.3 QUANTUM-MECHANICAL DESCRIPTION AND UNCERTAINTIES

Certain observations cannot be described classically any more. This is particularly true for the experiments shown in Sec. 4, but basically the whole thesis is founded on the premise of quantum mechanics and quantum noise. A quantum-mechanical description thus is necessary, but not straightforward. Often, quantum-mechanical operators, which will replace classical variables, are just stated. Seeing that the used definitions result in correct experimental predictions is motivation enough, further justification on how to arrive at correctly quantised operators is not deemed necessary. At times, this feels a but unsatisfying, but there are reasons for that. There is no such thing as 'the one' quantisation procedure. Not even historically, the path from classical variables to quantum mechanical operators was all that clear. Classical equations can be derived from their quantum mechanical counterparts. Doing it the other way round is not straightforward, similar to how the derivative of a function can easily be found whereas the integral not. Quantum-mechanical operators are *constructed* rather than derived.

The starting point of the quantisation procedure for electromagnetic fields is usually the notion that the fields in a finite volume can be expanded into a set of orthogonal (eigen-)modes.[33] The volume integral over their energy density leads to a Hamiltonian expression as in Eq. 1.17. For orthogonal modes, the Hamiltonian can be written as the Hamiltonian of independent harmonic oscillators by identifying canonical coordinates, see also Eq. 1.18. Up to now, everything has happened in the classical domain. The quantisation follows from knowing how to quantise (mechanical) harmonic oscillators, and imposing similar commutation relations onto the canonical coordinates in the light field's Hamiltonian. The correspondence between the Poisson bracket generating classical equations of motion and the quantum-mechanical commutation relation determining quantum-mechanical equations of motion then leads to similar results.[34]

A not too different procedure[35] identifies Fourier amplitudes of the electromagnetic field vector with (dimensionsless) creation and annihilation operators

---

[33]Gerry and Knight (2005), Sec. 2.1.

[34]The derivation in more or less detail can be found in many textbooks, for a quite detailed account, the reader is referred, e.g., to G. M. Wysin, 'Quantization of the Free Electromagnetic Field: Photons and Operators', 2011, URL: https://www.phys.ksu.edu/personal/wysin/notes/quantumEM.pdf.

[35]D. F. Walls and G. J. Milburn, *Quantum Optics*, Berlin, Heidelberg: Springer, 2008, Sec. 2.1.

and introduces bosonic commutation relations:

$$[\hat{a}_k, \hat{a}'^{\dagger}_k] = \delta_{kk'},\qquad(1.29)$$

where $\hat{a}_k$ belongs to one particular electromagnetic field mode denoted with k. With this, the Hamiltonian of mode $\hat{a}$ is written as

$$\hat{H} = \hbar\omega_{\mathrm{a}}\left(\hat{a}^{\dagger}\hat{a} + \frac{1}{2}\right).\qquad(1.30)$$

The annihilation and creation operators of a specific mode give rise to dimensionless quadrature operators $\hat{x}$ and $\hat{p}$ via

$$\hat{x} = \frac{\hat{a} + \hat{a}^{\dagger}}{m},\quad \hat{p} = \frac{\hat{a} - \hat{a}^{\dagger}}{im},\qquad(1.31)$$

such that

$$[\hat{x}, \hat{p}] = \frac{2i}{m^2}.\qquad(1.32)$$

In terms of quadrature operators, the Hamiltonian becomes

$$\hat{H} = \hbar\omega_{\mathrm{a}}\frac{m^2}{4}\left(\hat{x}^2 + \hat{p}^2\right).\qquad(1.33)$$

Common choices for the constant m are $m = \{1, \sqrt{2}, 2\}$.[36] From the commutation relation, an uncertainty relation follows due to $\operatorname{var}\hat{A}\operatorname{var}\hat{B} \geq \frac{1}{4}\langle\hat{C}\rangle^2$ for $[\hat{A}, \hat{B}] = i\hat{C}$:

$$\operatorname{var}\hat{x}\operatorname{var}\hat{p} \geq \frac{1}{m^4}.\qquad(1.34)$$

With the choice of m, the vacuum uncertainty is fixed to $\operatorname{var}\hat{x}_{\mathrm{vac}} = m^{-2}$. In this thesis, the prevailing conventions of different fields are used. In Sec. 2 for theoretical studies of CQNC, this is $m = \sqrt{2}$, in Sec. 4, when dealing with squeezed light, it is $m = 2$.

---

[36] $m = 1$ is chosen, e.g., by Bachor and Ralph (2004), Eq. 2.1.3 and Sec.4.1.2, Walls and Milburn (2008), Sec. 2.4 and C. W. Gardiner and P. Zoller, *Quantum noise : a handbook of Markovian and non-Markovian quantum stochastic methods with applications to quantum optics*, Berlin et al.: Springer, 2000, Sec. 10.2; $m = 2$ is chosen by Gerry and Knight (2005), Sec. 2.3 and Gardiner and Zoller (2000), Sec. 7.2.9. A choice of $m = \sqrt{2}$ leads to the same Hamiltonian as in Eq. 1.66 and the same commutation relation as the quantum harmonic oscillator, and has the advantage that expressions for creation and annihilation operators and quadrature operators are symmetric. It is used, e.g., in M. H. Wimmer, D. Steinmeyer, K. Hammerer and M. Heurs, 'Coherent cancellation of backaction noise in optomechanical force measurements', *Phys. Rev. A* **89** (2014), 053836. Cf. also Sec. 1.1.1.

In the above, the variance of the operator $\hat{x}$ is defined as the expectation value of the operator squared minus its mean,

$$\mathrm{var}\,\hat{x} = \langle \hat{x}^2 \rangle - \langle \hat{x} \rangle^2. \tag{1.35}$$

Correspondingly, a symmetrised covariance can be defined between to operators $\hat{x}_1, \hat{x}_2$,

$$\mathrm{cov}\,\hat{x}_1, \hat{x}_2 = \frac{1}{2}\langle \hat{x}_1 \hat{x}_2 + \hat{x}_2 \hat{x}_1 \rangle - \langle \hat{x}_1 \rangle \langle \hat{x}_2 \rangle. \tag{1.36}$$

Covariances and means of modes completely define the probability distribution of a normally distributed mode. The modes in this thesis all fall in this category as they are either vacuum modes, coherent modes or squeezed light fields.

Equations can become easier to solve in Fourier space. The Fourier-transformed versions of annihilation and creation operators are

$$\hat{a}(\omega) = \frac{1}{\sqrt{2\pi}} \int \mathrm{d}t\,\hat{a}(t)e^{i\omega t}, \tag{1.37}$$

$$\hat{a}^\dagger(\omega) = \frac{1}{\sqrt{2\pi}} \int \mathrm{d}t\,\hat{a}(t)^\dagger e^{i\omega t}$$

$$= \left[\frac{1}{\sqrt{2\pi}} \int \mathrm{d}t\,\hat{a}(t)e^{-i\omega t} \right]^\dagger$$

$$= \hat{a}(-\omega)^\dagger. \tag{1.38}$$

Care has to be taken with the signs in front of the frequencies. The commutation relation of the Fourier transformed pair is

$$[\hat{a}(\omega), \hat{a}^\dagger(\omega')] = \sqrt{2\pi}\delta(\omega - \omega'). \tag{1.39}$$

The factor of $\sqrt{2\pi}$ comes from the symmetric definition of the Fourier transform and the definition of the commutator in time domain.[37]

Often, also in the experiments in Secs. 3 and 4, a noise spectral density is

---

[37] Again, several conventions exist. Often, the Fourier transform is defined symmetric to keep it unitary. If working in frequency space, it is convenient to absorb the factor $\sqrt{2\pi}$ into the operators. It then shows up again by backtransformation into time domain. Alternatively, the Fourier transform can be defined asymmetric. Then, there is a factor 2π in front of one of the commutation relations.

measured. Looking at the expectation value in Fourier space,

$$\langle \hat{x}(\omega)\hat{x}(\omega')^{\dagger} \rangle = \frac{1}{2\pi} \left\langle \int \mathrm{d}t \int \mathrm{d}t' \, \hat{x}(t)e^{i\omega t}\hat{x}(t')e^{-i\omega' t'} \right\rangle$$

$$= \frac{1}{2\pi} \left\langle \int \mathrm{d}t \int \mathrm{d}\tau \, \hat{x}(t)e^{i(\omega-\omega')t}\hat{x}(t+\tau)e^{-i\omega'\tau} \right\rangle$$

$$= \delta(\omega-\omega')\frac{1}{\sqrt{2\pi}} \int \mathrm{d}\tau \, \langle \hat{x}(t)\hat{x}(t+\tau) \rangle \, e^{-i\omega'\tau}$$

$$= \delta(\omega-\omega')\frac{1}{\sqrt{2\pi}} \int \mathrm{d}\tau \, G(\tau)e^{i\omega'\tau}$$

$$= \delta(\omega-\omega')S_{xx}(\omega'), \tag{1.40}$$

where $G(\tau)$ is the auto-correlation function and the noise spectral density S_{xx} is its Fourier transform. Thus, a covariance matrix in frequency space, a *stationary spectral covariance*,[38] is connected to a noise spectral density. Note that $\hat{x}(t)$ and $\hat{x}(t')$ usually do not commute. The same is true for $\hat{x}(\omega)$ and $\hat{x}(\omega')$. An ordering of the operators has to be fixed, because different orderings result in different spectral densities. *Normal ordering* has all annihilation operators to the right of creation operators, *anti-normal ordering* has it the other way round. The former is often used by theorists and simplifies calculations because spectra and variances become zero for vacuum or coherent states. Most popular among experimentalists is the *symmetrised* version:

$$\delta(\omega-\omega')S_{xx}(\omega') = \int \mathrm{d}\tau \, \frac{1}{2} \left\langle \hat{x}(0)\hat{x}(\tau) + \hat{x}(\tau)\hat{x}(0) \right\rangle e^{-i\omega'\tau}, \tag{1.41}$$

with a corresponding symmetric spectral covariance (see also Eq. 1.36). For the purpose of this thesis, the differences between normally-ordered, anti-normally ordered and symmetrised version can be broken down to different levels of vacuum fluctuations, i.e. the variance of the vacuum state.[39]

---

[38] Walls and Milburn (2008), p. 281. 'Stationary' because the periodicity assumed for the Fourier transformation implies stationarity.

[39] It is interesting to note, but not important for the remainder of the thesis, that the different orderings correspond to different quasi-probability distribution functions, namely normally-ordered to the Glauber-Sudarshan *P*-distribution, the anti-normally ordered to Husimi *Q*-distribution, and the symmetrised to the Wigner distribution, cf., e.g., Gerry and Knight (2005), Secs. 3.7 and 3.8. Which one to use depends on the problem at hand.

1.1.4 LOSSES

Classically, losses mean a reduction in amplitude of the light field, down to zero amplitude in the case of total losses. With zero amplitude, both quadratures become zero as in Eq. 1.2. Quantum-mechanically, amplitude and phase quadrature cannot be exactly zero at the same time, this is forbidden by the uncertainty relation, Eq. 1.34. The classical description of loss cannot be valid quantum-mechanically. Instead, losses are always a two-way process. A loss does not exist without another field coupling in. Losses of a field $\hat{a}$ can be modelled as mixing mode $\hat{a}$ with a vacuum mode $\hat{a}_{\text{vac}}$,

$$\hat{a}_{\text{out}} = \sqrt{\eta}\hat{a}_{\text{in}} + \sqrt{1-\eta}\hat{a}_{\text{vac}}. \tag{1.42}$$

$\eta \in [0,1]$ gives the efficiency of the process, the smaller η, the less efficient the process and the higher the losses. The second output mode, $\hat{a}_{\text{out,2}} = \sqrt{1-\eta}\hat{a}_{\text{in}} - \sqrt{\eta}\hat{a}_{\text{vac}}$, is lost, or *traced out*.

The same idea can be applied to a (co-)variance. The (co-)variance of the output modes is a combination of the (co-)variance of input modes with the variances of vacuum. Then,

$$\text{var}\,\hat{a}_{\text{out}} = \langle \hat{a}_{\text{out}}^2 \rangle - \langle \hat{a}_{\text{out}} \rangle^2 = \left\langle \left(\sqrt{\eta}\hat{a}_{\text{in}} + \sqrt{1-\eta}\hat{a}_{\text{vac}} \right)^2 \right\rangle$$

$$= \eta\,\text{var}\,\hat{a}_{\text{in}} + (1-\eta)\,\text{var}\,\hat{a}_{\text{vac}}, \tag{1.43a}$$

$$\text{cov}\,\hat{a}_{\text{out}}, \hat{c}_{\text{out}} = \frac{1}{2}\left\langle \left(\sqrt{\eta_a}\hat{a}_{\text{in}} + \sqrt{1-\eta_a}\hat{a}_{\text{vac}} \right)\left(\sqrt{\eta_c}\hat{c}_{\text{in}} + \sqrt{1-\eta_c}\hat{c}_{\text{vac}} \right) \right\rangle$$

$$+ \frac{1}{2}\left\langle \left(\sqrt{\eta_c}\hat{c}_{\text{in}} + \sqrt{1-\eta_c}\hat{c}_{\text{vac}} \right)\left(\sqrt{\eta_a}\hat{a}_{\text{in}} + \sqrt{1-\eta_a}\hat{a}_{\text{vac}} \right) \right\rangle$$

$$= \sqrt{\eta_a\eta_c}\,\text{cov}\,\hat{a}_{\text{in}}, \hat{c}_{\text{in}}, \tag{1.43b}$$

where the vacuum input is assumed to be uncorrelated and the modes $\hat{a}$ and $\hat{c}$ have zero means.

From these Eqs. 1.42 and 1.43, it becomes clear that losses change the state of light. Large losses make a state more and more similar the a vacuum state. Losses become particularly important for quantum-noise cancellation, see Sec. 2.3, and for squeezes states of light, see Sec. 4.1.2.

1.2 INTERFEROMETRY

An electromagnetic wave experiences a phase shift **kr** when travelling a distance $|\mathbf{r}| = |\mathbf{r}_2 - \mathbf{r}_1|$ through space, see Fig. 1.1 and Eq. 1.1. This is often

used to measure distances between objects: If one object moves compared to a reference object, for example due to a force, the movement can be observed and the force onto the object measured. The phase of an electromagnetic wave is not directly accessible, but translates into a change in intensity when superimposed with a second, reference wave. This is called interferometry, the important concepts are introduced in Sec. 1.2.1.

Optical resonators or *cavities* form a special type of interferometers with particular characteristics such that they warrant a sub-chapter, Sec. 1.2.2, on their own.

1.2.1 Interferometers

Adding (plane) waves E_1 and E_2 travelling in the same direction with amplitudes A_1 and A_2, frequencies ω_1 and ω_2 and a relative phase difference $\delta\phi = \phi_1 - \phi_2$ at a point $\mathbf{r} = 0$ in space and taking the absolute squared, $|E|^2 = |E_1 + E_2|^2$, to obtain an expression proportional to the intensity leads to

$$
\begin{aligned}
|E|^2 &= |A_1 \cos(\omega_1 t + \phi_1) + A_2 \cos(\omega_2 t + \phi_2)|^2 \\
&= \tfrac{1}{2} A_1^2 \left[1 + \cos(2\omega_1 t + 2\phi_1) \right] + \tfrac{1}{2} A_2^2 \left[1 + \cos(2\omega_1 t + 2\phi_2) \right] \\
&\quad + A_1 A_2 \left[\cos\left((\omega_1 - \omega_2)t + \phi_1 - \phi_2 \right) + \cos\left((\omega_1 + \omega_2) + \phi_1 + \phi_2 \right) \right] \\
&= \frac{A_1^2 + A_2^2}{2} + A_1 A_2 \cos\left((\omega_1 - \omega_2)t + \delta\phi \right),
\end{aligned}
\tag{1.44}
$$

where in the last step, high optical frequencies $\gtrsim \omega_1, \omega_2$ were averages out. This is justified because detectors integrate over the very high frequencies of light. If $\omega_1 = \omega_2$, the signal is directly related to the phase difference $\delta\phi$, this is called homodyne interferometry. If $\omega_1 \neq \omega_2$, the signal is modulated by the difference of the frequencies, $\Omega = |\omega_1 - \omega_2|$, this is called heterodyne interferometry. To obtain phase information from heterodyne interferometry, the signal needs to be *demodulated*. It is mixed electronically with a local oscillator wave of frequency Ω and low-pass filtered by throwing away all frequencies $\gtrsim \Omega$,

$$
\begin{aligned}
|E|^2 \cos(\Omega t) &= \left(\frac{A_1^2 + A_2^2}{2} + A_1 A_2 \cos\left((\omega_1 - \omega_2)t + \delta\phi \right) \right) \cos(\Omega t) \\
&= \frac{A_1 A_2}{2} \cos\delta\phi.
\end{aligned}
\tag{1.45}
$$

In homodyne detection, a signal is directly mixed down, whereas heterodyne detection requires two mixing steps, first the optical interference, then the electronic mixing.

The homodyne detection can also be written in terms of the complex amplitude:

$$|E|^2 = |a_1 + a_2|^2 = A_1^2 + A_2^2 + 2A_1 A_2 \cos \delta\phi. \qquad (1.46)$$

An important parameter quantifying the signal strength in a homodyne set-up is called visibility $\mathcal{VIS}$, the ratio of maximum and minimum signal,

$$\mathcal{VIS} = \frac{|E_0|^2 - |E_\pi|^2}{|E_0|^2 + |E_\pi|^2} = \frac{2A_1 A_2}{A_1^2 + A_2^2} = \frac{2\sqrt{P_1 P_2}}{P_1 + P_2}, \qquad (1.47)$$

with $E(\delta\phi) = E_{\delta\phi}$, and $0 \leq \mathcal{VIS} \leq 1$. The higher the visibility, the more sensitive is the measurement to phase changes with an optimum at $A_1 = A_2$. This notion can be extended including other parameters than amplitudes A_i and more realistic electromagnetic waves, in this thesis polarised Gaussian modes. Then, the visibility is a measure of how well two modes of light interact with each other. Interference or the ability to interact nonlinearly can be quantified by their spatial mode overlap. This is often sought to be maximised, e.g. when coupling into a cavity (Sec. 1.2.2), performing homodyne detection (Sec. 4.1.2) or increasing the efficiency of nonlinear processes (Sec. 4.2.4), and can be formalised as

$$\eta_{VIS} = \left| \int \int dx \, dy \, u_1^*(x,y) \, u_2(x,y) \right| \qquad (1.48)$$

with normalised mode functions u_i as in Eq. 1.28 for waves travelling in z-direction.[40] In an experiment, the ratio of minimum to maximum power when changing the relative phase $\delta\phi$ from 0 to 2π serves as a measure for mode overlap,

$$\mathcal{VIS} = \frac{P_{\max} - P_{\min}}{P_{\max} + P_{\min}}, \qquad (1.49)$$

as long as both waves contain the same power and are otherwise able to interfere, e.g. have the same polarisation. The mode overlap is zero for modes of orthogonal transverse mode shape.

The simplest interferometer is constructed with a beam splitter overlaying two electromagnetic waves with each other as in Fig. 1.7. Homodyne detection

---

[40]Cf. L.-A. Wu, M. Xiao and H. J. Kimble, 'Squeezed states of light from an optical parametric oscillator', *J. Opt. Soc. Am. B* **4** (2008), 1465, Eq. 24.
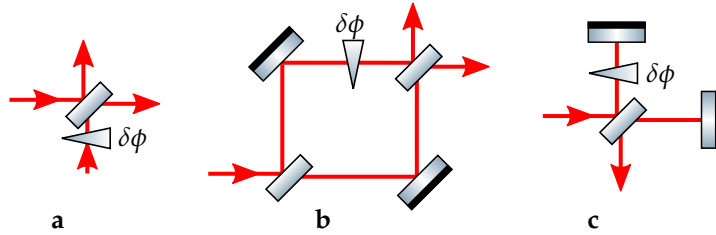
FIGURE 1.7: Interferometers. Interference after a beam splitter (a), Mach-Zehnder interferometer (b), Michelson interferometer (c). The triangle symbolises the differential phase shift $\delta\phi$ between the two interfering beams.

can be realised by two other interferometers, the Michelson interferometer and the Mach-Zehnder interferometer, also depicted in Fig. 1.7.

In this thesis, interferometers are used for characterising opto-mechanical devices (Michelson interferometer, see Sec. 3.2.1), and characterising quantum statistics of light via homodyne detection, see Sec. 4.1.2. Furthermore, several different cavities are employed. Their use is explained in the following Sec. 1.2.2.

1.2.2 Optical resonators

Another means of interfering light is via optical resonators or *cavities*. Cavities are a set of mirrors and, sometimes, lenses, aiming to superimpose an incoming beam with itself. This serves mainly two reasons:

- A cavity can provide a mode reference with respect to frequency, polarisation, spatial mode shape, and direction of propagation, and can filter the light accordingly, if necessary.

- A cavity can enhance the incoming light field in order to enhance a certain intracavity interaction.

In this thesis, the first purpose is served by mode-cleaning and mode-matching cavities, the second for enhancing the interaction with a nonlinear crystal or with an opto-mechanical oscillator.
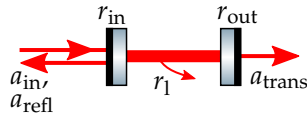
FIGURE 1.8: Input and output beams of a linear cavity, characterised by input coupler amplitude reflectivity r_{in}, output coupler amplitude reflectivity r_{out} and intracavity propagation efficiency r_l.

LONGITUDINAL MODES – FREE SPECTRAL RANGE, LINEWIDTH, FINESSE, IMPEDANCE MATCHING, REFLECTED PHASE[41]

For the light to constructively interfere with itself, the phase ϕ after one round-trip of length L_{rt}[42] has to be the same as the phase of the incoming light, $\phi(0) = \phi(L_{rt})$, which, together with $\phi(z) = 2\pi z / \lambda + \phi_0$ leads to the following condition for the cavity length L_{rt}:

$$L_{rt} = n\lambda. \tag{1.50}$$

The modes which fulfil the equation for different n are called longitudinal modes. They are spaced a frequency distance

$$\text{FSR} = \frac{c}{L_{rt}} \tag{1.51}$$

apart, called *free spectral range*. Intracavity losses limit the average number of reflections and the intracavity power stays finite. The system in equilibrium requires that a light field replicate after one round-trip. On that round-trip, it experiences a phase shift kL_{rt} due to propagation, reflections on input and end mirrors with amplitude reflectivities of r_{in} and r_{out}, losses inside the cavity, quantified via r_l and addition of incoming light through the input coupler

---

[41]A very good overview on the following is given by N. Ismail, C. C. Kores, D. Geskus and M. Pollnau, 'Fabry-Pérot resonator: spectral line shapes, generic and related Airy distributions, linewidths, finesses, and performance at low or frequency-dependent reflectivity', *Opt. Express* 24 (2016), 16366, and the Wikipedia article *Fabry-Pérot interferometer*, which is based on that paper.

[42]For standing-wave cavities, the cavity length L as the distance between the two end mirrors is usually half the round-trip length, $2L = L_{rt}$, whereas for travelling-wave cavities, the cavity length is equal to the round-trip length, $L = L_{rt}$.
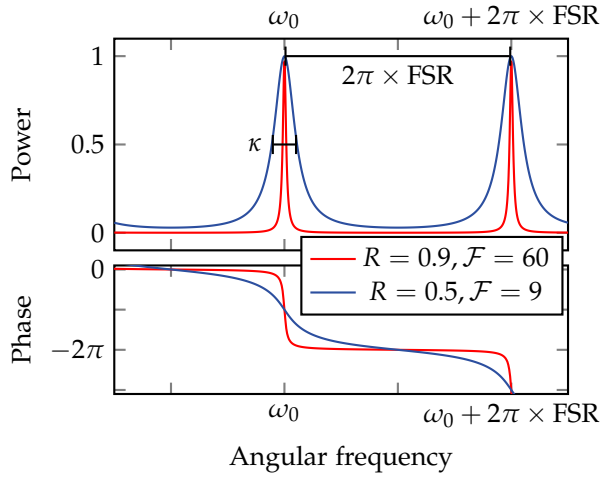
FIGURE 1.9: Intracavity resonance enhancement and phase of reflected light, plotted from Eqs. 1.53 and 1.55 for two different values for the cavity Finesse.

with amplitude transmission t_{in}, see Fig. 1.8. The equilibrium condition is[43]

$$a(L_{\text{rt}}) = r_{\text{in}}r_{\text{out}}r_1 e^{-ikL_{\text{rt}}}a(0) + it_{\text{in}}a_{\text{in}} \overset{!}{=} a(0). \tag{1.52}$$

This can be solved for the intracavity field a right after the input coupler,

$$a = \left(1 - r_{\text{in}}r_{\text{out}}r_1 e^{-ikL_{\text{rt}}}\right)^{-1} it_{\text{in}}a_{\text{in}}, \tag{1.53}$$

with a maximum of $t_{\text{in}}/(1 - r_{\text{in}}r_{\text{out}}r_1)$ at resonance ($kL_{\text{rt}} \mod 2\pi = 0$). The power build-up inside the cavity is determined by the product $r = r_{\text{in}}r_1 r_{\text{out}}$ (or, equivalently, by $R = r^2$). On resonance it is given by $(1 - \sqrt{R})^{-2} \approx 4(T_{\text{in}} + L)^{-2}$, where $L + T_{\text{in}}$ are the total round-trip power losses with T_{in} the power transmission of the input coupler and L other power losses. An often used measure for the power build-up or optical quality of a cavity is the

---

[43]Here, the convention of multiplication of i at each transmission is used. Also, for a single-sided, lossless cavity, just set $r_1 = r_{\text{out}} = 1$, and thus $t_{\text{out}} = 0$.

Finesse, defined by

$$\mathcal{F} = \frac{\pi}{2} \left(\arcsin \frac{1-r}{2\sqrt{r}} \right) \tag{1.54a}$$

$$\approx \pi \frac{\sqrt{r}}{1-r} \tag{1.54b}$$

$$\approx \frac{\pi}{1-r} \tag{1.54c}$$

$$\approx \frac{2\pi}{1-R} \tag{1.54d}$$

$$\approx \frac{2\pi}{T_{\mathrm{in}} + L} \tag{1.54e}$$

where the approximations are valid for increasing values of $r \to 1$.

The reflected and transmitted fields are

$$a_{\mathrm{refl}} = r_{\mathrm{in}} a_{\mathrm{in}} + i t_{\mathrm{in}} r_{\mathrm{out}} r_1 a$$

$$= \left(r_{\mathrm{in}} - \frac{t_{\mathrm{in}}^2 r_{\mathrm{out}} r_1}{1 - r_{\mathrm{in}} r_{\mathrm{out}} r_1 e^{-ikL_{\mathrm{rt}}}} \right) a_{\mathrm{in}}, \tag{1.55}$$

$$a_{\mathrm{trans}} = i t_{\mathrm{out}} a$$

$$= -\frac{t_{\mathrm{in}} t_{\mathrm{out}}}{r_{\mathrm{in}} r_{\mathrm{out}} r_1 e^{ikL_{\mathrm{rt}}}} a_{\mathrm{in}}. \tag{1.56}$$

The transmitted power is maximised if $r_{\mathrm{in}} = r_1 r_{\mathrm{out}}$, because then the reflected field on resonance becomes zero. Under this condition, the cavity is called *impedance-matched*. The phase of the reflected field changes with the distance from resonance, see Fig. 1.9. This fact is used for stabilising cavities, see Sec. 1.2.3.

Another cavity characteristic is its linewidth κ, in this thesis used as the full-width-half-maximum (FWHM) value as in Fig. 1.9 with units of angular frequency. It is defined via the relation

$$\mathcal{F} = \frac{\mathrm{FSR}}{\kappa/2\pi}. \tag{1.57}$$

The linewidth, or rather its reciprocal, is a measure of storage time of the cavity. κ becomes smaller for longer cavities and less intracavity losses. Additionally, the coupling to the outside of a cavity is quantified by the linewidth, it then resembles a tunnelling rate.
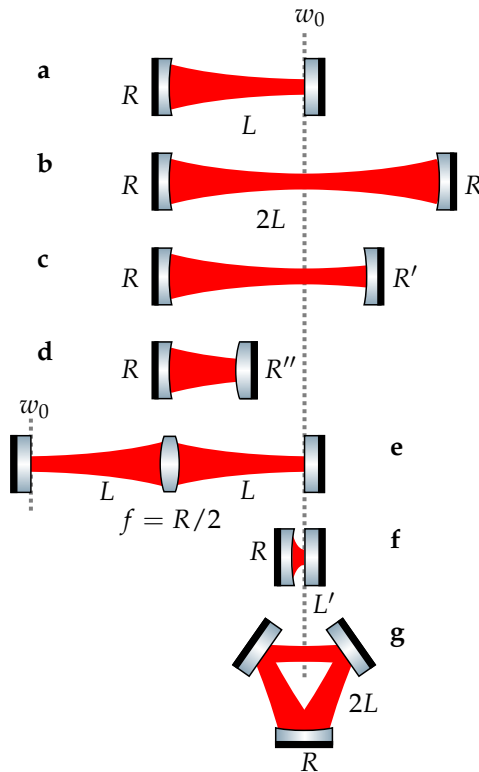
FIGURE 1.10: Single-waist cavities. Despite their different geometrical set-up, all seven cavities have the same Gaussian eigenmode with beam waist w_0 at the same position z_0. Mirrors have radii of curvature R, R', R'', cavities have lengths L, $2L$, L' (lengths of c and d not specified). Lens has focal length $f = R/2$.

Transversal modes and resonator geometries

The paraxial approximation results in transversally confined beams, which describe well the type of light found in the lab. In order for this light to be resonant between a set of mirrors, not only the phase has to replicate after one round-trip, but also the spatial, i.e. transversal mode shape. Because Gaussian beams diverge, this cannot be accomplished with only plane mirrors. A focusing element inside the cavity is needed to refocus the light beam onto itself is needed. The simplest set-up consists of one plane and one curved mirror as depicted in Fig. 1.10a. The cavity geometry is determined by the beam waist w_0, the mirror's radius of curvature R and the cavity's length L. Any two of them yield the third parameter. In practice, the radius of curvature R is fixed and a cavity length L chosen such as to obtain a certain waist w_0. If $R \neq z_R$, two possible cavity lengths to form a stable cavity exist (as long as $L < R$), one with $L > z_R$ and one with $L < z_R$, see Fig. 1.10a and f. Both are solutions to Eq. 1.20c with the wave front's radius of curvature at $z = L$ matching the mirror's radius of curvature. For cavities as in Fig. 1.10c and especially d, it is not a priori obvious whether R, R' (or R'') and the cavity length permit a beam shape which replicates after one round-trip, but stability criteria in form of so-called g-parameters exist.[44]

The same geometrical mode inside a cavity can be realised with different linear or travelling-wave cavities as in Fig. 1.10g. With the latter, astigmatism has to be taken into account. The travelling-wave cavity is no longer radially symmetric due to non-normal incidence on the curved mirror, resulting in different effective radii of curvature in x- and y-direction, see Eq. 1.25. This leads to different beam waists in horizontal and vertical direction. Also, for an odd number of mirrors, higher-order modes with an odd mode-number in the plane of incidence experience an additional phase shift,[45] see Fig. 1.12.

Sometimes, a long cavity with a small beam waist is needed. This is for example the case if a strong interaction with a nonlinear crystal and, at the same time, a small linewidth or small angles of incidence on curved mirrors are required. The small beam waist results in strong divergence and the need to refocus the beam. This leads to 'two-waist' cavities, cavities with beams of two different beam parameters as depicted in Fig. 1.11. The simplest case is that with two flat mirrors and a lens in between, Fig. 1.11a. Then, five parameters, namely the two beam waists w_0 and w_0', the two distances

---

[44]Cf. Kogelnik and Li (1966).
[45]Mathis et al. (1996).
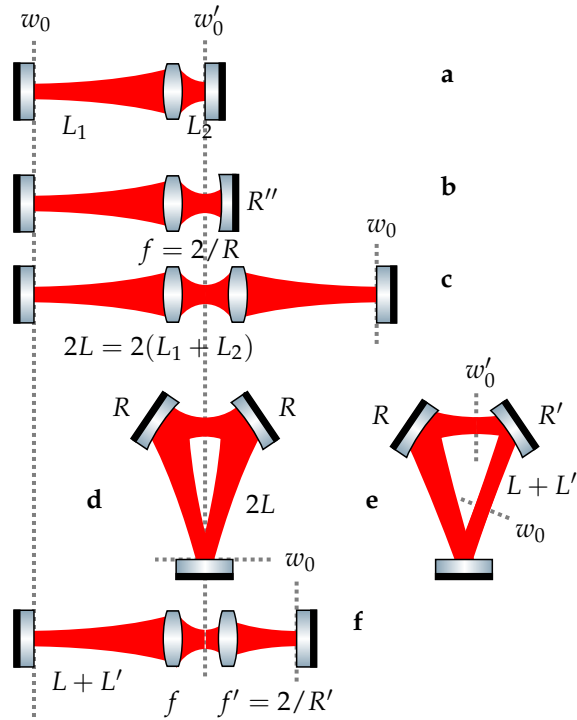
FIGURE 1.11: Two-waist cavities. Cavities a to d have the same two waists w_0 and w_0' at the same positions. Cavities e and f extend this to asymmetric set-ups, still with the same waists. Mirrors have radii of curvature R, R', R'', lenses focal lengths $f = 2/R$, $f' = 2/R'$, cavities lengths $L = L_1 + L_2$, $2L$, $L + L'$ with $L' = L_1' + L_2'$ (length of cavity b not specified).

between mirror and focusing element L_1 and L_2, and focal length f (or, radius of curvature R, if a curved mirror is used instead of a lens) describe the cavity. For any given three of them, the other two follow. Set-ups as in Fig. 1.11b–d lead to the same spatial mode with two waists w_0, w_0' at the same positions. Two unequal radii of curvature in the cavity Fig. 1.11e result in an asymmetric cavity with the same beam waists w_0, w_0'. This set-up is equivalent to the one in Fig. 1.11f. Further generalisations are possible. For linear cavities, if there is no flat mirror exactly at waist position (for travelling-wave cavities, if the cavity is not symmetric around the waists), an additional focusing element is needed to refocus the beam onto itself.[46] Cavity design is mostly a question of symmetries, as can be seen in Sec. 5.3.1, where a cavity is being designed.

Because of different Gouy phases of higher-order modes (cf. Eq. 1.23), cavities can be used to separate transverse Gaussian modes as was mentioned at the beginning of this Sec. 1.2.2. The mode spacing for a cavity as in Fig. 1.10a depends on the ratio of cavity length L to Rayleigh range z_R, as can be seen in Eq. 1.20d:

$$\psi(L) = \arctan \frac{L}{z_R}. \tag{1.58}$$

For $L = z_R$, the acquired Gouy phase and thus the mode-spacing $\psi(L) - \psi(-L)$ becomes $\pi/2$ (see also Fig. 1.5), meaning the fundamental and the even-numbered modes are resonant at the same time, and all odd-numbered modes are resonant at the same time. For $L \to 0$ or $L \to R$ (as the cavity approaches instability), the cavity becomes completely degenerate. Most often, the resonances of modes with lower mode numbers should be far away from the fundamental TEM$_{00}$ resonance so that remaining misalignment does not cause higher-order modes couple into the cavity. Instead, they should be off-resonant and get reflected. The Gouy phase then should be a fraction $\frac{m}{n}\pi$ with a big least common multiple of n and m (but $\frac{m}{n}$ far enough away from an integer number such that $\frac{m}{n}\pi$ and its smaller multiples do not lie within the 00 mode's linewidth).

ALIGNMENT OF CAVITIES

A cavity defines a spatial eigenmode, which is the transversal mode shape replicating after one round-trip. The incoming beam can be written in the

---

[46] All cavities can in principle be extended with an arbitrary number of flat mirrors without changing the cavity's eigenmode (if the total length stays constant; note also the additional phase flip in case of odd-numbered mirrors).

basis of the cavity's eigenmode. This is most probably a superposition of the fundamental mode and several higher-order modes. Usually, the incoming beam's shape is to be transformed such that it matches the cavity's eigenmode, this is called *mode matching*. There are six degrees of freedom. The beam can be shifted laterally and vertically with respect to the cavity's eigenmode, have an angle between its direction of propagation and the cavity beam's direction of propagation in either horizontal or vertical direction, or there might be a mismatch in either waist sizes or waist positions. The first four parameters[47] are called *misalignments* as they can be corrected for by changing the beam's path with adjusting mirrors, by realignment. To first order, misaligned beams couple to Hermite-Gaussian modes, most strongly to the first-order modes (01 and 10), whereas *mode mismatch*, a mismatch in waist size and/or waist position, couples to Laguerre-Gauss modes,[48] predominantly the first order-modes.[49] A mode spectrum of an intentionally misaligned cavity can be seen in Fig. 1.12.

Thoughts on cavity design

When designing a cavity, the most important design criterion is the cavity's purpose. This decides over the cavity's figures of merit, be it a particular beam intensity or beam waist, power build-up, linewidth, priority on mode separation, or even characteristics such as a small spatial footprint. Next the parameters important for the respective figure of merit need be determined and fixed, e.g. waist size, Finesse, cavity length, Gouy phases, . . . Now, the other free parameters need to be found and fixed according to convenience. Often, first design decisions regard the choice between single- and two-waist cavities or standing-wave and travelling-wave cavities. The basic single- or two-waist cavities in Fig. 1.10a and Fig. 1.11a can serve as a starting point and be expanded to other, slightly more complex geometries. Another possibility is to take an existing, working set-up and modify that as needed.

An example for designing a new cavity with particular requirements in

---

[47] Actually, three parameters are enough to describe the misalignment, see F. Bayer-Helms, 'Coupling coefficients of an incident wave and the modes of a spherical optical resonator in the case of mismatching and misalignment.', *Appl. Opt.* **23** (1984), 1369.

[48] If the cavity is astigmatic, the radial symmetry is broken and the mismatch also couples to HG modes. An addition of same order horizontal HG modes with the right relative phase is again radially symmetric, see Fig. 1.6.

[49] D. Z. Anderson, 'Alignment of resonant optical cavities.', *Appl. Opt.* **23** (1984), 2944; Bond, Brown, Freise and Strain (2016), Secs. 9.3, 9.16.
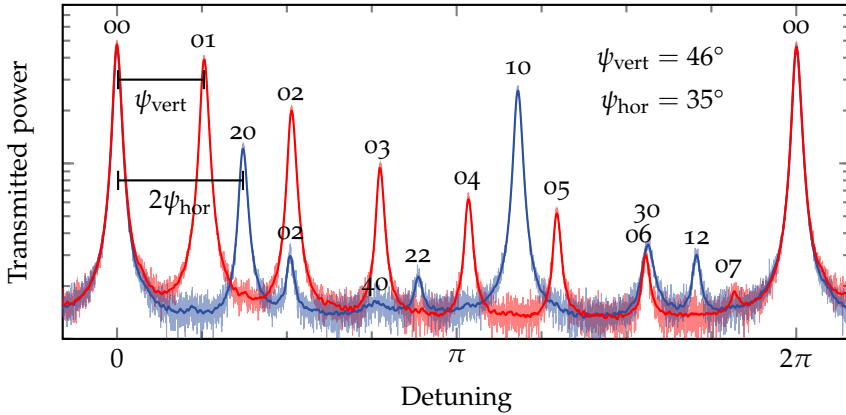
FIGURE 1.12: Higher-order modes in misaligned cavity. The plotted data stems from the 5-mirror cavity described in Sec. 5.3. Misalignment in horizontal direction caused the blue trace, misalignment in vertical direction the red trace. The cavity is astigmatic, a good mode matching can only be achieved for either horizontal or vertical direction (here, there is a remaining mode mismatch in vertical direction causing the 02 mode still being present in the blue trace). The cavity was not misaligned horizontally and vertically at the same time, therefore there is no coupling to modes of higher order in both, *m* and *n* (except for remaining vertical mode-mismatch resulting, together with horizontal misalignment, in coupling to the 12 and 22 mode). Because of the odd number of mirrors, there is a phase flip for odd-numbered horizontal modes leading to an additional phase of π (here for modes 10, 30, 12). From the traces, the Gouy phases ψ_{vert} and ψ_{hor} can be extracted and used to characterise the optical system, see Appendix C.

mind is given in Sec. 5.3 when setting up an experiment with coupled cavities.

1.2.3 Stabilising interferometers and optical resonators

Usually, interferometers and cavities need to be kept at a certain operating point. This means holding the length fixed, such that the relative phase between the interfering beams (which, in a cavity, is the beam itself after one round-trip) stays constant. In the case of cavities, often, resonant enhancement of the incoming light is desired. This means for both, the cavities and the interferometers, knowledge of the relative phase and its changes is to be acquired. The phase of a light beam is not directly accessible, it can be seen only as a relative phase in interference patterns. Different methods exist to create an apt interference.

The interference inherent to the system to be stabilised can be used in order to lock the device. The power transmitted through a cavity or an interferometer depends on the path length, i.e. accumulated phase of the cavity/interferometer. This is called side-fringe locking. Disadvantages are that this scheme is sensitive to power fluctuations, and that the single most important operating point of a cavity is not accessible with this method: At resonance, the interference signal does not provide a sign for the control loop – it is not clear in which direction to change the cavity length in order to counteract the phase change, see Fig. 1.9. The same applies to an interferometer operated at maximum or minimum interference. Hence, a reference beam is needed which can interfere with the beam leaving the system.

The reference beam for cavities is often not resonant in the cavity, but is directly reflected. This beam interferes with the beam leaking out of the cavity, thereby providing a relative phase measurement, where the relative phase only depends on what happens inside the cavity and not on any other path differences. There are several options to make a beam not resonant in the cavity. Creating side-bands via modulation which then are not resonant inside the cavity (cf. Sec. 1.1.1) is one of them. This scheme is called Pound-Drever-Hall locking.[50] Alternatively, a different polarisation which is not resonant due to residual birefringence of cavity elements (homodyne locking[51]) or due

---

[50] R. W. Drever et al., 'Laser phase and frequency stabilization using an optical resonator', *Appl. Phys. B* **31** (1983), 97–105; E. D. Black, 'An introduction to Pound–Drever–Hall laser frequency stabilization', *Am. J. Phys.* **69** (2001), 79–87.

[51] M. Heurs, I. R. Petersen, M. R. James and E. H. Huntington, 'Homodyne locking of a squeezer', *Opt. Lett.* **34** (2009), 2465.

to the cavity being non-existent for a certain polarisation because of high losses for that polarisation (Hänsch-Coulliaud[52]), or a different transverse mode which is not resonant due to a different Gouy phase shift (cf. Sec. 1.1.2, tilt locking[53]) could be used. A beam not completely off-resonant but slightly resonant still experiences a different phase shift than the resonant beam, which then also scales differently with disturbances. The interference can also lead to to an error signal. This is achieved modulation-based (slow PDH, also known as dither-locking[54]).

In principle, only relative phases matter – it depends on experimental circumstances whether to lock a beam to a cavity/to the reference beam, or the other way round. In this thesis, the laser beam acts as frequency reference. The cavities are controlled as to accommodate the laser beam. It also does not matter in theory whether one modulates the reference beam or the cavity (experimentally, very fast modulations of the order of some Megahertz might be difficult to do mechanically).

In this thesis, polarisation-based homodyne locking (for the mode cleaner), PDH-locking (for the nonlinear cavities and the coupled cavities), dither-locking (for the pump phase) and side-fringe locking (for the opto-mechanical interferometer and the homodyne detector) were deployed.[55]

1.3 Opto-mechanical interaction and the Standard Quantum Limit

Light and matter interact in various ways. In this thesis, the interaction via radiation pressure is the one of importance. The radiation pressure of a light beam exerts a force on a moveable mass. In the particle picture, photons transfer momentum onto the mass. This becomes problematic if the light beam is to observe the movement of a mass under some force. Then, a fluctuating radiation pressure force disturbs the measurement by also causing the mass to move. This is true even for quantum radiation-pressure fluctuations if the measurement is sensitive enough, and gives rise to the Standard Quantum

---

[52]T. Hansch and B. Couillaud, 'Laser frequency stabilization by polarization spectroscopy of a reflecting reference cavity', *Opt. Commun.* **35** (1980), 441–444.

[53]D. A. Shaddock, M. B. Gray and D. E. McClelland, 'Frequency locking a laser to an optical cavity by use of spatial mode interference', *Opt. Lett.* **24** (1999), 1499.

[54]Black (2001).

[55]Cf. Sec. 4.4.1, 3.2.1, and 5.3.2, respectively.

Limit (SQL).

Usually, the mass is modelled as a damped harmonic oscillator. This oscillator is characterised by its resonance frequency ω_m (in the single-mode approximation, only one resonance is considered) and its linewidth γ_m. The two give rise to the Q-factor, $Q = \frac{\omega_m}{\gamma_m}$, characterising the rate of energy loss to the environment. An oscillator is harmonic if the force counteracting its displacement is proportional to the displacement, $m\ddot{X} = -kX$. Introducing a damping γ_m proportional to its velocity $\dot{X}$ and an additional driving force F, the equations of motion of a (classical) harmonic oscillator can be written as

$$\ddot{X} + \gamma_m \dot{X} + \omega_m^2 X = \frac{F(t)}{m}, \tag{1.59}$$

where ω_m is the oscillator's resonance frequency. For the undamped, undriven oscillator ($\gamma_m = 0$, $F(t) = 0$), the Hamiltonian H as the sum of potential and kinetic energy can be constructed,

$$H = \frac{m\omega_m^2 X^2}{2} + \frac{P^2}{2m}. \tag{1.60}$$

From this Hamiltonian, the equations of motion can be found and solved with boundary conditions $X(t = 0) = X_0$ and $P(t = 0) = P_0$:

$$X(t) = X_0 \cos \omega_m t + \frac{P_0}{m\omega_m} \sin \omega_m t. \tag{1.61}$$

The Hamiltonian can be quantised with requiring $[\hat{X}, \hat{P}] = i\hbar$. Then,

$$\hat{H} = \frac{m\omega_m^2 \hat{X}^2}{2} + \frac{\hat{P}^2}{2m}, \tag{1.62}$$

$$\hat{X}(t) = \hat{X}_0 \cos \omega_m t + \frac{\hat{P}_0}{m\omega_m} \sin \omega_m t. \tag{1.63}$$

In order to precisely measure the position over time, both, position and momentum at time $t = 0$ would have to be known. Because they do not commute, this is not possible. The precision of a position measurement over time is limited. Another way to see it: $\hat{X}$ does not commute with itself at later times,[56]

$$[\hat{X}(t), \hat{X}(0)] = \frac{\sin \omega_m t}{m\omega_m} [\hat{P}_0, \hat{X}_0] \neq 0. \tag{1.64}$$

---

[56] For the special case of $t =$ multiples of $\pi/2\omega_m$, see next Sec. 1.4.
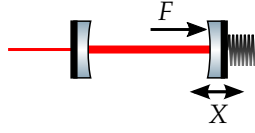
FIGURE 1.13: Simple opto-mechanical cavity with force F causing a displacement X of the moveable end mirror.

Position and momentum operators can be rescaled to dimensionless quantities, which are more convenient to use later on: $\hat{x}_m = \hat{X}/x_{ZPF}$, $\hat{p}_m = x_{ZPF}\hat{P}/\hbar$ with the mechanical zero point fluctuation x_{ZPF},[57]

$$x_{ZPF} = \sqrt{\hbar/m\omega_m}. \tag{1.65}$$

Their commutation relation is $[\hat{x}_m, \hat{p}_m] = i$. With this, the quantum-mechanical Hamiltonian can be written as

$$\hat{H} = \tfrac{1}{2}\hbar\omega_m\left(\hat{p}_m^2 + \hat{x}_m^2\right) = \hbar\omega_m\left(\hat{b}^\dagger\hat{b} + \tfrac{1}{2}\right), \tag{1.66}$$

with the phonon creation operator $\hat{b} = (x_m + ip_m)/\sqrt{2}$. The equations of motion follow to be

$$\dot{x}_m = \omega_m\hat{p}_m, \quad \dot{p}_m = -\omega_m\hat{x}_m, \quad \hat{x}(t) = \hat{x}_0\cos\omega_m t + \hat{p}_0\sin\omega_m t. \tag{1.67}$$

Let the mechanical oscillator now be an end mirror of an optical cavity as in Fig. 1.13. The cavity's resonance frequency ω_a depends on its length L and thus on the position X of the mechanical oscillator, $L(X) = L + X$. Together with the resonance condition Eq. 1.50, the resonance frequency of mode $\hat{a}$, expanded around small length changes X, is

$$\omega_a(X) = \omega_a + \left.\frac{d\omega_a(X)}{dX}\right|_{X=0}X + \mathcal{O}(X^2) \approx \omega_a + \frac{\omega_a}{L}X. \tag{1.68}$$

Using the dimensionless position operator $\hat{x}_m$ and the single-photon coupling strength g_0, the opto-mechanical Hamiltonian can be written as

$$\hat{H} = \omega_a(1 + g_0\hat{x}_m)\hat{a}^\dagger\hat{a} + \omega_m\hat{b}^\dagger\hat{b} \tag{1.69}$$

---

[57]Sometimes, an additional factor of $2^{-1/2}$ is included in the definition of x_{ZPF}, due to a different definition of quadratures, see, e.g., M. Aspelmeyer, T. J. Kippenberg and F. Marquardt, 'Cavity optomechanics', *Rev. Mod. Phys.* **86** (2014), 1391–1452, p. 1397.

with $\hbar$ set to one, which leads to the standard opto-mechanical (radiation pressure) interaction Hamiltonian[58]

$$\hat{H}_{\text{rp}} = g_0 \hat{x}_{\text{m}} \hat{a}^\dagger \hat{a} \tag{1.70}$$

with the single-photon coupling strength g_0 as

$$g_0 = \frac{\omega_{\text{c}}}{L} x_{\text{ZPF}}. \tag{1.71}$$

In Eq. 1.70, the force $\hat{a}^\dagger \hat{a}$ is coupled to the position $\hat{x}$ with strength (rate) g_0 similar to other Hamiltonians coupling a force to a position.

Usually, the cavity field $\hat{a}$ is strong and can be linearised via $\hat{a} \to \alpha + \hat{a}$ with α the mean complex amplitude. Dropping higher-order terms in $\hat{a}$ leads to

$$\hat{H}_{\text{rp}} = \alpha g_0 (\hat{a} + \hat{a}^\dagger) \hat{x}_{\text{m}} = g \hat{x}_{\text{a}} \hat{x}_{\text{m}} = \frac{g}{2} (\hat{a}\hat{b} + \hat{a}^\dagger \hat{b}^\dagger + \hat{a}\hat{b}^\dagger + \hat{a}^\dagger \hat{b}) \tag{1.72}$$

with the opto-mechanical coupling strength g as

$$g = \sqrt{2}\alpha g_0 = \sqrt{2}\alpha \frac{\omega_{\text{a}}}{L} x_{\text{ZPF}} = \sqrt{2}\alpha \frac{\omega_{\text{a}}}{L} \sqrt{\frac{1}{m\omega_{\text{m}}}}, \tag{1.73}$$

where the factor of $\sqrt{2}$, again, comes from the definition of quadratures, cf. Sec. 1.1.3.

In order to quantify the limit on measurement precision, which was argued for rather intuitively above, the set-up is as follows:[59] Again, there is an opto-mechanical cavity as in Fig. 1.13, giving rise to the same Hamiltonian as in Eq. 1.69. One cavity mirror is moving due to some force $\hat{F}$ and due to radiation pressure. Including driving and damping terms with optical linewidth κ_{a} and mechanical linewidth γ_{m} yields the following equations of motion:

$$\dot{\hat{x}}_{\text{a}} = -\kappa_{\text{a}}/2 + \sqrt{\kappa_{\text{a}}}\hat{x}_{\text{a}}^{\text{in}}, \tag{1.74a}$$

$$\dot{\hat{p}}_{\text{a}} = -\kappa_{\text{a}}/2 - g\hat{x}_{\text{m}} + \sqrt{\kappa_{\text{a}}}\hat{p}_{\text{a}}^{\text{in}}, \tag{1.74b}$$

$$\dot{\hat{x}}_{\text{m}} = \omega_{\text{m}}\hat{p}_{\text{m}}, \tag{1.74c}$$

$$\dot{\hat{p}}_{\text{m}} = -\omega_{\text{m}}\hat{x}_{\text{m}} - g\hat{x}_{\text{a}} - \gamma_{\text{m}}\hat{p}_{\text{m}} + \sqrt{\gamma_{\text{m}}}\hat{F}. \tag{1.74d}$$

[58]C. K. Law, 'Interaction between a moving mirror and radiation pressure: A Hamiltonian formulation', *Phys. Rev. A* **51** (1995), 2537–2541.

[59]For the derivation, see, e.g., Wimmer, Steinmeyer, Hammerer and Heurs (2014).

The light's phase quadrature $\hat{p}_a$ is coupled to the mechanical position $\hat{x}_m$. The evolution of the position $\hat{x}_m$ is governed by the mechanical momentum $\hat{p}_m$, which carries information about the input force $\hat{F}$ and the light's amplitude quadrature $\hat{x}_a$. The equations can be solved in Fourier space. Together with input-output relations, $\hat{p}_a^{in} + \hat{p}_a^{out} = \sqrt{\kappa_a}\hat{p}_a$, the output phase becomes

$$\hat{p}_a^{out} = e^{i\phi}\hat{p}_a^{in} - \sqrt{\kappa_a}g\chi_a x_m^0 + g^2\chi_a^2\chi_m x_a^{in} \tag{1.75}$$

with

$$e^{i\phi} = \frac{i\omega - \kappa_a/2}{i\omega + \kappa_a/2}, \quad \chi_a = \frac{1}{i\omega + \kappa_a/2}, \tag{1.76}$$

$$\chi_m = \omega_m(\omega^2 - \omega_m^2 + i\gamma_m\omega)^{-1}, \tag{1.77}$$

and the position $x_m^0 = \chi_m\sqrt{\gamma_m}F$ due to the influence of the force. The position can be estimated to be[60]

$$\hat{x}_m = -\frac{\hat{p}_a^{out}}{\sqrt{\kappa_a}g\chi_a} = x_m^0 - \frac{e^{i\phi}}{\sqrt{\kappa_a}g\chi_a}\hat{p}_a^{in} - \sqrt{\kappa_a}g\chi_a\chi_m\hat{x}_a^{in}, \tag{1.78}$$

with the 'true' position x_0 and added terms proportional to input phase and input amplitude quadrature, $\hat{p}_{in}$ and $\hat{x}_{in}$. Due to the uncertainty relation, Eg. 1.34, there is a lower limit to the product of variances of $\hat{x}_{in}$ and $\hat{p}_{in}$, leading to a trade-off between larger and smaller measurement strengths: The measurement strength, here the opto-mechanical coupling g proportional to the intracavity field amplitude, can be found once in the denominator and once in the numerator of Eq. 1.78. Additionally, the expression is frequency-dependent. For each frequency, there exists a specific measurement strength which minimises the noise. This becomes clearer if looking at the output spectral density,

$$S_{x_m x_m}^{out} = \frac{\text{var}\,\hat{p}_a^{in}}{G} + |\chi_m|^2 G\,\text{var}\,\hat{x}_a^{in}, \tag{1.79}$$

with the frequency-dependent measurement strength $G = \kappa_a|\chi_a|^2g^2 = |\chi_m|^{-1}$. Stronger measurements enhance the second term proportional to the input amplitude quadrature, this is the radiation pressure/back-action part. Weaker measurements enhance the first term proportional to the input phase quadrature, this is the shot noise/measurement imprecision part. The optimal

---

[60]Equally, one could choose to measure the force via $F = x_m^0\gamma_m^{-1/2}\chi_m^{-1}$.

measurement strength $G = |\chi_m|^{-1}$ for vacuum inputs reduces the noise spectral density to

$$S_{x_m x_m}^{\text{SQL}} = |\chi_m|. \tag{1.80}$$

In the field of weak continuous measurements, opto-mechanics and gravitational-wave detection, this limit is called *Standard Quantum Limit* (SQL).[61] The position as well as the force spectral densities and the respective Standard Quantum Limits are plotted in Fig. 1.14.

The here presented effect is *very* small and a challenge to even observe. This is mainly because of other noise sources such as thermal noise, which was neglected above, dominating the sensitivity. Nevertheless, it has the potential to limit sensitive measurements[62] and has been seen in experiments. In an opto-mechanical set-up similar to the one above, the first observation of radiation-pressure noise was by Purdy and co-workers with a membrane as mechanical oscillar inside an optical cavity.[63] Using the collective motion of atoms as mechanical oscillators, it was observed even earlier.[64] Recently, quantum fluctuations in a micro-mechanical set-up at room temperature have been published.[65]

1.4 Below the Standard Quantum Limit

The preceding Sec. 1.3 showed how the uncertainty relation for quadratures of a light field gives rise to the Standard Quantum Limit (SQL) in opto-mechanical measurements. The careful reader, however, might already have noticed that loopholes exist and this limit can be circumvented. Most of the ideas to overcome the SQL have been developed in the context of gravitational-wave detection around 1980,[66] but only recently have experiments reached

---

[61]In other fields, where there is a one-time measurement instead of a continuous measurement, and thus back-action is not relevant, *Standard Quantum Limit* refers to the measurement precision limited by measurement strength alone.

[62]Cf., e.g., J. Aasi et al., 'Advanced LIGO', *Class. Quantum Gravity* **32** (2015), 074001, Sec. 3.1 and Fig. 2.

[63]T. P. Purdy, R. W. Peterson and C. A. Regal, 'Observation of Radiation Pressure Shot Noise on a Macroscopic Object', *Science* **339** (2013), 801–804.

[64]K. W. Murch, K. L. Moore, S. Gupta and D. M. Stamper-Kurn, 'Observation of quantum-measurement backaction with an ultracold atomic gas', *Nat. Phys.* **4** (2008), 561–564.

[65]J. Cripe et al., 'Observation of a room-temperature oscillator's motion dominated by quantum fluctuations over a broad audio-frequency band' (2018).

[66]C. M. Caves et al., 'On the measurement of a weak classical force coupled to a quantum-mechanical oscillator. I. Issues of principle', *Rev. Mod. Phys.* **52** (1980), 341–392; V. B.
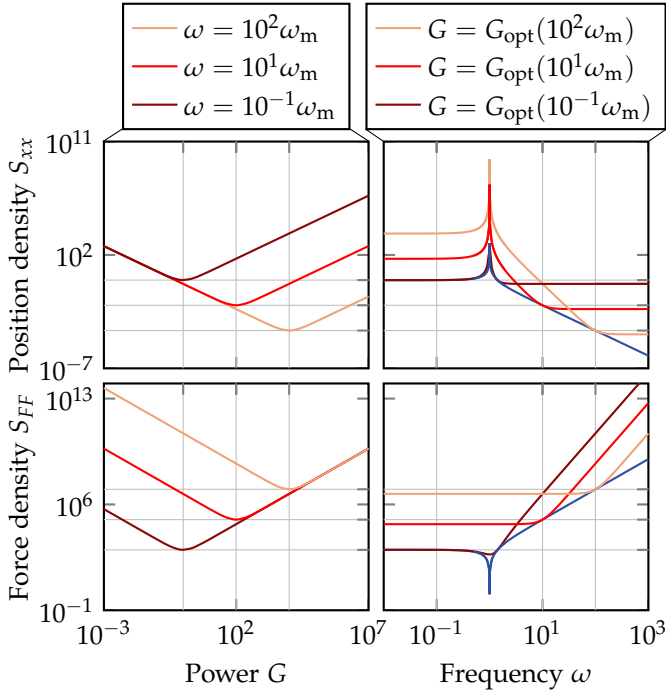
FIGURE 1.14: Noise spectral densities for measurements of a harmonic oscillator, plotted from Eq. 1.79. Crossings of grid lines indicate where the SQL (blue traces) is reached. Top row: Position sensitivity. Bottom row: Force sensitivity. Both are connected via the mechanical susceptibility χ_{m} translating applied force into position of the oscillator. Left column: Noise over measurement strength with frequencies ω fixed to $10^{-2}\omega_{\mathrm{m}}$, $10\omega_{\mathrm{m}}$, and $10^2\omega_{\mathrm{m}}$, respectively. The frequency-dependent optimal measurement strength $G_{\mathrm{opt}}(\omega) = |\chi_{\mathrm{m}}|^{-1}$ is the same for position and for force measurements. The sensitivity reached is called Standard Quantum Limit, $S_{xx}^{\mathrm{SQL}} = |\chi_{\mathrm{m}}|$, $S_{FF}^{\mathrm{SQL}} = \gamma_{\mathrm{m}}^{-1}|\chi_{\mathrm{m}}|^{-1}$. Right column: Sensitivity in frequency space with powers fixed to the optimal measurement strength $G_{\mathrm{opt}}(\omega_i) = |\chi_{\mathrm{m}}|^{-1}$ for different frequencies $\omega_i = 10^{-2}\omega_{\mathrm{m}}$, $10\omega_{\mathrm{m}}$, and $10^2\omega_{\mathrm{m}}$, respectively. The envelope with the optimal power at each frequency is the Standard Quantum Limit (blue traces).

this limit (see preceding Sec. 1.3).

One rationale behind a limit in measurement precision, given with Eq. 1.64, is that for a harmonic oscillator, the position does not commute with itself at later times. This is not true for *all* times, though: If measurement times are chosen wisely such that the measurements happen at times $t_n = n\pi/\omega_{\mathrm{m}}$ with integer n, the commutation relation $[\hat{X}(t_n), \hat{X}(0)]$ becomes zero, the measurement is back-action-free. This is called *stroboscopic* measurement.[67]

Another possibility is to use a different observable altogether. Whereas the position does not commute with itself at later times, the momentum does. A continuous measurement of the momentum is also back-action-free, this idea is known under the term *speed meter*.[68]

Observations of a system which do not result in a disturbance of the observable are called *back-action evasion* or *quantum non-demolition* (QND) measurements.[69] Modifications of the input or output of an opto-mechanical measurement apparatus can also lead to a reduction of quantum noise and to surpassing the SQL, rendering the apparatus QND, as described by by Kimble and co-workers in their similarly named paper.[70] One such modification, which has been in use in gravitational-wave detectors, is the transformation of noise characteristics of the input light, known as *squeezing*. Squeezed light shows a reduced uncertainty in one quadrature at the cost of an increased uncertainty in the orthogonal quadrature. This is very similar to using a different amount of power, as can be seen in Eq. 1.79.[71] It also means that for different measurement frequencies, the input field needs be squeezed in different quadrature angles, resulting in frequency-dependent squeezing.[72]

Braginsky, Y. I. Vorontsov and K. S. Thorne, 'Quantum Nondemolition Measurements', *Science* **209** (1980), 547–557, and references therein.

[67] Caves et al. (1980), Sec. II.F.2. realised for atoms by G. Vasilakis, V. Shah and M. V. Romalis, 'Stroboscopic Backaction Evasion in a Dense Alkali-Metal Vapor', *Phys. Rev. Lett.* **106** (2011), 143601.

[68] V. Braginsky and F. Khalili, 'Gravitational wave antenna with QND speed meter', *Phys. Lett. A* **147** (1990), 251–256.

[69] There is no clear distinction between the two nor to a third concept, *quantum-noise cancellation*. If at all, the difference might lie in what point of view is emphasised by the respective term. See also Sec. 2.1 for different angles on the same system.

[70] H. J. Kimble et al., 'Conversion of conventional gravitational-wave interferometers into quantum nondemolition interferometers by modifying their input and/or output optics', *Phys. Rev. D* **65** (2001), 022002.

[71] But not quite, as with squeezing under an angle of 45°, the SQL can be surpassed, see S. L. Danilishin, F. Y. Khalili and H. Miao, 'Advanced quantum techniques for future gravitational-wave detectors', *Living Rev. Relativ.* **22** (2019), 2–89, Fig. 10.

[72] Kimble et al. (2001), Sec. IV.B.

Conceptually similar is a technique known as *variational readout*.[73] It aims at a frequency-dependent measurement angle. For each frequency, the quadrature with the lowest back-action noise is measured, the back-action is *evaded*.

The idea studied in this thesis, coherent quantum-noise cancellation, can be understood as measuring a QND variable as well – more of that in the next Sec. 2. All these concepts, back-action evasion, QND, coherent noise cancellation, are subsumed under the broad term *quantum mechanics free subsystem* by Tsang and Caves[74] – a quantum-mechanical system constructed to be governed only by classical laws, which allow for arbitrary precision.

In gravitational-wave detection, a different approach is to modify the interferometer dynamics. The SQL of a harmonic oscillator depends on its resonance frequency, see Fig. 1.14. With a second cavity coupled to the interferometer (Signal recycling[75]) or with detuning the arms (optical spring, coupling mechanics and optics[76]), the resonance frequencies can be shifted.[77] The system leaves the free-mass domain and becomes more similar to an optical bar, one of the first devices built to measure gravitational waves. Conceptually, these schemes of coupled resonators are similar to the coupled cavities presented in Sec. 5. These approaches usually come at the cost of a reduced bandwidth. Mizuno found a sensitivity-bandwidth limit,[78] ideas to overcome this is to shape the dispersion inside a cavity, e.g. with opto-mechanical or nonlinear white-light cavities and with internal squeezing.[79]

For gravitational-wave detectors, current approaches and efforts including the above-mentioned are put together in a review by Danilishin, Khalili and Miao.[80]

---

[73] Kimble et al. (2001), Sec. IV.C.

[74] M. Tsang and C. M. Caves, 'Evading quantum mechanics: Engineering a classical subsystem within a quantum environment', *Phys. Rev. X* **2** (2012), 031016.

[75] B. J. Meers, 'Recycling in laser-interferometric gravitational-wave detectors', *Phys. Rev. D* **38** (1988), 2317–2326.

[76] A. Buonanno and Y. Chen, 'Optical noise correlations and beating the standard quantum limit in advanced gravitational-wave detectors', *Class. Quantum Gravity* **18** (2001), L95–L101.

[77] See also S. L. Danilishin and F. Y. Khalili, 'Quantum Measurement Theory in Gravitational-Wave Detectors', *Living Rev. Relativ.* **15** (2012), 5–147, Sec. 5.3.1.

[78] J. Mizuno, 'Comparison of optical configurations for laser-interferometric gravitational-wave detectors', PhD thesis, Universität Hannover and Max-Planck-Institut für Quantenoptik, Garching, 1995.

[79] Danilishin, Khalili and Miao (2019), Sec. 7.2.

[80] Danilishin, Khalili and Miao (2019).

Works referenced in the preceding chapter

Aasi, J. et al., 'Advanced LIGO', *Class. Quantum Gravity* **32** (2015), 074001, DOI: 10.1088/0264-9381/32/7/074001.

Abramochkin, E. and V. Volostnikov, 'Beam transformations and nontransformed beams', *Opt. Commun.* **83** (1991), 123–135, DOI: 10.1016/0030-4018(91)90534-K.

Abramowitz, M. and I. A. Stegun, eds., *Handbook of Mathematical Functions: With Formulas, Graphs, and Mathematical Tables*, New York: Dover, 1972, URL: http://people.math.sfu.ca/%7B~%7Dcbm/aands/abramowitz%7B%5C_%7Dand%7B%5C_%7Dstegun.pdf.

Anderson, D. Z., 'Alignment of resonant optical cavities.', *Appl. Opt.* **23** (1984), 2944, DOI: 10.1364/AO.23.002944.

Arai, K., *On the accumulated round-trip Gouy phase shift for a general optical cavity*, tech. rep., LIGO-T1300189, 2013, URL: https://dcc.ligo.org/LIGO-T1300189/public.

Aspelmeyer, M., T. J. Kippenberg and F. Marquardt, 'Cavity optomechanics', *Rev. Mod. Phys.* **86** (2014), 1391–1452, DOI: 10.1103/RevModPhys.86.1391, arXiv: 1303.0733.

Bachor, H.-A. and T. C. Ralph, *A Guide to Experiments in Quantum Optics*, Weinheim: Wiley, 2004, DOI: 10.1002/9783527619238.

Bayer-Helms, F., 'Coupling coefficients of an incident wave and the modes of a spherical optical resonator in the case of mismatching and misalignment.', *Appl. Opt.* **23** (1984), 1369, DOI: 10.1364/AO.23.001369.

Black, E. D., 'An introduction to Pound–Drever–Hall laser frequency stabilization', *Am. J. Phys.* **69** (2001), 79–87, DOI: 10.1119/1.1286663, arXiv: 1309.7933.

Bond, C., D. Brown, A. Freise and K. A. Strain, 'Interferometer techniques for gravitational-wave detection', *Living Rev. Relativ.* **19** (2016), 1–221, DOI: 10.1007/s41114-016-0002-8.

Boyd, R. W., *Nonlinear Optics*, Amsterdam et al.: Acad. Press, 2008.

Braginsky, V. and F. Khalili, 'Gravitational wave antenna with QND speed meter', *Phys. Lett. A* **147** (1990), 251–256, DOI: 10.1016/0375-9601(90)90442-Q.

Braginsky, V. B., Y. I. Vorontsov and K. S. Thorne, 'Quantum Nondemolition Measurements', *Science* **209** (1980), 547–557, DOI: 10.1126/science.209.4456.547.

Buonanno, A. and Y. Chen, 'Optical noise correlations and beating the standard quantum limit in advanced gravitational-wave detectors', *Class. Quantum Gravity* **18** (2001), L95–L101, DOI: 10.1088/0264-9381/18/15/102.

Caves, C. M., K. S. Thorne, R. W. Drever, V. D. Sandberg and M. Zimmermann, 'On the measurement of a weak classical force coupled to a quantum-mechanical oscillator. I. Issues of principle', *Rev. Mod. Phys.* **52** (1980), 341–392, DOI: 10.1103/RevModPhys.52.341.

Cripe, J., N. Aggarwal, R. Lanza, A. Libson, R. Singh, P. Heu, D. Follman, G. D. Cole, N. Mavalvala and T. Corbitt, 'Observation of a room-temperature oscillator's motion

dominated by quantum fluctuations over a broad audio-frequency band' (2018), arXiv: 1802.10069.

Danilishin, S. L. and F. Y. Khalili, 'Quantum Measurement Theory in Gravitational-Wave Detectors', *Living Rev. Relativ.* **15** (2012), 5–147, DOI: 10.12942/lrr-2012-5.

Danilishin, S. L., F. Y. Khalili and H. Miao, 'Advanced quantum techniques for future gravitational-wave detectors', *Living Rev. Relativ.* **22** (2019), 2–89, DOI: 10.1007/s41114-019-0018-y.

Drever, R. W., J. L. Hall, F. V. Kowalski, J. Hough, G. M. Ford, A. J. Munley and H. Ward, 'Laser phase and frequency stabilization using an optical resonator', *Appl. Phys. B* **31** (1983), 97–105, DOI: 10.1007/BF00702605, arXiv: 1602.03504.

Erden, M. F. and H. M. Ozaktas, 'Accumulated Gouy phase shift in Gaussian beam propagation through first-order optical systems', *J. Opt. Soc. Am. A* **14** (2008), 2190, DOI: 10.1364/josaa.14.002190.

Gardiner, C. W. and P. Zoller, *Quantum noise : a handbook of Markovian and non-Markovian quantum stochastic methods with applications to quantum optics*, Berlin et al.: Springer, 2000.

Gerry, C. C. and P. L. Knight, *Introductory Quantum Optics*, Cambridge et al.: Cambridge University Press, 2005.

Hansch, T. and B. Couillaud, 'Laser frequency stabilization by polarization spectroscopy of a reflecting reference cavity', *Opt. Commun.* **35** (1980), 441–444, DOI: 10.1016/0030-4018(80)90069-3.

Heurs, M., I. R. Petersen, M. R. James and E. H. Huntington, 'Homodyne locking of a squeezer', *Opt. Lett.* **34** (2009), 2465, DOI: 10.1364/OL.34.002465, arXiv: 0907.3323.

Ismail, N., C. C. Kores, D. Geskus and M. Pollnau, 'Fabry-Pérot resonator: spectral line shapes, generic and related Airy distributions, linewidths, finesses, and performance at low or frequency-dependent reflectivity', *Opt. Express* **24** (2016), 16366, DOI: 10.1364/OE.24.016366.

Kimble, H. J., Y. Levin, A. B. Matsko, K. S. Thorne and S. P. Vyatchanin, 'Conversion of conventional gravitational-wave interferometers into quantum nondemolition interferometers by modifying their input and/or output optics', *Phys. Rev. D* **65** (2001), 022002, DOI: 10.1103/PhysRevD.65.022002.

Kogelnik, H. and T. Li, 'Laser Beams and Resonators', *Proc. IEEE* **54** (1966), 1312–1329, DOI: 10.1109/PROC.1966.5119.

Law, C. K., 'Interaction between a moving mirror and radiation pressure: A Hamiltonian formulation', *Phys. Rev. A* **51** (1995), 2537–2541, DOI: 10.1103/PhysRevA.51.2537.

Mathis, C., C. Taggiasco, L. Bertarelli, I. Boscolo and J. R. Tredicce, 'Resonances and instabilities in a bidirectional ring laser', *Phys. D Nonlinear Phenom.* **96** (1996), 242–250, DOI: 10.1016/0167-2789(96)00024-3.

Meers, B. J., 'Recycling in laser-interferometric gravitational-wave detectors', *Phys. Rev. D* **38** (1988), 2317–2326, DOI: 10.1103/PhysRevD.38.2317.

Mizuno, J., 'Comparison of optical configurations for laser-interferometric gravitational-wave detectors', PhD thesis, Universität Hannover and Max-Planck-Institut für Quantenoptik, Garching, 1995.

Murch, K. W., K. L. Moore, S. Gupta and D. M. Stamper-Kurn, 'Observation of quantum-measurement backaction with an ultracold atomic gas', *Nat. Phys.* **4** (2008), 561–564, DOI: 10.1038/nphys965.

Purdy, T. P., R. W. Peterson and C. A. Regal, 'Observation of Radiation Pressure Shot Noise on a Macroscopic Object', *Science* **339** (2013), 801–804, DOI: 10.1126/science.1231282.

Saleh, B. E. A. and M. C. Teich, *Fundamentals of Photonics*, 2nd, Hoboken, NJ: Wiley, 2007.

Schnabel, R., 'Squeezed states of light and their applications in laser interferometers', *Phys. Rep.* **684** (2017), 1–51, DOI: 10.1016/j.physrep.2017.04.001, arXiv: 1611.03986.

Shaddock, D. A., M. B. Gray and D. E. McClelland, 'Frequency locking a laser to an optical cavity by use of spatial mode interference', *Opt. Lett.* **24** (1999), 1499, DOI: 10.1364/OL.24.001499, arXiv: 0809.0545.

Siegman, A. E., *Lasers*, Sausalito, CA: University Science Books, 1986.

Tsang, M. and C. M. Caves, 'Evading quantum mechanics: Engineering a classical subsystem within a quantum environment', *Phys. Rev. X* **2** (2012), 031016, DOI: 10.1103/PhysRevX.2.031016, arXiv: 1203.2317.

Vasilakis, G., V. Shah and M. V. Romalis, 'Stroboscopic Backaction Evasion in a Dense Alkali-Metal Vapor', *Phys. Rev. Lett.* **106** (2011), 143601, DOI: 10.1103/PhysRevLett.106.143601.

Walls, D. F. and G. J. Milburn, *Quantum Optics*, Berlin, Heidelberg: Springer, 2008, DOI: 10.1007/978-3-540-28574-8.

Wimmer, M. H., D. Steinmeyer, K. Hammerer and M. Heurs, 'Coherent cancellation of backaction noise in optomechanical force measurements', *Phys. Rev. A* **89** (2014), 053836, DOI: 10.1103/PhysRevA.89.053836, arXiv: 1403.2992.

Wu, L.-A., M. Xiao and H. J. Kimble, 'Squeezed states of light from an optical parametric oscillator', *J. Opt. Soc. Am. B* **4** (2008), 1465, DOI: 10.1364/josab.4.001465, URL: https://authors.library.caltech.edu/4725/1/WULjosab87.pdf.

Wysin, G. M., 'Quantization of the Free Electromagnetic Field: Photons and Operators', 2011, URL: https://www.phys.ksu.edu/personal/wysin/notes/quantumEM.pdf.

2

Coherent quantum-noise cancellation

The previous chapter showed the inherent limitations to opto-mechanical measurements and presented ideas to overcome the so-called Standard Quantum Limit. In this chapter, one of the ideas, which is a method to reduce back-action noise in the form of quantum radiation-pressure noise and was coined *coherent quantum-noise cancellation* (CQNC) by Tsang and Caves,[81] will be explored in detail. The first section gives intuitive explanations of how CQNC can be understood to work. Then, realisations of an effective negative mass which have been proposed, being worked on, or realised, are presented. An emphasis lies on the all-optical scheme studied in this thesis. The third section is devoted to a detailed theoretical analysis of all-optical CQNC with its requirements and limitations in two possible realisations, an integrated set-up already discussed earlier,[82] and a cascaded set-up. Both set-ups lead to, in principle, similar results. The last section of this chapter makes the link to the experiments shown in the remainder of the thesis. The evolution of design proposals is shown and the reasoning for design decisions given. A set of experimentally achievable parameters, also to be found in the above-mentioned publications,[83] is presented together with possible reductions in quantum noise for both set-ups.

---

[81] M. Tsang and C. M. Caves, 'Coherent quantum-noise cancellation for optomechanical sensors', *Phys. Rev. Lett.* **105** (2010), 123601.

[82] M. H. Wimmer, D. Steinmeyer, K. Hammerer and M. Heurs, 'Coherent cancellation of back-action noise in optomechanical force measurements', *Phys. Rev. A* **89** (2014), 053836; D. Steinmeyer, 'Towards Coherent Quantum Noise Cancellation. Untersuchungen zur kohärenten Unterdrückung von Quantenrauschen in Interferometern', Master thesis, Leibniz Universität Hannover, 2014.

[83] Wimmer, Steinmeyer, Hammerer and Heurs (2014); Steinmeyer, Master thesis (2014).
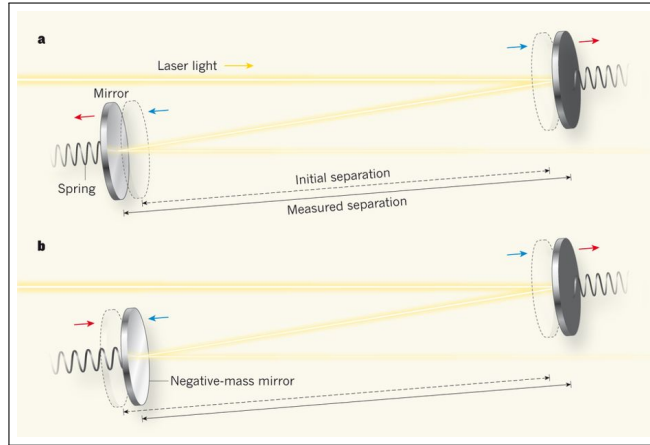
Figure 2.1: Relative position measurement with effective negative-mass oscillator. The effective negative-mass oscillator reacts oppositely to a positive-mass oscillator to a push by the reflected light. The measured separation between two mirrors, one of them with positive, one with negative mass, stays the same as their initial separation. Figure from C. G. Baker and W. P. Bowen, 'Precision measurement: Sensing past the quantum limit', *Nature* **547** (2017), 164–165.

2.1 How to think of CQNC

Different pictures for looking at back-action noise exist as shown in the previous Sec. 1.3. Consequently, a method to overcome back-action noise can also be seen in different frameworks. Three of them are presented in this section, followed by an overarching control-theoretic viewpoint.

2.1.1 CQNC as an entangled negative-mass oscillator

Measuring the position X of an object with light influences its motion as the light applies a force F to the object. The acceleration $\ddot{X}$ of a *negative* mass is opposite to the direction of the force acting on it. Newton's second law, $m\ddot{X} = F$, results in $\ddot{X} = -F/m$ for a negative mass. Sending light first onto a positive-mass object and then onto a similar object with negative mass, the *relative* distance between the two stays the same, see Fig. 2.1. The term *negative mass* in the context of back-action evasion was first used by Hammerer and

co-workers.[84] Negative masses do not exist in nature, but certain systems behave effectively as if they had a negative mass, see the next Sec. 2.2.

On a more formal level, back-action in opto-mechanical measurements is caused by measuring a variable which does not commute with itself at later times. A new observable can be constructed which *does* commute with itself as later times. This new observable is the relative position between two objects, one of them with a negative mass. The reasoning for a harmonically bound mass, i.e. a harmonic oscillator, goes along the following lines.[85]

The equation of motion for a harmonic oscillator with mass m and resonance frequency ω_{m} is as in Eq. 1.63,

$$\hat{X}(t) = \hat{X}_0 \cos \omega_{\mathrm{m}} t + \frac{\hat{P}_0}{m \omega_{\mathrm{m}}} \sin \omega_{\mathrm{m}} t. \tag{2.1}$$

The position $\hat{X}(t)$ over time cannot be known exactly because position and momentum operators $\hat{X}$ and $\hat{P}$ do not commute. Including as a reference a second harmonic oscillator with the same frequency ω_{m} and position $\hat{X}'$, momentum $\hat{P}'$, and mass m' into the measurement, the equation of motion of the relative positions is

$$\hat{X}(t) - \hat{X}'(t) = \left(\hat{X}_0 - \hat{X}_0'\right) \cos \omega_{\mathrm{m}} t + \left(\frac{\hat{P}_0}{m \omega_{\mathrm{m}}} - \frac{\hat{P}_0'}{m' \omega_{\mathrm{m}}}\right) \sin \omega_{\mathrm{m}} t. \tag{2.2}$$

If the mass of the reference oscillator is the same as that of the first oscillator but negative, $m' = -m$, the evolution of the *difference* in position,

$$\hat{X}(t) - \hat{X}'(t) = \left(\hat{X}_0 - \hat{X}_0'\right) \cos \omega_{\mathrm{m}} t + \frac{\hat{P}_0 + \hat{P}_0'}{m \omega_{\mathrm{m}}} \sin \omega_{\mathrm{m}} t, \tag{2.3}$$

depends on the *sum* of the initial momenta – which commutes with the difference in positions:

$$[\hat{X} - \hat{X}', \hat{P} + \hat{P}'] = [\hat{X}, \hat{P}] - [\hat{X}', \hat{P}'] = 0. \tag{2.4}$$

Thus, the relative position can be known arbitrarily well at all times. In other words, measuring the position of one object, the position of the other object

[84]K. Hammerer, M. Aspelmeyer, E. S. Polzik and P. Zoller, 'Establishing Einstein-Poldosky-Rosen Channels between Nanomechanics and Atomic Ensembles', *Phys. Rev. Lett.* **102** (2009), 020501.

[85]E. S. Polzik and K. Hammerer, 'Trajectories without quantum uncertainties', *Ann. Phys.* **527** (2015), A15–A20.

follows due to the relative position $\hat{X} - \hat{X}'$ being defined – the two objects became entangled through the interaction with light.

For a negative mass, the Hamiltonian is the same as the one for a positive mass, but with a negative sign, $\hat{H} = -\frac{1}{2}(m\omega_{\mathrm{m}}\hat{X}^2 + \hat{P}^2/2m)$. This points towards negative energies. Changing to dimensionless position and momentum operators as in Sec. 1.3, Eqs. 1.66 and 1.67, the negative energies correspond to negative frequencies. This is important to understand the optical realisation of negative-mass oscillators, particularly the detuning of the ancilla cavity in Sec. 2.2.

Another finding from the reasoning above is that the negative-mass oscillator has to match the positive-mass oscillator in its characteristics, which in the above are mass and resonance frequency. The picture presented here is especially handy for looking at a cascaded set-up, where the interactions of the light field with the two oscillators are sequential.

2.1.2 CQNC as destructive interference of quantum noise

Back-action is introduced by an opto-mechanical oscillator because the oscillator couples noise from one quadrature of the light field, $\hat{x}_{\mathrm{in}}$, into the other, measured quadrature, $\hat{p}_{\mathrm{out}}$, see Eqs. 1.74 in Sec. 1.3. An evasion technique might be to couple the noise from $\hat{x}_{\mathrm{in}}$ into the measured quadrature $\hat{p}_{\mathrm{out}}$ via an additional path, which provides a negative sign. In the measured quadrature, the two noises add up and cancel out – they interfere destructively. This view was proposed by Tsang and Caves[86] and can be visualised nicely with flowchart diagrams they introduced in their publication.

A flowchart diagram shows, similar to block diagrams, which variables are coupled and thus influence each other. With appropriate labelling, they are a visualisation of the equations of motion of a system. The equations of motion of an opto-mechanical system were introduced in Sec. 1.3, Eq. 1.74. The flowchart Fig. 2.2a depicts these equations. Input variables are visualised as circles, system variables as squares. Arrows lead from a variable on the right-hand side of an equation to a variable on the left-hand side. Signal and noise flow can easily be followed through the system. The readout quadrature $\hat{p}_{\mathrm{out}}$, which contains the signal to be measured, additionally includes noise from both input quadratures, $\hat{x}_{\mathrm{in}}$ and $\hat{p}_{\mathrm{in}}$, because opto-mechanics couples the input amplitude quadrature $\hat{x}_{\mathrm{in}}$ to the output phase quadrature $\hat{p}_{\mathrm{out}}$. As

---

[86]Tsang and Caves (2010).
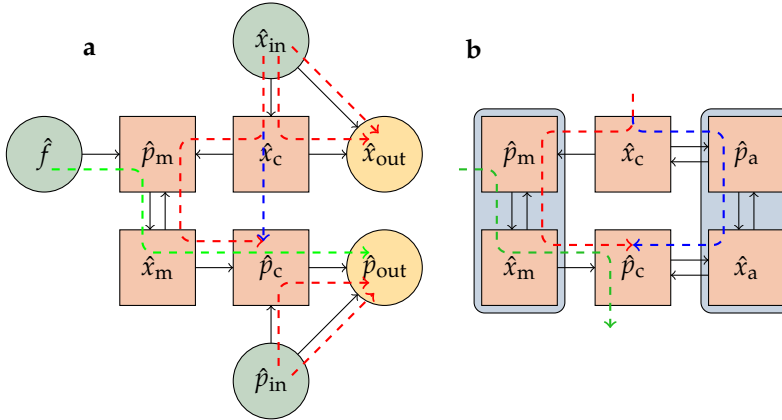
FIGURE 2.2: Flowchart of opto-mechanical interaction from Eqs. 1.74 (a), and anti-noise path (b). Green dashed line represents the signal flow, red dashed line the noise flow, blue dashed line the antinoise flow. Rectangles are system quadratures, green circles input quadratures, yellow circles output quadratures. The blue rectangles in the background denote the two harmonic oscillators coupling the light's amplitude quadrature $\hat{x}_c$ to its phase quadrature $\hat{p}_c$.

these two variables do not commute, they cannot be known or prepared both arbitrarily well. This is why squeezing does not help much: If one quadrature is prepared more precisely, the uncertainty in the other increases.

To overcome this dilemma, a second path between the input amplitude quadrature $\hat{x}_{in}$ and the output phase quadrature $\hat{p}_{out}$ is introduced. It couples these two system variables to each other in exactly the same way as the opto-mechanical oscillator couples them – only with a negative sign acquired on the way. This coupling is done with a second system with quadratures $\hat{x}_a$ and $\hat{p}_a$ as in Fig. 2.2b. Formally, it is equivalent to a negative-mass oscillator with the same characteristics as the positive-mass oscillator, which can be seen when looking at the transfer functions of both paths.[87]

This point of view stresses that not only the characteristics of the two oscillators have to be the same, but also that the couplings of the two systems to the light field need to be matched. It is especially useful when thinking in the wave picture instead of the particle picture. As the flowchart in Fig. 2.2b depicts the quadratures of both oscillators coupled to the same set of light

---

[87]Cf. Tsang and Caves (2010) and the following Sec. 2.3.2, especially Eq. 2.39.
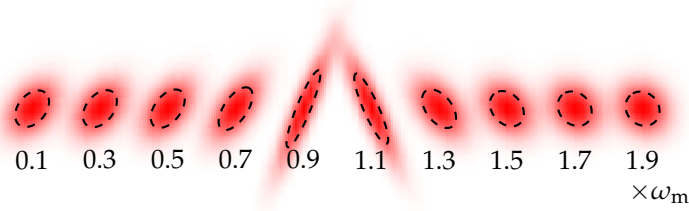
FIGURE 2.3: Ponderomotive squeezing. Quadrature uncertainties and probability density are calculated from Eq. 2.46 for different measurement frequencies for vacuum input interacting with an opto-mechanical oscillator and drawn in phase space. They show a frequency-dependent transformation of the input quadrature noises. Ellipses bound one-sigma uncertainty regions. Plot parameters as in Tab. 2.1. See also Fig. 2.12 for ponderomotive squeezing by a negative-mass oscillator.

quadratures $\hat{x}_c$ and $\hat{p}_c$, it is more useful for picturing the integrated set-up.

2.1.3 CQNC AS UNDOING PONDEROMOTIVE SQUEEZING

Opto-mechanical interactions are the cause of frequency-dependent transformation of the light quadrature uncertainties. The uncertainty ellipse in phase space is stretched, squeezed, and rotated, see Fig. 2.3. Correlations between amplitude and phase of a light field are introduced, their cause can be understood as follows: A larger field amplitude causes a larger displacement of the opto-mechanical oscillator, which leads to a bigger phase acquired by the light field reflected off that oscillator. These frequency-dependent correlations are calculated in Sec. 2.3.3, Eq. 2.46, and are called *ponderomotive squeezing*.

Ponderomotive squeezing is problematic when uncertainties of quadratures which also contain the signal to be measured are increased. CQNC can be seen as back-stretching, -squeezing and -rotating the quadrature uncertainties, as 'undoing' ponderomotive squeezing.

This picture emphasises the transformation of the light field by interacting with a mechanical oscillator instead of stressing the introduction of noise.

2.1.4 CQNC AS A FEED-FORWARD COHERENT CONTROL SCHEME

Measurement-based control of noise in the light field is not possible when dealing with quantum noise. Not all involved observables, here the two
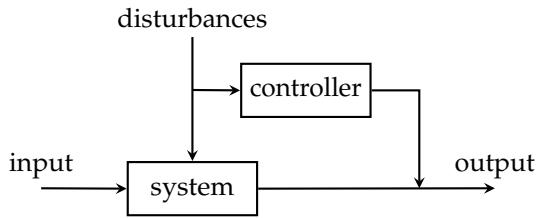
Figure 2.4: Block diagram of CQNC as a coherent feed-forward scheme. Input is the signal, i.e. the force on the mechanical oscillator. System imprints the signal on the light field. Disturbances are fluctuations in the incoming light field. Output is light field now containing signal and disturbances. Controller is the effective negative-mass oscillator. Flow from input to output corresponds to the green arrow in the flowchart diagram, Fig. 2.2, from disturbances to output through system to the red arrows, from disturbances to output through controller to blue arrow.

quadratures of the incoming light field, can be known to the needed arbitrary precision at the same time. Or, similarly, a measurement disturbs the quantum state, introducing additional uncertainties, up to the point where the state is destroyed by a projective measurement. With quantum radiation-pressure noise, one has to make do without measurement. Still, a control loop can be designed that does not disturb the quantum system. In control terminology[88] and in Fig. 2.4, a *system* translates inputs into outputs. External disturbances act on the system and cause noise in the system's output. A *controller* is introduced, which acts onto the system's output or input according to some external input to the controller. In *feed-forward* or *open-loop* control, the external input to the controller is the disturbances or some unrelated signal, e.g. a timer. In *feed-back* control, the input to the controller is the output of the system, compared to a desired reference state.

With CQNC, the input of the system is the signal to be measured. The system is the mechanical oscillator. Its output is the output phase quadrature of light, $\hat{p}_{\mathrm{out}}$, containing the signal. The disturbances acting on the system are fluctuations in the input quadratures, specifically in the input amplitude quadrature $\hat{x}_{\mathrm{in}}$. The controller is the negative-mass oscillator, also experiencing the disturbances. Taking the fluctuations $\hat{x}_{\mathrm{in}}$ as input, it acts on the output of

---

[88]Cf. K. Ogata, *Modern Control Engineering*, 5th ed., Upper Saddle River, NJ: Pearson, 2010, Sec. 1-1.

the system, the phase quadrature $\hat{p}_{\text{out}}$, to control it.[89]

In this picture, CQNC is a feed-forward control scheme.[90] As usual for feed-forward control, the system has to be known/modelled very well in order to counteract the disturbances.[91] The action of the controller needs to have exactly the opposite effect as the disturbances acting on the system. This corresponds to tailoring the negative-mass oscillator such that it matches the positive-mass oscillator.

Picturing CQNC as a feed-forward control scheme unifies the three approaches presented before and again stresses the importance of matching the two oscillators.

2.2 ALL-OPTICAL SCHEME AND OTHER REALISATIONS

The previous section aimed at helping to develop an understanding of how CQNC can work. A major question arises: How is a negative-mass oscillator to be realised when there is no negative mass available in nature? This section searches to clarify that. Two main concepts, an all-optical realisation, which this thesis is about, and an atomic realisation are presented in the following.

2.2.1 ALL-OPTICAL SCHEME

Tsang and Caves proposed a detuned cavity as a negative-mass oscillator, which is not at all intuitive. It can be explained with the following rationale. Light in a cavity can be described as a harmonic oscillator (cf. Sec. 1.1.3). To excite a harmonic oscillator means to increase its particle number by one. For a cavity mode, its photon number has to increase, which can be accomplished by a photon decaying into the cavity. If the frequency ω_{a} of the cavity mode is smaller than the frequency ω_{c} of the incoming photon, energy is won by converting the *meter* photon[92] into the cavity photon. The frequency difference can be realised by a negative detuning $\Delta_{\text{a}} = \omega_{\text{a}} - \omega_{\text{c}}$ of the cavity from the

---

[89]It could also act on the input. The symmetry of negative- and positive-mass oscillator make 'system' and 'controller' interchangeable if neglecting the signal.

[90]Tsang and Caves (2010) call it 'coherent feedforward quantum control', 'coherent' because coherence is preserved due to the lack of measurements. Yamamoto seems to sort it into the feed-back category, though (N. Yamamoto, 'Coherent versus Measurement Feedback: Linear Systems Theory for Quantum Information', *Phys. Rev. X* **4** (2014), 041029).

[91]See, e.g. Ogata (2010), Sec. 1-1.

[92]The photon is called meter photon because it is the same photon which also interacts with the positive-mass oscillator in order to measure its position.
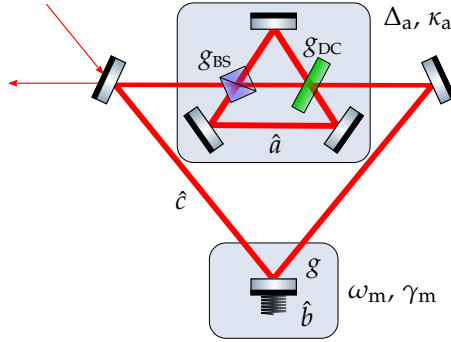
FIGURE 2.5: Schematic set-up of an all-optical CQNC scheme, proposed in M. Tsang and C. M. Caves, 'Coherent quantum-noise cancellation for optomechanical sensors', *Phys. Rev. Lett.* **105** (2010), 123601. The two rectangles denote the two harmonic oscillators, characterised by their resonance frequencies, ω_m and Δ_a, and their linewidths, γ_m and κ_a, coupled to each other via cavity mode $\hat{c}$ with coupling strengths g, g_{BS}, and g_{DC}.

incoming light.[93] Seen in a frame rotating with the frequency of the incoming light,[94] the cavity has a negative energy.[95] The Hamiltonian of that cavity can be written as

$$\hat{H} = \Delta_a \hat{a}^\dagger \hat{a} \tag{2.5}$$

with cavity mode $\hat{a}$ and the detuning $\Delta_a = \omega_a - \omega_c$ the difference of the ancilla cavity frequency ω_a from the impinging light's frequency ω_c. If the detuning is negative as required, the Hamiltonian, in this rotating frame, is the one of a negative-energy/negative-mass harmonic oscillator.

One part of the process of realising a negative-mass oscillator is done – with a detuned cavity, the so-called *ancilla* cavity, a system behaving like a negative mass, is found. The next step in order to realise CQNC is to imitate the coupling of light to a positive-mass oscillator, which is the radiation-pressure interaction. As seen in Sec. 1.3, Eq. 1.72, the linearised radiation-pressure Hamiltonian looks like the combination of a two-mode squeezing (TMS) process and a beam-splitter (BS) process,

$$H_{rp} \propto (\hat{c} + \hat{c}^\dagger)(\hat{b} + \hat{b}^\dagger) = \underbrace{\hat{b}\hat{c} + \hat{b}^\dagger \hat{c}^\dagger}_{\text{TMS}} + \underbrace{\hat{b}\hat{c}^\dagger + \hat{b}^\dagger \hat{c}}_{\text{BS}}, \tag{2.6}$$

---

[93] A requirement detailed in Sec. 2.3.2, see e.g. Eq. 2.39.

[94] Regarding rotating frames and especially the interaction picture, see Sec. 2.3.1.

[95] For the equivalence between mass and energy here, see Sec. 2.1.1.

where $\hat{c}$ is a photon annihilation operator for a cavity field and $\hat{b}$ a phonon annihilation operator for the positive-mass oscillator. In the TMS process, one particle in each mode is created. It can optically be realised by a pumped nonlinear crystal, where a pump photon is converted down into two photons of lower frequency. In the BS process, photons of the two modes are exchanged by annihilating a photon in one mode and creating one in the other. This is why Tsang and Caves suggested using a down-conversion crystal and a beam splitter to couple the meter light to the detuned ancilla cavity. Schematically, the set-up then looks as in Fig. 2.5.

Hence, the two-mode squeezing or down-conversion process will play one part in coupling the meter light to the ancilla cavity, the other part being a beam-splitterlike process. Ideas of concrete realisations will be presented in Sec. 2.4. The down-conversion and the beam-splitterlike interaction will be explored in detail in Secs. 4 and 5, respectively.

2.2.2 Other realisations

Apart from the all-optical scheme suggested by Tsang and Caves, other ideas of realising coherent quantum-noise cancellation have been around. A special mention deserves the earlier proposal by Hammerer and co-workers of realising a negative-mass oscillator with a spin ensemble[96] because with this system, back-action evasion has recently been shown experimentally.[97]

Spin ensemble

In the proposal by Hammerer and co-workers,[98] a spin ensemble in a magnetic field acts as a negative-mass oscillator. The commutation relation of three orthogonal spin components $\hat{J}_{i,j,k}$ is given by $[\hat{J}_i, \hat{J}_j] = i\epsilon_{ijk}\hat{J}_k$. If the spins of the ensemble are mainly aligned along the direction of the magnetic field **B** (e.g. along the x-axis), which can be accomplished by optically pumping them in a corresponding state, then the spin component in the x-direction can be approximated classically to J_x. The commutation relation for the other two

---

[96] Hammerer, Aspelmeyer, Polzik and Zoller (2009).

[97] C. B. Møller et al., 'Quantum back-action-evading measurement of motion in a negative mass reference frame', *Nature* **547** (2017), 191–195.

[98] Hammerer, Aspelmeyer, Polzik and Zoller (2009).
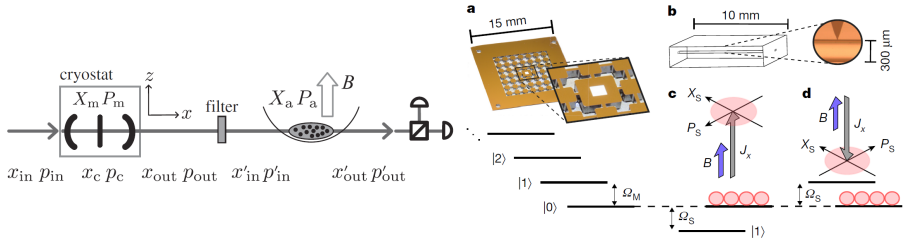
FIGURE 2.6: CQNC with a spin ensemble. Left: Scheme of experimental set-up. Figure from K. Hammerer, M. Aspelmeyer, E. S. Polzik and P. Zoller, 'Establishing Einstein-Poldosky-Rosen Channels between Nanomechanics and Atomic Ensembles', *Phys. Rev. Lett.* **102** (2009), 020501. Light passes through an optomechanical membrane-in-the-middle cavity acquiring back-action noise on the way. The filtered light is fed into a spin ensemble in a magnetic field and then detected. Right: Scheme of oscillators. Figure from C. B. Møller et al., 'Quantum back-action-evading measurement of motion in a negative mass reference frame', *Nature* **547** (2017), 191–195. The membrane constitutes the positive-mass oscillator. The spin ensemble, polarised along its J_x-component, consists of caesium atoms in a magnetic field. Its level scheme depending on (the direction of) the magnetic field can be inverted, thus rendering it an effective negative-mass oscillator.

spin operators (now normalised) becomes

$$[\hat{X}_s, \hat{P}_s] = \left[\frac{\hat{J}_y}{\sqrt{J_x}}, \frac{\hat{J}_z}{\sqrt{J_x}} \right] = i, \qquad (2.7)$$

with quadrature operators $\hat{X}_s$ and $\hat{P}_s$ and the Hamiltonian

$$\hat{H}_s = \frac{1}{2}\omega_s \left(\hat{X}_s^2 + \hat{P}_s^2 \right) \qquad (2.8)$$

that of a harmonic oscillator. This is the so-called Holstein-Primakoff transformation.[99] In a magnetic field $\mathbf{B} = B\hat{\mathbf{e}}_x$, the spin vector **J** precesses around the direction of the magnetic field with the Larmor frequency ω_s,

$$\omega_s \propto B, \qquad (2.9)$$

which is proportional to the magnetic field strength B. As the magnetic field can be made negative by reversing its direction, a harmonic oscillator with a

---

[99] K. Hammerer, A. S. Sørensen and E. S. Polzik, 'Quantum interface between light and atomic ensembles', *Rev. Mod. Phys.* **82** (2010), 1041–1093, Sec. II.A.3.

negative resonance frequency equivalent to a negative-mass oscillator can be realised.

In Polzik's group in Copenhagen, such a system has been shown to be able to reduce back-action noise.[100] Light was coupled via the Faraday effect[101] to a spin ensemble consisting of room-temperature caesium atoms. Due to its polarisation opposite to the direction of the applied magnetic field, the spin ensemble has an effective negative mass (see Fig. 2.6).

By using the spin ensemble as a negative mass, the frequency of light used to mediate the interactions is restricted to certain frequencies suitable for the interaction with the atoms. Alternatively, different frequencies could be used for interaction with atoms and with opto-mechanics as has been suggested for gravitational-wave detection:[102] A nonlinear dielectric material entangles two electromagnetic modes of different frequencies, one suited for interaction with atoms, the other at the frequency required for the (opto-mechanical) gravitational-wave detection, which then interact with their respective system. After the interactions, they are detected separately, where a suitable combination of the detections can show noise reductions below the Standard Quantum Limit.

The main benefit of using a spin system for coherent quantum-noise cancellation lies in the very small linewidth, which can be realised by the spin oscillator and which makes it easier to match the mechanical resonator in its linewidth.[103] Another advantage is the (polarisation-based) interaction between the spin ensemble and the light field, which inherently matches the opto-mechanical interaction. Only one coupling process is required as opposed to two in case of the all-optical scheme. This comes at the cost of leaving the all-optical domain and the need of handling atoms. Overcoming their frequency restrictions introduces more complexity as it adds an additional system, a nonlinear optical device similar to the one needed for all-optical CQNC.

---

[100]Møller et al. (2017).

[101]See also Hammerer, Sørensen and Polzik (2010), Sec. II.C.3.

[102]F. Y. Khalili and E. S. Polzik, 'Overcoming the Standard Quantum Limit in Gravitational Wave Detectors Using Spin Systems with a Negative Effective Mass', *Phys. Rev. Lett.* **121** (2018), 031101.

[103]In Møller et al. (2017), the linewidth is $\gamma_s \approx 2\pi \times 2\,\mathrm{kHz}$, whereas in Khalili and Polzik (2018), a linewidth as small as $\gamma_s = 3\,\mathrm{Hz}$ is assumed. For matching requirements, see next Sec. 2.3.2, particularly Eq. 2.40.

Other realisations

There are other ways to realise an effective negative mass. Similar to above, atomic gas consisting of trapped ultra-cold rubidium atoms realises a positive-mass and a negative-mass oscillator at the same time, the positive-mass mode being the atoms' centre-of-mass motion in the trapping potential, the negative-mass mode being, again, the Larmor precession of polarised spins in a magnetic field.[104] A Bose-Einstein condensate in a moving optical lattice can also be interpreted as having a negative mass and used to cancel back-action noise.[105]

A more general formalism incorporating all this was introduced by Woolley and Clerk[106] and suggests the use of a two-tone driving field to measure the combined quadrature of two harmonic oscillators. With suitable driving frequencies at $\pm$ the frequency of the harmonic oscillators, one of the harmonic oscillators becomes, in the rotating frame, a negative-mass oscillator. This has been experimentally demonstrated in the microwave regime.[107]

2.3 Theoretical studies

The previous sections clarified intuitions and ideas behind coherent quantum-noise cancellation. In this section, the theoretical foundation will be laid for an experimental realisation of all-optical CQNC. First, the general theoretical framework is laid out and it is shown how noise spectral densities can be derived from a Hamiltonian description. This is applied in the following two sections, first to an integrated and then to a cascaded set-up of all-optical CQNC. Parameters and requirements for both set-ups will be derived[108] and deviations from ideal matching of the required parameters will be studied with respect to their influence on the sensitivity. As in the corresponding

[104] J. Kohler, J. A. Gerber, E. Dowd and D. M. Stamper-Kurn, 'Negative-Mass Instability of the Spin and Motion of an Atomic Gas Driven by Optical Cavity Backaction', *Phys. Rev. Lett.* **120** (2018), 013601.

[105] B. Eiermann et al., 'Dispersion Management for Atomic Matter Waves', *Phys. Rev. Lett.* **91** (2003), 060402; K. Zhang, P. Meystre and W. Zhang, 'Back-action-free quantum optomechanics with negative-mass Bose-Einstein condensates', *Phys. Rev. A* **88** (2013), 043632.

[106] M. J. Woolley and A. A. Clerk, 'Two-mode back-action-evading measurements in cavity optomechanics', *Phys. Rev. A* **87** (2013), 063846.

[107] C. F. Ockeloen-Korppi et al., 'Quantum Backaction Evading Measurement of Collective Mechanical Modes', *Phys. Rev. Lett.* **117** (2016), 140401.

[108] For the integrated set-up, this has been published, cf. Steinmeyer, Master thesis (2014); Wimmer, Steinmeyer, Hammerer and Heurs (2014).

theoretical publication, the sensitivity is that of a force measurement,[109] but transferring the results to potentially more familiar position measurements is straightforward, see Sec. 1.3.

2.3.1 Some remarks on the methods

Most of the systems described in this thesis are calculated from a Hamiltonian describing their evolution. This is true for the calculations of CQNC later in this section as well as the detailed calculation of the down-conversion interaction and the beam-splitterlike interaction in Sec. 4.2 and Sec. 5.1.2. The approach was also used in Sec. 1.3. Using the Heisenberg equation, together with the coupling to the environment given by Langevin equations and the input-output formalism, equations of motion can be derived from the system's Hamiltonian. These equations describe the time evolution of observables – the interaction picture is used which means the uninteresting time dynamics are transferred to the wave functions, whereas the observables follow the interesting dynamics. These often will be linearised and approximated, meaning higher-order terms will be neglected as was already done in Sec. 1.3, and can be solved in frequency space as steady-state solutions suffice. From this, noise spectral densities can be derived and a signal-to-noise ratio can be calculated.

Inherent to the Hamiltonian formulation is the single-mode approximation, its validity for the systems under study needs to be ensured. In this thesis, it is usually assumed that only one mode of each system takes part in the interaction, which is, of course, generally not true. Close to the resonances of each system, the approximations are valid.

Because most of the equations of motion are coupled differential equations, they are usually conveniently described using matrices.

The interaction picture

In quantum physics as well as in classical physics, a Hamiltonian determines the time evolution of the system. In quantum physics, this happens via the

---

[109]Wimmer, Steinmeyer, Hammerer and Heurs (2014), note that the force is dimensionless.

Schrödinger equation,[110]

$$ i\hbar \frac{\mathrm{d}}{\mathrm{d}t}|\psi_S(t)\rangle = \hat{H}|\psi_S(t)\rangle. \tag{2.10} $$

For a time-independent Hamiltonian $\hat{H}$, it can easily be solved:

$$ |\psi_S(t)\rangle = e^{-i\hat{H}t/\hbar}|\psi_S(0)\rangle. \tag{2.11} $$

The time evolution operator $\hat{U}(t)$ transports the state $|\psi_S(t)\rangle$ from 0 to t,

$$ \hat{U}(t) = e^{-i\hat{H}t/\hbar}. \tag{2.12} $$

Expectation values of measurements are found from Born's rule,[111]

$$ \overline{A}(t) = \langle \hat{A} \rangle = \langle \psi_S(t)|\hat{A}_S|\psi_S(t)\rangle, \tag{2.13} $$

where $\hat{A}$ is an operator required to be Hermitian and represents the quantity to be measured. Up to now, the equations were written in the Schrödinger picture. Now choose $\hat{A}$ instead of $|\psi\rangle$ to evolve in time,

$$ \overline{A}(t) = \langle \psi_H|\hat{U}^\dagger(t)\hat{A}_S\hat{U}(t)|\psi_H\rangle = \langle \psi_H|\hat{A}_H(t)|\psi_H\rangle \tag{2.14} $$

with $|\psi_H\rangle = |\psi_S(0)\rangle$. This is called Heisenberg picture. The time evolution of the operators can be written as

$$ \frac{\mathrm{d}}{\mathrm{d}t}\hat{A}_H = -i\hbar[\hat{H}, \hat{A}_H], \tag{2.15} $$

which can be easily verified by taking the derivative of $\hat{A}_H = \hat{U}^\dagger \hat{A}_S \hat{U}$.

Predominantly used in this thesis is the interaction picture: Trivial time evolutions, in this thesis mainly the oscillation of a light field with a certain frequency, are imposed onto the states $|\psi_I(t)\rangle$, whereas the interesting time evolutions, such as changes of the state due to interactions, are imposed onto the operators $\hat{A}_I(t)$. This is equivalent to moving into a frame rotating

---

[110]The indices S, H, and I clarify whether the Schrödinger, the Heisenberg, or the Interaction picture is used. For the treatment in this subsection, see, e.g., the brief overviews in C. C. Gerry and P. L. Knight, *Introductory Quantum Optics*, Cambridge et al.: Cambridge University Press, 2005, Appendix C, and C. W. Gardiner and P. Zoller, *Quantum noise : a handbook of Markovian and non-Markovian quantum stochastic methods with applications to quantum optics*, Berlin et al.: Springer, 2000, Secs. 4.1.2–4.1.4, or any other textbook on quantum physics.

[111]The expectation value here is time-dependent, requiring it be taken on timescales much shorter than the evolution of the system.

with the oscillation frequency. The Hamiltonian is split into two parts, $\hat{H} = \hat{H}_0 + \hat{H}'$, where $\hat{H}_0$ contains the trivial evolution and $\hat{H}'$ the interesting part (the perturbation). The trivial evolution can be written with $U_0 = \exp i\hat{H}_0 t/\hbar$. Then,

$$\hat{A}_I = \hat{U}_0^\dagger A_S \hat{U}_0, \tag{2.16}$$

$$i\hbar \frac{\mathrm{d}}{\mathrm{d}t} |\psi_I(t)\rangle = \hat{H}_0 |\psi_I(t)\rangle. \tag{2.17}$$

This gives rise to the equations of motion for an operator in the interaction picture:

$$\hat{H}_I = i\frac{\mathrm{d}\hat{U}_0}{\mathrm{d}t}\hat{U}_0^\dagger + \hat{U}_0 \hat{H} \hat{U}_0^\dagger = \hat{U}_0 \hat{H}' \hat{U}_0^\dagger, \tag{2.18}$$

such that, again,

$$i\hbar \frac{\mathrm{d}}{\mathrm{d}t} \hat{A}_I(t) = [\hat{A}_I(t), \hat{H}_I]. \tag{2.19}$$

The new Hamiltonian $\hat{H}_I$ contains $\hat{H}'$ but might not be time-independent any more. Often, the rotating wave approximation is used and all terms rotating fast are averaged to zero, thus getting rid of the time dependence.

Note two things: First, only *pure* states are handled in this formalism. For mixed states, described with a density matrix, the equations are similar, but not needed in the context of this thesis. Second, only *closed* systems are subject to the above treatment. In reality, the systems dealt with in this thesis are *open*, that means they are coupled to some bath in the course of which information is lost. This coupling can be modelled with Lindblad operators.[112] For the purpose of this thesis it is enough to obtain the equations of motion with added damping and driving terms as in Eq. 2.20. The emerging equations are called *Langevin* equations.[113]

The interesting part is to actually find a Hamiltonian which describes the system to then derive equations of motion. Often, this is done the other way round – a Hamiltonian is constructed such that the wanted equations of motion can be derived. This has been done for a variety of systems. In this thesis, the important ones are the Hamiltonian of an optical cavity, which is the one of a harmonic oscillator, the opto-mechanical Hamiltonian,[114]

---

[112] As long as Markov approximation is valid, cf. Gardiner and Zoller (2000), Sec. 5.2.2.

[113] Gardiner and Zoller (2000), Sec. 5.3.2.

[114] C. K. Law, 'Interaction between a moving mirror and radiation pressure: A Hamiltonian formulation', *Phys. Rev. A* **51** (1995), 2537–2541.

the squeezing Hamiltonian[115] and the beam-splitter Hamiltonian.[116] An effective Hamiltonian for a wave plate is constructed in Sec. 5.2.1. As common for Hamiltonians, all these cases require the *single-mode approximation* to be valid.[117] Only one of the resonant frequencies the systems exhibit is of interest. It is usually justified, at least for the use cases opto-mechanics and squeezing. Care has to be taken with coupled cavities as the coupling becomes easily strong enough to reach towards higher-order modes, cf. Sec. 5.

FROM A HAMILTONIAN TO A NOISE SPECTRAL DENSITY

A Hamiltonian H_{sys} together with the quantum Langevin equations[118] gives rise to the equation of motion for an operator $\hat{a}$ via

$$\dot{\hat{a}} = \frac{i}{\hbar}[\hat{H}, \hat{a}] - \frac{\kappa}{2}\hat{a} + \sqrt{\kappa}\hat{a}_{in}. \tag{2.20}$$

The damping term $\kappa\hat{a}$ and the driving term $\sqrt{\kappa}\hat{a}_{in}$ with linewidth κ stem from using the Lindblad equation to couple the system to a bath via a jump operator. Alternatively, one can write above equation as[119]

$$\dot{\hat{a}} = \frac{i}{\hbar}[\hat{H}, \hat{a}] + \frac{\kappa}{2}\hat{a} - \sqrt{\kappa}\hat{a}_{out}, \tag{2.21}$$

which is the time reversal of the previous equation. Both together give rise to the boundary conditions

$$\hat{a}_{in} + \hat{a}_{out} = \sqrt{\kappa}\hat{a}. \tag{2.22}$$

This so-called *input-output formalism* uses the Markov approximation. The system's time evolution only depends on the actual state – the system and its bath have no memory of past interactions.

A vector $\hat{x}$ contains all n system variables (quadratures). Damping and system evolution are included into M_{sys}. The input-output relations can be

[115] W. H. Louisell, A. Yariv and A. E. Siegman, 'Quantum fluctuations and noise in parametric processes. I.', *Phys. Rev.* **124** (1961), 1646–1654.
[116] Gerry and Knight (2005), Sec. 6.2, Eq. 6.12.
[117] Especially the interaction Hamiltonians. Hamiltonians for independent modes can easily be written as sums of the single-mode Hamiltonian.
[118] Gardiner and Zoller (2000), Eq. 5.3.15, D. F. Walls and G. J. Milburn, *Quantum Optics*, Berlin, Heidelberg: Springer, 2008, Eq. 7.16.
[119] Walls and Milburn (2008), Eq. 7.17. See also A. A. Clerk et al., 'Introduction to quantum noise, measurement, and amplification', *Rev. Mod. Phys.* **82** (2010), 1155–1208, Sec. E.2, particularly Eqs. E32 and E36.

written as

$$\hat{\mathbf{x}}_{\text{out}} = K_{\text{in}}^{\text{T}} \hat{\mathbf{x}} - \hat{\mathbf{x}}_{\text{in}} \tag{2.23}$$

with $\hat{\mathbf{x}}_{\text{in}}$ and $\hat{\mathbf{x}}_{\text{out}}$ each containing k input and output quadratures, respectively, making K_{in}, a diagonal matrix describing the driving, $n \times k$-dimensional. The whole system description then reads

$$\dot{\hat{\mathbf{x}}} = M_{\text{sys}} \hat{\mathbf{x}} + K_{\text{in}} \hat{\mathbf{x}}_{\text{in}} + K_{\text{bath}} \hat{\mathbf{x}}_{\text{bath}}, \tag{2.24}$$

$\hat{\mathbf{x}}_{\text{bath}}$ has m entries, K_{bath} is $n \times m$-dimensional. The equations of motion can be solved in the Fourier domain, where $\dot{x}(t) = i\omega \mathbf{x}[\omega]$:

$$\hat{\mathbf{x}} = (i\omega - M_{\text{sys}})^{-1} \left(K_{\text{in}} \hat{\mathbf{x}}_{\text{in}} + K_{\text{bath}} \hat{\mathbf{x}}_{\text{bath}} \right), \tag{2.25}$$

$$\begin{aligned}
\hat{\mathbf{x}}_{\text{out}} &= K_{\text{in}}^{\text{T}} \hat{\mathbf{x}} - \hat{\mathbf{x}}_{\text{in}} \\
&= \left(K_{\text{in}}^{\text{T}} (i\omega - M_{\text{sys}})^{-1} K_{\text{in}} - 1 \right) \hat{\mathbf{x}}_{\text{in}} + K_{\text{in}}^{\text{T}} (i\omega - M_{\text{sys}})^{-1} K_{\text{bath}} \hat{\mathbf{x}}_{\text{bath}} \\
&= P \tilde{\mathbf{x}}_{\text{in}}, \tag{2.26}
\end{aligned}$$

where

$$\tilde{\mathbf{x}}_{\text{in}} = \begin{pmatrix} \hat{\mathbf{x}}_{\text{in}} \\ \hat{\mathbf{x}}_{\text{bath}} \end{pmatrix}, \tag{2.27}$$

$$P = \left(K_{\text{in}}^{\text{T}} (i\omega - M_{\text{sys}})^{-1} K_{\text{in}} - 1 \,\middle|\, K_{\text{in}}^{\text{T}} (i\omega - M_{\text{sys}})^{-1} K_{\text{bath}} \right), \tag{2.28}$$

and thus $\tilde{\mathbf{x}}_{\text{in}}$ is $k + m \times 1$-dimensional and P is $k \times (k + m)$-dimensional.

The (symmetrised) covariance matrix of the output quadratures follows to be

$$\begin{aligned}
\delta(\omega - \omega') S_{\text{out}}(\omega) &= \tfrac{1}{2} \langle \hat{\mathbf{x}}_{\text{out}}(\omega), \hat{\mathbf{x}}_{\text{out}}(\omega') \rangle + \text{c.c.} \\
&= \tfrac{1}{2} \langle \hat{\mathbf{x}}_{\text{out}}(\omega) \hat{\mathbf{x}}_{\text{out}}^{\dagger}(\omega') \rangle + \text{c.c.} \\
&= \tfrac{1}{2} \langle P(\omega) \mathbf{x}_{\text{in}} \tilde{\mathbf{x}}_{\text{in}}^{\dagger} P^{\dagger}(-\omega') \rangle + \text{c.c.} \\
&= \tfrac{1}{2} P(\omega) S_{\text{in}} P^{\dagger}(-\omega') + \text{c.c.} \tag{2.29}
\end{aligned}$$

where S_{in} is a $(k + m) \times (k + m)$-matrix and S_{out} is $k \times k$-dimensional.

2.3.2 Ideal and non-ideal CQNC in an integrated set-up

In this section, the method presented above is used for calculations of an integrated all-optical set-up, mostly as they were also published by Wimmer
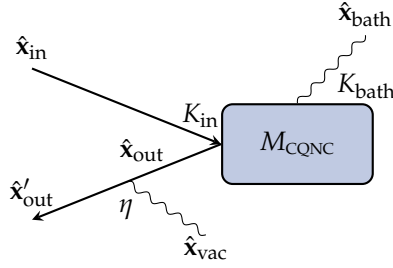
FIGURE 2.7: Block diagram of CQNC in an integrated set-up. The matrix M_{CQNC} describes the system evolution, matrices K_i the coupling to and from the system, η denotes losses on the way to detection. Transport from $\hat{\mathbf{x}}_{\text{in}}$ to $\hat{\mathbf{x}}_{\text{out}}$ can be described with P.

and co-workers[120] and can be found elsewhere.[121]

CQNC in an integrated set-up consists of $n = 6$ system variables, $k = 2$ input- and output quadratures and $m = 6$ bath quadratures coupling to the system (cf. flowchart representation, Fig. 2.2b, and block diagram, Fig. 2.7). Its Hamiltonian can be written as the sum of three Hamiltonians, the system Hamiltonian $\hat{H}_{\text{sys}}$, the radiation-pressure Hamiltonian $\hat{H}_{\text{rp}}$ and the ancilla cavity Hamiltonian $\hat{H}_{\text{anc}}$ (omitting the harmonic oscillators' zero point energies and, for the moment, coupling to a bath):

$$\hat{H} = \hat{H}_{\text{sys}} + \hat{H}_{\text{rp}} + \hat{H}_{\text{anc}}, \tag{2.30a}$$

$$\hat{H}_{\text{sys}} = \hbar\omega_c \hat{c}^\dagger \hat{c} + \hbar\omega_a \hat{a}^\dagger \hat{a} + \hbar\omega_m \hat{b}^\dagger \hat{b}, \tag{2.30b}$$

$$\hat{H}_{\text{rp}} = \hbar\frac{g}{2}(\hat{c} + \hat{c}^\dagger)(\hat{b} + \hat{b}^\dagger), \tag{2.30c}$$

$$\hat{H}_{\text{anc}} = \hbar g_{\text{DC}}(\hat{a}\hat{c} + \hat{a}^\dagger \hat{c}^\dagger) + \hbar g_{\text{BS}}(\hat{a}\hat{c}^\dagger + \hat{a}^\dagger \hat{c}), \tag{2.30d}$$

where the linearised opto-mechanical Hamiltonian $\hat{H}_{\text{rp}}$ with dimensionless phonon number operators is known from Sec. 1.3. The meter cavity mode $\hat{c}$ has frequency ω_c, the ancilla cavity mode $\hat{a}$, coupled to mode $\hat{c}$ via a beam-splitter interaction with strength g_{BS} and a down-conversion interaction with strength g_{DC}, has frequency ω_a, the phononic mode $\hat{b}$ coupled to mode $\hat{c}$ via g has frequency ω_m as in Fig. 2.5. In the following, $\hbar = 1$ and a frame rotating

[120]Wimmer, Steinmeyer, Hammerer and Heurs (2014).
[121]Steinmeyer, Master thesis (2014); M. H. Wimmer, 'Coupled nonclassical systems for coherent backaction noise cancellation', PhD thesis, Leibniz Universität Hannover, 2016.

with the frequency ω_L of the driving field is used. This leads, together with damping and driving terms to an equation of motion

$$\dot{\hat{x}} = M_{CQNC}\hat{x} + K_{in}\hat{x}_{in} + K_{bath}\hat{x}_{bath} \tag{2.31}$$

with

$$M_{CQNC} = \begin{pmatrix} -\kappa_c/2 & \Delta_c & 0 & g_{BS} - g_{DC} & 0 & 0 \\ -\Delta_c & -\kappa_c/2 & -(g_{BS} + g_{DC}) & 0 & -g & 0 \\ 0 & g_{BS} - g_{DC} & -\kappa_a/2 & \Delta_a & 0 & 0 \\ -(g_{BS} + g_{DC}) & 0 & -\Delta_a & -\kappa_a/2 & 0 & 0 \\ 0 & 0 & 0 & 0 & 0 & \omega_m \\ -g & 0 & 0 & 0 & -\omega_m & -\gamma_m \end{pmatrix},$$

$$K_{in} = \begin{pmatrix} \sqrt{\kappa_c^{in}} & 0 \\ 0 & \sqrt{\kappa_c^{in}} \\ 0 & 0 \\ 0 & 0 \\ 0 & 0 \\ 0 & 0 \end{pmatrix}, \qquad \begin{aligned} K_{bath} &= \text{diag}\left(\sqrt{\kappa_c^{bath}}, \sqrt{\kappa_c^{bath}}, \sqrt{\kappa_a}, \sqrt{\kappa_a}, 0, \sqrt{\gamma_m}\right), \\ \hat{x} &= (\hat{x}_c, \hat{p}_c, \hat{x}_a, \hat{p}_a, \hat{x}_m, \hat{p}_m)^T, \\ \hat{x}_{in} &= (\hat{x}_{in}, \hat{p}_{in})^T, \\ \hat{x}_{bath} &= \left(\hat{x}_c^{bath}, \hat{p}_c^{bath}, \hat{x}_a^{bath}, \hat{p}_a^{bath}, \hat{x}_m^{bath}, \hat{p}_m^{bath}\right)^T. \end{aligned}$$

$$\tag{2.32}$$

$\kappa_c = \kappa_c^{in} + \kappa_c^{bath}$ is the linewidth of the meter cavity, with κ_c^{in} describing the coupling to the driving field and κ_c^{bath} the losses caused by coupling to the bath. κ_a is the linewidth of the ancilla cavity and describes losses caused by coupling to the bath. γ_m is the damping of the mechanical oscillator. $\Delta_a = \omega_a - \omega_L$ is the detuning of the ancilla cavity and $\Delta_c = \omega_c - \omega_L$ the detuning of the meter cavity to the incoming laser light. After solving the equations of motion in Fourier domain and using input-output relations,

$$\hat{x}_{out} + \hat{x}_{in} = K_{in}^T \hat{x}, \tag{2.33}$$

the resulting spectral density is

$$2\delta(\omega - \omega')S_{out} = P(\omega)S_{in}P^\dagger(-\omega') + \text{c.c.} \tag{2.34}$$

with

$$P(\omega) = \left(K_{in}^T(i\omega - M_{CQNC})^{-1}K_{in} - 1 \,\middle|\, K_{in}^T(i\omega - M_{CQNC})^{-1}K_{bath}\right). \tag{2.35}$$

S_{in} contains the input noise which is assumed to be uncorrelated and at vacuum level for the light fields:

$$S_{in} = \frac{1}{2}\,\text{diag}\left(1, 1, 1, 1, 1, 1, 0, 2S_{in}^{FF}\right) \tag{2.36}$$

with S_{in}^{FF} being the spectral density of the force applied to the mechanical oscillator, which is the sum of thermal noise and other forces.[122]

Using the ideas from Sec. 2.1, the coupling of light to negative-mass oscillator needs mimic the coupling of light to positive-mass oscillator. This means $g = g_{\text{BS}} + g_{\text{DC}}$, $g_{\text{BS}} = g_{\text{DC}}$. Additionally, the meter cavity is assumed to be resonant with the incoming light field, $\Delta_c = 0$, which results in $\Delta_a = \omega_a - \omega_c$, and to be one-sided, $\kappa_c^{\text{bath}} = 0$. These assumptions simplify the expressions to the point where they can be easily written down. The phase quadrature's noise spectral density, where the measurement information is encoded, becomes (if all input quadratures are uncorrelated)

$$S_{\text{out}}^{p_c p_c}(\omega) = S_{\text{in}}^{p_c p_c} + G^2 |\chi_m + \chi_a|^2 S_{\text{in}}^{x_c x_c} \tag{2.37a}$$

$$+ G\gamma_m |\chi_m|^2 S_{\text{in}}^{FF} \tag{2.37b}$$

$$+ G\kappa_a |\chi_a|^2 \left(\frac{\omega^2 + \kappa_a^2/4}{\Delta_a^2} S_{\text{in}}^{x_a x_a} + S_{\text{in}}^{p_a p_a} \right), \tag{2.37c}$$

with a mechanical susceptibility χ_m, an ancilla cavity susceptibility χ_a, a measurement strength G and a meter cavity susceptibility χ_c,

$$\chi_m = \frac{\omega_m}{\omega^2 - \omega_m^2 - i\gamma_m\omega}, \quad \chi_a = \frac{\Delta_a}{\omega^2 - \Delta_a^2 - \kappa_a^2/4 - i\kappa_a\omega},$$
$$G = \kappa_c |\chi_c|^2 g^2, \quad \chi_c = \frac{1}{\kappa_c/2 + i\omega}. \tag{2.38}$$

Equation 2.37a contains the noise of the incoming light field, coupled through the cavity. The first term contains shot noise, the second term, proportional to the squared measurement strength G^2, radiation-pressure noise. Equation 2.37b contains incoming force noise, most importantly thermal noise and the signal. Equation 2.37c contains noise coupled into the detuned ancilla cavity, which is ultimately the limit for CQNC under ideal assumptions. As the radiation-pressure term is proportional to the sum of two susceptibilities, the mechanical susceptibility χ_m and the ancilla cavity susceptibility χ_a,

$$\chi_m + \chi_a = \frac{\omega_m}{\omega^2 - \omega_m^2 - i\gamma_m\omega} + \frac{\Delta_a}{\omega^2 - \Delta_a^2 - \kappa_a^2/4 - i\kappa_a\omega}. \tag{2.39}$$

it can be made to vanish: If $\chi_m = -\chi_a$, the back-action term cancels to zero. This implies what was already suggested in Sec. 2.1. For perfect back-action

---

[122]Here, the convention that $[\hat{x}, \hat{p}] = i$ is employed, resulting in var $\hat{x} = 1/2$. There is no noise coupling to the mechanical position quadrature, leading to an asymmetry in the description of negative- and positive-mass oscillator.

cancellation, the two oscillators need to have equal characteristics, but a negative sign. The complete list of requirements for ideal CQNC is

$$g = g_{BS} + g_{DC}, \tag{2.40a}$$

$$g_{BS} = g_{DC}, \tag{2.40b}$$

$$\Delta_a = -\omega_m, \tag{2.40c}$$

$$\kappa_a = \gamma_m, \tag{2.40d}$$

$$|\Delta_a| \gg \kappa_a, \quad \Rightarrow \quad Q = \frac{\omega_m}{\gamma_m} \gg 1. \tag{2.40e}$$

With this, the radiation-pressure term cancels and the signal can be made arbitrarily large compared to the shot-noise term either with increasing measurement strength G or with decreasing input phase noise due to squeezing. Both are not detrimental any more due to back-action cancellation.

The noise-to-signal ratio can be obtained from Eq. 2.37 via dividing $S_{out}^{p_c p_c}$ by the prefactors of S_{in}^{FF} for the force sensitivity and an additional multiplication of $\gamma_m |\chi_m|^2$ for the position sensitivity. This leads, if all requirements are fulfilled and thermal noise is neglected, to a limit to the (force) noise density of

$$S_{CQNC} = \frac{\omega^2 + \omega_m^2 + \gamma_m^2/4}{\omega_m^2} \stackrel{\omega \neq \omega_m}{=} \frac{1}{2Q} \times S_{SQL} \tag{2.41}$$

away from the mechanical resonance. The limit on sensitivity is now caused by noise coupling in from the ancilla cavity bath. It leads to decoherence and, due to matching positive- and negative-mass oscillators, limits the noise suppression to $1/2Q$. The effect of ideal CQNC on force sensitivity in frequency space is shown in Fig. 2.8.

The assumptions made above are in practice not met perfectly. Especially assuming an ancilla cavity linewidth of the size of the mechanical oscillator's linewidth is often not reasonable. Relaxing this assumption and instead requiring only that $\kappa_a < \omega_m$ (which follows from having a mechanical oscillator with $Q > 1$ and still requiring $\Delta_a = -\omega_m$) results in a noise spectral density

$$S = \frac{\kappa_a}{2\omega_m} \times S_{SQL}. \tag{2.42}$$

Even without perfect linewidth matching, an improvement of $\kappa_a/2\omega_m$ is possible, see Fig. 2.8. In this case, the back-action noise is not cancelled completely. If the measurement strength becomes too high, the sensitivity decreases again, see Fig. 2.10. For each frequency, there is an optimal measurement strength as
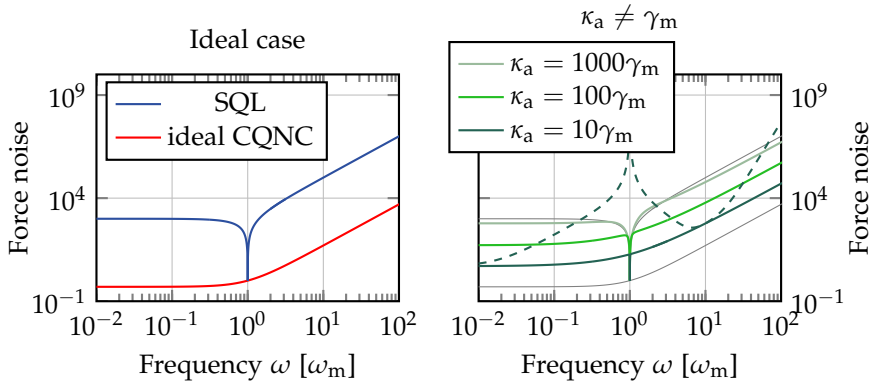
FIGURE 2.8: Back-action evasion in an integrated set-up. Left: Perfect back-action evasion and SQL. Away from the mechanical resonance frequency, the SQL can be surpassed by $1/2Q$. Right: Possible improvement if linewidths of positive- and negative-mass oscillator are not perfectly matched, for different degrees of mismatch. The dashed line shows the sensitivity with $\kappa_a = 10\gamma_m$ at a fixed measurement strength (solid lines have their measurement strength optimised at each frequency). Grey lines show SQL and ideal CQNC for orientation. Plot parameters as in Tab. 2.1.
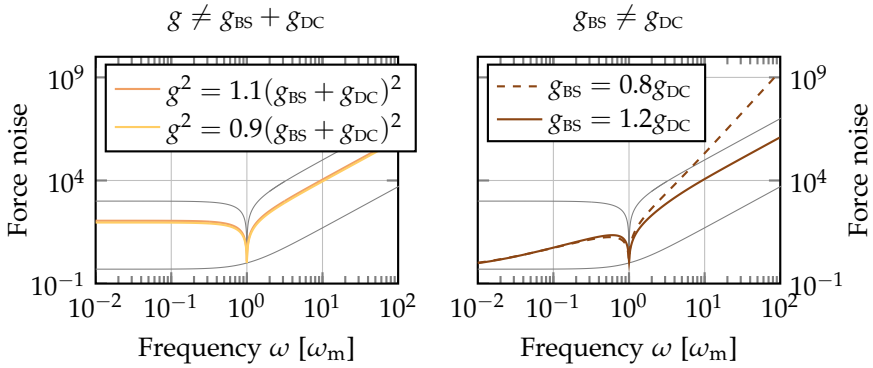
FIGURE 2.9: Imperfect matching of coupling strengths in an integrated set-up. Left: Imperfect matching $g \neq \frac{1}{2}(g_{\mathrm{BS}} + g_{\mathrm{DC}})$. Right: Imperfect matching $g_{\mathrm{BS}} \neq g_{\mathrm{DC}}$. Grey lines show SQL and ideal CQNC for orientation. Plot parameters as in Tab. 2.1.

for the classical case without CQNC, which also be seen from the dashed line in Fig. 2.8.

Other imperfections regard the coupling strengths. They are twofold: A difference in g_{BS} and g_{DC} makes the interaction with the ancilla system deviate from a radiation-pressurelike interaction. A difference in g and $\frac{1}{2}(g_{\mathrm{BS}} + g_{\mathrm{DC}})$ causes different interaction strengths between the light and the respective harmonic oscillator. These effects are shown in Fig. 2.9.

It has not been checked whether the system is stable at all. This is the case if all coefficients of its characteristic equation are positive (the Routh-Hurwitz criterion). The characteristic equation is $\det(M_{\mathrm{CQNC}} - \lambda \mathbb{1}) = 0$. The coefficients

FIGURE 2.10: Noise at fixed measurement frequency $\omega = 10\omega_\mathrm{m}$ over measurement strength. Red trace is without CQNC, blue shows ideal CQNC. Other colours indicate the type of mismatch as in Figs. 2.8 and 2.9. Plot parameters as in Tab. 2.1.

for the system are listed below.

$$
\begin{aligned}
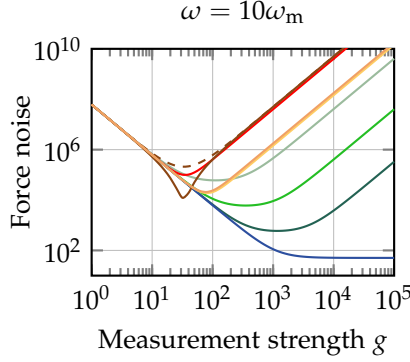c_0 &= \omega_\mathrm{m}^2(g_\mathrm{BS}^2 - g_\mathrm{DC}^2)^2 + \frac{1}{2}\omega_\mathrm{m}^2\kappa_\mathrm{a}\kappa_\mathrm{c}(g_\mathrm{BS}^2 - g_\mathrm{DC}^2) - 2\Delta_\mathrm{a}\Delta_\mathrm{c}(g_\mathrm{BS}^2 + g_\mathrm{DC}^2)\omega_\mathrm{m}^2 \\
&\quad + g^2\Delta_\mathrm{a}\omega_\mathrm{m}(g_\mathrm{BS}^2 - g_\mathrm{DC}^2) - g^2\omega_\mathrm{m}\Delta_\mathrm{c}(\Delta_\mathrm{a}^2 + \frac{\kappa_\mathrm{a}^2}{4}) + \omega_\mathrm{m}^2(\Delta_\mathrm{a}^2 + \frac{\kappa_\mathrm{a}^2}{4})(\Delta_\mathrm{c}^2 + \frac{\kappa_\mathrm{c}^2}{4}) \\
c_1 &= \gamma_\mathrm{m}(g_\mathrm{BS}^2 - g_\mathrm{DC}^2)^2 - 2\gamma_\mathrm{m}\Delta_\mathrm{a}\Delta_\mathrm{c}(g_\mathrm{BS}^2 + g_\mathrm{DC}^2) + \omega_\mathrm{m}^2(\kappa_\mathrm{c} + \kappa_\mathrm{a})(g_\mathrm{BS}^2 - g_\mathrm{DC}^2) \\
&\quad + \frac{1}{2}\gamma_\mathrm{m}\kappa_\mathrm{a}\kappa_\mathrm{c}(g_\mathrm{BS}^2 - g_\mathrm{DC}^2) + \gamma_\mathrm{m}(\Delta_\mathrm{a}^2 + \frac{\kappa_\mathrm{a}^2}{4})(\Delta_\mathrm{c}^2 + \frac{\kappa_\mathrm{c}^2}{4}) - g^2\Delta_\mathrm{c}\kappa_\mathrm{a}\omega_\mathrm{m} \\
&\quad + (\kappa_\mathrm{a}(\Delta_\mathrm{c}^2 + \frac{\kappa_\mathrm{c}^2}{4}) + \kappa_\mathrm{c}(\Delta_\mathrm{a}^2 + \frac{\kappa_\mathrm{a}^2}{4}))\omega_\mathrm{m}^2 \\
c_2 &= (g_\mathrm{BS}^2 - g_\mathrm{DC}^2)^2 + 2(g_\mathrm{BS}^2 - g_\mathrm{DC}^2)(\frac{\kappa_\mathrm{a}\kappa_\mathrm{c}}{4} + \gamma_\mathrm{m}\frac{\kappa_\mathrm{a} + \kappa_\mathrm{c}}{2} + \omega_\mathrm{m}^2) - 2\Delta_\mathrm{a}\Delta_\mathrm{c}(g_\mathrm{BS}^2 + g_\mathrm{DC}^2) \\
&\quad - g^2\Delta_\mathrm{c}\omega_\mathrm{m} + \omega_\mathrm{m}^2(\Delta_\mathrm{a}^2 + \frac{\kappa_\mathrm{a}^2}{4} + \Delta_\mathrm{c}^2 + \frac{\kappa_\mathrm{c}^2}{4} + \kappa_\mathrm{a}\kappa_\mathrm{c}) \\
&\quad + \gamma_\mathrm{m}(\kappa_\mathrm{a}(\Delta_\mathrm{c}^2 + \frac{\kappa_\mathrm{c}}{4}) + \kappa_\mathrm{c}(\Delta_\mathrm{a}^2 + \frac{\kappa_\mathrm{a}}{4})) + (\Delta_\mathrm{a}^2 + \frac{\kappa_\mathrm{a}^2}{4})(\Delta_\mathrm{c}^2 + \frac{\kappa_\mathrm{c}^2}{4}) \\
c_3 &= 2(g_\mathrm{BS}^2 - g_\mathrm{DC}^2)(\gamma_\mathrm{m} + \frac{\kappa_\mathrm{a}}{2} + \frac{\kappa_\mathrm{c}}{2}) + \gamma_\mathrm{m}(\Delta_\mathrm{a}^2 + \frac{\kappa_\mathrm{a}^2}{4} + \Delta_\mathrm{c}^2 + \frac{\kappa_\mathrm{c}^2}{4} + \kappa_\mathrm{a}\kappa_\mathrm{c}) \\
&\quad + (\Delta_\mathrm{a}^2 + \frac{\kappa_\mathrm{a}^2}{4})\kappa_\mathrm{c} + (\Delta_\mathrm{c}^2 + \frac{\kappa_\mathrm{c}^2}{4})\kappa_\mathrm{a} + \omega_\mathrm{m}^2(\kappa_\mathrm{a} + \kappa_\mathrm{c}) \\
c_4 &= 2(g_\mathrm{BS}^2 - g_\mathrm{DC}^2) + \Delta_\mathrm{a}^2 + \frac{\kappa_\mathrm{a}^2}{4} + \Delta_\mathrm{c}^2 + \frac{\kappa_\mathrm{c}^2}{4} + \kappa_\mathrm{a}\kappa_\mathrm{c} + \omega_\mathrm{m}^2 + \gamma_\mathrm{m}(\kappa_\mathrm{a} + \kappa_\mathrm{c}) \\
c_5 &= \gamma_\mathrm{m} + \kappa_\mathrm{a} + \kappa_\mathrm{c} \\
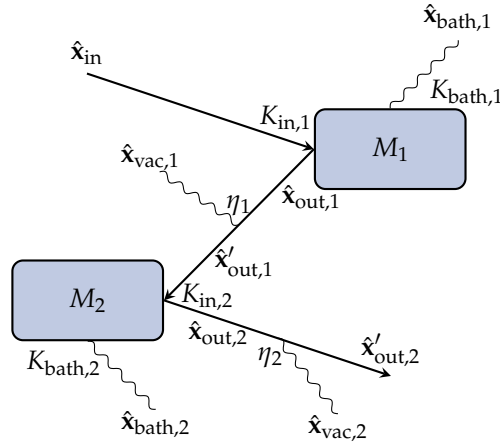c_6 &= 1
\end{aligned}
\tag{2.43}
$$

FIGURE 2.11: Block diagram of CQNC in a cascaded set-up. Note the similarity to the conceptual scheme in Fig. 2.1. The matrices M_i describe the system evolution, K_i the coupling to and from the system, η_i losses on the way. Transport from $\hat{\mathbf{x}}_{in}$ to $\hat{\mathbf{x}}'_{out,1}$ can be described with P_1, from $\hat{\mathbf{x}}'_{out,1}$ to $\hat{\mathbf{x}}'_{out,2}$ with P_2, from $\hat{\mathbf{x}}_{in}$ to $\hat{\mathbf{x}}'_{out,2}$ with $\tilde{P}$ as in Eqs. 2.53 and 2.54.

Most of the terms are quadratic or inherently positive. Under ideal conditions with all requirements from Eq. 2.40 fulfilled, the system is stable. The main sources for instability are a mismatch in coupling strengths, $g_{DC} > g_{BS}$ (in coefficients c_0 to c_4 with red underline), $g_{BS} > g_{DC}$ (in coefficient c_0 with yellow underline), and a high coupling strength g if the detuning Δ_c becomes positive (in coefficients c_0 to c_3 with green underline) or negative (in coefficients c_0 to c_2 with blue underline).[123] The system is actively pumped with g_{DC}, which gives an intuitive reason why it can become unstable with high down-conversion coupling. The same phenomenon is the cause of opto-mechanical instability: With a positive detuning Δ_c, the two-mode squeezing term in the radiation-pressure Hamiltonian becomes dominant, the opto-mechanical system resembles a pumped squeezing cavity.

TABLE 2.1: Plot parameters integrated set-up used in Figs. 2.8 to 2.10 if not specified otherwise. In the third column, all parameters are normalised to the mechanical resonance frequency ω_m. Parameters are the same as used for the theoretical plots in M. H. Wimmer, D. Steinmeyer, K. Hammerer and M. Heurs, 'Coherent cancellation of backaction noise in optomechanical force measurements', *Phys. Rev. A* **89** (2014), 053836. Parameters in the fourth column are obtained from the third column via setting $\omega_\mathrm{m} = 2\pi \times 500\,\mathrm{kHz}$.

Parameter		Norm. value	Value
ω_m	mechanical resonance frequency	1	500 kHz
γ_m	mechanical linewidth	$10^{-3}\omega_\mathrm{m}$	5 kHz
Q	mechanical quality factor	$\frac{\omega_\mathrm{m}}{\gamma_\mathrm{m}}$	10^3
Δ_a	detuning ancilla cavity	$-\omega_\mathrm{m}$	-500 kHz
κ_a	linewidth ancilla cavity	γ_m	5 kHz
Δ_c	detuning meter cavity	0	
κ_c	linewidth meter cavity	$10\omega_\mathrm{m}$	5 MHz
g	opto-mechanical coupling strength	ω_m	500 kHz
g_BS	beam-splitter coupling strength	$\frac{1}{2}g$	250 kHz
g_DC	down-conversion coupling strength	$\frac{1}{2}g$	250 kHz
η	propagation efficiency	1	
ω	measurement (Fourier) frequency	$10\omega_\mathrm{m}$	5 MHz

2.3.3 Ideal and non-ideal CQNC in a cascaded set-up

A cascaded set-up has been used with a spin ensemble as negative-mass oscillator and a membrane as the positive-mass oscillator.[124] Here, the two harmonic oscillators are not part of the same cavity. Instead, light leaving one cavity after interaction with the first harmonic oscillator interacts with the second harmonic oscillator in a different cavity (see Fig. 2.11 and also Fig. 2.6). In the all-optical case, this gives more freedom in designing the experiment, as further explicated in Sec. 2.4, and also leads to results similar to the integrated set-up, as will be seen below. The main differences to the integrated set-up are that, instead of coupling strengths, measurement strengths have to be matched, which include the systems' linewidths, and that losses occurring between the two systems become important.

First, the positive-mass and the negative-mass oscillator will be studied on their own. For the opto-mechanical system, this has already been done in Sec. 1.3. The system's matrix is

$$
M_{OM} = \begin{pmatrix} -\kappa_{om}/2 & \Delta_{om} & 0 & 0 \\ -\Delta_{om} & -\kappa_{om}/2 & -g & 0 \\ 0 & 0 & 0 & \omega_m \\ -g & 0 & -\omega_m & -\gamma_m \end{pmatrix},
\tag{2.44}
$$

again with detuning Δ_{om} of the cavity mode with linewidth κ_{om}, coupled to the mechanical oscillator, characterised by its resonance frequency ω_m and linewidth γ_m, with coupling strength g. For simplification and illustration, the cavity is assumed to to be on resonance ($\Delta_{om} = 0$), and lossless ($\kappa_{om} = \kappa_{om}^{in}$). The output quadratures are then

$$
\hat{x}_{om}^{out} = e^{i\phi}\hat{x}_{in},
\tag{2.45a}
$$

$$
\begin{aligned}
\hat{p}_{om}^{out} = {} & e^{i\phi}\hat{p}_{in} - \kappa_{om}\chi_m g^2 \chi_{om}^2 \hat{x}_{in} \\
& + \chi_m\sqrt{\kappa_{om}}g\chi_{om}\sqrt{\gamma_m}\hat{F}
\end{aligned}
\tag{2.45b}
$$

with $\exp i\phi = \frac{\kappa_{om}/2 - i\omega}{\kappa_{om}/2 + i\omega}$, $\chi_{om} = 1/(\kappa_{om}/2 + i\omega)$ and the known mechanical susceptibility χ_m from Eq. 2.38. A frequency-dependent rotation of the input quadratures can be seen as already shown in Sec. 2.1 and Fig. 2.3. The output

---

[123]Numerical calculations for stability are done in Steinmeyer, Master thesis (2014), Fig. 6.4.
[124]Møller et al. (2017).

spectral density matrix for uncorrelated inputs ($\langle \hat{x}_{in}, \hat{p}_{in} \rangle = 0$) is

$$S_{out}^{OM} = \frac{1}{2} \begin{pmatrix} 1 & G|\chi_m| \\ G|\chi_m| & 1 + G^2|\chi_m|^2 + 2G|\chi_m|^2\gamma_m S_F \end{pmatrix} \qquad (2.46)$$

with measurement strength $G = \kappa_{om}|\chi_{om}|^2 g^2$ as before. In the output spectrum, there are now correlations between amplitude quadratures $\hat{x}_{out}$ and $\hat{p}_{out}$, which correspond to (ponderomotive) squeezing of the output field.

For the negative-mass oscillator realised by a detuned cavity, the system matrix is

$$M_{negmass} = \begin{pmatrix} -\kappa_c/2 & \Delta_c & 0 & g_{BS} - g_{DC} \\ -\Delta_c & -\kappa_c/2 & -(g_{BS} + g_{DC}) & 0 \\ 0 & g_{BS} - g_{DC} & -\kappa_a/2 & \Delta_a \\ -(g_{BS} + g_{DC}) & 0 & -\Delta_a & -\kappa_a/2 \end{pmatrix}, \qquad (2.47)$$

as before with the detuning Δ_c of the meter cavity with linewidth κ_c, coupled to the ancilla cavity, characterised by its detuning Δ_a and linewidth κ_a, with a down-conversion interaction of strength g_{DC} and a beam-splitter interaction of strength g_{BS}. Again, a lossless meter cavity ($\kappa_c = \kappa_c^{in}$) on resonance ($\Delta_c = 0$) is assumed. Furthermore, equal coupling strengths of beam-splitter coupling and down-conversion coupling are assumed ($g_{BS} = g_{DC} = \frac{1}{2}g_{anc}$). The output quadratures are then

$$\hat{x}_{negmass}^{out} = e^{i\phi'}\hat{x}_{in}, \qquad (2.48a)$$

$$\hat{p}_{negmass}^{out} = e^{i\phi'}\hat{p}_{in} - \kappa_c \chi_a g_{anc}^2 \chi_c^2 \hat{x}_{in}$$
$$+ \chi_a \sqrt{\kappa_c} g_{anc} \chi_c \sqrt{\kappa_a} \left(\frac{\kappa_a/2 + i\omega}{\Delta_a} \hat{x}_a^{bath} + \hat{p}_a^{bath} \right) \qquad (2.48b)$$

with $\exp i\phi' = (\kappa_c/2 - i\omega)/(\kappa_c/2 + i\omega)$.

The spectral density matrix for uncorrelated inputs, $\langle \hat{x}_{in}, \hat{p}_{in} \rangle = \langle \hat{x}_a^{bath}, \hat{p}_a^{bath} \rangle = 0$, can be written as

$$S_{out}^{negmass} = \frac{1}{2} \begin{pmatrix} 1 & G_{anc}|\chi_a| \\ G_{anc}|\chi_a| & 1 + G_{anc}^2|\chi_a|^2 + 2G_{anc}|\chi_a|^2\kappa_a \frac{\kappa_a^2/4 + \Delta_a^2 + \omega^2}{\Delta_a^2} \end{pmatrix} \qquad (2.49)$$

with a measurement strength $G_{anc} = \kappa_c|\chi_c|^2 g_{anc}^2$ and the known ancilla cavity susceptibility χ_a from Eq. 2.38

The system matrices, Eqs. 2.44 and 2.47, as well as the solutions for the output quadratures, Eqs. 2.45 and 2.48, and the output spectra, Eqs. 2.46
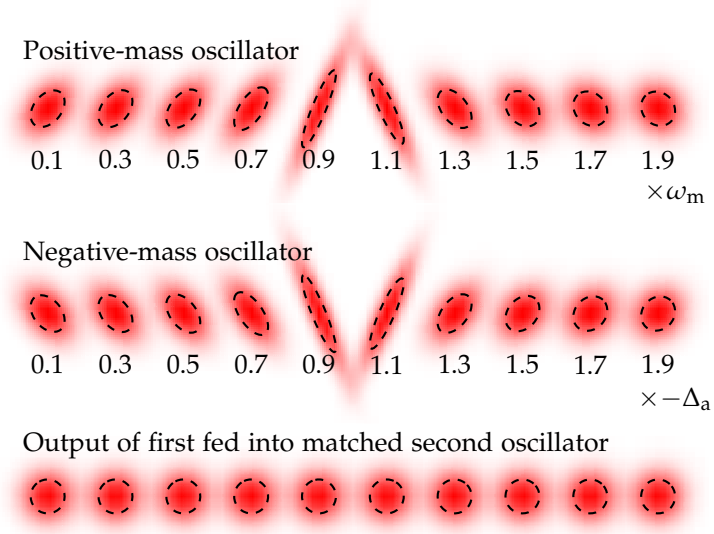
FIGURE 2.12: Squeezing spectra of positive- and negative-mass oscillators at different frequencies. First row, the squeezing over frequency caused by a positive-mass oscillator, here the mechanical oscillator in an optical cavity (spectrum from Eq. 2.46), second row, the squeezing over frequency caused by a negative-mass oscillator, here the ancilla cavity with negative detuning in an optical cavity (spectrum from Eq. 2.49), each with vacuum input. The spectrum of the output of a positive-mass oscillator fed into a matched negative-mass oscillator (third row) shows perfect back-rotation and back-squeezing. Plot parameters as in Tab. 2.2.

and 2.49, reveal an almost exact symmetry of the two systems. There is, as in the susceptibilities in Sec. 2.3.2, Eq. 2.39 above, a nearly one-to-one correspondence between the two oscillators (as long as beam-splitter and down-conversion coupling match). The difference shows in the asymmetric coupling of the quadratures of positive- and negative-mass oscillator to a bath. This is because there is no damping on the mechanical oscillator's position, only on its momentum, which translates to a difference of the susceptibilities χ_{m} and χ_{a} with an additional $\kappa_{\mathrm{a}}^2/4$ in the denominator of the latter (cf. Eq. 2.39).

For matching the systems, the coupling strengths do not need to be matched

any more, but instead the measurement strengths G and G_{anc},[125] which leads to

$$\frac{\kappa_c}{\omega^2 + \kappa_c^2/2}(g_{\text{BS}} + g_{\text{DC}})^2 \overset{!}{=} \frac{\kappa_{\text{om}}}{\omega^2 + \kappa_{\text{om}}^2/2}g^2. \tag{2.50}$$

The output spectra for matched systems are plotted at different frequencies in Fig. 2.12. Ponderomotive squeezing by a positive-mass and by a negative-mass oscillator differ in their squeezing angle. Feeding the output of a positive-mass oscillator into a matched negative-mass oscillator results in back-rotation and back-squeezing of the uncertainties such that one again obtains vacuum uncertainties. The formalism combining the two systems is shown in the following.

A combination of the positive-mass and the negative-mass oscillator into one formalism allows full calculation of all effects (in the single-mode approximation required by using a Hamiltonian formalism). The notation of the participating matrices and vectors is as in Fig. 2.11. The Hamiltonians to derive equations of motion from are similar to the ones in the integrated set-up, only that now, two separate systems have to be considered with the output of one system as the input of the other, see again Fig. 2.11. The order does not matter much from a theoretical point of view. It can rather be chosen according to experimental needs, which is why the two systems are just indexed with 1 and 2. The equations of motion amount to

$$\hat{x}_i = (i\omega - M_i)^{-1}\left(K_{\text{in},i}\hat{x}_{\text{in},i} + K_{\text{bath},i}\hat{x}_{\text{bath},i}\right), \tag{2.51}$$

$$\begin{aligned}
\hat{x}_{\text{out},i} &= K_{\text{in},i}^{\text{T}}\hat{x}_i - \hat{x}_{\text{in},i} \\
&= \underbrace{\left(K_{\text{in},i}^{\text{T}}(i\omega - M_i)^{-1}K_{\text{in},i} - 1\right)}_{P_i^{\text{sys}}}\hat{x}_{\text{in},i} + \underbrace{K_{\text{in},i}^{\text{T}}(i\omega - M_i)^{-1}K_{\text{bath},i}}_{P_i^{\text{bath}}}\hat{x}_{\text{bath},i}
\end{aligned}$$

$$\tag{2.52}$$

with index $i = 1, 2$ for the first and second system. There are four system variables for each system, meaning $M_{\text{om}}, M_{\text{anc}}, K_{\text{bath,om}}, K_{\text{bath,anc}}$ are all 4×4-dimensional. In- and output quadratures are the two quadratures of the meter light, meaning $K_{\text{in,om}}, K_{\text{in,anc}}$ are 4×2-dimensional. Then, P_i^{sys} are 2×2- and P_i^{bath} are 2×4-dimensional.

Losses can be modelled as mixing $\hat{x}_{\text{out}}$ with a vacuum mode in a beam-

---

[125]These are called readout rates Γ_i by Møller et al. (2017).

splitterlike fashion characterised by the efficiency η_i as in Sec. 1.1.4. Then,

$$
\hat{\mathbf{x}}'_{\text{out},i} = \underbrace{\begin{pmatrix} 1 & 0 & 0 & 0 \\ 0 & 1 & 0 & 0 \end{pmatrix} \eta_{i4\times4} \begin{pmatrix} P_i^{\text{sys}} & P_i^{\text{bath}} & 0 \\ 0 & 0 & \mathbb{1}_{2\times2} \end{pmatrix}_{4\times8}}_{P_i\ 2\times8} \begin{pmatrix} \hat{\mathbf{x}}_{\text{in},i} \\ \hat{\mathbf{x}}_{\text{bath},i} \\ \hat{\mathbf{x}}_{\text{vac},i} \end{pmatrix}_{8\times1} \tag{2.53}
$$

The first matrix traces out the modes lost in the beam-splitterlike interaction, the second matrix mixes the cavity output with vacuum, the third transports input modes into output modes and traces out modes lost to the bath.

Now choosing $\hat{\mathbf{x}}_{\text{in},2} = \hat{\mathbf{x}}'_{\text{out},1}$, the output quadratures become

$$
\begin{aligned}
\hat{\mathbf{x}}'_{\text{out},2} &= \sqrt{\eta_2} \left(P_2^{\text{sys}} \left[\sqrt{\eta_1} \left(P_1^{\text{sys}} \hat{\mathbf{x}}_{\text{in},1} + P_1^{\text{bath}} \hat{\mathbf{x}}_{\text{bath},1} \right) + \sqrt{1-\eta_1} \hat{\mathbf{x}}_{\text{vac},1} \right] \right. \\
&\qquad \left. + P_2^{\text{bath}} \hat{\mathbf{x}}_{\text{bath},2} \right) \\
&\qquad + \sqrt{1-\eta_2} \hat{\mathbf{x}}_{\text{vac},2}
\end{aligned} \tag{2.54a}
$$

$$
= P_2 \begin{pmatrix} P_1 & 0 & 0 \\ 0 & \mathbb{1}_{4\times4} & 0 \\ 0 & 0 & \mathbb{1}_{2\times2} \end{pmatrix}_{8\times14} \begin{pmatrix} \hat{\mathbf{x}}_{\text{in}} \\ \hat{\mathbf{x}}_{\text{bath},1} \\ \hat{\mathbf{x}}_{\text{vac},1} \\ \hat{\mathbf{x}}_{\text{bath},2} \\ \hat{\mathbf{x}}_{\text{vac},2} \end{pmatrix}_{14\times1} \tag{2.54b}
$$

$$
= \tilde{P}_{2\times14} \tilde{\mathbf{x}}_{\text{in}}. \tag{2.54c}
$$

The first term in Eq. 2.54a describes the coupling of the input quadratures of system 1 through system 1 and 2, the second term the coupling of mixing of system 1's output with vacuum noise through system 2, the third then the coupling of system 2's bath through system 2 and the forth the mixing of system 2's output with vacuum noise.

Similar to the preceding section, noise spectral densities of the added force noise in the output phase quadrature are calculated from Eq. 2.54 and Eq. 2.29. For these calculations, the light passes the opto-mechanical cavity first and then the negative-mass oscillator. The spectral densities are plotted for different deviations from the requirements with otherwise perfectly matched parameters: a difference in linewidths between positive- and negative-mass oscillators (Fig. 2.13), and differences in coupling and measurement strengths (Fig. 2.14). This still requires matching g_{BS} and g_{DC}, but an imbalance of $g \neq g_{\text{BS}} + g_{\text{DC}}$ can be adjusted with the linewidths κ_{c} and κ_{om}, see Eq. 2.50 – at least in the bad cavity limit ($\kappa_i \gg \omega$) because then, the cavity transfer functions χ_{om} and χ_{c} can be approximated to be frequency-independent.
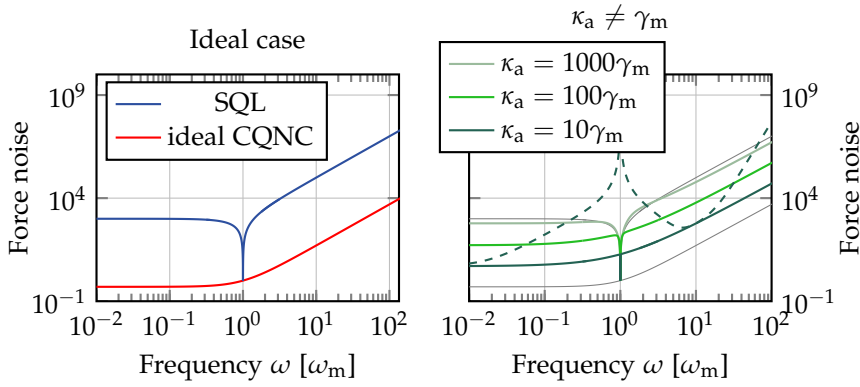
FIGURE 2.13: Back-action evasion in a cascaded set-up. Left: Perfect back-action evasion and SQL. Right: Possible improvement if linewidths of positive- and negative-mass oscillator are not perfectly matched, for different degrees of mismatch. The dashed line shows the sensitivity with $\kappa_a = 10\gamma_m$ at a fixed measurement strength (solid lines have their measurement strength optimised at each frequency). Grey lines show SQL and ideal CQNC for orientation. Plot parameters as in Tab. 2.2. The resulting noise curves are the same as for the integrated set-up, see Fig. 2.8.
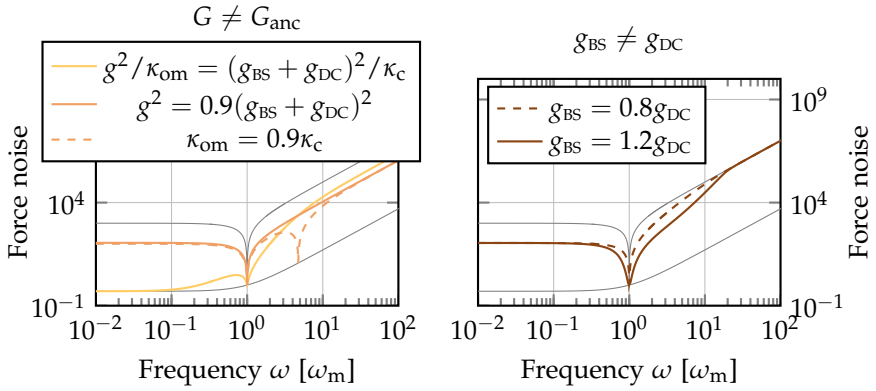
FIGURE 2.14: Imperfect matching of coupling and/or measurement strengths in a cascaded set-up. For an imperfect linewidth matching (but still matched coupling strengths), a frequency exists, here $\omega \approx 5\omega_m$, where the cavity transfer functions match, $|\chi_{om}|^2 = |\chi_c|^2$, and perfect noise cancellation is possible (dashed orange line). For imperfect linewidth matching, compensated by coupling strengths mismatch such that the measurement strengths match, perfect cancellation is still possible at low frequencies in the bad-cavity limit (solid yellow line, see also Fig. 2.16). Grey lines show SQL ideal and CQNC for orientation. Plot parameters as in Tab. 2.2.
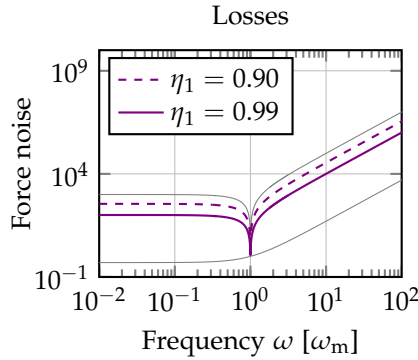

FIGURE 2.15: Losses in a cascaded set-up. Losses acquired on the way from system 1 to system 2 prevent perfect cancellation. Grey lines show SQL and ideal CQNC for orientation. Plot parameters as in Tab. 2.2.
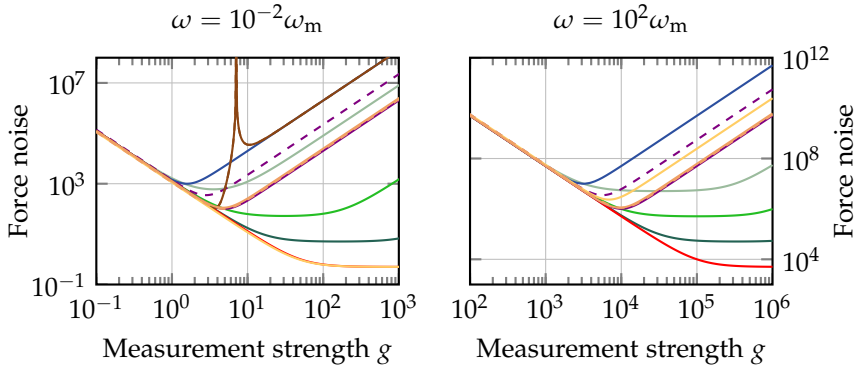
FIGURE 2.16: Sensitivity over measurement strength in a cascaded set-up. Blue trace is without CQNC, red shows ideal CQNC. Other colours indicate the type of mismatch as in Figs. 2.13–2.15. At low frequencies (left), perfect cancellation for unmatched coupling strengths, but matched linewidths is possible, not so for higher frequencies (right) – see yellow lines and Fig. 2.14. Plot parameters as in Tab. 2.2.

Additionally, losses are taken into account (Fig. 2.15), which, apart from vacuum noise coupling into the ancilla cavity, were ignored up to now. Losses after system 2 do not change the noise cancellation but only affect the detection, so η_2 is set to $\eta_2 = 1$. Propagation losses become important, as can be seen in Fig. 2.15. Intracavity losses can be modelled as escape efficiencies, one for the opto-mechanical cavity, and one for the ancilla cavity,

$$\eta_{\text{esc}}^{\text{om}} = \frac{\kappa_{\text{om}}^{\text{in}}}{\kappa_{\text{om}}^{\text{in}} + \kappa_{\text{om}}^{\text{bath}}}, \quad \eta_{\text{esc}}^{\text{negmass}} = \frac{\kappa_{\text{c}}^{\text{in}}}{\kappa_{\text{c}}^{\text{in}} + \kappa_{\text{c}}^{\text{bath}}}. \tag{2.55}$$

The same formalism can also cover mode-matching losses. From Fig. 2.15 it becomes clear that even modest losses are detrimental to the possible noise reduction.

Again, the stability of the systems can be studied by looking at their characteristic equation, $\det(M_i - \lambda \mathbb{1}) = 0$. A system is stable if all coefficients in front of its characteristic equation are positive, which is true if all requirements are fulfilled. The coefficients for the negative-mass oscillator, Eq. 2.56, and the

opto-mechanical system, Eq. 2.57, are listed below.

$$c_0^{anc} = (g_{BS}^2 - g_{DC}^2)^2 - 2\Delta_a\Delta_c(g_{BS}^2 + g_{DC}^2) + 2\frac{\kappa_a\kappa_c}{4}(g_{BS}^2 - g_{DC}^2) + (\Delta_a^2 + \frac{\kappa_a^2}{4})(\Delta_c^2 + \frac{\kappa_c^2}{4})$$
$$c_1^{anc} = 2\frac{\kappa_a + \kappa_c}{2}(g_{BS}^2 - g_{DC}^2) + 2(\Delta_a^2 + \frac{\kappa_a^2}{4})\frac{\kappa_c}{2} + 2(\Delta_c^2 + \frac{\kappa_c^2}{4})\frac{\kappa_a}{2}$$
$$c_2^{anc} = 2(g_{BS}^2 - g_{DC}^2) + \Delta_a^2 + \frac{\kappa_a^2}{4} + \Delta_c^2 + \frac{\kappa_c^2}{4} + \kappa_a\kappa_c$$
$$c_3^{anc} = \kappa_a + \kappa_c$$
$$c_4^{anc} = 1$$

$$(2.56)$$

$$c_0^{om} = -\omega_m\Delta_{om}g^2 + \omega_m^2(\Delta_{om}^2 + \frac{\kappa_{om}^2}{4})$$
$$c_1^{om} = (\Delta_{om}^2 + \frac{\kappa_{om}^2}{4})\gamma_m + \omega_m^2\kappa_{om}$$
$$c_2^{om} = \Delta_{om}^2 + \frac{\kappa_{om}^2}{4} + \omega_m^2 + \gamma_m\kappa_{om}$$
$$c_3^{om} = \gamma_m + \kappa_{om}$$
$$c_4^{om} = 1$$

$$(2.57)$$

For the opto-mechanical system, the only critical part is c_0^{om}. If the detuning is non-zero and positive and the coupling is strong enough, the system becomes unstable, similar to the integrated system.

For the ancilla cavity, as $\Delta_a = -\omega_m < 0$ is required, the main source of instability is $g_{DC} > g_{BS}$ (red underline), again similar to the integrated set-up. A strong measurement strength can render the system unstable in the case of negative detunings Δ_c (blue underline). As the two systems are separated, a momentary non-zero positive detuning Δ_{om} in the opto-mechanical system cannot bring the ancilla system, which may be close to instability, over the edge as could happen in the integrated set-up. A positive detuning Δ_c is not an issue here.

2.4 TOWARDS THE EXPERIMENT

Up to now, all considerations have been quite far from actual physical and experimental quantities. This chapter takes a closer look at what is feasible, i.e. how and in which parameter range a potential experiment can be set up. It further makes suggestions on how to implement the interactions required from the previous chapter.

Table 2.2: Plot parameters cascaded set-up used in Figs. 2.13 to 2.16 if not specified otherwise. In the third column, all parameters are normalised to the mechanical resonance frequency ω_m. Parameters in the fourth column are obtained from the third column via setting $\omega_\mathrm{m} = 2\pi \times 500\,\mathrm{kHz}$. Plot parameters are the same as for integrated set-up (Tab. 2.1) with the addition of κ_om, Δ_om, η_1 and η_2.

Parameter		Norm. value	Value
ω_m	mechanical resonance frequency	1	$500\,\mathrm{kHz}$
γ_m	mechanical linewidth	$10^{-3}\omega_\mathrm{m}$	$5\,\mathrm{kHz}$
Q	mechanical quality factor	$\frac{\omega_\mathrm{m}}{\gamma_\mathrm{m}}$	10^3
Δ_a	detuning ancilla cavity	$-\omega_\mathrm{m}$	$-500\,\mathrm{kHz}$
κ_a	linewidth ancilla cavity	γ_m	$5\,\mathrm{kHz}$
Δ_c	detuning meter cavity	0	
κ_c	linewidth meter cavity	$10\omega_\mathrm{m}$	$5\,\mathrm{MHz}$
Δ_om	detuning OM cavity	0	
κ_om	linewidth OM cavity	κ_c	$5\,\mathrm{MHz}$
g	opto-mechanical coupling strength	ω_m	$500\,\mathrm{kHz}$
g_BS	beam-splitter coupling strength	$\frac{1}{2}g$	$250\,\mathrm{kHz}$
g_DC	down-conversion coupling strength	$\frac{1}{2}g$	$250\,\mathrm{kHz}$
η_1	efficiency OM to negative mass	1	
η_2	efficiency negative mass to detection	1	
ω	measurement (Fourier) frequency	$10\omega_\mathrm{m}$	$5\,\mathrm{MHz}$

2.4.1 Design desicions and parameter search

The first restrictions on a possible experimental realisation arise from the down-conversion interaction and the beam-splitter interaction, which are needed to couple two in principle distinguishable modes of light. To make the two modes, mode $\hat{c}$ of the meter and mode $\hat{a}$ of the ancilla cavity, distinguishable, any of the characteristics of a mode of light as presented in Sec. 1.1.2 could be used. It is worth noting that a beam-splitter interaction couples two modes not by splitting, but by mixing them, by converting one mode into another and vice versa. Hence, a polarisation beam splitter for instance does not couple two polarisation modes.

A beam-splitterlike interaction is not as easily realised for modes of different frequencies[126] or different transverse mode shapes[127] as it is for modes of different polarisations or directions of propagation. A power beam splitter can realise the beam-splitter interaction for modes different only in their direction of propagation. A wave plate (actually any rotated birefringent medium, as can be seen later in Sec. 5.2) can couple any two linear orthogonally polarised modes in a beam-splitterlike fashion.

The down-conversion interaction can be enhanced by a surrounding cavity, which is difficult to accomplish when the modes differ in their direction of propagation. Additionally, two modes of light interact longer and thus stronger inside a nonlinear medium when propagating in the same direction (cf. Sec. 4.2.4).[128] Hence, the two modes shall differ only in their polarisation. They can additionally be separated spatially with a polarising beam splitter. This might become necessary in an integrated set-up because only one of two modes is to interact with the opto-mechanical device.

A set of parameters for a proof-of-principle experiment was devised be-

---

[126] A frequency beam splitter could be realised with a nonlinear crystal or an acousto-optic modulator (AOM). The AOM would diffract light from zeroth to first order and vice versa. The nonlinear process would convert modes of different frequencies via sum and difference frequency generation. Actually, the AOM process and the up- or down-conversion process are very similar – both caused by 'diffraction' at a periodically modulated material, see Louisell, Yariv and Siegman (1961).

[127] A mode shape beam splitter could maybe look like a misaligned cavity or realised with the use of a spatial light modulator, but losses definitely become a problem.

[128] Down-conversion interaction coupling two modes of different frequencies are common. A coupling of two modes of different mode-shapes should be possible with the pump photon's shape being a superposition of the two down-conversion photons. It would, however, require both modes being resonant in the same cavity, which is usually not the case, see 1.2.2.

TABLE 2.3: Parameters for CQNC. As in the original publications, the system is assumed to be lossless and the requirements are fulfilled (apart from $\kappa_a = \gamma_m$), see, for the integrated set-up, D. Steinmeyer, 'Towards Coherent Quantum Noise Cancellation. Untersuchungen zur kohärenten Unterdrückung von Quantenrauschen in Interferometern', Master thesis, Leibniz Universität Hannover, 2014; M. H. Wimmer, D. Steinmeyer, K. Hammerer and M. Heurs, 'Coherent cancellation of backaction noise in optomechanical force measurements', *Phys. Rev. A* **89** (2014), 053836. For an updated table see Tab. 6.1.

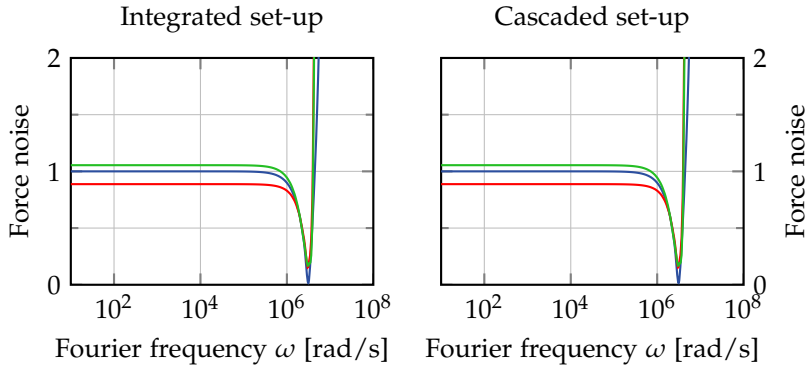|	Parameter	Given by	Value
Common parameters	ω_m		$500\,\text{kHz}$
	γ_m	ω_m/Q	$500\,\text{Hz}$
	Q		10^3
	Δ_a	$-\omega_m$	$-500\,\text{kHz}$
	κ_a	$400\gamma_m$	$200\,\text{kHz}$
	Δ_c		0
	κ_c		$1\,\text{MHz}$
	κ_c^{bath}		0
	g		$300\,\text{kHz}$
	g_{BS}	$\frac{g}{2}$	$150\,\text{kHz}$
	g_{DC}	$\frac{g}{2}$	$150\,\text{kHz}$
Cascaded set-up	Δ_{om}		0
	κ_{om}	κ_c	$1\,\text{MHz}$
	κ_{om}^{bath}		0
	η_1		1
	η_2		1
Integrated set-up	η		1

Figure 2.17: Experimentally achievable sensitivity, normalised to the quality factor Q. Standard Quantum Limit (blue traces), improvement through CQNC (red traces) and sensitivities without coupling to a negative-mass oscillator (green traces) Plot parameters as in Tab. 2.3.

fore,[129] the parameters are given in Tab. 2.3 with additional parameters for a cascaded set-up added to the list. Main trade-offs and difficulties are:

- When matching the coupling strengths, the beam-splitter coupling g_{BS} is more challenging to make weak enough whereas the other two couplings, g and g_{DC}, are difficult to increase.

- In order to reach a regime where radiation-pressure noise is actually limiting, a large measurement strength $G \propto g^2$ is needed.

- The ancilla cavity linewidth κ_a is challenging to make very small. On the other hand, increasing the mechanical linewidth γ_m in order to match κ_a results in a small mechanical quality factor Q and thus small improvement in sensitivity. Additionally, the coupling to a thermal bath is increased, masking and decohering the quantum states.

With the parameters as in Tab. 2.3 and neglecting thermal noise, sensitivities as shown in Fig. 2.17 are possible. With the same set of parameters, the integrated and the cascaded set-up lead to the same results. Thermal noise can be mitigated by cooling the system to cryogenic temperatures and isolating it from the bath with high Q-factors,[130] or, in a first step, by creating artificial

---

[129]Wimmer, Steinmeyer, Hammerer and Heurs (2014); Steinmeyer, Master thesis (2014).
[130]Møller et al. (2017).

amplitude quadrature noise resulting in radiation-pressure noise above the thermal noise.

2.4.2 What it will look like in the end

Over time, schemes of potential experiments became more and more refined, see Fig. 2.18. Starting point was the flowchart representing the interactions in a very abstract way. Tsang and Caves gave implementation details in that they suggested an all-optical scheme to realise the effective negative mass and specified its parts, namely the beam-splitter and the down-conversion interactions as means of coupling to a detuned cavity. Their schematic still remained rather abstract, but they already suggested a cascaded set-up as an alternative to the integrated set-up. Wimmer and co-workers further modified the experimental scheme, mainly with the idea of using the polarisation as a means to distinguish the two modes (for this see Sec. 5).

This thesis suggests the use of a cascaded set-up as in Fig. 2.18f. Here, the opto-mechanical interaction is separated from the negative-mass interaction. This makes it easier to take care of the small beam waists needed for the down-conversion interaction and potentially also for the opto-mechanical interaction. Having the two set-ups separated, it is not necessary any more to spatially separate the two cavities coupled via the down-conversion and the beam-splitter interaction, where the latter is realised by a wave plate. The design considerations of the five-mirror coupled cavities are laid out in detail in Sec. 5.3.1.

Works referenced in the preceding chapter

Baker, C. G. and W. P. Bowen, 'Precision measurement: Sensing past the quantum limit', *Nature* **547** (2017), 164–165, DOI: 10.1038/547164a.

Clerk, A. A., M. H. Devoret, S. M. Girvin, F. Marquardt and R. J. Schoelkopf, 'Introduction to quantum noise, measurement, and amplification', *Rev. Mod. Phys.* **82** (2010), 1155–1208, DOI: 10.1103/RevModPhys.82.1155.

Eiermann, B., P. Treutlein, T. Anker, M. Albiez, M. Taglieber, K. P. Marzlin and M. K. Oberthaler, 'Dispersion Management for Atomic Matter Waves', *Phys. Rev. Lett.* **91** (2003), 060402, DOI: 10.1103/PhysRevLett.91.060402.

Gardiner, C. W. and P. Zoller, *Quantum noise : a handbook of Markovian and non-Markovian quantum stochastic methods with applications to quantum optics*, Berlin et al.: Springer, 2000.
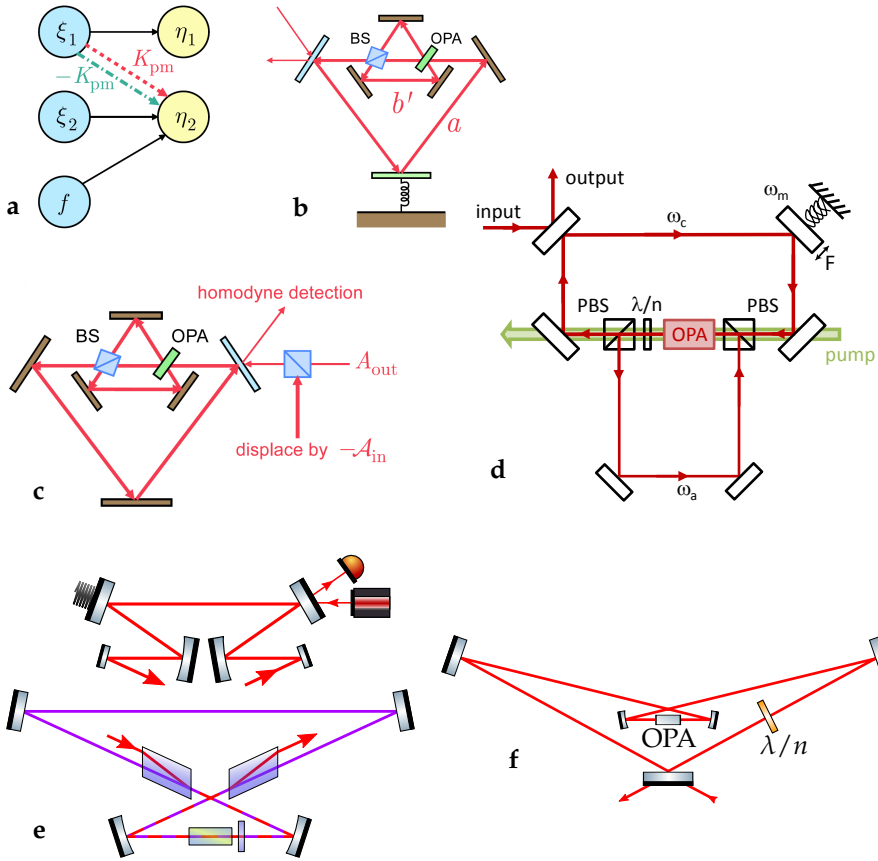
FIGURE 2.18: Evolution of all-optical CQNC scheme. a, representing the abstract flow of signals. b, detuned cavity as negative-mass oscillator coupled via a down-conversion and a beam-splitter interaction. c, suggesting cascaded set-up (all figures from M. Tsang and C. M. Caves, 'Coherent quantum-noise cancellation for optomechanical sensors', *Phys. Rev. Lett.* **105** (2010), 123601). d, set-up closer to an experimental realisation, with polarisation of modes as a means to distinguish them, (figure from M. H. Wimmer, D. Steinmeyer, K. Hammerer and M. Heurs, 'Coherent cancellation of backaction noise in optomechanical force measurements', *Phys. Rev. A* **89** (2014), 053836). e, even more realistic set-up, taking care of beam waists and using beam displacers as beam splitters (figure from D. Steinmeyer, 'Towards Coherent Quantum Noise Cancellation. Untersuchungen zur kohärenten Unterdrückung von Quantenrauschen in Interferometern', Master thesis, Leibniz Universität Hannover, 2014). f, cascaded set-up with separated positive- and negative-mass oscillators, simplifying the beam-splitter coupling and the set-up of coupled cavities (this thesis, Sec. 5).

Gerry, C. C. and P. L. Knight, *Introductory Quantum Optics*, Cambridge et al.: Cambridge University Press, 2005.

Hammerer, K., M. Aspelmeyer, E. S. Polzik and P. Zoller, 'Establishing Einstein-Poldosky-Rosen Channels between Nanomechanics and Atomic Ensembles', *Phys. Rev. Lett.* **102** (2009), 020501, DOI: 10.1103/PhysRevLett.102.020501, arXiv: 0804.3005.

Hammerer, K., A. S. Sørensen and E. S. Polzik, 'Quantum interface between light and atomic ensembles', *Rev. Mod. Phys.* **82** (2010), 1041–1093, DOI: 10.1103/RevModPhys.82.1041.

Khalili, F. Y. and E. S. Polzik, 'Overcoming the Standard Quantum Limit in Gravitational Wave Detectors Using Spin Systems with a Negative Effective Mass', *Phys. Rev. Lett.* **121** (2018), 031101, DOI: 10.1103/PhysRevLett.121.031101, arXiv: 1710.10405.

Kohler, J., J. A. Gerber, E. Dowd and D. M. Stamper-Kurn, 'Negative-Mass Instability of the Spin and Motion of an Atomic Gas Driven by Optical Cavity Backaction', *Phys. Rev. Lett.* **120** (2018), 013601, DOI: 10.1103/PhysRevLett.120.013601.

Law, C. K., 'Interaction between a moving mirror and radiation pressure: A Hamiltonian formulation', *Phys. Rev. A* **51** (1995), 2537–2541, DOI: 10.1103/PhysRevA.51.2537.

Louisell, W. H., A. Yariv and A. E. Siegman, 'Quantum fluctuations and noise in parametric processes. I.', *Phys. Rev.* **124** (1961), 1646–1654, DOI: 10.1103/PhysRev.124.1646.

Møller, C. B., R. A. Thomas, G. Vasilakis, E. Zeuthen, Y. Tsaturyan, M. Balabas, K. Jensen, A. Schliesser, K. Hammerer and E. S. Polzik, 'Quantum back-action-evading measurement of motion in a negative mass reference frame', *Nature* **547** (2017), 191–195, DOI: 10.1038/nature22980, arXiv: 1608.03613.

Ockeloen-Korppi, C. F., E. Damskägg, J. M. Pirkkalainen, A. A. Clerk, M. J. Woolley and M. A. Sillanpää, 'Quantum Backaction Evading Measurement of Collective Mechanical Modes', *Phys. Rev. Lett.* **117** (2016), 140401, DOI: 10.1103/PhysRevLett.117.140401.

Ogata, K., *Modern Control Engineering*, 5th ed., Upper Saddle River, NJ: Pearson, 2010.

Polzik, E. S. and K. Hammerer, 'Trajectories without quantum uncertainties', *Ann. Phys.* **527** (2015), A15–A20, DOI: 10.1002/andp.201400099, arXiv: 1405.3067.

Steinmeyer, D., 'Towards Coherent Quantum Noise Cancellation. Untersuchungen zur kohärenten Unterdrückung von Quantenrauschen in Interferometern', Master thesis, Leibniz Universität Hannover, 2014.

Tsang, M. and C. M. Caves, 'Coherent quantum-noise cancellation for optomechanical sensors', *Phys. Rev. Lett.* **105** (2010), 123601, DOI: 10.1103/PhysRevLett.105.123601, arXiv: 1006.1005.

Walls, D. F. and G. J. Milburn, *Quantum Optics*, Berlin, Heidelberg: Springer, 2008, DOI: 10.1007/978-3-540-28574-8.

Wimmer, M. H., 'Coupled nonclassical systems for coherent backaction noise cancellation', PhD thesis, Leibniz Universität Hannover, 2016, URL: http://edok01.tib.uni-hannover.de/edoks/e01dh16/863136931.pdf.

Wimmer, M. H., D. Steinmeyer, K. Hammerer and M. Heurs, 'Coherent cancellation of backaction noise in optomechanical force measurements', *Phys. Rev. A* **89** (2014), 053836, DOI: 10.1103/PhysRevA.89.053836, arXiv: 1403.2992.

Woolley, M. J. and A. A. Clerk, 'Two-mode back-action-evading measurements in cavity optomechanics', *Phys. Rev. A* **87** (2013), 063846, DOI: 10.1103/PhysRevA.87.063846.

Yamamoto, N., 'Coherent versus Measurement Feedback: Linear Systems Theory for Quantum Information', *Phys. Rev. X* **4** (2014), 041029, DOI: 10.1103/PhysRevX.4.041029.

Zhang, K., P. Meystre and W. Zhang, 'Back-action-free quantum optomechanics with negative-mass Bose-Einstein condensates', *Phys. Rev. A* **88** (2013), 043632, DOI: 10.1103/PhysRevA.88.043632.

3

RADIATION PRESSURE INTERACTION

This chapter deals with the opto-mechanics needed to create measurable radiation-pressure noise in a table-top experiment. First, an introduction into opto-mechanical devices and their use is given. Then, the experiments conducted for studying opto-mechanical devices, namely mirrors on cantilevers and photonic-crystal membranes obtained from Simon Gröblacher,[131] are presented. They resulted in measurements of resonance frequencies ω_{m}, linewidths γ_{m}, and effective masses m_{eff}. These are important parameters for coherent quantum-noise cancellation (CQNC), as ω_{m} and γ_{m} characterise a mechanical oscillator and the effective mass m_{eff} determines the device's zero point fluctuation x_{ZPF} and with that the opto-mechanical coupling strength g.

All experiments, which were the first conducted with opto-mechanical devices in our group, were done together with Bernd Schulte. During the assembly of an opto-mechanical cavity, the experiments were interrupted by closure of the lab for almost one year due to construction work. After moving to a new lab, I was not involved in opto-mechanical experiments any more but started to set up the experiments presented in the following Secs. 4 and 5.

3.1 Opto-mechanical devices

The interaction between light and matter through radiation pressure can be mediated by a variety of devices ranging from very heavy (several tens of kilograms for large mirrors) to very lightweight (centre-of-mass motion of atoms). This makes the techniques used to realise an opto-mechanical interaction differ a lot between different implementations, particularly in scale,

---

[131] S. Gröblacher, now at TU Delft, fabricated the devices during his time at University of Vienna and kindly left us some samples for our studies.

although the underlying theory is rather straightforward (cf. Sec. 1.3) and in all cases very similar. The Fig. 3.1, taken from a review by M. Aspelmeyer, T. Kippenberg and F. Marquardt,[132] shows a broad range of opto-mechanical devices.

The interest in opto-mechanics originated in the gravitational-wave community as early as in the 1980's as mentioned in the introduction to this thesis. But it was not until the beginning of this century when technical progress made it possible for opto-mechanical table-top experiments to approach quantum level and renewed interest in opto-mechanical systems.[133] The main reasons for doing opto-mechanics are:[134]

MEASUREMENTS. Opto-mechanical devices are used as sensors. Usually, the position of a moveable mechanical device is optically monitored. Changes in position enable inference of forces acting on that device. When used for sensing, the quantum nature of the light–mechanics interaction is often unwanted. The gravitational wave community speaks of radiation-pressure *noise*.

QUANTUM FOUNDATIONS. With opto-mechanics approaching the quantum level, it became possible to realise truly macroscopic quantum systems, to explore and to shift the boundary between the classical and the quantum world. Entangled macroscopic objects are one such system.[135] Here, light is not only a means for reading out, but actually mediates the entanglement. Such systems facilitate studying fundamental decoherence processes.[136]

QUANTUM COMPUTING AND NETWORKS. Quantum computing requires systems to store, manipulate and send or exchange information on a quantum level. Two characteristics of opto-mechanical devices might render them useful. Larger systems tend to operate at larger timescales making mechanics as a comparatively large quantum system an option for storage of quantum states. Additionally, because the radiation-pressure interaction is not wavelength-dependent as opposed

---

[132] M. Aspelmeyer, T. J. Kippenberg and F. Marquardt, 'Cavity optomechanics', *Rev. Mod. Phys.* **86** (2014), 1391–1452.

[133] Aspelmeyer, Kippenberg and Marquardt (2014), Sec. I.

[134] Aspelmeyer, Kippenberg and Marquardt (2014), Sec. I.

[135] R. Riedinger et al., 'Remote quantum entanglement between two micromechanical oscillators', *Nature* **556** (2018), 473–477.

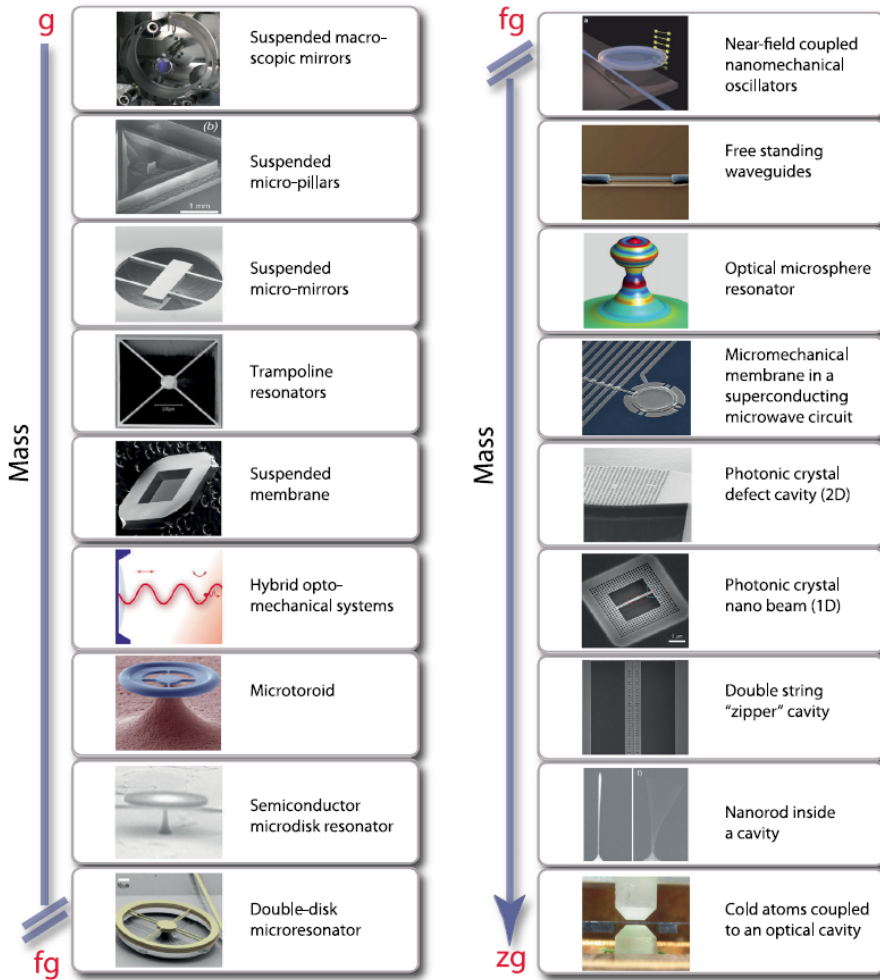[136] Aspelmeyer, Kippenberg and Marquardt (2014), Sec. X.C.

Figure 3.1: Overview of opto-mechanical devices. Figure from M. Aspelmeyer, T. J. Kippenberg and F. Marquardt, 'Cavity optomechanics', *Rev. Mod. Phys.* **86** (2014), 1391–1452. Pictures courtesy of (from high to low masses) N. Mavalvala, A. Heidmann, M. Aspelmeyer, D. Bouwmeester, J. Harris, P. Treutlein, T. J. Kippenberg, I. Favero, M. Lipson, T. J. Kippenberg/E. Weig/J. Kotthaus, H. Tang, K. Vahala/T. Carmon, J. Teufel/K. Lehnert, I. Robert, O. Painter, O. Painter, I. Favero/ E. Weig/K. Karrai, and D. Stamper-Kurn.

to interactions in nonlinear optics or atomic physics, mechanical devices could be used as as an interface, e.g. between light in the optical and in the microwave regime.[137] Hybrid systems with the mechanical element coupled to atoms have also been realised.[138]

For CQNC, an opto-mechanical interaction is needed which can be assembled in a table-top experiment and is able to work in the parameter range specified in Sec. 2.4.1 (see Tab. 2.3). The main figure of merit[139] of opto-mechanical devices for CQNC is their coupling strength g. This coupling strength is known from Sec. 1.3,

$$g = \sqrt{2}\alpha g_0, \qquad g_0 = \frac{\omega_a}{L} x_{ZPF} = \frac{\omega_a}{L} \sqrt{\frac{\hbar}{m_{eff}\omega_m}}, \tag{3.1}$$

again with α the amplitude of a light field with frequency ω_a in a cavity with length L, the single-photon coupling strength g_0, and the zero point fluctuation x_{ZPF}, which contains the device parameters. In order to be limited by radiation-pressure noise, a strong coupling g is needed, which requires a lightweight mechanical device and a high-finesse cavity for strong intracavity power. This can be intuitively understood because the lighter the mass, the easier it is to move it with radiation pressure, and is why the effective-mass measurement is important in the next Sec. 3.2.1.

The devices used in the context of this thesis are shown in Fig. 3.2. The Bragg mirror on a cantilever is, just like an ordinary Bragg mirror, made of layers of materials with different refractive indices as to increase the reflection of the incoming light field. The surroundings and the material below the cantilever is etched away.[140] These additional layers make the devices rather heavy, resulting in a smaller coupling strength g. The samples at hand can also only be used as an end mirror as the substrate is not transparent.

By structuring photonic-crystal membranes such that band-gaps for certain frequencies of light and certain directions of propagation are formed, akin to

---

[137] R. W. Andrews et al., 'Bidirectional and efficient conversion between microwave and optical light', *Nat. Phys.* **10** (2014), 321–326.

[138] See, e.g., S. Camerer et al., 'Realization of an optomechanical interface between ultracold atoms and a membrane', *Phys. Rev. Lett.* **107** (2011).

[139] Other important parameters are cooperativity $C = \frac{4g^2}{\kappa\gamma_m}$ comparing time-scales of coupling and decoherence rates, and the Qf-product, quantifying the degree of isolation to a thermal bath, see Aspelmeyer, Kippenberg and Marquardt (2014), IV.A.

[140] S. Gröblacher, 'Quantum opto-mechanics with micromirrors: combining nano-mechanics with quantum optics', PhD thesis, Universität Wien, 2010.
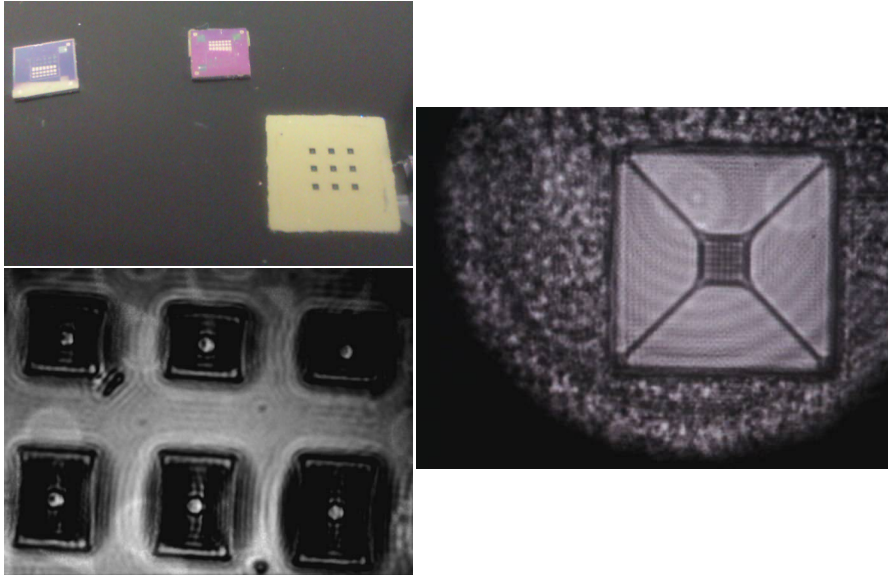
Figure 3.2: Membranes and cantilevers. Upper left: Chips housing the opto-mechanical devices, top two with Bragg mirrors on a cantilever, bottom right with membranes. Lower left: Close-up of Bragg mirrors on cantilevers, taken in reflection of chip (cf. Fig. 3.3). Bright spots are mirrors (ca. 40 μm in diameter), sitting on a bridge with the material below etched away. Right: Close-up of a photonic-crystal membrane, taken in transmission of chip (cf. Fig. 3.3). The dark square in the centre is the actual membrane with a length of ca. 90 μm, held by trampoline-like ligaments. Devices were fabricated by S. Gröblacher, TU Delft (formerly in Vienna).

band-gaps known from solid state physics, propagation of light is prevented in directions other than normal to the surface and the reflection enhanced.[141] This makes them potentially very lightweight, while higher reflectivities increase the radiation-pressure force and thus the coupling strength.

Micro-mirrors and photonic-crystal membranes where chosen because of their low mass m_{eff} facilitating high coupling strengths g, and their high resonance frequency ω_{m} compared to larger opto-mechanical systems (e.g. suspended mirrors). The latter characteristic makes it easier to have a cavity linewidth smaller than the mechanical resonance frequency, cf. Eqs. 2.40.

The most prominent way to realise opto-mechanical set-ups has been that of a membrane-in-the-middle set-up ever since Jayich and co-workers showed that a membrane in a linear cavity is equivalent to a linear cavity with a moveable end mirror.[142] Compared to conventional cavities with a moving end mirror, optical and mechanical characteristics are decoupled in a membrane-in-the-middle set-up, defeating the need to compromise between good optical properties (meaning high reflectivities/low losses for large power build-up inside the cavity) and good mechanical properties (low mass and high quality factor) of a membrane/a mirror.

In opto-mechanical experiments with membranes and reflective mirrors, coupling strengths of some hundreds of kilohertz to some megahertz have been achieved in the optical domain, e.g. $g = 2\pi \times 325\,\text{kHz}$ with $11\,\text{mW}$ input power[143] already ten years ago, $g = 2\pi \times 440\,\text{kHz}$ with $38\,\mu\text{W}$ input power more recently.[144] With new highly reflective trampoline membranes, it is expected to easily reach coupling strength of more than $1\,\text{MHz}$ with just $10\,\mu\text{W}$ driving power and at the same time very high quality factors.[145] Even better quality factors in a similar effective-mass regime are obtained by phononic shielding.[146]

[141] R. A. Norte, J. P. Moura and S. Gröblacher, 'Mechanical Resonators for Quantum Optomechanics Experiments at Room Temperature', *Phys. Rev. Lett.* **116** (2016), 147202.

[142] A. M. Jayich et al., 'Dispersive optomechanics: A membrane inside a cavity', *New J. Phys.* **10** (2008), 095008.

[143] S. Gröblacher, K. Hammerer, M. R. Vanner and M. Aspelmeyer, 'Observation of strong coupling between a micromechanical resonator and an optical cavity field', *Nature* **460** (2009), 724–727.

[144] C. B. Møller et al., 'Quantum back-action-evading measurement of motion in a negative mass reference frame', *Nature* **547** (2017), 191–195.

[145] Norte, Moura and Gröblacher (2016).

[146] Y. Tsaturyan, A. Barg, E. S. Polzik and A. Schliesser, 'Ultracoherent nanomechanical resonators via soft clamping and dissipation dilution', *Nat. Nanotechnol.* **12** (2017), 776–783.
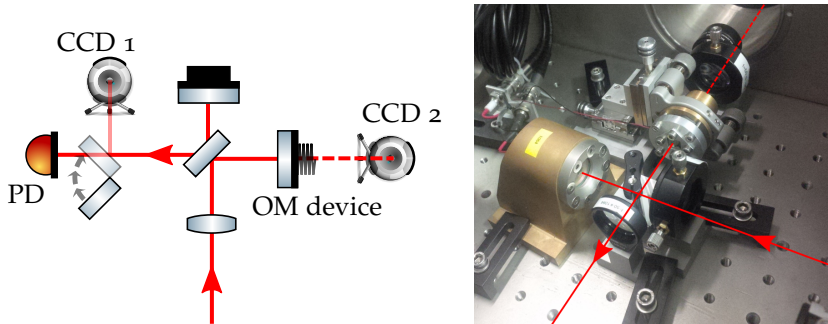
FIGURE 3.3: Opto-mechanical interferometer. Opto-mechanical (OM) device constitutes one end mirror, the other, highly reflective end mirror attached to a piezo is used for stabilising the Michelson interferometer. The OM device is also attached to a piezo, which can be used to externally excite the device's resonances.

3.2 DETERMINING g

For the characterisation of the opto-mechanical devices at hand, a Michelson interferometer was used, with the end mirror of one arm being the opto-mechanical device under test, see Fig. 3.3. A piezo-electric element was attached to each of the two end mirrors. The one behind the opto-mechanical device served as a means to excite mechanical resonances, the one behind the other end mirror was used for locking the interferometer to mid-fringe via the side-/fringe-locking technique (cf. Sec. 1.2.3). At this operation point, relative phase changes cause the largest change in output power, meaning the interferometer is most sensitive here.

The whole set-up was put into a vacuum tank and pumped down to less than 2×10^{-2} mbar.[147] The outgoing beam was split with a power beam splitter. One part was sent onto a photodiode, the other for imaging onto a modified commercial CCD camera.[148] The pictures in Fig. 3.2 were made using this imaging procedure.

The main challenge with these opto-mechanical devices is to create a waist small enough and at the right position so that one is actually probing the device and not the surrounding frame or other elements. Due to the devices'

---

[147]A tank formerly used for GEO600 was used. The vacuum pump was a scroll pump by Agilent, *Datasheet Agilent IDP-15 Dry Scroll Vacuum Pump*, Agilent, URL: https://www.agilent.com/cs/library/datasheets/public/IDP-15_5991-7604EN_DataSheet_LR.pdf.

[148]Lens and infra-red filter were removed from a Namtai EyeToy camera, model no SCEH-0004.
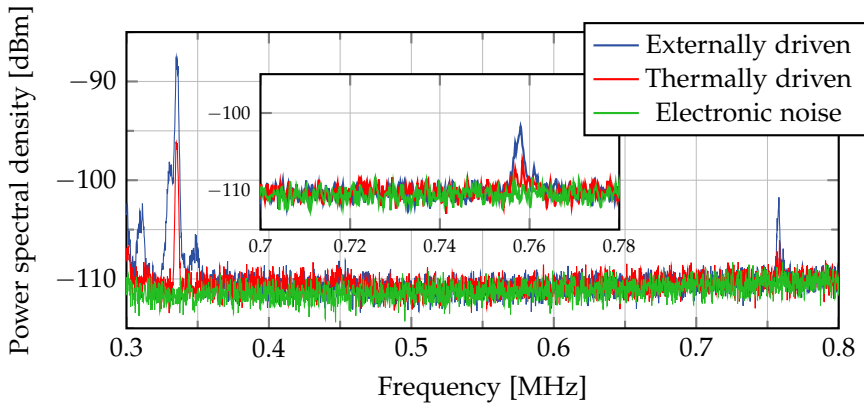
FIGURE 3.4: Resonances of membrane no. 9. First resonance found at 335 kHz, second and third, for clarity also shown in the inset, at 758 kHz and 761 kHz. Second and third resonance are non-degenerate due to the membrane not being perfectly quadratic. Measurement was taken with a RBW of 2 kHz and a VBW of 300 Hz.

dimensions, waists smaller than 10 µm were needed to limit diffraction losses.

3.2.1 Characterisation of devices

The devices' resonances can be found with feeding the photodiode's output into a spectrum analyser. Comparing spectra of exciting the device with white noise fed onto the piezo-electric element behind the device and not exciting it shows mechanical resonances, see Fig. 3.4 The found resonances can further be confirmed by driving the piezo with a modulation around the mechanical resonance frequency and observing the transfer of electronic drive into movement and thus power in optical side-bands at the respective frequencies.

The linewidth of an opto-mechanical element was measured with two different methods (Fig. 3.6): First, a device's thermally excited resonance peak can be measured with a spectrum analyser and the linewidth can be extracted. This is because, with the equations of motion for a mechanical device in Fourier domain,

$$\left(\omega_{\mathrm{m}}^2 - \omega^2 + i\gamma\omega\right) x(\omega) = F_{\mathrm{th}}/m, \tag{3.2}$$

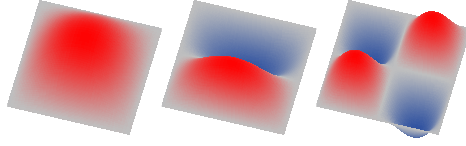where F_{th} is the thermal force acting on the mechanical device and is white,

FIGURE 3.5: Eigenmodes of a membrane. The areas in grey do not move, a probe beam positioned there sees an infinite effective mass of that mode.

i.e. independent of the frequency. The position spectral density is then

$$S_{xx} = \lim_{T \to \infty} \frac{1}{T} 2|x(\omega)|^2 = \text{const.} \times \frac{1}{(\omega_{\mathrm{m}}^2 - \omega^2)^2 + \gamma_{\mathrm{m}}^2 \omega^2}, \qquad (3.3)$$

which can be used to model the data with resonance frequency ω_{m} and linewidth γ_{m} and a constant as fit parameters.[149]

Second, the mode resonance can be excited with the piezo element. After switching off the excitation, the decay of that resonance can be observed in a ring-down measurement using a spectrum analyser in zero-span mode – the power contained in a frequency band around the resonance is measured over time. Here, one can see the decaying resonances as a time-dependent phase modulation of one of the interferometer arms. The output of the interferometer is then[150]

$$E = E_1 \cos(\omega_{\mathrm{L}} t + \phi_0) + E_2 \cos\left(\omega_{\mathrm{L}} t + \frac{2\pi}{\lambda} A_0 e^{-\gamma_{\mathrm{m}} t/2} \cos \omega_{\mathrm{m}} t\right), \qquad (3.4)$$

with $E_{1,2}$ the field amplitudes in the two interferometer arms and $E_1 = E_2$ for a 50:50 beam splitter. For small phase modulations, this can be approximated to (see Sec. 1.1.1)

$$E = E_1 \cos(\omega_{\mathrm{L}} t + \phi_0) + \frac{E_2}{2} e^{i\omega_{\mathrm{L}} t}(1 + im \cos \omega_{\mathrm{m}} t) + \frac{E_2}{2} e^{-i\omega_{\mathrm{L}} t}(1 - m \cos \omega_{\mathrm{m}} t), \qquad (3.5)$$

where the modulation index m is $m = \frac{2\pi}{\lambda} A_0 e^{-\gamma_{\mathrm{m}} t/2}$. The output power of the interferometer, after averaging over the very fast oscillations ω_{L}, is proportional to $|E|^2$:

$$P_{\mathrm{out}} \propto \text{const.} + \frac{P_{\mathrm{in}}}{2} m \sin \phi_0 \cos \omega_{\mathrm{m}} t, \qquad (3.6)$$

---

[149]The units of the noise spectral density do not really matter here since we model the shape and the only important parameter is the x-axis – the frequency which we do not need to convert.

[150]It is important to take care whether the linewidth is defined as HWHM or FWHM in the initial equation of motion.
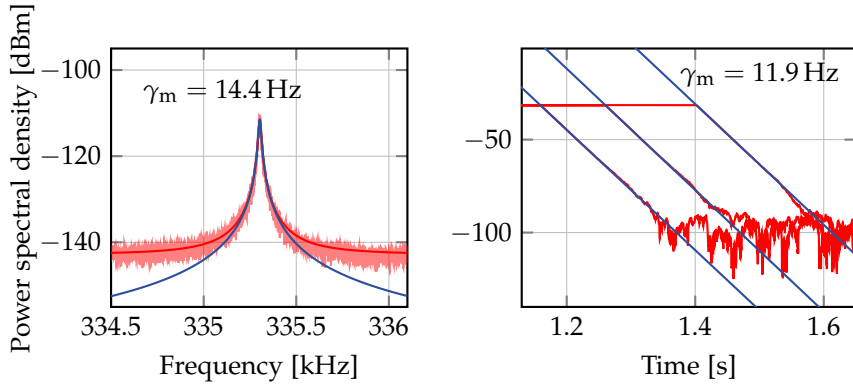
FIGURE 3.6: Opto-mechanical linewidth measurements, here of first resonance of membrane no. 9. Left: Directly fitting the linewidth of a thermally excited membrane. Right: Three ring-down measurements of externally driven membrane after switching off the drive. The Lorentzian best-fit linewidth 14.4 Hz does not differ visually from using the ring-down linewidth 11.9 Hz for plotting the Lorentzian. The linewidths determined by ring-down measurements were used for further calculations. Both measurements were done at a pressure of 1.5×10^{-2} mbar. RBWs are 1 Hz and 1 kHz, respectively, VBWs are also 1 Hz and 1 kHz, respectively.

where ϕ_0 is the operation point of the interferometer (the relative phase caused by length difference of the interferometer arms, here for maximum signal stabilised to $\phi_0 = \pi/2$). The output light power causes a photocurrent, converted into a voltage by the photodetector, which is fed into the signal analyser. This device shows the power caused by the rms input voltage dropped over its $50\,\Omega$ input impedance contained in a frequency band. In this measurement, the power contained in the frequency band around ω_m over time is of interest. The remaining time dependency is the exponential decay depending on the linewidth. In logarithmic display, all the conversion factors cause a shift of the offset, the slope only changes with different exponents. The slope k has to be converted from units of power, dBm/Hz, to units of voltage, which is then proportional to optical power. Furthermore, the slope is obtained being to base 10 and not to the natural logarithm. The linewidth in rad/s ends up being

$$\gamma_m = 2\frac{\ln 10}{20}k \approx 0.23k, \tag{3.7}$$

where k has dimensions dBm/s and the factor in front of k accounts for conversion to voltage and change of base.

All the linewidth measurements are limited not by the devices' intrinsic damping properties, but by residual pressure inside the vacuum chamber. Pressures lower than $1 \times 10^{-4}\,\text{mbar}$ to $1 \times 10^{-6}\,\text{mbar}$ would be needed in order to be limited by intrinsic damping properties. For different devices, the measurement results are listed in Tab. 3.1.

3.2.2 Inferring g

The fluctuation-dissipation theorem is a powerful theorem stating that, whenever there is dissipation, the process is two-way and there is a corresponding driving term. This is the reason for thermal noise exciting the membrane. The variance $\langle x^2 \rangle$ of the fluctuations in position caused by this driving term can further be expressed as a function only of the temperature T (as the thermal noise is frequency-independent) and of the characteristics of the mechanical device. These characteristics are its resonance frequency ω_m, its linewidth γ_m (which quantifies the coupling to the thermal bath) and its effective mass m_{eff}, lending the system inertia, its resistance towards movements. Measuring the variance, one can thus extract the temperature, knowing the effective mass, or the effective mass, knowing the temperature.

Table 3.1: Characterisation results for different opto-mechanical devices. 'mem' denotes a membrane, the other devices are Bragg mirrors on a cantilever. Note how higher pressure is not as detrimental to the quality factor of the heavier Bragg mirrors.

Device	ω_m [kHz]	Pressure [mbar]	γ_m [Hz]	m_eff [ng]	Q
mem 9	335	1.5×10^{-2}	11.7	1.8	29 000
	758	1.5×10^{-2}	10.0	3.4	76 000
	761	1.6×10^{-2}	11.7	11	65 000
mem 5	210	2.8×10^{-2}	7.0		30 000
		2.1×10^{-1}	10.6		20 000
		5.1	75		2800
		31	160		1300
2-3D	220	5.8×10^{-2}	4.0		55 000
		9.4×10^{-2}	4.7		47 000
		1.6×10^{-1}	5.8		38 000
		3.2×10^{-1}	9.1		24 000
		1	21.1		10 000
2-3E	188	1.9×10^{-2}	8.2	44	23 000
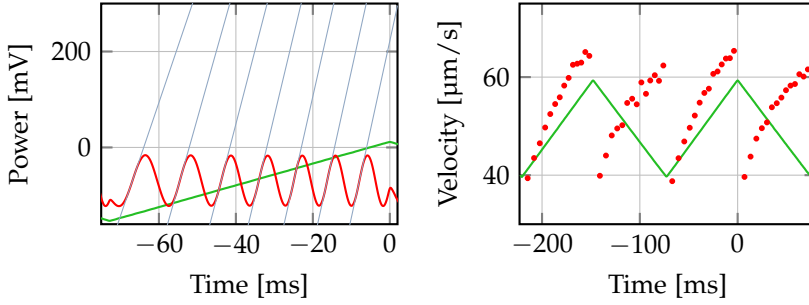
FIGURE 3.7: Nonlinearity of a piezo-electric element. Left: Interference fringes (red) created by changing the length of one arm in the Michelson interferometer, cf. Fig. 3.3. The voltage (green) on the piezo element changes linearly, but the spacing of detected minima and maxima (red) is not equidistant. The latter is further visualised by fitting the slope, i.e. the power change per unit time, $\mathrm{d}U/\mathrm{d}t$ (blue), on mid-fringe. Right: Velocity of piezo element (red dots), calculated from travel time between extrema in left figure, at different voltages (green). After each turning point, the piezo element is moving rather slowly, but then accelerates until the next turning point. See also Figs. 4.18 and 5.14.

The term *effective mass* is used in the preceding paragraph because the inertia of a system depends on several parameters, which can be demonstrated with the help of Fig. 3.9. Not the whole membrane moves, but only a fraction of the membrane's mass. If a probe beam is positioned on a node, it does not see any moving, resulting in an infinite effective mass for that mode. More generally, if there is no mode overlap between modes of membrane and of light beam, the light field cannot excite the membrane's mode. In addition to material and dimension of a device, the effective mass thus depends on the mechanical mode and the mode overlap of light field and mechanical mode.[151]

The effective mass can be extracted from the positional variance, which is equal to the integral over the noise spectral density in Eq. 3.3,[152]

$$\int S_{xx} \frac{\mathrm{d}\omega}{2\pi} = \langle x(t)^2 \rangle = \frac{k_\mathrm{B} T}{m_\mathrm{eff} \omega_\mathrm{m}^2}. \tag{3.8}$$

[151] M. Pinard, Y. Hadjar and A. Heidmann, 'Effective mass in quantum effects of radiation pressure', *Eur. Phys. J. C* **7** (1999), 107–111.

[152] A. A. Clerk et al., 'Introduction to quantum noise, measurement, and amplification', *Rev. Mod. Phys.* **82** (2010), 1155–1208, Eq. 3.52 and Appendix A, Aspelmeyer, Kippenberg and Marquardt (2014), Sec. II.B.3.

The first equality follows from the Wiener-Khinchin theorem, the second from the fluctuation-dissipation theorem in the limit of weak damping.[153] The noise spectral density has already been measured in the preceding Sec. 3.2.1, see Fig. 3.6. It needs to be calibrated to obtain a position spectral density.

A change in position x of the mechanical device causes a change in the photodetector's output voltage U, see also Fig. 3.7,

$$\frac{\mathrm{d}U}{\mathrm{d}x} = \frac{\mathrm{d}U}{\mathrm{d}t}\frac{\mathrm{d}t}{\mathrm{d}x}, \qquad \frac{\mathrm{d}t}{\mathrm{d}x} \approx \frac{\Delta t}{\Delta x}, \qquad (3.9)$$

where the first term, $\mathrm{d}U/\mathrm{d}t$, is the slope of the interference pattern at the interferometer's operation point and the second equation is valid if the piezo is assumed to move linearly between two extrema. Δt can be measured and $\Delta x = \lambda/4$ because of interference. The conversion from power spectrum measured by the spectrum analyser to a voltage spectrum is straightforward, as it just measures the power dissipated over a $50\,\Omega$ input resistor by voltage U_{rms} and $P = IU = U^2/R$:[154]

$$S_{UU}[\mathrm{V}^2/\mathrm{Hz}] = 50\,\Omega \times 10^{S_{PP}[\mathrm{dBm/Hz}]/10} \times 10^{-3}. \qquad (3.10)$$

The voltage spectral density can be converted into position spectral density via

$$S_{xx}[\mathrm{m}^2/\mathrm{Hz}] = \frac{\mathrm{d}U}{\mathrm{d}x}^{-2} S_{UU}[\mathrm{V}^2/\mathrm{Hz}]. \qquad (3.11)$$

One inconsistency took some time to figure out: The calibration of position to voltage, $\mathrm{d}U/\mathrm{d}x$, is done at a frequency $10\,\mathrm{Hz}$ to $100\,\mathrm{Hz}$, the ramping frequency of the piezo, whereas the actual measurement takes place at some $100\,\mathrm{kHz}$, at the resonance frequencies ω_{m} of the mechanical oscillator. If the input for the spectrum analyser is not buffered, the voltage dropping over the oscilloscope for calibration depends on the spectrum analyser's input impedance, which is frequency-dependent and renders the calibration incorrect. The different measurement set-ups are shown in Fig. 3.8. After correcting for these effects the measurements agree. The membranes were measured to have effective masses of nanograms. In Fig. 3.9, one exemplary measurement resulting in $m_{\mathrm{eff}} = 1.8\,\mathrm{ng}$ is shown. The effective masses of Bragg mirrors on a cantilever was higher and of the order of tens of nanograms. Additionally taking linewidths γ_{m} and resonance frequencies ω_{m} into account,

---

[153] Aspelmeyer, Kippenberg and Marquardt (2014), Sec. II.B.3.
[154] If the spectrum analyser's RBW is not equal to $1\,\mathrm{Hz}$, the power spectral density has to be corrected for that.
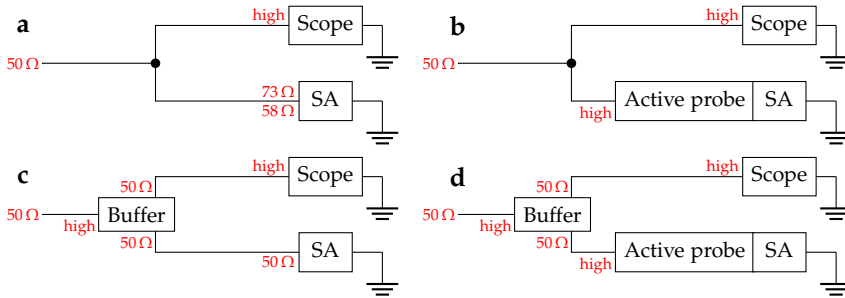
FIGURE 3.8: Set-ups for calibration of position spectral density measurements. b and d lead to the same results. In c, only half the voltage is dropped over the spectrum analyser (SA) compared to b an d, leading to a power spectral density 6 dB below that of b and d. In a, in addition to c, the voltage dropping over the scope is frequency-dependent because of the SA's frequency-dependent input impedance leading to a wrong measurement calibration.
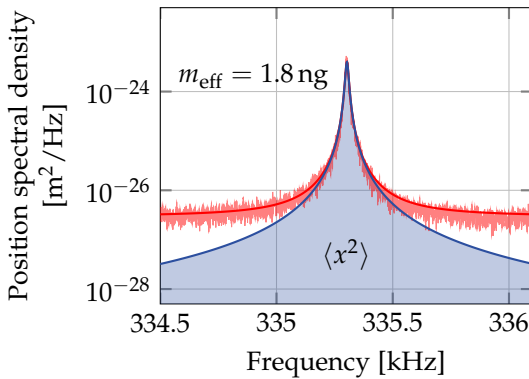

FIGURE 3.9: Effective-mass measurement. The power spectral density from Fig. 3.6 is calibrated and converted into a position spectral density (cf. Eqs. 3.9–3.11). The membrane's thermal Lorentz function (red) is fitted (red, with added electronic noise; blue, resulting spectrum without noise), the shaded area is the variance in position, $\langle x^2 \rangle$. From here, with a given temperature, the effective mass m_{eff} can be calculated according to Eq. 3.8.

photonic-crystal membranes seem suited for a set-up demonstrating coherent quantum-noise cancellation.

There is a caveat to this measurement of the effective mass: The temperature was assumed to be roughly room temperature. If it was higher, e.g. due to absorption and bad thermalisation in vacuum, the effective mass would be underestimated. It would be desirable to measure the effective mass, or directly the coupling strength, without resorting to the temperature. For this, several other methods exist:[155] When *normal-mode splitting* is observed, which is the hybridisation of the optical and mechanical mode due to strong coupling resulting in shifts of the system's resonances, the coupling strength is proportional to the splitting distance.[156] A related effect is *opto-mechanically induced transparency*. Here, the coupling between modes of a strong cavity field to a mechanical resonance changes the system characteristics for a probe beam. The reflectivity of the system for the probe beam is directly related to the cooperativity, which depends on the coupling strength.[157] A third possible way to determine the coupling strength is from the output spectral noise density of the cavity field, i.e. from ponderomotive squeezing. The output spectrum of Eq. 2.46 could be used for that.

Works referenced in the preceding chapter

Andrews, R. W., R. W. Peterson, T. P. Purdy, K. Cicak, R. W. Simmonds, C. A. Regal and K. W. Lehnert, 'Bidirectional and efficient conversion between microwave and optical light', *Nat. Phys.* **10** (2014), 321–326, DOI: 10.1038/nphys2911.

Aspelmeyer, M., T. J. Kippenberg and F. Marquardt, 'Cavity optomechanics', *Rev. Mod. Phys.* **86** (2014), 1391–1452, DOI: 10.1103/RevModPhys.86.1391, arXiv: 1303.0733.

Camerer, S., M. Korppi, A. Jöckel, D. Hunger, T. W. Hänsch and P. Treutlein, 'Realization of an optomechanical interface between ultracold atoms and a membrane', *Phys. Rev. Lett.* **107** (2011), DOI: 10.1103/PhysRevLett.107.223001.

Clerk, A. A., M. H. Devoret, S. M. Girvin, F. Marquardt and R. J. Schoelkopf, 'Introduction to quantum noise, measurement, and amplification', *Rev. Mod. Phys.* **82** (2010), 1155–1208, DOI: 10.1103/RevModPhys.82.1155.

Datasheet Agilent IDP-15 Dry Scroll Vacuum Pump, Agilent, URL: https://www.agilent.com/cs/library/datasheets/public/IDP-15_5991-7604EN_DataSheet_LR.pdf.

---

[155] All rely on having a cavity for strong interaction, which is why the explanation is held rather short here.

[156] For this, see Sec. 5, where this technique is employed in a different context to measure the coupling strength.

[157] S. Weis et al., 'Optomechanically Induced Transparency', *Science* **330** (2010), 1520–1523; Aspelmeyer, Kippenberg and Marquardt (2014), Sec. VII.C.2.

Gröblacher, S., 'Quantum opto-mechanics with micromirrors: combining nano-mechanics with quantum optics', PhD thesis, Universität Wien, 2010.

Gröblacher, S., K. Hammerer, M. R. Vanner and M. Aspelmeyer, 'Observation of strong coupling between a micromechanical resonator and an optical cavity field', *Nature* **460** (2009), 724–727, DOI: 10.1038/nature08171, arXiv: 0903.5293.

Jayich, A. M., J. C. Sankey, B. M. Zwickl, C. Yang, J. D. Thompson, S. M. Girvin, A. A. Clerk, F. Marquardt and J. G. Harris, 'Dispersive optomechanics: A membrane inside a cavity', *New J. Phys.* **10** (2008), 095008, DOI: 10.1088/1367-2630/10/9/095008.

Møller, C. B., R. A. Thomas, G. Vasilakis, E. Zeuthen, Y. Tsaturyan, M. Balabas, K. Jensen, A. Schliesser, K. Hammerer and E. S. Polzik, 'Quantum back-action-evading measurement of motion in a negative mass reference frame', *Nature* **547** (2017), 191–195, DOI: 10.1038/nature22980, arXiv: 1608.03613.

Norte, R. A., J. P. Moura and S. Gröblacher, 'Mechanical Resonators for Quantum Optomechanics Experiments at Room Temperature', *Phys. Rev. Lett.* **116** (2016), 147202, DOI: 10.1103/PhysRevLett.116.147202, arXiv: 1511.06235.

Pinard, M., Y. Hadjar and A. Heidmann, 'Effective mass in quantum effects of radiation pressure', *Eur. Phys. J. C* **7** (1999), 107–111, DOI: 10.1007/s100530050354.

Riedinger, R., A. Wallucks, I. Marinković, C. Löschnauer, M. Aspelmeyer, S. Hong and S. Gröblacher, 'Remote quantum entanglement between two micromechanical oscillators', *Nature* **556** (2018), 473–477, DOI: 10.1038/s41586-018-0036-z.

Tsaturyan, Y., A. Barg, E. S. Polzik and A. Schliesser, 'Ultracoherent nanomechanical resonators via soft clamping and dissipation dilution', *Nat. Nanotechnol.* **12** (2017), 776–783, DOI: 10.1038/nnano.2017.101, arXiv: 1608.00937.

Weis, S., R. Rivière, S. Deléglise, E. Gavartin, O. Arcizet, A. Schliesser and T. J. Kippenberg, 'Optomechanically Induced Transparency', *Science* **330** (2010), 1520–1523, DOI: 10.1126/science.1195596.

4

TWO-MODE SQUEEZING INTERACTION

The interaction between light and a mechanical oscillator through radiation pressure can, in its linearised form, be written as a two-mode squeezing interaction plus a beam-splitter interaction, cf. Eq. 2.6. The interaction with the negative-mass oscillator is supposed to mimic the radiation-pressure interaction and thus also needs a two-mode squeezing process. This chapter deals with what squeezing is, how to detect and how to create it. For CQNC, in order to match the coupling strengths of the participating processes (see Eq. 2.40), the down-conversion coupling strength g_{DC} needs to be determined. Theory for that is provided for the classical and quantum domain. The chapter concludes with measurements of this coupling strength and a discussion of said measurements.

4.1 SQUEEZED LIGHT

There is a minimum to the product of the quadrature uncertainties of a light field, stemming from the fact that amplitude and phase quadrature do not commute, which leads to an uncertainty relation,[158]

$$\operatorname{var} \hat{x} \operatorname{var} \hat{p} \geq \frac{1}{16}. \tag{4.1}$$

This, however, does not restrict the uncertainty of a single quadrature. If one of the uncertainties becomes very small and the other correspondingly large, the inequality Eq. 4.1 is not violated. Such states exist and are called *squeezed states*.

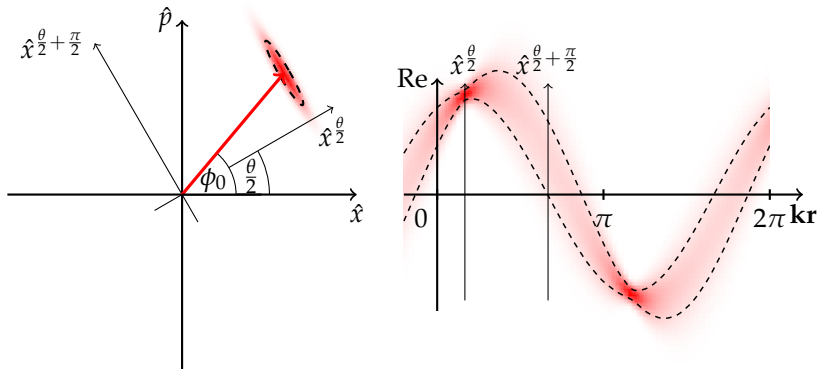[158]See Sec. 1.1.3, Eq. 1.34. In this chapter, the convention with $m = 2$ is used.

FIGURE 4.1: Phasor of squeezed light at time $t = 0$. Left: Colour-coded probability density in phase space. Right: Colour-coded probability density of field strength as projection on $\hat{x}$-quadrature. Both with phase $\phi_0 = 50°$, squeezing angle $\frac{\theta}{2} = 30°$, squeezing parameter $r = 0.97$, corresponding to 7.2 dB squeezing. Dashed uncertainty regions are one standard deviation per quadrature.

4.1.1 WHAT IS SQUEEZED LIGHT?

The term *squeezed light* suggests some kind of deformation of light. 'Deformation' refers to shaping uncertainty regions in phase space. Usually (i.e. for vacuum and coherent states), the uncertainty is independent of the quadrature angle. A region of equal probability density in phase space is denoted by a circle. Squeezing reduces the uncertainty along one direction, confines the probability density along that direction, and can result in a variance below the vacuum variance for the respective quadrature. To satisfy the uncertainty relation, the uncertainty region has to be stretched by at least the same factor in the orthogonal direction, which results in an ellipse. This is exemplarily shown in Fig. 4.1. The squeezing parameter r determines the amount of squeezing, the squeezing angle θ the direction of stretching and squeezing in phase space. For a wave with $\phi_0 = 0$, an angle $\theta = 0$ corresponds to amplitude-quadrature squeezing, an angle $\theta = \pi$ to phase-quadrature squeezing. Its probability density in time or space looks then as depicted in Fig. 4.2. At some quadratures, the uncertainty is smaller (squeezed), at others larger (anti-squeezed). In this picture, similarities to amplitude and phase modulation can be seen (cf. Figs. 1.3 and 1.4).
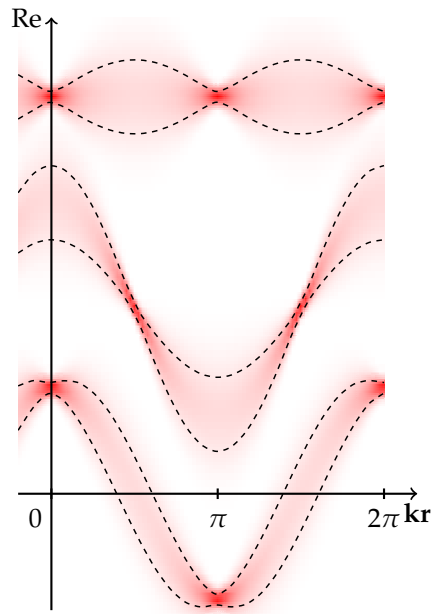
Figure 4.2: Uncertainty of squeezed light wave. Top: Vacuum-squeezed state. Middle: Phase-quadrature squeezed state. Bottom: Amplitude-quadrature squeezed state. In all plots, $\phi_0 = 0$ and $r = 0.97$, corresponding to 7.2 dB squeezing. θ equals 0, π and 0, respectively. Compare these to amplitude- and phase-modulated waves, Figs. 1.3 and 1.4.

Theoretically, the deformation can be described by a Bogoliubov trans-formation, which maps Gaussian states onto Gaussian states.[159] The unitary operator realising this operation is the squeezing operator $\hat{S}(\zeta)$,[160]

$$\hat{S}(\zeta) = e^{\frac{1}{2}\left(\zeta^* \hat{a}^2 - \zeta \hat{a}^{\dagger 2}\right)} \tag{4.2}$$

with $\zeta = r \exp i\theta$. Due to the quadratic occurrence of creation and annihilation operators, photons in squeezed states of light come in pairs (this is already a hint on how to create squeezed states, see Sec. 4.1.3). It also means the photon statistics is changed compared to coherent states of light. In fact, one can think of squeezed states as being more 'regular' than coherent states.[161] This can be seen in the photon number distribution in Fig. 4.3: Amplitude-quadrature squeezed states show a smaller uncertainty in photon number than coherent states, whereas phase-quadrature squeezed states have a bigger uncertainty in photon number.[162]

Letting the squeezing operator with squeezing angle $\theta = 0$ act on vacuum input results in a covariance matrix $C(\hat{x}, \hat{p})$ for quadratures $\hat{x}$ and $\hat{p}$,[163]

$$C(\hat{x}, \hat{p}) = \frac{1}{4} \begin{pmatrix} e^{-2r} & 0 \\ 0 & e^{2r} \end{pmatrix}. \tag{4.3}$$

The uncertainty in one quadrature is reduced, in the orthogonal quadrature enhanced.

A different view on squeezed light originates in a comparison with amplitude and phase modulation. The frequency-independent – white – shot noise of coherent states can be imagined as a superposition of a carrier wave and side-bands at all frequencies around the carrier, all of them uncorrelated in amplitude and phase. If now side-bands at $\pm\Omega$ are correlated, the resulting distribution changes. Squeezing can be thought of side-bands correlated in

---

[159] L. S. Braunstein and P. Van Loock, 'Quantum information with continuous variables', *Rev. Mod. Phys.* **77** (2005), 513–577, Sec. II.E.

[160] C. C. Gerry and P. L. Knight, *Introductory Quantum Optics*, Cambridge et al.: Cambridge University Press, 2005, Eq. 7.10.

[161] See also R. Schnabel, 'Squeezed states of light and their applications in laser interferometers', *Phys. Rep.* **684** (2017), 1–51, particularly Fig. 2.

[162] This shows similarities between amplitude-quadrature squeezed states and photon-number squeezed states. They are *not* the same, though – see the difference between amplitude of a wave and amplitude quadrature of the same wave in Sec. 1.1.1.

[163] Here and in the following, the convention with the commutator $[\hat{x}, \hat{p}] = i/2$ is used – the same as in Schnabel (2017) and Gerry and Knight (2005), Sec. 7.1. See also Sec. 1.1.3.
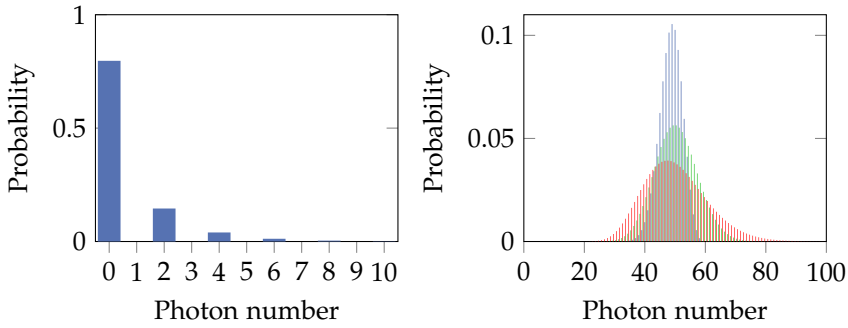
Figure 4.3: Photon-number distribution of squeezed states. Left: Vacuum-squeezed state with $r = 0.7$, corresponding to 6.1 dB squeezing. Right: Displaced amplitude-quadrature squeezed state (blue trace), displaced phase-quadrature squeezed state (red trace), coherent state (green trace). Again, $r = 0.7$. Squeezed states with an average photon number of $\langle \hat{a}^\dagger \hat{a} \rangle = |\alpha|^2 + \sinh^2 r$ and $|\alpha|^2 = 50$ the average photon number of the coherent state, see C. C. Gerry and P. L. Knight, *Introductory Quantum Optics*, Cambridge et al.: Cambridge University Press, 2005, Eq. 7.26 and Eq. 7.81.

amplitude and phase around the carrier frequency similar to side-bands in amplitude and phase modulation (see again Figs. 1.3 and 1.4). The relation in phase between side-bands at $\pm\Omega$ determines the squeezing angle. Again, the quadratic nature of the squeezing operator is visible, seeing that *two* correlated photons, one at $-\Omega$, one at Ω, are needed.[164]

Up to now, squeezing was restricted to two quadratures of the same mode. It is also possible to look at quadratures of different modes. To correlate different modes, an operator similar to the single-mode squeezing operator is used, called *two-mode squeezing* operator:[165]

$$\hat{S}_{\text{TMS}}(\zeta) = e^{\frac{1}{2}(\zeta^* \hat{a}\hat{c} - \zeta \hat{a}^\dagger \hat{c}^\dagger)}. \tag{4.4}$$

---

[164]See also S. Chelkowski, 'Squeezed light and laser interferometric gravitational wave detectors', PhD thesis, Leibniz Universität Hannover, 2007, Sec. 2.10.2.6, and H.-A. Bachor and T. C. Ralph, *A Guide to Experiments in Quantum Optics*, Weinheim: Wiley, 2004, Fig. 4.9.

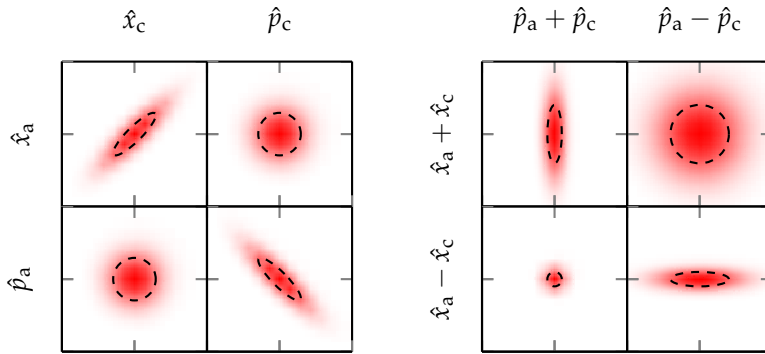[165]Gerry and Knight (2005), Sec. 7.7, see also Sec. 4.2.2 of this thesis.

FIGURE 4.4: Two-mode squeezing in phase space. Left: Correlations between amplitude quadratures and phase quadratures of the two modes. The two amplitude quadratures, $\hat{x}_a$ and $\hat{x}_c$, are correlated, the two phase quadratures, $\hat{p}_a$ and $\hat{p}_c$, anti-correlated. Right: Uncertainties of suitably combined quadratures. Subtraction of correlated quadratures as well as addition of anti-correlated quadratures lead to reduced uncertainties. $\hat{x}_a - \hat{x}_c$ and $\hat{p}_a + \hat{p}_c$ are a realisation of the EPR paradox and a combination of QND variables. All plots after Eq. 4.5 with $r = 0.7$. Colour is normalised to the maximum in each of the eight plots individually.

The resulting covariance matrix for an angle $\theta = 0$ is (see Eq. 4.46)

$$C(\hat{x}_a, \hat{p}_a, \hat{x}_c, \hat{p}_c) = \frac{1}{4} \begin{pmatrix} \cosh 2r & 0 & \sinh 2r & 0 \\ 0 & \cosh 2r & 0 & -\sinh 2r \\ \sinh 2r & 0 & \cosh 2r & 0 \\ 0 & -\sinh 2r & 0 & \cosh 2r \end{pmatrix}. \qquad (4.5)$$

With two-mode squeezing, quadratures on their own show enhanced uncertainties. But the introduced correlations between different quadratures lead to an uncertainty reduction below the vacuum uncertainty for a suitable combination of quadratures, see Fig. 4.4. Particularly, the EPR paradox[166] can be demonstrated by measuring both, $\hat{x}_a - \hat{x}_c$ and $\hat{p}_a + \hat{p}_c$, with arbitrary precision at the same time.[167]

[166] A. Einstein, B. Podolsky and N. Rosen, 'Can Quantum-Mechanical Description of Physical Reality Be Considered Complete?', *Phys. Rev.* **47** (1935), 777–780.

[167] Z. Y. Ou, S. F. Pereira and H. J. Kimble, 'Realization of the Einstein-Podolsky-Rosen paradox for continuous variables in nondegenerate parametric amplification', *Appl. Phys. B* **55** (1992), 265–278, particularly p.271.
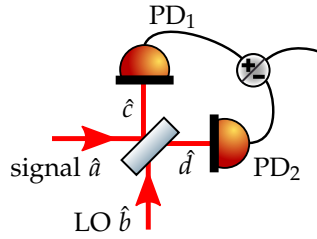
FIGURE 4.5: Homodyne detector. A local oscillator (LO) interferes with a signal beam. The subtraction of photocurrents results in a measurement of a signal beam's quadrature.

4.1.2 DETECTING SQUEEZED LIGHT

To detect squeezed light, one needs to measure the quadrature of a light field in order to determine its variance. This can be done directly,[168] but usually a balanced homodyne detector as depicted in Fig. 4.5 is used. A local oscillator field (LO) interferes with the signal beam containing the squeezed light. The photodiodes convert photons into a photocurrent. The currents are subtracted from each other and converted into a voltage by a transimpedance amplifier. The output of the photodetector is usually fed into a spectrum analyser to measure noise powers in certain frequency bands, similar to Sec. 3.2.1.

In an experiment, the measured statistics do not directly reflect the quantum state produced due to decoherence from losses on the way to the measurement apparatus as described in Sec. 1.1.4. Decoherence due to an unbalanced beam splitter is usually neglected. For the detection of two-mode squeezing, however, a beam splitter efficiency η_{BS}, introduced in the following, becomes important.

SINGLE-MODE DETECTION

The detection process can be formalised as follows, using modes $\hat{a}$ and $\hat{b}$ as input modes onto a beam splitter. The beam splitter is characterised[169] by its amplitude reflectivity r and transmissivity $t = \sqrt{1 - r^2}$. The resulting modes $\hat{c}$ and $\hat{d}$ then become (here, the convention with a phase flip on reflection of

---

[168]If one is interested in the amplitude quadrature, cf. Schnabel (2017), Sec. 2.2.

[169]A lossless beam splitter is assumed, i.e. $r^2 + t^2 = 1$. Losses can be modelled separately, if necessary, see Sec. 1.1.4.
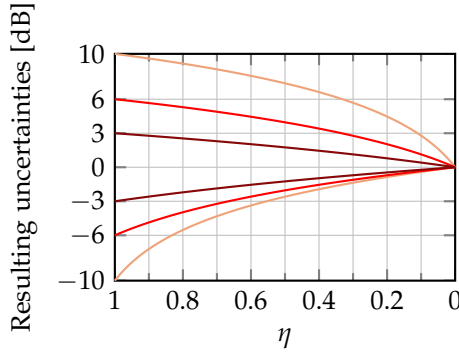
FIGURE 4.6: Influence of losses on single-mode squeezing. Starting with reduction in uncertainties of $\pm 10\,\text{dB}$, $\pm 6\,\text{dB}$, and $\pm 3\,\text{dB}$ above/below the uncertainty of vacuum fields from light to dark, the resulting uncertainties are shown over the efficiency η. Plotted from Eq. 4.9.

mode $\hat{b}$ is used),

$$\hat{c} = r\hat{a} + t\hat{b}, \tag{4.6a}$$

$$\hat{d} = t\hat{a} - r\hat{b}, \tag{4.6b}$$

$$\hat{c}^\dagger\hat{c} = r^2\hat{a}^\dagger\hat{a} + t^2\hat{b}^\dagger\hat{b} + rt(\hat{a}^\dagger\hat{b} + \hat{a}\hat{b}^\dagger), \tag{4.6c}$$

$$\hat{d}^\dagger\hat{d} = t^2\hat{a}^\dagger\hat{a} + r^2\hat{b}^\dagger\hat{b} - rt(\hat{a}^\dagger\hat{b} + \hat{a}\hat{b}^\dagger), \tag{4.6d}$$

where $\hat{c}^\dagger\hat{c}$ and $\hat{d}^\dagger\hat{d}$ are the photon numbers in the respective modes, counted by the photodetectors. Linearising the the modes, they can be written as $\hat{b} \rightarrow (\beta + \hat{b})e^{i\phi}$ and $\hat{a} \rightarrow \alpha + \hat{a}$, where ϕ is the relative phase between modes $\hat{a}$ and $\hat{b}$. From now on, $\hat{b}$ is supposed to be the local oscillator and assumed to be a lot bigger than mode $\hat{a}$, such that $\beta = \langle\hat{b}\rangle \gg \alpha = \langle\hat{a}\rangle$. In the following approximation, all terms higher order in $\hat{a}$, $\hat{b}$, α are dropped, only terms proportional to β or β^2 are kept. With this, the photocurrents become

$$I_+ \propto \hat{c}^\dagger\hat{c} + \hat{d}^\dagger\hat{d} \approx (r^2 + t^2)\left(\hat{x}_{\text{b}}\beta + \beta^2\right), \tag{4.7a}$$

$$I_- \propto \hat{c}^\dagger\hat{c} - \hat{d}^\dagger\hat{d} \approx 2rt\hat{x}_{\text{a}}^\phi\beta - (r^2 - t^2)\left(\hat{x}_{\text{b}}\beta + \beta^2\right) + 4rt\alpha\beta\cos\phi, \tag{4.7b}$$

with the quadrature operators $\hat{x}$ known from Sec. 1.1.3. The difference in photocurrents contains information about a quadrature $\hat{x}_{\text{a}}^\phi$ of the signal field, chosen by the phase ϕ between local oscillator and signal field, and amplified
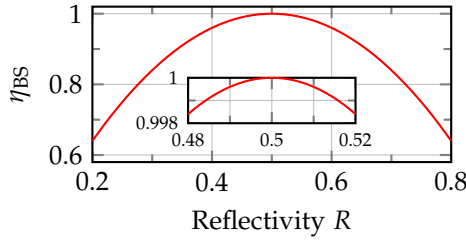
FIGURE 4.7: Beam-splitter efficiency. The efficiency of a lossless beam splitter is $\eta_{\mathrm{BS}} = 4R(1-R)$ with R being the beam splitter's power reflectivity, cf. Eq. 4.10.

with the local oscillator's mean field β. It also contains a DC part offset, proportional to $\cos\phi$. This can be used to stabilise the interferometer (the balanced homodyne detector) at an appropriate operating point. The variance of the difference in photocurrents is

$$\operatorname{var} I_- \propto 4r^2 t^2 \operatorname{var} \hat{x}_a^\phi + (r^2 - t^2)^2 \operatorname{var} \hat{x}_b. \tag{4.8}$$

The local oscillator is assumed to be shot-noise limited at the frequencies of interest, $\operatorname{var} \hat{x}_b = \operatorname{var} \hat{x}_{\mathrm{vac}}$, and the variance normalised to shot-noise level,[170] to obtain

$$
\begin{aligned}
\operatorname{var} \hat{x}_{\phi,\mathrm{meas}} &= \frac{4r^2 t^2 \operatorname{var} \hat{x}^\phi + (r^2 - t^2)^2}{(r^2 + t^2)^2} \\
&= \eta_{\mathrm{BS}} \operatorname{var} \hat{x}^\phi + 1 - \eta_{\mathrm{BS}}
\end{aligned} \tag{4.9}
$$

with

$$\eta_{\mathrm{BS}} = 4r^2 t^2 = 4R(1-R) \tag{4.10}$$

for a lossless beam splitter and $\operatorname{var} \hat{x}^\phi = \operatorname{var} \hat{x}_a^\phi / \operatorname{var} \hat{x}_{\mathrm{vac}}$. An imbalanced beam splitter thus can be modelled as an additional loss channel with an efficiency η_{BS}.[171] The efficiency of an unbalanced beam splitter over the reflectivity is plotted in Fig. 4.7 and becomes very close to one in the realistic case of an almost 50:50 beam splitter. Note that this is only true if the local oscillator is shot-noise limited – if not, the effect of an unbalanced beam splitter is

---

[170] This means dividing by the same expression, but with $\operatorname{var} \hat{x}_a^\phi$ and $\operatorname{var} \hat{x}_b$ set to one.

[171] A more complete picture including gain and quantum efficiency differences in photodetectors is given by L.-A. Wu, M. Xiao and H. J. Kimble, 'Squeezed states of light from an optical parametric oscillator', *J. Opt. Soc. Am. B* **4** (2008), 1465, particularly Eq. 23.

more serious as then technical noise in the local oscillator is not suppressed completely.

In the preceding paragraph, it was stated that the local oscillator $\hat{b}$ enhances one quadrature of signal mode $\hat{a}$, chosen by the relative phase between signal and local oscillator. This is only true for the part of mode $\hat{a}$ which is in the same spatial mode as $\hat{b}$ – a classical mode matching problem as in Sec. 1.1.2. Mode $\hat{a}$ is decomposed into mode $\hat{b}$'s basis. The fractions of mode $\hat{a}$ orthogonal to $\hat{b}$ are lost, vacuum noise couples in instead. The result of this loss channel, usually called homodyne efficiency, is quantified as[172]

$$\eta_{\text{HD}} = \mathcal{VIS}^2 \tag{4.11}$$

with the visibility $\mathcal{VIS}$ quantifying the mode overlap as in Sec. 1.1.2. Choosing to measure a certain mode $\hat{a}$ can thus be accomplished by shaping the local oscillator accordingly.[173] The parameters of the local oscillator determining the mode quadrature under test are phase, polarisation, and spatial mode shape.

Two-mode detection

The calculation from the preceding Sec. 4.1.2 can be done with two orthogonal modes (in the following denoted with subscripts s, p) in each of the four beams $\hat{a}$, $\hat{b}$, $\hat{c}$, $\hat{d}$ (see again Fig. 4.5) instead of only one mode. This is similar to the experiment presented in Sec. 4.4.1: There, orthogonally polarised photons are created in the down-conversion process and consequently measured. All participating beams $\hat{a}$, $\hat{b}$, $\hat{c}$, $\hat{d}$ can contain both polarisations. The measurement can be accomplished with a single homodyne detector[174] as will be shown in this section's calculation and later experimentally (Sec. 4.4.1). The intuitive reason for that is the following: As long as nothing distinguishes between the two in principle distinguishable modes, the system should behave just as an ordinary single-mode squeezer.

The detection process can be formalised as follows, again with amplitude reflectivities r_i and transmissivities $t_i = \sqrt{1 - r_i^2}$, but this time with possibly

---

[172] For more regarding the mode overlap integral and the corresponding efficiency, see Wu, Xiao and Kimble (2008), Eq. 24.

[173] This enables full Gaussian mode estimation with a single homodyne detector, as described in Appendix B.

[174] Actually contrary to earlier belief, cf. M. H. Wimmer, 'Coupled nonclassical systems for coherent backaction noise cancellation', PhD thesis, Leibniz Universität Hannover, 2016, p. 34.
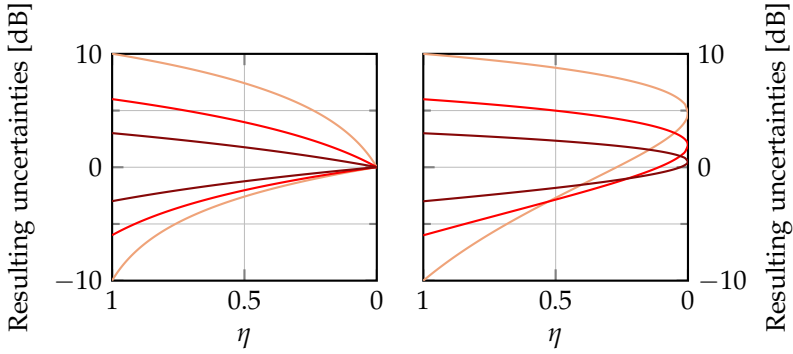
Figure 4.8: Influence of losses on two-mode squeezing. Starting with reduction in uncertainties of $\pm 10\,\mathrm{dB}$, $\pm 6\,\mathrm{dB}$, and $\pm 3\,\mathrm{dB}$ above/below the uncertainty of vacuum fields from light to dark, the resulting uncertainties are shown over the efficiency η. Left: Losses affecting both modes equally. Right: Losses affecting only one of the modes. Plotted from Eqs. 4.48 and 4.51.

different values for the two modes $i = \mathrm{s}, \mathrm{p}$:[175]

$$\hat{c} \propto r_\mathrm{s}\hat{a}_\mathrm{s} + r_\mathrm{p}\hat{a}_\mathrm{p} + t_\mathrm{s}\hat{b}_\mathrm{s} + t_\mathrm{p}\hat{b}_\mathrm{p}, \tag{4.12a}$$

$$\hat{d} \propto t_\mathrm{s}\hat{a}_\mathrm{s} + t_\mathrm{p}\hat{a}_\mathrm{p} - r_\mathrm{s}\hat{b}_\mathrm{s} - r_\mathrm{p}\hat{b}_\mathrm{p}, \tag{4.12b}$$

$$\begin{aligned}\hat{c}^\dagger\hat{c} \propto\, & r_\mathrm{s}^2\hat{a}_\mathrm{s}^\dagger\hat{a}_\mathrm{s} + r_\mathrm{p}^2\hat{a}_\mathrm{p}^\dagger\hat{a}_\mathrm{p} + t_\mathrm{s}^2\hat{b}_\mathrm{s}^\dagger\hat{b}_\mathrm{s} + t_\mathrm{p}^2\hat{b}_\mathrm{p}^\dagger\hat{b}_\mathrm{p} \\ & + r_\mathrm{s}t_\mathrm{s}(\hat{a}_\mathrm{s}^\dagger\hat{b}_\mathrm{s} + \hat{a}_\mathrm{s}\hat{b}_\mathrm{s}^\dagger) + r_\mathrm{p}t_\mathrm{p}(\hat{a}_\mathrm{p}^\dagger\hat{b}_\mathrm{p} + \hat{a}_\mathrm{p}\hat{b}_\mathrm{p}^\dagger),\end{aligned} \tag{4.12c}$$

$$\begin{aligned}\hat{d}^\dagger\hat{d} \propto\, & r_\mathrm{s}^2\hat{a}_\mathrm{s}^\dagger\hat{a}_\mathrm{s} + r_\mathrm{p}^2\hat{a}_\mathrm{p}^\dagger\hat{a}_\mathrm{p} + t_\mathrm{s}^2\hat{b}_\mathrm{s}^\dagger\hat{b}_\mathrm{s} + t_\mathrm{p}^2\hat{b}_\mathrm{p}^\dagger\hat{b}_\mathrm{p} \\ & - r_\mathrm{s}t_\mathrm{s}(\hat{a}_\mathrm{s}^\dagger\hat{b}_\mathrm{s} + \hat{a}_\mathrm{s}\hat{b}_\mathrm{s}^\dagger) - r_\mathrm{p}t_\mathrm{p}(\hat{a}_\mathrm{p}^\dagger\hat{b}_\mathrm{p} + \hat{a}_\mathrm{p}\hat{b}_\mathrm{p}^\dagger).\end{aligned} \tag{4.12d}$$

The sum and difference currents become, after assuming a strong local oscillator and linearisation via neglecting higher-order terms similar to the

---

[175]This is generally true for different polarisations due to non-normal incidence of the light field onto the beam splitters.

single-mode case (Eqs. 4.7),

$$I_+ \propto \left((r_s^2 + t_s^2)\hat{x}_{b,s} + (r_p^2 + t_p^2)\hat{x}_{b,p} \right) \beta + \left(r_s^2 + t_s^2 + r_p^2 + t_p^2 \right) \beta^2, \qquad (4.13)$$

$$
\begin{aligned}
I_- \propto\ & 2r_s t_s \beta \hat{x}_{a,s}^{\phi} + 2r_p t_p \beta \hat{x}_{a,p}^{\phi} \\
& - \left(r_s^2 - t_s^2 \right) \beta \hat{x}_{b,s} - \left(r_p^2 - t_p^2 \right) \beta \hat{x}_{b,p} - \left(r_s^2 - t_s^2 + r_p^2 - t_p^2 \right) \beta^2 \\
& + 4 \left(r_s t_s + r_p t_p \right) \alpha \beta \cos\phi.
\end{aligned}
\qquad (4.14)
$$

The variance of the difference photocurrent becomes (where all operators are assumed uncorrelated except for $\hat{x}_s^{a,\phi}$ and $\hat{x}_{a,p}^{\phi}$)

$$
\begin{aligned}
\operatorname{var} I_- \propto\ & 4r_s^2 t_s^2 \operatorname{var} \hat{x}_{a,s}^{\phi} + 4r_p^2 t_p^2 \operatorname{var} \hat{x}_{a,p}^{\phi} + 8r_s t_s r_p t_p \operatorname{cov} \hat{x}_{a,s}^{\phi}, \hat{x}_{a,p}^{\phi} \\
& + (r_s^2 - t_s^2)^2 \operatorname{var} \hat{x}_{b,s} + (r_p^2 - t_p^2)^2 \operatorname{var} \hat{x}_{b,p}.
\end{aligned}
\qquad (4.15)
$$

Normalised to shot noise with $\hat{x}_{b,i} = \hat{x}_{\text{vac}}$, the variance becomes

$$
\begin{aligned}
\operatorname{var} I_- =\ & \eta_{\text{BS}}^s \operatorname{var} \hat{x}_{a,s}^{\phi} + \eta_{\text{BS}}^p \operatorname{var} \hat{x}_{a,p}^{\phi} + 2\sqrt{\eta_{\text{BS}}^s \eta_{\text{BS}}^p} \operatorname{cov} \hat{x}_{a,s}^{\phi}, \hat{x}_{a,p}^{\phi} \\
& + 2 - \eta_{\text{BS}}^s - \eta_{\text{BS}}^p.
\end{aligned}
\qquad (4.16)
$$

The variance is twice as high as before because of two uncorrelated inputs – one for each polarisation mode.[176] Note the different role of losses in the measurement outcome: For equal losses in s- and p-polarised light, the variance simplifies to (normalised to shot noise)

$$
\begin{aligned}
\operatorname{var} I_- &= \eta \left(\operatorname{var} \hat{x}_s^{a,\phi} + \operatorname{var} \hat{x}_p^{a,\phi} + 2\operatorname{cov} \hat{x}_s^{a,\phi}, \hat{x}_p^{a,\phi} \right) + 2 - 2\eta \\
&= \eta \operatorname{var}(\hat{x}_s^{a,\phi} + \hat{x}_p^{a,\phi}) + 2 - 2\eta.
\end{aligned}
\qquad (4.17)
$$

This is very similar to the single-mode squeezed case and results in vacuum variance in the limit of zero efficiency, see also Fig. 4.8. For unequal losses in the two modes, however, the measured variance can be enhanced above shot noise (see same Fig. 4.8). This is not surprising, as in the limit of zero efficiency in one mode, the variance of a vacuum quadrature mixed with a quadrature of the second mode is detected – and the uncertainties of two-mode squeezed state quadratures on their own are enhanced, see Eq. 4.5.

Not only is it possible to measure two-mode squeezed states with a single homodyne detector. In fact, one can even do a full Gaussian state estimation of a bipartite state, as is shown in Appendix. B.[177]

---

[176]Cf. Eq. 24 and paragraph thereafter in Ou, Pereira and Kimble (1992).
[177]A different scheme for state estimation with a single homodyne detector, where not the local

4.1.3 CREATING SQUEEZED LIGHT

Squeezing as the deformation of the uncertainty region in phase space, Fig. 4.1, hints at the nonlinearity involved in creating squeezed light. A linear process would only *scale* the region, not *deform* it. Many different nonlinear interactions are able create squeezed light. There is Kerr squeezing, optomechanical/ponderomotive squeezing, even two-photon absorption,[178] to name but a few. This can be understood quite intuitively: If the interaction is nonlinear, there is a disproportionally higher chance of interaction with more light being present – if more photons arrive at a time, they get processed (converted, absorbed) with a higher probability. Through the interaction, the light has become more regular. This interaction could for example be an intensity-dependent phase shift as in Kerr- or ponderomotive squeezing, or nonlinear absorption as in two-photon absorption or in down-conversion and second harmonic generation in a nonlinear crystal.

The most common technique for creating squeezed light is indeed the down-conversion process. This is a rather simple nonlinear interaction, as it is, in the limit of a strong pump beam, 'only' a quadratic one. Hints that this interaction might result in squeezed states come from the occurrence of only even photon numbers in squeezed vacuum states, see Fig. 4.3, and from the side-band picture, where squeezing is being thought of as correlated side-bands around a carrier frequency. In a down-conversion process, one pump photon is converted into *two* signal photons.[179] In this second-order nonlinear process, squeezing is actually not limited to the below-threshold case[180] of the down-converted field, but can also be observed in other configurations. (Single-mode) squeezed states with a second-order nonlinear crystal can be generated[181]

---

oscillator is shaped but the signal beam, is proposed by V. D'Auria et al., 'Characterization of bipartite states using a single homodyne detector', *J. Opt. B* **7** (2005), S750–S753 and realised by V. D'Auria et al., 'Full characterization of Gaussian bipartite entangled states by a single homodyne detector', *Phys. Rev. Lett.* **102** (2009).

[178] M. J. Collett and D. F. Walls, 'Squeezing spectra for nonlinear optical systems', *Phys. Rev. A* **32** (1985), 2887–2892. A good overview over experimental progress is given by U. L. Andersen, T. Gehring, C. Marquardt and G. Leuchs, '30 Years of Squeezed Light Generation', *Phys. Scr.* **91** (2016), 053001.

[179] In fact, down-conversion most closely resembles the squeezing Hamiltonian, cf. the following Sec. 4.2.

[180] For an explanation regarding the threshold, see remainder of this Section and Sec. 4.2.1.

[181] Collett and Walls (1985), D. F. Walls and G. J. Milburn, *Quantum Optics*, Berlin, Heidelberg: Springer, 2008, Secs. 8.1 and 8.2, for the different experimental realisations, see Andersen,
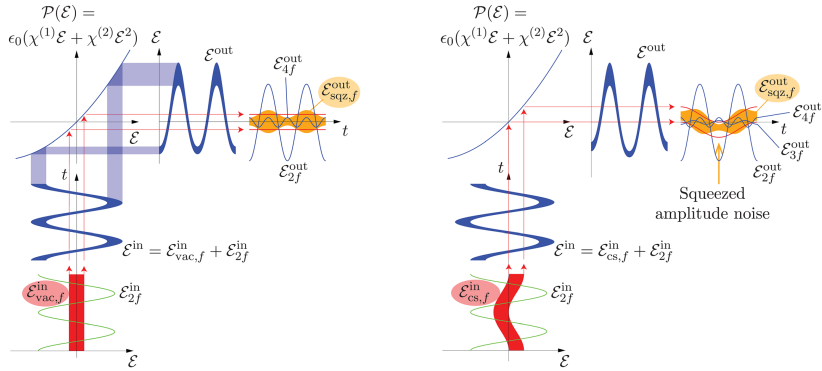
FIGURE 4.9: Nonlinear interaction resulting in squeezed light. Compare yellow output fields with plots in Fig. 4.2. Figure taken from J. Bauchrowitz, T. Westphal and R. Schnabel, 'A graphical description of optical parametric generation of squeezed states of light', *Am. J. Phys.* **81** (2013), 767–771.

- in second-harmonic generation in both, the harmonic and the fundamental mode;

- in down-conversion above threshold in the fundamental field (the more squeezing the closer to threshold);

- in down-conversion above threshold in the harmonic mode (but limited to 3 dB);

- in down-conversion below lasing threshold (also the better the closer to threshold) – this is the prevalent case, it also led to the best results to date with a measured noise reduction of 15 dB in one quadrature.[182]

In parametric down-conversion, a pump beam of frequency $2f$ displaces incoming vacuum fluctuations towards higher nonlinearities inside the crystal. This is effectively the parametric modulation (with frequency $2f$) of the light's dielectric constant as the displacement is phase-dependent.[183] A visual

Gehring, Marquardt and Leuchs (2016) and references therein.

[182] H. Vahlbruch, M. Mehmet, K. Danzmann and R. Schnabel, 'Detection of 15 dB Squeezed States of Light and their Application for the Absolute Calibration of Photoelectric Quantum Efficiency', *Phys. Rev. Lett.* **117** (2016), 110801.

[183] W. H. Louisell, A. Yariv and A. E. Siegman, 'Quantum fluctuations and noise in parametric processes. I.', *Phys. Rev.* **124** (1961), 1646–1654.

depiction was made by Bauchrowitz and co-workers,[184] see Fig. 4.9: Incoming light causes a time-dependent polarisation of the material according to its dielectric tensor χ. This oscillating polarisation is again the source of radiation. Abbreviating the description by skipping the polarisation, the second-order nonlinearity $\chi^{(2)}$ translates the incoming light of frequencies f and $2f$ nonlinearly into outgoing light. The outgoing light field can be decomposed back into original frequencies, the part with frequency f is squeezed. Because the amplification or attenuation of the incoming field depends on its phase, the pumped nonlinear crystal acts as a phase-sensitive amplifier. This picture can explain the dependence of the squeezing angle on the pump phase as long as a phase between squeezed light field and pump field can be defined,[185] see also Fig 4.9: Depending on where the anti-nodes of the squeezing field at f lie with respect to the pump field at $2f$ – at pump field minima or at maxima (or in between) – the outgoing field is amplitude-quadrature squeezed or phase-quadrature squeezed (or in-between). The example in Fig. 4.9 shows vacuum squeezing, where the phase is not defined due to the lack of a reference field with the same frequency, and amplitude-quadrature squeezing due to extrema of the squeezed field coinciding with maxima of the pump field. As is noted in their paper, this picture limited: it does not include a cavity, and it does not explain the exact crystal interactions, nor where vacuum fluctuations come from.

Due to generally small $\chi^{(2)}$-coefficients, the interaction and thus the resulting amplification/de-amplification and squeezing is also small. Options to increase the interaction strength are increasing the pump intensities, e.g. by using pulsed beams, or, what is done most often, enhancing the interaction by building a cavity around the crystal. The amplification is increased as long as one stays below the cavity's *threshold*: The system becomes unstable if the amplification of one quadrature is too big, larger then the attenuation due to the light leaving the cavity, leading to unlimited growth of that quadrature.[186] At this point, the threshold, the orthogonal quadrature is de-amplified by a factor one half. This leads to the 3 dB-limit of intracavity squeezing.[187] At

---

[184] J. Bauchrowitz, T. Westphal and R. Schnabel, 'A graphical description of optical parametric generation of squeezed states of light', *Am. J. Phys.* **81** (2013), 767–771.

[185] This is the case if one deals with bright squeezing or if there is some kind of seed field within the cavity, e.g. for locking purposes.

[186] In practice, at some point, saturation sets in and limits the growth.

[187] C. W. Gardiner and P. Zoller, *Quantum noise : a handbook of Markovian and non-Markovian quantum stochastic methods with applications to quantum optics*, Berlin et al.: Springer, 2000, Sec. 10.2.1c. The limit corresponds to a classical gain limit as derived in Sec. 4.2.3.

first, the threshold was thought to prevent reductions of quantum noise of more than 3 dB.[188] It then turned out that arbitrarily high reductions are still possible, albeit not *inside* the squeezing cavity. There is no limit to squeezing of the light *reflected off* the cavity.

This can be understood with a different picture of creating squeezed light: Squeezing can be viewed as destructive interference of quantum noise in reflection off a cavity. As shown in Sec. 1.2.2, the light directly reflected off a cavity interferes with the light leaking out of the cavity – with complete destructive interference on resonance if the cavity is impedance-matched (Eq. 1.55). This is valid not only for classical fields but also for quantum noise. Of course, the light field and the quantum noise have to go somewhere, they are transmitted through the cavity. That there is no noise in reflection off an impedance-matched cavity is, however, not true, the process is both ways. Although there is no light sent into the cavity from the opposite side, there are vacuum fluctuations, which also 'see' an impedance-matched cavity and are transmitted through the cavity. To prevent the quantum fluctuations from coupling in from the other side of the cavity, the cavity could be made single-ended. But then it is not impedance-matched any more, which means the quantum noise does not interfere destructively in reflection. The impedance-matching condition can be revived with a medium inside the cavity which introduces attenuation of the size of the input-coupler transmission. Ordinary attenuation in the form of losses would not help because then, vacuum fluctuations would couple in (see Sec. 1.1.4). The process has to be realised by the above-mentioned phase-sensitive amplifier. Then, only one quadrature is attenuated, leading to the impedance-matching condition being fulfilled for the respective quadrature and complete destructive interference in reflection off the cavity – in that quadrature. The other quadrature is amplified and anti-squeezed, no light is lost.

Squeezing as destructive interference in reflection off a nonlinear cavity also explains the limited band-width of quantum-noise reduction. Impedance-matching is only fulfilled around the cavity resonance, with the cavity's linewidth determining the band-width of the process.

---

[188]Cf. G. Milburn and D. Walls, 'Production of squeezed states in a degenerate parametric amplifier', *Opt. Commun.* **39** (1981), 401–404.

4.2 THEORY OF PARAMETRIC DOWN-CONVERSION

After introducing squeezing in the preceding Sec. 4.1, goal of this section is to connect the down-conversion coupling strength g_{DC} with experimentally obtainable parameters.

The first part starts with the single-mode squeezing Hamiltonian and solves the resulting equations of motion to obtain noise spectra. Neglecting losses and on resonance, the resulting variance depends on a single parameter – the pump parameter x. Following the same path for two-mode squeezing yields similar results. In the classical limit of amplification and de-amplification, the classical gain G, again, depends only on the pump parameter x. This pump parameter x is proportional to the desired coupling strength g_{DC}, see Eq. 4.28. The coupling strength g_{DC} can be obtained from squeezing measurements as well as from amplification/de-amplification measurements.

The starting point for the mentioned calculations is the rather abstract quantum-mechanical Hamiltonian. The fourth part, instead, starts with Maxwell's equations to obtain the pump threshold P_{th} of a system where a material's dielectric tensor couples modes of light to each other. This leads to a relation between the effective nonlinearity E_{NL} in a second-harmonic-generation process and the pump threshold P_{th} in parametric down-conversion and thus to another means of measuring the coupling strength g_{DC}. It can be obtained from the conversion efficiency in second-harmonic generation. This approach makes clear the dependencies of the pump threshold and thus the coupling strength on a more concrete level: In a nutshell, the nonlinear coupling strength g_{DC} is given by the effective nonlinear coefficient d_{eff} (which is a material parameter) multiplied with the pump power and the cavity's free spectral range, and weighted by the mode overlap of the participating beams, integrated over the volume of the crystal.

4.2.1 SINGLE-MODE SQUEEZING

The common starting Hamiltonian of parametric down-conversion is[189]

$$H = \hbar\omega\hat{a}^\dagger\hat{a} + i\chi(\hat{b}\hat{a}^{\dagger 2} - \hat{b}^\dagger\hat{a}^2) + \text{driving and decay terms}, \qquad (4.18)$$

---

[189]For the following treatment, see M. J. Collett and C. W. Gardiner, 'Squeezing of intracavity and traveling-wave light fields produced in parametric amplification', *Phys. Rev. A* **30** (1984), 1386–1391.

where χ is the coupling strength (cf. Fig. 4.12 for dependencies). This is quite intuitive because higher frequency pump photons $\hat{b}$ decay into two lower-frequency photons $\hat{a}$ (down-conversion) or two lower-frequency photons generate one higher-frequency photon (second harmonic generation). In the limit of no pump depletion (valid below threshold), a semi-classical approach can be used by substituting $\hat{b} \to \beta e^{i\theta}$ with β the mean pump field and θ the phase between pump and signal field. The new Hamiltonian in the interaction picture then is

$$H = i\epsilon \hat{a}^{\dagger 2} - i\epsilon^* \hat{a}^2, \tag{4.19}$$

where ϵ is complex and proportional to χ, the pump's mean amplitude β, and $e^{i\theta}$ with θ the phase between pump field and cavity field. This ϵ is equal to the coupling strength g_{DC} from Sec. 2,

$$\epsilon = g_{\mathrm{DC}} \propto \chi \beta e^{i\theta}. \tag{4.20}$$

The pump frequency ω_{p} of mode $\hat{b}$ was assumed to be twice the frequency of mode $\hat{a}$, which makes the Hamiltonian in the interaction picture time-independent. Together with damping and driving terms, the equations of motion for $\hat{a}$ and $\hat{a}^{\dagger}$ are

$$\dot{\hat{a}} = \epsilon \hat{a}^{\dagger} - \frac{1}{2}(\kappa_1 + \kappa_2)\hat{a} + \sqrt{\kappa_1}\hat{a}_{\mathrm{in},1} + \sqrt{\kappa_2}\hat{a}_{\mathrm{in},2},$$
$$\dot{\hat{a}}^{\dagger} = \epsilon^* \hat{a} - \frac{1}{2}(\kappa_1 + \kappa_2)\hat{a}^{\dagger} + \sqrt{\kappa_1}\hat{a}_{\mathrm{in},1}^{\dagger} + \sqrt{\kappa_2}\hat{a}_{\mathrm{in},2}^{\dagger}. \tag{4.21}$$

κ_1 specifies the coupling of light to the driving mode, which happens via the input coupler, κ_2 the coupling to the bath through all other loss channels. Both are full-width-half-maximum (FWHM) linewidths. The equations can be solved in the Fourier domain. Defining the Fourier transform as $\hat{a}(\omega) = (2\pi)^{-1/2} \int \mathrm{d}t\, e^{i\omega t} \hat{a}$, the equations become

$$-i\omega \hat{a}(\omega) = \epsilon \hat{a}^{\dagger}(-\omega) - \tfrac{1}{2}(\kappa_1 + \kappa_2)\hat{a}(\omega) + \sqrt{\kappa_1}\hat{a}_{\mathrm{in},1}(\omega) + \sqrt{\kappa_2}\hat{a}_{\mathrm{in},2}(\omega),$$
$$-i\omega \hat{a}^{\dagger}(-\omega) = \epsilon^* \hat{a}(\omega) - \tfrac{1}{2}(\kappa_1 + \kappa_2)\hat{a}^{\dagger}(-\omega) + \sqrt{\kappa_1}\hat{a}_{\mathrm{in},1}^{\dagger}(-\omega) + \sqrt{\kappa_2}\hat{a}_{\mathrm{in},2}^{\dagger}(-\omega).$$
$$\tag{4.22}$$

The solutions for $\hat{a}(\omega)$ and $\hat{a}^\dagger(-\omega)$ are

$$a(\omega) = -\frac{(\kappa/2 - i\omega)}{(\kappa/2 - i\omega)^2 - |\epsilon|^2} \left[\sqrt{\kappa_1} a_{\text{in},1}(\omega) + \sqrt{\kappa_2} a_{\text{in},2}(\omega) \right]$$
$$- \frac{\epsilon}{(\kappa/2 - i\omega)^2 - |\epsilon|^2} \left[\sqrt{\kappa_1} a^\dagger_{\text{in},1}(-\omega) + \sqrt{\kappa_2} a^\dagger_{\text{in},2}(-\omega) \right], \quad (4.23)$$

$$a^\dagger(-\omega) = -\frac{(\kappa/2 - i\omega)}{(\kappa - i\omega)^2 - |\epsilon|^2} \left[\sqrt{\kappa_1} a^\dagger_{\text{in},1}(-\omega) + \sqrt{\kappa_2} a^\dagger_{\text{in},2}(-\omega) \right]$$
$$- \frac{\epsilon^*}{(\kappa/2 - i\omega)^2 - |\epsilon|^2} \left[\sqrt{\kappa_1} a_{\text{in},1}(\omega) + \sqrt{\kappa_2} a_{\text{in},2}(\omega) \right], \quad (4.24)$$

with $\kappa = \kappa_1 + \kappa_2$. From here, with the input-output relations $\hat{a}_{\text{in}} + \hat{a}_{\text{out}} = \sqrt{\kappa_1}\hat{a}$, the output-fields follow to be

$$\hat{a}_{\text{out}}(\omega) = -\frac{(\kappa/2 - i\omega)}{(\kappa/2 - i\omega)^2 - |\epsilon|^2} \left[\kappa_1 \hat{a}_{\text{in},1}(\omega) + \sqrt{\kappa_1\kappa_2} \hat{a}_{\text{in},2}(\omega) \right] - \hat{a}_{\text{in},1}$$
$$- \frac{\epsilon}{(\kappa/2 - i\omega)^2 - |\epsilon|^2} \left[\kappa_1 a^\dagger_{\text{in},1}(-\omega) + \sqrt{\kappa_1\kappa_2} a^\dagger_{\text{in},2}(-\omega) \right] \quad (4.25)$$

The interesting quantity is the noise spectrum of the quadrature variances, $S_{x_i x_j} = \int d\omega' \langle \hat{x}_i(\omega) \hat{x}_j(\omega') \rangle$. Collett and Gardiner calculate normally-ordered spectra.[190] They can be connected to for us more common symmetrised spectra via adding vacuum noise and rescaling, such that vacuum noise corresponds to a spectral density of one ($= 0\,\text{dB}$) and perfect squeezing to a spectral density of zero ($\to -\infty\,\text{dB}$): $S_{x_i x_i} = 1 + 4 : S_{x_i x_i} :$. The output spectra for the two quadratures follow to be

$$V^+ = S_{\hat{x}\hat{x}} = 1 + 4\frac{|\epsilon|\kappa_1/2}{(\kappa/2 - |\epsilon|)^2 + \omega^2}$$
$$= 1 + \eta_{\text{esc}} \frac{4x}{(1-x)^2 + 4\Omega^2}, \quad (4.26a)$$

$$V^- = S_{\hat{p}\hat{p}} = 1 - 4\frac{|\epsilon|\kappa_1/2}{(\kappa/2 + |\epsilon|)^2 + \omega^2}$$
$$= 1 - \eta_{\text{esc}} \frac{4x}{(1+x)^2 + 4\Omega^2}, \quad (4.26b)$$

where the escape efficiency η_{esc}, the pump parameter x, and the frequency

[190]Cf. Collett and Gardiner (1984), Eqs. 49 and 52.

normalised to the cavity's linewidth $\Omega = \omega/(\kappa_1 + \kappa_2)$ were introduced,

$$\eta_{\text{esc}} = \frac{\kappa_1}{\kappa_1 + \kappa_2}, \tag{4.27}$$

$$x = \frac{|\epsilon|}{\frac{1}{2}(\kappa_1 + \kappa_2)} = \sqrt{\frac{P}{P_{\text{th}}}}. \tag{4.28}$$

The noise in the $\hat{p}$-quadrature is smallest on resonance ($\Omega = 0$) at threshold ($x = 1$), and becomes zero for perfect escape efficiency ($\eta_{\text{esc}} = 1$), which correponds to a single-sided, or lossless, cavity ($\kappa_2 = 0$). Other losses on the way to detection can also be written as efficiencies (see Sec. 1.1.4), such that

$$V^+_{\text{meas}} = 1 + \eta_{\text{total}}\frac{4x}{(1-x)^2 + 4\Omega^2}, \tag{4.29a}$$

$$V^-_{\text{meas}} = 1 - \eta_{\text{total}}\frac{4x}{(1+x)^2 + 4\Omega^2}. \tag{4.29b}$$

Choosing $\eta_{\text{total}} = 1$ leads to a (only theoretically) possible squeezing value called *initial squeezing*. On resonance,

$$V^-_{\text{init}} = \left(\frac{1-x}{1+x}\right)^2 = \frac{1}{V^+_{\text{init}}}. \tag{4.30}$$

Introducing losses via an efficiency $\eta_{\text{total}} < 1$ as well as deviating from measuring on resonance, $\Omega \neq 0$, results in smaller detectable squeezing values as can be seen in Fig. 4.10.

The initial squeezing value, as well as pump parameter and total losses, can be derived from just measuring squeezing and anti-squeezing at DC or higher FSRs (meaning $\Omega = 0$):

$$V^-_{\text{init}} = -\frac{V^-_{\text{meas}} - 1}{V^+_{\text{meas}} - 1}, \tag{4.31}$$

$$\eta_{\text{total}} = \frac{V^\pm_{\text{meas}} - 1}{V^\pm_{\text{init}} - 1} = -\frac{(V^-_{\text{meas}} - 1)(V^+_{\text{meas}} - 1)}{V^-_{\text{meas}} + V^+_{\text{meas}} - 2}, \tag{4.32}$$

$$x = \frac{1 - \sqrt{V^-_{\text{init}}}}{1 + \sqrt{V^-_{\text{init}}}} = \frac{1 - \sqrt{-\frac{V^-_{\text{meas}} - 1}{V^+_{\text{meas}} - 1}}}{1 + \sqrt{-\frac{V^-_{\text{meas}} - 1}{V^+_{\text{meas}} - 1}}}. \tag{4.33}$$

Note that all the inconvenient subtrahends '-1' after the variances come from the fact that we are not looking at normally-ordered variances but at symmetric
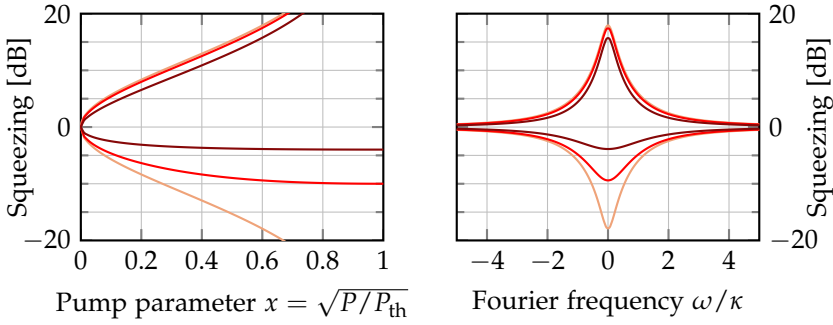
Figure 4.10: Left: Squeezing over pump parameter for different values of η. Right: Squeezing in frequency domain at a pump power of $x = 0.6$ and at resonance ($\Omega = 0$) for different values of η. Efficiency η in both plots 1, 0.9, and 0.6 from light to dark. Plotted from Eq. 4.29. See also Fig. 4.6.

variances. Note also that the formulae above are only true if efficiencies are the dominant degradation factor and other contributing processes such as phase noise or electronic noise are not limiting (or included in the modelling, see also Fig. 4.11).

4.2.2 Two-mode squeezing

The treatment for two-mode squeezed states (also called bipartite entangled states[191]) is very similar to those of single-mode squeezing, but starting with a different Hamiltonian (already with linearised pump field and in the rotating frame),[192]

$$\hat{H} = i\epsilon\hat{a}\hat{c} - i\epsilon^*\hat{a}^\dagger\hat{c}^\dagger, \tag{4.34}$$

leading to equations of motion for two modes $\hat{a}$, $\hat{c}$,

$$\dot{\hat{a}} = \epsilon\hat{c}^\dagger - \tfrac{1}{2}(\kappa_{a,1} + \kappa_{a,2})\hat{a} + \sqrt{\kappa_{a,1}}\hat{a}_{\text{in},1} + \sqrt{\kappa_{a,2}}\hat{a}_{\text{in},2}, \tag{4.35}$$

$$\dot{\hat{c}} = \epsilon\hat{a}^\dagger - \tfrac{1}{2}(\kappa_{c,1} + \kappa_{c,2})\hat{c} + \sqrt{\kappa_{c,1}}\hat{c}_{\text{in},1} + \sqrt{\kappa_{c,2}}\hat{c}_{\text{in},2}, \tag{4.36}$$

again with linewidth $\kappa_{i,1}$ and $\kappa_{i,c}$ being the coupling rates of modes i through the input coupler and to the bath, respectively. It becomes complicated if the cavity is different for the two modes $\hat{a}$ and $\hat{c}$, meaning especially different

---

[191]Cf. e.g. Schnabel (2017), Sec. 3.4.
[192]Cf. Ou, Pereira and Kimble (1992), who themselves follow again Collett and Gardiner (1984).

linewidths for the two modes. In Eqs. 4.35 and 4.36, the detuning was already set to zero for both modes such that both modes are resonant at the same time,[193] which will be the case later in the experiment. Additionally, the cavity losses are approximately the same for both modes because of almost normal incidence on all intracavity optics (cf. experimental set-up in Sec. 4.4.1). With the resulting assumption of equal linewidths for both modes, the equations of motion can be decoupled via defining two new modes $\hat{b} = (\hat{a} + \hat{c})/\sqrt{2}$ and $\hat{d} = (\hat{a} - \hat{c})/\sqrt{2}$:

$$\dot{\hat{b}} = \epsilon \hat{b}^{\dagger} - \tfrac{1}{2}(\kappa_1 + \kappa_2)\hat{b} + \sqrt{\kappa_1}\hat{b}_{\text{in},1} + \sqrt{\kappa_2}\hat{b}_{\text{in},2}, \qquad (4.37)$$

$$\dot{\hat{d}} = \epsilon \hat{d}^{\dagger} - \tfrac{1}{2}(\kappa_1 + \kappa_2)\hat{d} + \sqrt{\kappa_1}\hat{d}_{\text{in},1} + \sqrt{\kappa_2}\hat{d}_{\text{in},2}. \qquad (4.38)$$

These are the same equations of motion as for the single-mode case – see Eq. 4.21 above! The quadratures of mode $\hat{d}$ (and also mode $\hat{b}$) will be squeezed and anti-squeezed, only that these quadratures are a superposition of quadratures of modes $\hat{a}$ and $\hat{c}$:

$$\hat{x}_{\text{b}} \propto \hat{b} + \hat{b}^{\dagger} \propto \hat{a} + \hat{c} + \hat{a}^{\dagger} + \hat{c}^{\dagger} \propto \hat{x}_{\text{a}} + \hat{x}_{\text{c}}, \qquad (4.39\text{a})$$

$$\hat{p}_{\text{b}} \propto -i(\hat{b} - \hat{b}^{\dagger}) \propto -i(\hat{a} + \hat{c} - \hat{a}^{\dagger} - \hat{c}^{\dagger}) \propto \hat{p}_{\text{a}} + \hat{p}_{\text{c}}, \qquad (4.39\text{b})$$

$$\hat{x}_{\text{d}} \propto \hat{d} + \hat{d}^{\dagger} \propto \hat{a} - \hat{c} + \hat{a}^{\dagger} - \hat{c}^{\dagger} \propto \hat{x}_{\text{a}} - \hat{x}_{\text{c}}, \qquad (4.39\text{c})$$

$$\hat{p}_{\text{d}} \propto -i(\hat{d} - \hat{d}^{\dagger}) \propto -i(\hat{a} - \hat{c} - \hat{a}^{\dagger} + \hat{c}^{\dagger}) \propto \hat{p}_{\text{a}} - \hat{p}_{\text{c}}. \qquad (4.39\text{d})$$

To see squeezing, a combination of the original quadratures $\hat{x}_{\text{a}}$, $\hat{x}_{\text{c}}$, $\hat{p}_{\text{a}}$, $\hat{p}_{\text{c}}$ needs to be measured, for example

$$\langle \hat{x}_{\text{b}}^2 \rangle \propto \langle (\hat{x}_{\text{a}} + \hat{x}_{\text{c}})^2 \rangle = \text{var}\,\hat{x}_{\text{a}} + \text{var}\,\hat{x}_{\text{c}} + 2\,\text{cov}\,\hat{x}_{\text{a}}, \hat{x}_{\text{c}} \qquad (4.40)$$

– and that is exactly what a homodyne detector can do, cf. Sec. 4.1.2, especially Eq. 4.16. For $\langle \hat{x}_{\text{b}}^2 \rangle$ (for $\langle \hat{x}_{\text{d}}^2 \rangle$) to vanish, $\hat{x}_{\text{a}}$ and $\hat{x}_{\text{c}}$ need to be perfectly anti-correlated (correlated), see also the corresponding plots in Fig. 4.4.

For a closer look at how to generate the correlations between these two modes/quadratures, the equations of motion need to be solved, again in the Fourier domain. To simplify the calculation, a single-ended cavity, again with the same linewidth in both modes, is assumed.[194] The output field

[193]C. Schori, J. L. Sørensen and E. S. Polzik, 'Narrow-band frequency tunable light source of continuous quadrature entanglement', *Phys. Rev. A* **66** (2002), 10.

[194]Calculations for double-ended cavities are done by Ou, Pereira and Kimble (1992), different losses for the modes are included by Schori, Sørensen and Polzik (2002).

quadratures amount to[195]

$$\hat{x}_a^{out}(\omega) = G(\omega)\hat{x}_a^{in}(\omega) + g(\omega)\hat{x}_c^{in}(\omega), \tag{4.41a}$$

$$\hat{p}_a^{out}(\omega) = G(\omega)\hat{p}_a^{in}(\omega) - g(\omega)\hat{p}_c^{in}(\omega), \tag{4.41b}$$

$$\hat{x}_c^{out}(\omega) = G(\omega)\hat{x}_c^{in}(\omega) + g(\omega)\hat{x}_a^{in}(\omega), \tag{4.41c}$$

$$\hat{p}_c^{out}(\omega) = G(\omega)\hat{p}_c^{in}(\omega) - g(\omega)\hat{p}_a^{in}(\omega), \tag{4.41d}$$

where

$$G(\omega) = \frac{\epsilon^2 + \kappa^2/4 + \omega^2}{(\kappa/2 - i\omega)^2 - \epsilon^2}, \tag{4.42}$$

$$g(\omega) = \frac{\epsilon\kappa}{(\kappa/2 - i\omega)^2 - \epsilon^2}. \tag{4.43}$$

Because $|G(\omega)|^2 - |g(\omega)|^2 = 1$ as can be checked from Eqs. 4.42 and 4.43, one can identify $|G(\omega)| = \cosh r$ and $|g(\omega)| = \sinh r$ (on resonance for $\omega = 0$, $G = G^* = G_0$ and $g = g^* = g_0$).[196] Each quadrature on its own has the same variance of

$$\langle \hat{x}_i^{out}(\omega)\hat{x}_i^{out}(\omega')\rangle = \langle \hat{p}_i^{out}(\omega)\hat{p}_i^{out}(\omega')\rangle = \delta(\omega + \omega')\left(|G(\omega)|^2 + |g(\omega)|^2\right)$$

$$= \delta(\omega + \omega')\left(\cosh^2 r + \sinh^2 r\right)$$

$$= \delta(\omega + \omega')\cosh 2r. \tag{4.44}$$

The noise is enhanced compared to vacuum. Looking at combined quadratures, though, shows that, on resonance,

$$\langle(\hat{x}_a^{out} \pm \hat{x}_c^{out})^2\rangle = (G_0 \pm g_0)^2$$

$$= \cosh^2 r + \sinh^2 r \pm 2\cosh r \sinh r$$

$$= \cosh 2r \pm \sinh 2r = e^{\pm 2r}. \tag{4.45}$$

The same is true for $\langle(\hat{p}_a^{out} \pm \hat{p}_c^{out})^2\rangle$. From Eqs. 4.44 and 4.45, $-\langle p_a^{out}p_c^{out}\rangle = \langle x_a^{out}x_c^{out}\rangle = \pm\sinh 2r$. Thus, the covariance matrix can be written as

$$C(\hat{x}_a, \hat{p}_a, \hat{x}_c, \hat{p}_c) = \begin{pmatrix} \cosh 2r & 0 & \sinh 2r & 0 \\ 0 & \cosh 2r & 0 & -\sinh 2r \\ \sinh 2r & 0 & \cosh 2r & 0 \\ 0 & -\sinh 2r & 0 & \cosh 2r \end{pmatrix}, \tag{4.46}$$

---

[195]Eq. 15 in Ou, Pereira and Kimble (1992).

[196]Cf. equations after their Eq. 13 and Eq. 34 in Ou, Pereira and Kimble (1992).

the same as in Eq. 4.5.

Again, r is the squeezing parameter, related to frequency ω and pump parameter $x = 2\epsilon/\kappa$ via $|g(\omega)|$. Also on resonance,

$$(G_0 \pm g_0)^2 = 1 \pm \frac{4x}{(1 \mp x)^2 + 4\Omega'} \tag{4.47}$$

with $x = 2\epsilon/\kappa$ and $\Omega = \omega/\kappa$, which is again similar to the single-mode case, see eq. 4.29.

Losses can now be introduced with mixing the covariance matrix with vacuum states as in Sec. 1.1.4. Including different efficiencies η_a and η_c for the two modes results in a covariance matrix

$$C(\hat{x}_a, \hat{p}_a, \hat{x}_c, \hat{p}_c) =$$
$$\begin{pmatrix} 1 - \eta_a + \eta_a \cosh 2r & 0 & \sqrt{\eta_a \eta_c} \sinh 2r & 0 \\ 0 & 1 - \eta_a + \eta_a \cosh 2r & 0 & -\sqrt{\eta_a \eta_c} \sinh 2r \\ \sqrt{\eta_a \eta_c} \sinh 2r & 0 & 1 - \eta_c + \eta_c \cosh 2r & 0 \\ 0 & -\sqrt{\eta_a \eta_c} \sinh 2r & 0 & 1 - \eta_c + \eta_c \cosh 2r \end{pmatrix}.$$
$$\tag{4.48}$$

The measured variance can be connected to the pump parameter x with $\cosh 2r = |G(\omega)|^2 + |g(\omega)|^2$ and $\sinh 2r = 2 \cosh r \sinh r = 2|G(\omega)||g(\omega)|$. On resonance, this leads to

$$\cosh 2r = 1 + \frac{8x}{(1 - x^2)^2}, \quad \sinh 2r = 4x\frac{1 + x^2}{(1 - x^2)^2}. \tag{4.49}$$

With this, the variance var $\hat{x}_a \pm \hat{x}_c$ can be written as

$$\text{var } \hat{x}_a \pm \hat{x}_c = 1 + \eta_a\frac{8x^2}{(1 - x^2)^2} + 1 + \eta_c\frac{8x^2}{(1 - x^2)^2} \pm \sqrt{\eta_a \eta_c}8x\frac{1 + x^2}{(1 - x^2)^2}. \tag{4.50}$$

For $\eta_a = \eta_c = \eta$, this simplifies to

$$\text{var } \hat{x}_a \pm \hat{x}_c = 2\left(1 \pm \eta\frac{4x}{(1 \mp x)^2}\right). \tag{4.51}$$

Note again the similarities to the single-mode case, Eq. 4.29, and the additional factor of 2. Normalising to the case of no coupling/no pump ($x = 0$), which is done in the experiment (and in Fig. 4.8), cancels the factor.

4.2.3 Parametric amplification and de-amplification

It is straightforward to take the classical limit of the above results. The mode operators become complex variables, the driving field $a_{\text{in},1}$ is (without loss of generality) a real variable, the phase difference between input field and pump field is included in the complex coupling strength ϵ. The vacuum input mode $a_{\text{in},2}$ becomes zero. On resonance ($\omega = 0$), the intracavity power in the single-mode case from Eqs. 4.23 and 4.24 is proportional to

$$|a|^2 = -\frac{\kappa_1}{(\kappa^2 - |\epsilon|^2)^2} \left(\kappa^2 + \kappa(\epsilon^* + \epsilon) + |\epsilon|^2 \right) a_{\text{in}}^2. \tag{4.52}$$

The gain, here defined as the ratio of the intracavity field with pump and without pump, is[197]

$$\frac{P}{P(\epsilon = 0)} = \frac{\kappa^2}{(\kappa^2 - |\epsilon|^2)^2} \left(\kappa^2 + 2\kappa|\epsilon| \cos\theta + |\epsilon|^2 \right)$$

$$= \frac{1 + x^2 + 2x\cos\theta}{(1 - x^2)^2} \overset{\theta=0,\pi}{=\!=} \frac{(1 \pm x)^2}{(1 - x)^2(1 + x)^2} = \frac{1}{(1 \mp x)^2}. \tag{4.53}$$

For $\theta = 0$, this equals the classical parametric amplification gain $G = 1/(1 - x)^2$.

The gain G can be determined from amplification and de-amplification measurements:

$$\frac{1}{4} \left(\sqrt{\frac{P_{\text{max}}}{P_{\text{min}}}} + 1 \right)^2 = \frac{1}{4} \left(\sqrt{\frac{P_{\theta=0}}{P_{\theta=\pi}}} + 1 \right)^2$$

$$= \frac{1}{4} \left(\frac{1+x}{1-x} + 1 \right)^2 = \frac{1}{(1-x)^2} = G, \tag{4.54}$$

where the phase of the pump beam is swept and the driving field's power is measured in transmission of the cavity to obtain P_{max} and P_{min}. With knowledge of the gain G at a given pump power, the pump parameter x and also (with a known linewidth κ) the coupling strength $|\epsilon| = g_{\text{DC}}$ can be computed.

---

[197]This definition is also used by T. Aoki, G. Takahashi and A. Furusawa, 'Squeezing at 946nm with periodically poled KTiOPO$_4$', *Opt. Express* **14** (2006), 6930, Eq. 3, and by T. C. Zhang et al., 'Quantum teleportation of light beams', *Phys. Rev. A* **67** (2003), 16, Eq. 15. Note that this gain needs to be measured at *another* port than the input port. If measured in reflection of the input port, a different gain definition needs to be used, taking account the destructive interferences. *This* gain is employed, e.g., by Wu, Xiao and Kimble (2008), Eq. 2, with their d being our pump parameter x. It is then the classical analogue to the quantum-mechanical squeezing in reflection off a cavity.

4.2.4 Threshold power from crystal parameters

From the previous sections it is known that the coupling strength g_{DC} is proportional to the pump field (Eq. 4.20) and connected to the pump parameter x (Eq. 4.28). At threshold, x becomes one, see for example Eq. 4.53 and 4.54. It can also be defined as the ratio of applied pump amplitude to the pump amplitude at threshold (or, as the ratio of the squareroot of pump power to threshold power, Eq. 4.28), also evaluating to one at threshold.

At threshold, the gain from nonlinear conversion *just* balances the losses. Equating the single-pass power gain for a light mode with the power lost per round-trip and solving for the pump power yields an expression for the threshold power. The task of finding the single-pass gain of a nonlinear material for threshold computations can be approached classically or quantum-mechanically, the ideas are similar. Quantum-mechanically, one starts with the Hamiltonian which is the volume integral of the electromagnetic energy density.[198] Classically, one uses Maxwell's equations to obtain the single-pass power gain from the same energy considerations.[199] Both approaches assume a negligible pump depletion. Alternatively, the coupled equations of motion derived from Maxwell's equations need to be solved, which can be done via a Green's function approach.[200] All these options lead to a mode-overlap integral, which can be simplified making several assumptions, but still needs to be solved numerically. The full numerical solution of the coupled equations of motion is another option and is provided by Lastzka's *Nonlinear Cavity Simulator*.[201]

In a semi-classical picture,[202] the incoming (pump) field accelerates electrons in the dielectric material, which induces an oscillating polarisation. Because the electrons might not sit in a purely harmonic potential,[203] their movement also contains higher harmonic frequencies – of interest is here the second harmonic. The oscillating polarisation is again the source of radiation. The second-order susceptibility tensor $\chi^{(2)}(\omega_{m+n}; \omega_m, \omega_n)$ describes how incoming electrical fields of frequencies ω_m and ω_n induce a polarisation of frequency

---

[198] A. Yariv, *Quantum Electronics*, New York et al., 1989, Sec. 17.5.

[199] G. D. Boyd and D. A. Kleinman, 'Parametric interaction of focused Gaussian light beams', *J. Appl. Phys.* **39** (1968), 3597–3639.

[200] S. Guha, F. J. Wu and J. Falk, 'The Effects of Focusing on Parametric Oscillation', *IEEE J. Quantum Electron.* **18** (1982), 907–912.

[201] N. Lastzka, 'Numerical modelling of classical and quantum effects in non-linear optical systems', PhD thesis, Leibniz Universität Hannover, 2010.

[202] The calculations follow Boyd and Kleinman (1968).

[203] Yariv (1989), Sec. 16.3.

$\omega_m + \omega_n$ in the material (see Appendix A.2.2),[204]

$$\mathcal{P}^{\omega_{m+n}}(\mathbf{r}) = \epsilon_0 \frac{D}{2} \chi^{(2)}(\omega_{m+n}; \omega_m, \omega_n) \mathbf{E}^{\omega_m}(\mathbf{r}) \mathbf{E}^{\omega_n}(\mathbf{r}). \tag{4.55}$$

The degeneracy factor D is 2 (see Appendix A.2.2) and $\omega_{m+n} = \omega_m + \omega_n$. For specific polarisations, beam directions and wave frequencies in a particular crystal under certain symmetries (e.g. neglecting dispersion), an effective second-order susceptibility[205] d_{eff} can be defined,

$$d_{\text{eff}} = \frac{2}{\pi} \hat{e}^i_{m+n} d_{ijk} \hat{e}^j_m \hat{e}^k_n = \frac{2}{\pi} \hat{e}^i_{m+n} \frac{1}{2} \chi^{(2)}_{ijk}(\omega_{m+n}; \omega_m, \omega_n) \hat{e}^j_m \hat{e}^k_n, \tag{4.56}$$

which is reduced by a factor $\frac{2}{\pi}$ due to quasi phase-matching.[206] $\hat{e}^i_m$ denotes the polarisation component of light of frequency ω_{m} in direction i.

The average power from the polarisation $\mathcal{P}$ in the material which is deposited in the fundamental field can be be calculated from energy considerations. The average power per unit volume in the dielectric material needs to be integrated over the volume of the material to obtain the power transferred from a polarisation mode to the field mode,[207]

$$\overline{\frac{\text{Power}}{\text{Volume}}} = \overline{\mathbf{E} \frac{\partial \mathcal{P}}{\partial t}}. \tag{4.57}$$

The total power transferred is zero (neglecting losses in the material) due to energy conservation but it need not be zero if looking at one particular frequency. From Eq. 4.57, the average power $\overline{P_n}$ transferred to mode ω_n is (see

---

[204] In the following, m and n denote frequencies, whereas i, j, k stand for spatial directions.

[205] A. Smith, *SNLO*, URL: http://www.as-photonics.com/snlo, provides a collection of nonlinear materials and calculates effective coefficients for almost arbitrary configurations. Lots of materials and references are also to be found in D. N. Nikogosyan, *Nonlinear Optical Crystals: A Complete Survey*, New York: Springer, 2005.

[206] Phase matching is necessary for efficient conversion. Quasi phase matching is one of three processes enabling phase matching, the other two being critical/angular phase matching and non-critical/temperature phase matching, see R. W. Boyd, *Nonlinear Optics*, Amsterdam et al.: Acad. Press, 2008, Secs. 2.2 and 2.3. Phase matching is touched again in Sec. 4.3 and also the remainder of this section.

[207] Cf. Yariv (1989), Eq. 5.1-13, and Boyd and Kleinman (1968), Eq. A2.57, see also derivation in Appendix A.2.3. Note that here, polarisation refers to the material's polarisation, not to a polarised light field.

Appendix A.2.4)

$$\overline{P_n} = \frac{1}{2T} \int\limits_{-T}^{T} dt \int\limits_{V} d\mathbf{r} \, \mathbf{E}^{\omega_n}(\mathbf{r}, t) \frac{\partial \mathcal{P}^{\omega_n}(\mathbf{r}, t)}{\partial t} = -\mathrm{Im} \left[\frac{\omega_n}{2} \int\limits_{V} d\mathbf{r} \, \mathbf{E}^{*\omega_n}(\mathbf{r}) \mathcal{P}^{\omega_n}(\mathbf{r}) \right],$$

(4.58)

where the integration takes place over the volume V of the crystal. With the polarisation as in Eq. 4.55 and assuming Gaussian beams, the power transferred to a mode with frequency ω_1 is

$$\overline{P_1} = -\mathrm{Im} \left[\omega_1 \epsilon_0 d_{\mathrm{eff}} E^{\omega_1} E^{\omega_3} E^{\omega_2} \int\limits_{V} d\mathbf{r} \, u_1^*(\mathbf{r}) u_3(\mathbf{r}) u_2^*(\mathbf{r}) e^{i(\Delta k z + \varphi)} \right]$$

(4.59)

where $u_i(\mathbf{r})$ are the transversal mode functions known from Sec. 1.1.2. When evaluating the integrals, it was assumed that the (product of the) amplitudes do not change over the length of the crystal.

Equation 4.59 is an important intermediate result: The power gain depends on the strength of the participating beams, the nonlinear coefficient d_{eff}, the phase matching and phase relationship $\Delta k z + \varphi$, and the mode overlap. The mode-overlap integral can be evaluated in radial direction, assuming the crystal's aperture not to be limiting. For further (analytical) evaluation, more simplifications are necessary. The position of the waist is assumed to be the same for all participating beams and lies in the centre of the crystal, and the Rayleigh ranges $z_{\mathrm{R},n}$ are assumed to be equal (which, for $\omega_1 = \omega_2 = \frac{1}{2}\omega_3$, leads to $w_{01} = w_{02} = w_{03}/\sqrt{2}$). This is the optimal case in terms of mode overlap (if there is no double refraction). The integral simplifies to

$$\int\limits_{0}^{\infty} dr \, r \int\limits_{0}^{2\pi} d\phi \int\limits_{0}^{l} dz \, u_1^*(r) u_3(r) u_2^*(r) e^{i(\Delta k z + \varphi)} = \frac{b}{2} \pi w_3^2 e^{i(\sigma\xi + \varphi)} \int\limits_{-\xi}^{\xi} dq \, \frac{e^{i\sigma q}}{1 + iq},$$

(4.60)

with the normalised beam parameter $q = 2(z - f)/b = 2z/b - l/b$, the confocal parameter $b = 2z_{\mathrm{R}}$, the focusing parameter $\xi = l/b$, which also determines the new integration limits in z-direction, the crystal length l, and the phase-mismatch parameter $\sigma = \frac{1}{2}b\Delta k$. The transferred power can now be written as

$$\overline{P_1} = \frac{\pi^2}{2} \omega_1 b \epsilon_0 d_{\mathrm{eff}} w_{03}^2 E^{\omega_1} E^{\omega_3} E^{\omega_2} \times \mathrm{Im} \left[e^{i(\sigma\xi + \varphi)} \right] \times H(\xi, \sigma)$$

(4.61)

with a function $H(\xi, \sigma) = \frac{1}{2\pi} \int_{-\xi}^{\xi} dq \frac{\exp i\sigma q}{1+iq}$ as given by Boyd and Kleinman,[208] which is assumed to be real as the beam waists are in the centre of the crystal[209] and can be optimised with regard to the focusing parameter ξ and the phase mismatch σ. Assuming perfect phase matching and adjusting the phase φ such that $\sigma\xi + \varphi = \frac{1}{2}b\Delta k + \varphi = \pm\frac{1}{2}\pi$ is usually justified.

Similarly, the power transferred to the idler mode is

$$\overline{P_2} = \frac{\pi^2}{2} \omega_2 b\epsilon_0 d_{\text{eff}} w_{03}^2 E^{\omega_2} E^{\omega_3} E^{\omega_1} \times H(\xi, \sigma). \tag{4.62}$$

With $E^{\omega_n} = (4P_n/c\pi\epsilon_0 n_n w_{0n}^2)^{1/2}$ for Gaussian beams and another focusing function h which is then the same as $\bar{h}$ in the paper by Boyd and Kleinman,[210]

$$h(\sigma, \xi) = \frac{\pi^2}{\xi}|H|^2 = \frac{1}{4\xi} \int_{-\xi}^{\xi} dq \int_{-\xi}^{\xi} dq' \frac{e^{i\sigma(q-q')}}{(1+iq)(1-iq')}, \tag{4.63}$$

the multiplication of $\overline{P_1}$ and $\overline{P_2}$ yields

$$\overline{P_1 P_2} = 2KP_1 P_2 P_3 \frac{l^2 w_{03}^2}{\xi w_{01}^2 w_{02}^2} h(\sigma, \xi) = KP_1 P_2 P_3 lkh(\sigma, \xi), \tag{4.64}$$

for equal beam waists of signal and idler beam, again with $\xi = l/kw_0^2$, where the constant K is

$$K = \frac{8\omega_1 \omega_2 d_{\text{eff}}^2}{\pi\epsilon_0 c^3 n_1 n_2 n_3}, \tag{4.65}$$

actually very similar to Γ^2 used by Wimmer and co-workers as gain parameter in their calculation of the down-conversion coupling strength g_{DC}.[211] At pump threshold, the average power transfer is equal to the power lost per cavity round-trip,

$$\overline{P_{1,2}} \stackrel{!}{=} (T_{\text{in}} + L)P_{1,2}, \tag{4.66}$$

assuming equal losses L and input coupler transmission T_{in} for signal and idler beam. After inserting Eq. 4.64, this can be solved for the power $P_3 = P_{\text{th}}$:

$$P_{\text{th}} = \frac{(T_{\text{in}} + L)^2}{Kklh(\sigma, \xi)} = \frac{(T_{\text{in}} + L)^2}{4E_{\text{NL}}}. \tag{4.67}$$

---

[208] Boyd and Kleinman (1968), Eq. 3.20.
[209] Boyd and Kleinman (1968), Eq. A4.8.
[210] Boyd and Kleinman (1968), Eq. 3.32. $h(\xi)$ is also plotted in Fig. 4.13.
[211] M. H. Wimmer, D. Steinmeyer, K. Hammerer and M. Heurs, 'Coherent cancellation of backaction noise in optomechanical force measurements', *Phys. Rev. A* **89** (2014), 053836.

E_{NL} is the single-pass power gain from second harmonic generation.[212]The threshold power does not depend on the powers of signal and idler beam. It depends on total losses $T_{\text{in}} + L$ in the cavity and on the effective nonlinearity E_{NL}, which includes the crystal's nonlinear coefficient d_{eff}, the crystal length l, and $h(\sigma, \xi)$ quantifying focusing, mode overlap and phase matching. For optimal focusing in the case of no double refraction and small losses, i.e. $\xi = l/b = 2.84$, h evaluates to $h = 1.086$.[213] Equation 4.67 is equal to the result given by Guha and co-workers[214] derived via solving Maxwell's equations with a Green's function approach, if one takes care of different definitions of losses and nonlinear susceptibility.

The optimisation of $h(\sigma, \xi)$ corresponds to a trade-off between weaker focusing so that a larger interaction volume is used, and stronger focusing so that the beam intensity is higher. Lastzka speaks of it as the maximisation of the average field strength inside the crystal.[215] An optimum focusing exists for a specific configuration.

It makes sense to recall the assumptions made in the derivation of the pump threshold, which are:

1. monochromatic and collinear Gaussian beams (TEM$_{00}$),

2. optimal pump phase and phase matching,

3. no losses at or in the crystal,

4. no double refraction,

5. no reflection at crystal surfaces,

6. optimal mode overlap, i.e. equal waist positions and equal confocal parameters,

7. no change in amplitude over a single passing through the crystal,

8. QPM can be represented by factor of $2/\pi$ in d_{eff}.

---

[212]Boyd and Kleinman (1968), paragraph after Eq. 3.27, see also Wu, Xiao and Kimble (2008), Sec. 2.
[213]Boyd and Kleinman (1968), Eq. 3.39.
[214]Guha, Wu and Falk (1982).
[215]Lastzka, PhD thesis (2010), p. 61.

Assumptions 2 to 6 can be (and have been) relaxed[216], but then the equations get very cumbersome. In our case, Assumptions 1, 2, 4, 5 and – under usual circumstances – 6 are reasonable to make. Numerical calculations can be done, for example with Lastzka's *Nonlinear Cavity Simulator*,[217] but at this point, the qualitative implications are more important than quantitative results: The coupling strength g_{DC} depends on the material parameter d_{eff}, the mode overlap and focusing and the pump power. And: The threshold power, needed to determine coupling strength, can be estimated from measuring the single-pass gain in second harmonic generation, see Sec. 4.4.2.

4.3 How to improve squeezing and/or coupling strength

In the previous Sec. 4.2 it was shown how the amount of created and detected squeezing and the coupling strength are related. The qualitative findings are put together in Figs. 4.11 and 4.12. That does not mean, however, that improving one of them necessarily improves the other as can be seen in the mentioned figures.

The amount of measured squeezing depends on the initial squeezing and on processes which decohere or mask the quantum state and are detrimental to its measurement (Fig. 4.11). To improve squeezing, first and foremost the loss sources limiting the measured squeezing have to be identified and mitigated, which seems straightforward, but can be very challenging in practice. Most of the time *not* limiting is the available initial squeezing: It solely depends on the pump parameter and the relative detuning, and usually enough pump power is available.[218]

The pump parameter depends on the coupling strength – this way, squeezing and coupling strength are connected. A higher coupling strength leads to a lower threshold power. For squeezing, as mentioned above, this is only beneficial if the squeezing was limited by the available pump power. Coherent

---

[216]See, e.g., Boyd and Kleinman (1968), Guha, Wu and Falk (1982), J.-J. Zondy, D. Touahri and O. Acef, 'Absolute value of the d_{36} nonlinear coefficient of AgGaS$_2$: prospect for a low-threshold doubly resonant oscillator-based 3:1 frequency divider', *J. Opt. Soc. Am. B* **14** (2008), 2481, S. Guha, 'Focusing dependence of the efficiency of a singly resonant optical parametric oscillator', *Appl. Phys. B* **66** (1998), 663–675

[217]Lastzka, PhD thesis (2010).

[218]True so more for single-mode squeezing than for two-mode squeezing because of the larger interaction strength due to larger available nonlinear coefficients.
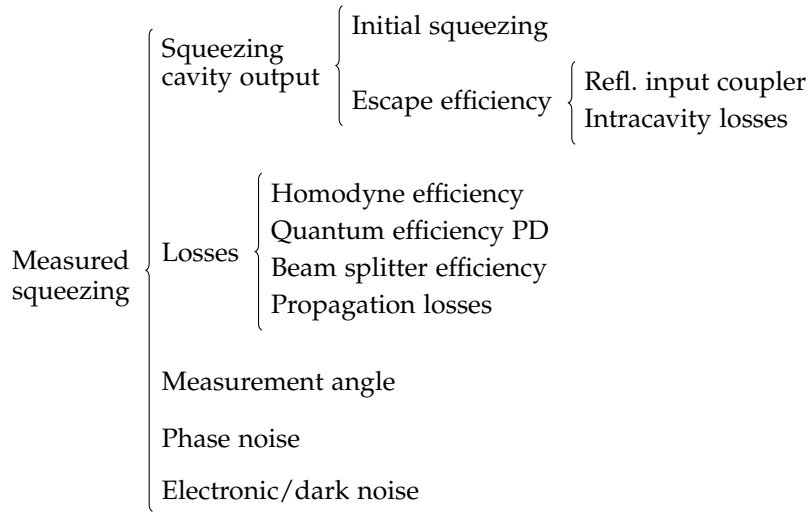
FIGURE 4.11: From initial squeezing to measured squeezing. This figure shows the dependency of the finally measured reduction in uncertainty on various parameters. The initial squeezing depends on the coupling strength, see Fig. 4.12.
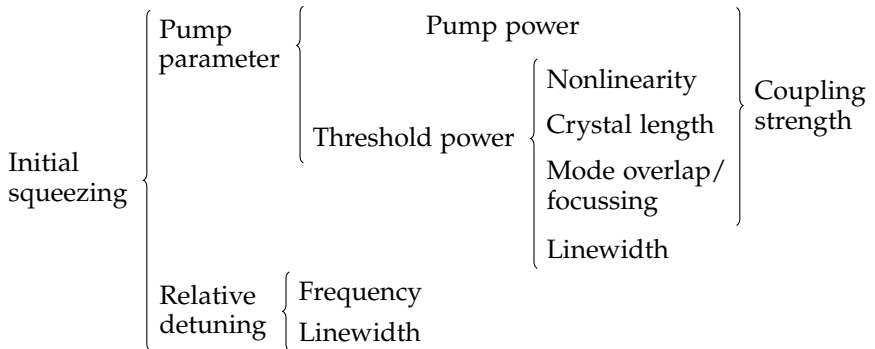
FIGURE 4.12: From experimental parameters to initial squeezing. This figure shows the dependency of initial squeezing and coupling strength on various parameters. They share the dependency on pump power and parameters pertaining to the crystal.

quantum-noise cancellation (CQNC) does not aim at producing squeezed states of light. Rather, a matching of coupling strengths is required to reduce back-action noise with CQNC. In the ideal case, the higher the measurement strength, the higher the sensitivity, which requires stronger coupling. For that reason, this section shows how parameters can be tuned towards higher coupling strength, investigating the nonlinear crystal, the beam shape of the participating modes, and the surrounding cavity.

4.3.1 Crystal

Crystal parameters influence the conversion efficiency and thereby the coupling strength. They also determine the pump threshold and hence the possible squeezing. The conversion is better with: a higher nonlinear coefficient, better phase matching, more pump power, and/or a longer interaction time – a longer crystal. The nonlinear coefficient is material-dependent. It is determined by the crystal structure and frequency-dependent.

Phase matching is needed for good conversion efficiency. For an efficient process, the created photons, which inherit their phase from the decayed photon, need to interfere constructively with the photons already in the cavity. One can also think of this condition as momentum conservation.[219] Phase matching depends on the interacting frequencies as the refractive index is frequency-dependent. It can be achieved with three different methods,[220] in our experiments, quasi phase-matching is used: Whenever the participating beams run out of phase, the nonlinear coefficient is reversed. The advantage of quasi phase-matching is its flexibility with respect to the addressed nonlinear coefficient and the frequencies used. This comes at the cost of the nonlinear coefficient reduced by a factor $2/\pi$. In order to create two-mode squeezing, an additional requirement is that both modes be resonant in the cavity. For polarisation two-mode squeezing as in this thesis, the birefringence of the crystal causes a differential phase shift on the two polarisations which adds to the phase shift caused by cavity mirror coatings. This results in different optical cavity lengths for the two polarisation modes – they are *not* necessarily both resonant at the same time. The cavity can be made resonant for both polarisations by tuning the crystal's temperature and thus length, which changes the differential phase shift but potentially decreases phase matching,

[219]N. Bloembergen, 'Conservation laws in nonlinear optics', *J. Opt. Soc. Am.* **70** (1980), 1429, Sec. 1C.

[220]Boyd (2008), Secs. 2.3 and 2.4.

see Sec. 4.4.2. To circumvent this and operate the crystal at its ideal phase matching temperature, a wedged crystal could be used, which can be moved laterally. By that its effective length can be varied to obtain resonance for both modes.

A longer crystal length would lead to increased interaction strength but often requires a larger aperture in order to not induce diffraction losses. Then, it becomes more difficult to apply the periodic poling needed for quasi phase-matching. Crystals considerably larger than $1\,\text{mm} \times 2\,\text{mm} \times 10\,\text{mm}$ are not commercially available. For squeezing light, it is actually not desirable to have longer crystals as the absorption loss scales with the crystal length – longer crystals are detrimental to the escape efficiency (see next Sec. 4.3.3).

The pump power could be limited by availability and damage threshold of the crystal (see next Sec. 4.3.2). Another adverse effect caused by higher pump powers is thermal lensing from heating due to absorption of the pump light. This changes the cavity's eigenmode and degrades mode matching.

Assuming perfect phase matching, the options when changing the crystal for an increased coupling strength are:

- find material and/or wavelengths and/or phase matching process where a higher nonlinear coefficient is possible,

- find material with higher damage threshold for more pump power,

- use longer crystal.

4.3.2 Beam shape

The participating beams influence the coupling strength and thus the squeezing via their intensities: Conversion is a nonlinear process, the higher the intensities, the more efficient the process. The intensity of a Gaussian beam varies spatially with its beam shape. Optimising the beam shape for the crystal geometry is an important part of designing the interaction process. One can look at two extreme cases: For plane waves, the whole crystal is used equally, but the peak intensity is small – the conversion is not very efficient. In contrast, for very small beam waists, the peak intensity and conversion efficiency in the waist is very high. Correspondingly strong divergence leads to an inefficient conversion in the remaining crystal. There is a trade-off between these two cases, which one can think of as maximising the mean intensity over the

crystal.[221] Boyd and Kleinman numerically integrated the mode-matching integral over the crystal length, resulting in a focusing function $h(\xi)$ (red trace in Fig. 4.13), depending on the ratio of crystal length to beam waist. For maximum efficiency, it needs to be maximised, the optimal ratio is[222] $\xi = l/2z_R \approx 2.84$.

It is also important that the participating beams have the same spatial shape. Stemming again from the mode overlap integrals, it can be informally thought of the photons keeping their mode shape when changing frequency.[223] An alternative explanation is in terms of phase fronts: With equal Rayleigh ranges, the phase fronts of the participating Gaussian beams are in sync, cf. Sec. 1.1.2, especially Fig. 1.5.

One might wonder: What if with optimal focusing the peak intensity becomes too high, i.e. lies above the material's damage threshold? An idea is to reduce the beam waist for smaller peak intensities resulting in less optimal focusing. Then, with more pump power, a stronger coupling might be possible. This hypothesis is tested in Fig. 4.13. The applied power P results in a peak intensity I_{pk} and in a coupling strength g_{DC}, related to power P and beam waist w_0/focusing parameter ξ via

$$I_{pk} = \frac{2P}{\pi w_0^2}, \qquad \xi = \frac{l}{2z_R}, \qquad z_R = \frac{\pi w_0^2}{\lambda}, \qquad (4.68)$$

and

$$x = \frac{g_{DC}}{\kappa/2} = \sqrt{\frac{P}{P_{th}}} \propto \sqrt{P \times h(\xi)}. \qquad (4.69)$$

Choosing the power P such that the coupling strength g_{DC} stays constant over different beam waists w_0 results in more power needed at less optimal focusing ($\xi \neq 2.84$), which is expected. At the same time, the peak intensity I_{pk} decreases with larger beam waists. Now, choosing the power P such that the peak intensity I_{pk} stays constant over different beam waists w_0 results in a lot more power needed with larger beam waists, which is expected. At the same time, the coupling strength g_{DC} also increases.

Within the approximation for the focusing function $h(\xi)$, it is thus possible to use a less optimal focusing with larger beam waists and apply more pump

---

[221] Lastzka, PhD thesis (2010), pp. 60–61, see also preceding Sec. 4.2.4.
[222] With several assumptions made, see Sec. 4.2.4, especially p. 140.
[223] Keeping their mode shape in this case means keeping their Rayleigh range, not their beam waist, which suggests that the Rayleigh range is the more fundamental quantity.
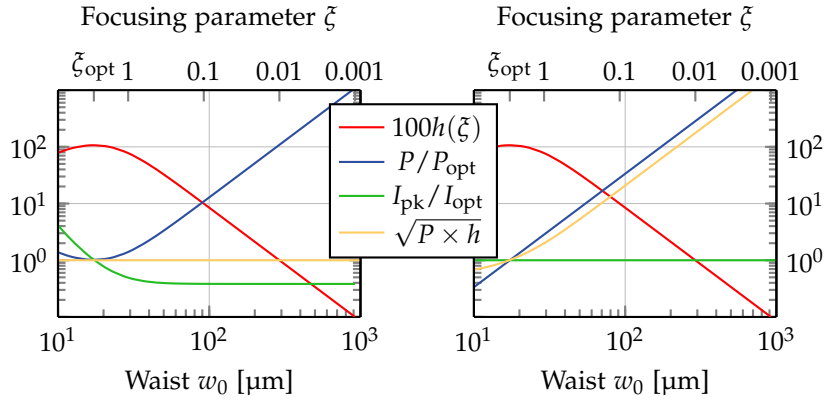
FIGURE 4.13: Effects of focusing and power change over different beam waists. x-axes are beam waist w_0 and focusing parameter ξ, related via Eq. 4.68. As all traces are normalised, the y-axis is dimensionless. In red, the focusing function $h(\xi)$ is shown with a maximum at $\xi_{\mathrm{opt}} = 2.84$. The applied power P (blue trace) results in a normalised peak intensity $I_{\mathrm{pk}}/I_{\mathrm{opt}}$ (green trace) and normalised coupling strength $\sqrt{P \times h}$ (yellow trace). Left: Pump power P chosen such that the normalised coupling strength $\sqrt{P \times h}$ stays constant. The peak intensity I_{pk} is reduced at larger beam waists. Right: Pump power P chosen such that the peak intensity I_{pk} stays constant over different beam waists. The coupling strength $\sqrt{P \times h}$ grows with the applied power with larger beam waists. Plot parameters are $\lambda = 532\,\mathrm{nm}$, $l = 10\,\mathrm{mm}$.
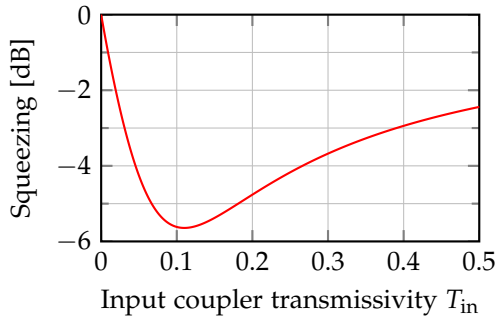
FIGURE 4.14: Measured squeezing over input coupler transmission. Plot parameters are $L = 3\%$ intracavity losses, $C = 2\sqrt{E_{\mathrm{NL}}P} = 8\%$ conversion, $\eta_{\mathrm{total}} = \eta_{\mathrm{escape}}$. The optimal input coupler transmission is $T_{\mathrm{in}} = L + C = 11\%$. Plotted from Eq. 4.70.

power, which would have damaged the crystal under the original focusing, to obtain a larger coupling strength g_{DC}.

4.3.3 CAVITY

The cavity influences squeezing via two things: First, the overall linewidth depending on input coupler transmission, length, and intracavity losses determines the pump threshold. At a given power, a smaller linewidth results in a smaller pump threshold and a larger pump parameter, which (usually) means more squeezing. Second, the ratio of input coupler to total cavity losses determines the escape efficiency – the fraction of the nonlinear state which leaves the cavity at the desired port. Both, smaller losses and higher input coupler transmission, lead to a better escape efficiency and thus more squeezing. Hence, there is a trade-off between higher input coupler transmission for better escape efficiency and lower input coupler transmission for larger pump parameter. For given losses L, an an optimal input coupler transmission T_{in} exists, which can be determined from Eq. 4.26b using the escape efficiency $\eta_{\mathrm{esc}} \approx T_{\mathrm{in}}/(T_{\mathrm{in}} + L)$ and the threshold power $P_{\mathrm{th}} = (T_{\mathrm{in}} + L)^2/4E_{\mathrm{NL}}$. Writing $P/P_{\mathrm{th}} = C^2/(T_{\mathrm{in}} + L)^2$ with C being related to the single-pass amplitude gain E_{NL}, the variance on resonance becomes

$$V^- = 1 - \frac{T_{\mathrm{in}}}{T_{\mathrm{in}} + L} \frac{4\frac{C}{T_{\mathrm{in}}+L}}{\left(1 + \frac{C}{T_{\mathrm{in}}+L}\right)^2}, \tag{4.70}$$

147

which can be minimised for T_{in} (see Fig. 4.14),

$$T_{in}^{opt} = L + C = L + 2\sqrt{E_{NL}P}, \qquad (4.71)$$

resulting in $V^- = L/(C + L)$. This is then an impedance-matched cavity with the input coupler transmission being the same as intracavity losses including conversion.

On the coupling strength, the cavity has no direct influence – except that the cavity length sets the rate at which the coupling happens. This is one over the cavity's round-trip time and equals the free spectral range, c/L_{rt}.

4.4 Measuring g_{DC}

In the previous Sec. 4.2, it was shown that the pump parameter x contains the coupling strength g_{DC}. This same pump parameter determines the classical gain of the nonlinear amplification/de-amplification process as well as the amount of initial squeezing (cf. Fig. 4.11 and 4.12). It is thus accessible with measurements of the parametric gain and with measurements of squeezing and anti-squeezing. Together with the knowledge of the cavity's linewidth, the coupling strength can be obtained from these measurements of the pump parameter x. Another method which can be used to determine the coupling strength is to retrieve the threshold power via equating the round-trip losses with the round-trip gain. The gain can be measured from second harmonic generation. All three ways to determine the coupling strength are employed in this section.

The first half entails the introduction of the experimental set-up, including the beam preparation and the generation of light at 532 nm needed for the down-conversion interaction. In the second half, the various measurements of the coupling strength g_{DC} together with a discussion of their implications for CQNC are presented.

4.4.1 Experimental set-up

A first version of this experiment in another lab was built by Maximilian Wimmer.[224] It served as a guide for the set-up presented in the following.

---

[224]Wimmer, PhD thesis (2016).
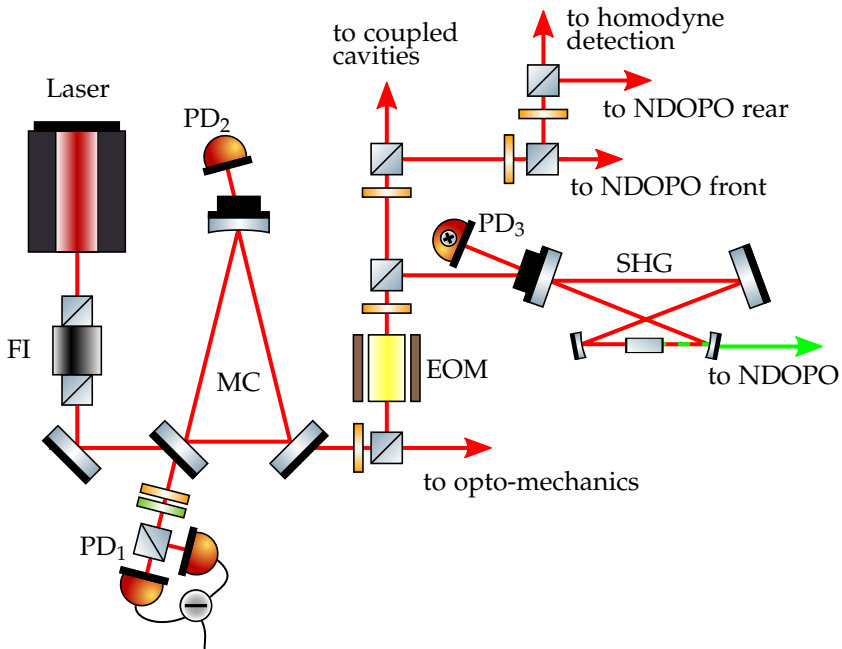
FIGURE 4.15: Set-up of beam preparation and SHG. After exiting the laser, the light passes a Faraday isolator (FI), which prevents back-reflection into the laser. The mode cleaner (MC) defines a spatial mode. The error signal for stabilisation of the MC is obtained with the photodetector PD$_1$ and sent onto a piezo-electric element behind the curved cavity mirror. Photodetector PD$_2$ monitors the locking status of the MC. Part of the light traverses the electro-optic modulator (EOM) and is fed into the second harmonic generator (SHG). With the mixing photodetector PD$_3$, an error signal for stabilising the SHG is obtained and sent onto a piezo-electric element attached to the incoupling mirror. The created green light and some of the infra-red light is sent to the non-degenerate optical parametric oscillator (NDOPO). Yellow plates are half-wave plates, green are quarter-wave plates. See also the picture of the experimental set-up in Appendix D.
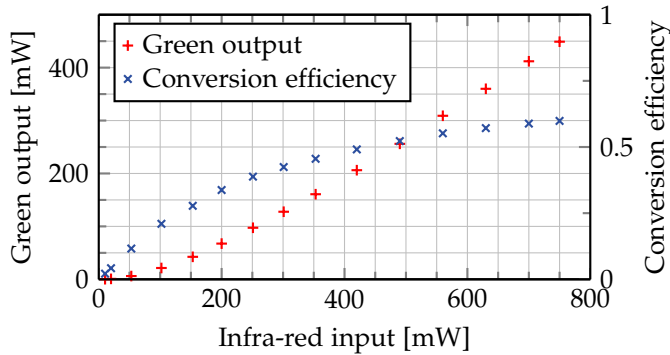
FIGURE 4.16: SHG efficiency. Generated green power and conversion efficiency over infra-red input power.

The beam preparation is depicted in Fig. 4.15. After the laser,[225] a Faraday rotator prevents back-reflection into the lasing system. The following mode cleaner defines a spatial mode with a waist of 370 μm and is locked via polarisation homodyne locking.[226] Part of its output is sent through an electro-optic modulator (EOM)[227] for phase modulation with a modulation frequency $\Omega = 2\pi \times 11.79$ MHz. Most of this light is fed into a second harmonic generator (SHG).[228] The SHG was stabilised with a Pound-Drever-Hall lock[229] using the phase-modulation side-bands generated by the EOM. It achieved a conversion from 1064 nm infra-red light into 532 nm green light with an efficiency of 60 % at an input power of 750 mW infra-red light. Its efficiency curve is shown in Fig. 4.16. The generated green light serves as pump light for the down-conversion process, which creates two-mode squeezed light.

Main part of this set-up is the non-degenerate optical parametric oscillator cavity (NDOPO). The tried-and-tested design of earlier squeezing cavities was

---

[225]Innolight (now Coherent) Mephisto, a Nd:YAG laser in a non-planar ring oscillator configuration with up to 2 W output power at 1064 nm with a linewidth of 1 kHz and shot-noise limited from some MHz, Cf. *Datasheet Mephisto*, Coherent, URL: `https://edge.coherent.com/assets/pdf/COHR%7B%5C_%7DMephisto%7B%5C_%7DDS%7B%5C_%7D0417%7B%5C_%7D2.pdf`.

[226]Cf. Sec. 1.2.3 and M. Heurs, I. R. Petersen, M. R. James and E. H. Huntington, 'Homodyne locking of a squeezer', *Opt. Lett.* **34** (2009), 2465.

[227]*Datasheet Newport 4004 Broadband Phase Modulator*, Newport, URL: `https://www.newport.com/medias/sys_master/images/images/h65/hcc/8797007839262/400X-and-406X-User-Manual-Rev-J.pdf`.

[228]Cf. Wimmer, PhD thesis (2016), Sec. 7.2.2 and Fig. 7.7.

[229]Cf. Sec. 1.2.3
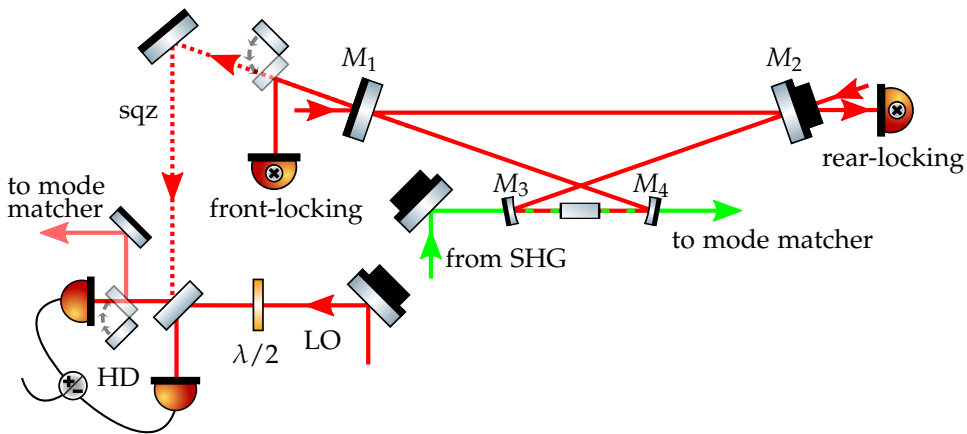
FIGURE 4.17: NDOPO set-up. Light can be coupled into the non-degenerate optical parametric oscillator (NDOPO) from the front through mirror M_1 ($R = 94.2\%$) or from the rear through mirror M_2 ($R = 99.98\%$). It is pumped with green light from the second harmonic generator (SHG). The squeezed light is detected with a homodyne detector (HD), where signal beam (sqz) and local oscillator (HD) interfere. The phases of green pump beam and LO, and the length of the NDOPO cavity can be actuated with piezo-electric elements behind the respective mirrors. See also picture of set-up in Fig. 4.20.

used.[230] Critical geometric parameters are:

- the waist $w_0 = 23\,\mu m$ inside the crystal for best conversion efficiency (cf. Boyd-Kleinman criterion in Sec. 4.2.4);

- the cavity round-trip length $L_{rt} = 1.51\,m$ determining among others the free spectral range, measured to be FSR = 199.65 MHz, and thus the measurement frequency, which is at the first free spectral range, not at DC.

Other design considerations such as the use of mirrors with an off-the-shelf radius of curvature, small angles of incidence on said mirrors for small astigmatism, and transversal mode distribution inside the cavity lead to a cavity design as depicted in Fig. 4.17.

---

[230]Wimmer, PhD thesis (2016); T. Denker, 'High-precision metrology with high-frequency nonclassical light sources', PhD thesis, Leibniz Universität Hannover, 2016.

The crystal in use[231] was made of Potassium Titanyl Phosphate (KTP) with a poling period of 458 μm to allow quasi-phase matching for two orthogonally polarised infra-red beams at 1064 nm and a green pump beam at 532 nm.[232]

The cavity has an input mirror M_1 with a measured transmission of $T_{in} \approx 5.8\%$. This transmission determines the cavity's linewidth with higher reflectivities leading to smaller linewidths and thus to a (desirable) lower threshold power. On the other hand, a higher reflectivity reduces the ratio of mirror transmission to losses inside the cavity and thus reduces the escape efficiency, leading to a trade-off between higher and lower front mirror reflectivity.[233] Its linewidth was measured to be $\kappa = 2\pi \times 2.02\,\text{MHz} \pm 2\pi \times 15\,\text{kHz}$ (Finesse $\mathcal{F} = 99$) by ramping the cavity, taking the Airy distribution in transmission of the cavity after setting the crystal temperature to minimal interaction, fitting a Lorentz function to the transmission peak, calibrating the time axis with PDH side-bands (see Fig. 4.18), and averaging over several measurements.[234] This corresponds to round-trip losses of $T_{in} + L \approx 6.2\%$, of which 5.8 % can be attributed to the input coupler, leaving $L \approx 0.4\%$ per round-trip lost to the bath. $\eta_{esc} \approx 93\%$ of the intracavity mode exits through the input coupler. The linewidth measurement is critical as it yields, together with the pump parameter x, the coupling strength g_{DC}, see Sec. 4.4.2.

When generating squeezed light, the front input coupler M_1 (cf. Fig. 4.17) cannot be used to couple light into the cavity for stabilisation because it is needed for outcoupling the squeezed light. Instead, the second flat mirror M_2 with a reflectivity of 99.98 % has to be used to lock the cavity. This poses a problem: Very little light – ca. $|t_1^2/(1 - r_1 r_2 r_1)|^2 \approx 50\,\text{ppm}$ of the incoming light (cf. Eq. 1.55) – leaks back out of that mirror to interfere with the reflected light. This leads to a very unfavourable ratio of signal to DC power and a

---

[231] For decision process regarding the crystal see Wimmer, PhD thesis (2016), Sec 4.1.2. Crystal parameters are available with the program SNLO, A. Smith, *SNLO*, URL: http://www.as-photonics.com/snlo.

[232] The infra-red beams are polarised along the crystal's *Y*- and *Z*-axes, the green beam along the crystal's *Y*-axis, direction of propagation is thus along the crystal's *X*-axis, leading to an effective nonlinear coefficient of $d_{eff} \approx 2.4\,\text{pm/V}$ (see also Eq. A.23). With single-mode squeezing, all participating beams are polarised along the same axis. Thus, the highest nonlinear coefficient, d_{33}, can be used leading to an effective nonlinearity of $d_{eff} \approx 10\,\text{pm/V}$, a lot higher than that for two-mode squeezing.

[233] Cf. Sec. 4.3.3. A smaller transmission than in earlier set-ups was chosen for lower threshold power. Cf. Wimmer, PhD thesis (2016), Sec. 7.1.1.

[234] Note that the piezo does not move linearly with the applied voltage, see Sec. 3.2.1, especially Fig. 3.7, which is why the free spectral range does not function as an accurate frequency reference.
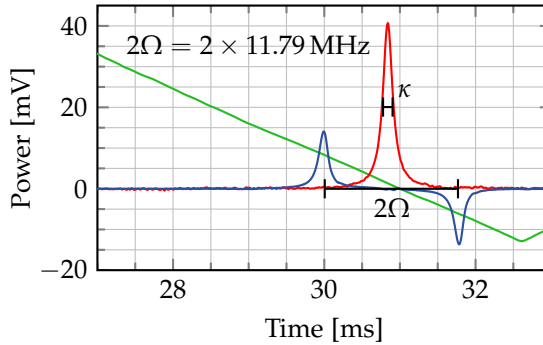
FIGURE 4.18: Linewidth measurement of the NDOPO. Red trace: Transmitted light. Blue trace: demodulated reflected (error) signal. Green trace: voltage on piezo. The demodulation phase was set such that no error signal is visible for the cavity's main resonance. Then, the side-band peaks are spaced two times the (de-)modulation frequency Ω apart. This can be used to convert time into frequency around a resonance.

small error signal: A gain of 100 at the limit of the operational amplifier's gain-bandwidth product[235] when demodulating the signal was required to obtain a usable error signal. Additionally, the demodulated signal was found to drift over timescales of some ten seconds to minutes. The drifts were a factor 5 to 20 larger than the error signal and prevented a stable cavity lock. After some time, it turned out that time-varying residual amplitude modulations caused by the EOM were the reason for this behaviour. The EOM not only modulates the phase with frequency Ω, but also slightly rotates the polarisation with the same frequency. Polarisation components such as polarising beam splitters convert the polarisation modulation in amplitude modulation, which is mixed down to DC by the mixing diode. The modulation index of the polarisation rotation turned out to be temperature-dependent. Three improvements were made to mitigate these drifts:

- A surprisingly reflective wave plate found to couple light back into the EOM and mode cleaner was turned slightly around its vertical axis to avoid reflection back along the optical path.

- The EOM was made resonant and impedance-matched to the signal-

---

[235]The op-amp used as transimpedance amplifier was a THS3201 with a gain-bandwidth product of 1.8 GHz.

153
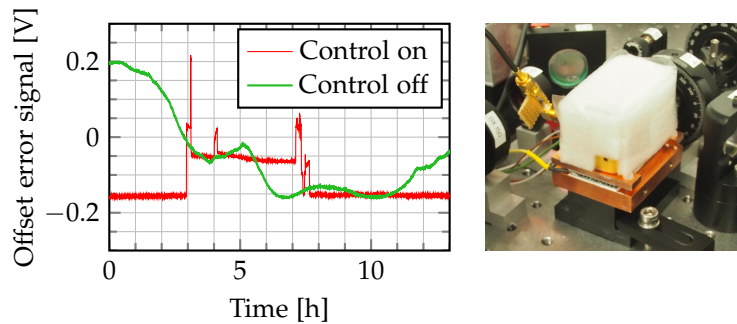
FIGURE 4.19: EOM drifts. Left: Offset of demodulated signal over two 13 h-periods, with (red) and without (green) active temperature stabilisation. Clearly visible in stabilised signal are jumps, caused by jumping DC light power and losing lock. Right: Picture of electro-optic modulator on its oven.

sending function generator by inserting an inductance and a resistance to prevent reflection off the EOM and the creation of a standing wave.

- (Most importantly) the EOM was temperature-stabilised by placing it onto a controlled oven (see Fig. 4.19).

The stabilisation and isolation of the EOM in particular is rather a work-around, inspired by Skorupka's solution.[236] Further improvement on the design was not needed at that time as can be seen in Fig. 4.19, which shows exemplary measurements of the drifts before and after installing the temperature stabilisation.

Furthermore, the stability was greatly enhanced by encasing the NDOPO in a plastic box to insulate it from acoustics and air flow, see Fig. 4.20. The latter turned out to be particularly pronounced because of the cavity's position directly in front of the flow box blowing clean air over the optical table.[237]

The front mirror M_1 was used as input coupler when characterising the cavity and when operating the NDOPO as SHG. The green light generated in the NDOPO possesses the optimal mode shape and overlaps best with the infra-red cavity mode. It serves as a mode reference for the green pump

---

[236]Cf. S. Skorupka, 'Rauschuntersuchungen an hochstabilen Lasersystemen für die wissenschaftliche Weltraummission LISA', PhD thesis, Leibniz Universität Hannover, 2007, Fig. 3.20.

[237]This was initially by design as the nonlinear cavity is the most critical part of the experiment regarding cleanliness.
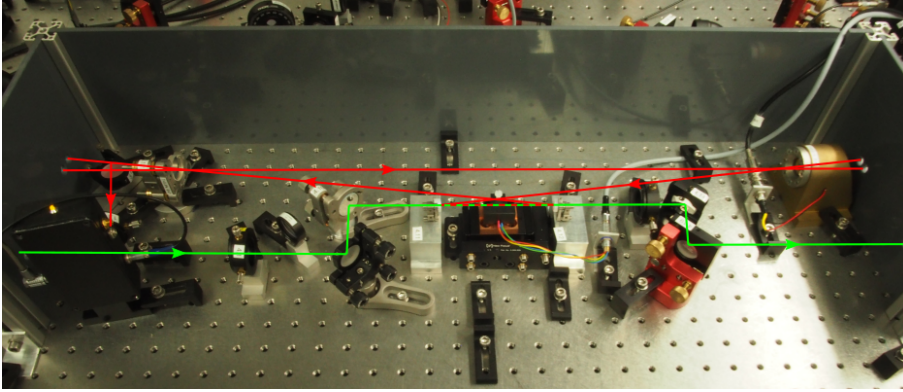
FIGURE 4.20: Picture of NDOPO as set up on the optical table. Compare with schematic in Fig. 4.17.

light needed for down-conversion: First, the green light generated inside the NDOPO via SHG is matched onto a mode reference (mode-matching) cavity. Then, the green pump light generated inside the SHG is matched to the very same cavity with optics in the beam path before the crystal. Now, the green pump light is in the same spatial mode shape as the green light generated by the NDOPO and thus in the mode shape best for nonlinear efficiency. A similar method was deployed to ensure that local oscillator for homodyne detection and the squeezed light field are in the same spatial mode for good conversion efficiency.

As noted above, the cavity itself is birefringent due to coatings and the crystal. The temperature-dependence of the crystal's refractive indices and of the crystal's length allow for tuning the cavity's optical lengths of both polarisations via temperature. With this, both modes can be made resonant at the same time. The temperature bandwidth of the phase-matching process ensures that the conversion away from the ideal phase-matching temperature is still acceptable, see Sec. 4.4.2.

The light was detected with a balanced homodyne detector.[238] In this set-up, the beam splitter turned out to be important because it introduces polarisation-dependent losses: The first beam splitter in use, made by B. Halle, was only specified for s-polarised light and reflected 50 % of it as expected, but only 20 % of p-polarised light. This leads to a beam splitter efficiency

---

[238]Wimmer, PhD thesis (2016), Sec. 7.2.5.

$\eta_{BS}^{P} \approx 0.64$ (Eq. 4.10) and is quite detrimental to the available squeezing (cf. Fig. 4.8). It was exchanged to a different beam splitter with reflectivities close to 50 % for both polarisations.[239]

4.4.2 Measurements of g_{DC}

To recap:

$$g_{DC} = \frac{\kappa}{2}x = \frac{\kappa}{2}\sqrt{\frac{P}{P_{th}}}. \tag{4.72}$$

Measurements of threshold power P_{th} and linewidth κ lead to the coupling strength g_{DC}. It can also be calculated from known material and cavity parameters: From Eqs. 4.67 and 4.65, as well as $\kappa = 2\pi \, \mathrm{FSR}/\mathcal{F} \approx c(T_{in} + L)/L_{rt}$ (cf. Eqs. 1.57 and 1.54), it follows that

$$g_{DC} = \frac{\mathrm{FSR}}{2} \times \sqrt{Kklh(\xi)P}. \tag{4.73}$$

Using, as explained in Sec. 4.4.1 above, a periodically-poled KTP crystal of length $l = 10\,\mathrm{mm}$ with an effective nonlinearity $d_{eff} \approx 2.4\,\mathrm{pm/V}$ for converting green light at 532 nm into infrared light at 1064 nm and with the refractive indices $n_1 = 1.8302$, $n_2 = 1.7458$, $n_3 = 1.7887$ from Sellmeier equations,[240] assuming optimal focussing ($h = 1.086$), a cavity with overall losses $T_{in} + L = 0.062$ leads to a pump threshold $P_{th} = 1.85\,\mathrm{W}$. The theoretical benchmark for the coupling strength at $P = 100\,\mathrm{mW}$ is thus $g_{DC} = 2\pi \times 230\,\mathrm{kHz}$.

In the following, three ways to determine the coupling strength are realised: First via the nonlinear efficiency E_{NL} and the threshold power P_{th} from single-pass second harmonic generation, second via the pump parameter x from parametric gain measurements, third via the pump parameter x from squeezing measurements.

From single pass conversion efficiency

Equating the single-pass conversion efficiency (which is the gain over one round-trip) depending on the pump power with the round-trip losses leads to

---

[239]The beam splitter was an off-the-shelf beam splitter, model BSW41-1064 by Thorlabs, with reflectivities of 50.1 % and 51.5 % for s- and p-polarised light, respectively. Then, $\eta_{BS}^{s,p} > 0.999$. This beam splitter turned out to be less sensitive to the angle of incidence than the beam splitter 10B20NP.29 by Newport.

[240]Nikogosyan (2005), p. 57 with green light polarised in Y-direction and signal and idler in Z- and Y-direction.
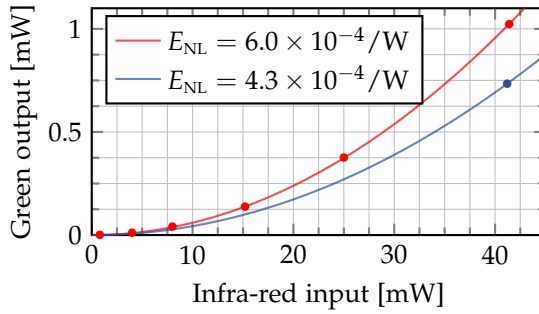
FIGURE 4.21: Single-pass conversion efficiency from SHG process in the NDOPO. Red trace: Crystal temperature set to maximum conversion. Blue trace: Crystal temperature set such that both polarisations are resonant in the cavity. Data was fitted with Eq. 4.74.

an expression for the pump threshold. The expressions for down-conversion efficiency and second harmonic generation efficiency are very similar, the nonlinear efficiency E_{NL} from second harmonic generation can also be used for the down-conversion process.[241] For single-pass second harmonic generation, E_{NL} is defined in units of W^{-1} as[242]

$$E_{NL} = \frac{P_{green}}{P_{IR}^2},\tag{4.74}$$

with P_{green} being the generated green output power and P_{IR} the infra-red input power. Then, the threshold power P_{th} for the down-conversion process can be obtained from

$$P_{th} = \frac{(T_{in} + L)^2}{4E_{NL}}.\tag{4.75}$$

For the measurement of E_{NL} from single-pass second harmonic generation, the cavity was blocked between second curved mirror M_4 and the front mirror M_1, see Fig. 4.17. Then, for different infra-red powers, the green output power was measured behind the second curved mirror M_4, which acts as a dichroic mirror. From these measurements (see Fig. 4.21), together with losses $T_{in} + L = 6.2\%$ obtained from linewidth measurements ($\kappa = 2\pi \times 2.02\,\text{MHz}$),

---

[241] Boyd and Kleinman (1968), Eq. 3.34 and paragraph thereafter, Eq. 2.22.

[242] Cf. G. Masada et al., 'Efficient generation of highly squeezed light with periodically poled MgO:LiNbO₃', *Opt. Express* **18** (2010), 13114, Tab. 1. For a microscopic definition see also Wu, Xiao and Kimble (2008), Eq. 11.
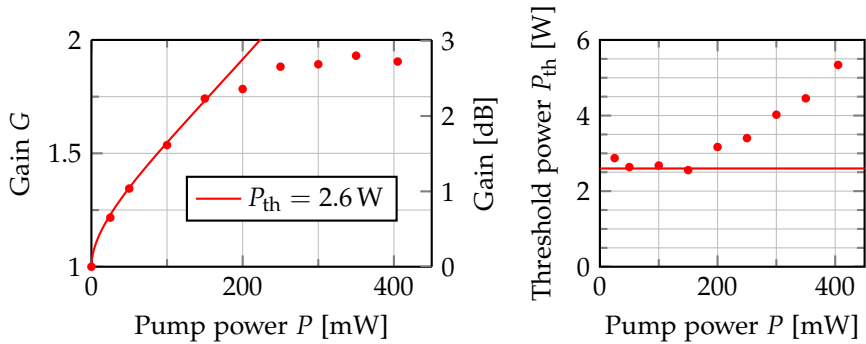
FIGURE 4.22: Gain from amplification/de-amplification measurements over pump power. Equation 4.54 was fitted to measurements with pump powers $P < 200$ mW. At higher pump powers, the pump threshold is not constant any more suggesting nonlinear losses in the system, probably caused by absorption-induced thermal lensing.

the threshold power at a temperature when both polarisations are resonant in the cavity is $P_{th} = 2.23$ W. The coupling strength for a given pump power is

$$g_{DC} = \frac{\kappa}{2}x = \frac{2\pi \times 2.02\,\text{MHz}}{2}\sqrt{\frac{P}{2.23\,\text{W}}} = 2\pi \times 215\,\text{kHz} \times \sqrt{\frac{P}{100\,\text{mW}}}. \quad (4.76)$$

This implies that even with a moderate pump power $P = 100$ mW of green light, a coupling strength g_{DC} larger than required in Sec. 2.4.1 is well possible. Further measurements suggest a higher threshold power P_{th} and thus a slightly smaller coupling strength g_{DC} (see following sections) but do not invalidate this point.

Making both polarisations resonant at optimal phase matching temperature would lead to a pump threshold of 1.9 W and a coupling strength of 232 kHz at 100 mW pump power, which is very close to the expected value given in the beginning of this Sec. 4.4.2. The difference between optimal and resonance temperature was ca. 7 °C.

FROM PARAMETRIC AMPLIFICATION/DEAMPLIFICATION

Amplification and de-amplification measurements can be used to obtain the pump parameter x at a given pump power P and thus the pump threshold P_{th}. From here, together with knowledge of losses, the coupling strength g_{DC} can

be determined. For this measurement, infra-red light was sent into the cavity through the front mirror M_1. Green light of different powers P was phase-modulated with a small modulation frequency of the order of Hz and sent into the crystal. The cavity output power changes were recorded in transmission of the rear mirror M_2. The results are displayed in Fig. 4.22. Equation 4.54 explains the measurement at lower pump powers. At higher pump powers $P \gtrsim 200\,\text{mW}$ the gain decreases, which corresponds to higher threshold powers caused by nonlinear loss. This might be due to thermal lensing degrading the mode matching and thus the effective pump power. Fitting only data points at lower powers results in a pump threshold $P_{th} = 2.6\,\text{W}$. With the same reasoning as above, this leads, together with the linewidth measurement, to a coupling strength of

$$g_{DC} = \frac{\kappa}{2}x = \frac{2\pi \times 2.02\,\text{MHz}}{2}\sqrt{\frac{P}{2.6\,\text{W}}} = 2\pi \times 198\,\text{kHz} \times \sqrt{\frac{P}{100\,\text{mW}}}. \quad (4.77)$$

Even with this lower pump threshold, the coupling strength at low pump powers, where the measurement agrees with theory, is still as big as required.

From squeezing/antisqueezing

Similar to parametric amplification, squeezing and anti-squeezing can be used to extract the pump parameter x at a given pump power P and thus the threshold power P_{th} and, again by using the linewidth κ, the coupling strength g_{DC}. This is done by measuring squeezing and anti-squeezing at different pump powers P. Most of the measurements were done with a swept pump phase and a local oscillator locked via side-fringe technique (see Sec. 1.2.2), as the lock for the pump phase was quite unstable due to very small signal (taken in transmission of the first curved mirror M_2). An exemplary squeezing measurement with swept pump phase is shown in Fig. 4.23. A squeezing spectrum obtained with both, the pump phase and the local oscillator's phase locked is shown in Fig. 4.24. This Fig. 4.24 was taken with the local oscillator not very well mode-matched to the squeezed mode, resulting in increased losses.

Fitting the measurements in Fig. 4.25, a pump threshold $P_{th} = 2.44\,\text{W}$ could be obtained. Thus, the coupling strength becomes

$$g_{DC} = \frac{\kappa}{2}x = \frac{2\pi \times 2.02\,\text{MHz}}{2}\sqrt{\frac{P}{2.44\,\text{W}}} = 2\pi \times 204\,\text{kHz} \times \sqrt{\frac{P}{100\,\text{mW}}}, \quad (4.78)$$

in agreement with the previously presented measurements.
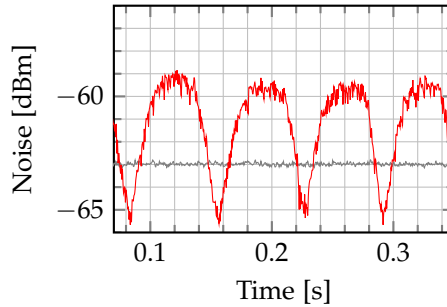
FIGURE 4.23: Squeezing spectrum with swept pump phase. Red trace is noise power of signal beam, black trace is shot noise. Here, a pump power $P = 390\,\mathrm{mW}$ results in up to 2.3 dB squeezing and 3.7 dB anti-squeezing, corresponding to an initial squeezing of 5.1 dB, a pump parameter $x = 0.29$, a total efficiency $\eta = 59\,\%$ and a threshold power $P_{\mathrm{th}} = 4.7\,\mathrm{W}$. RBW 300 kHz, VBW 200 Hz.
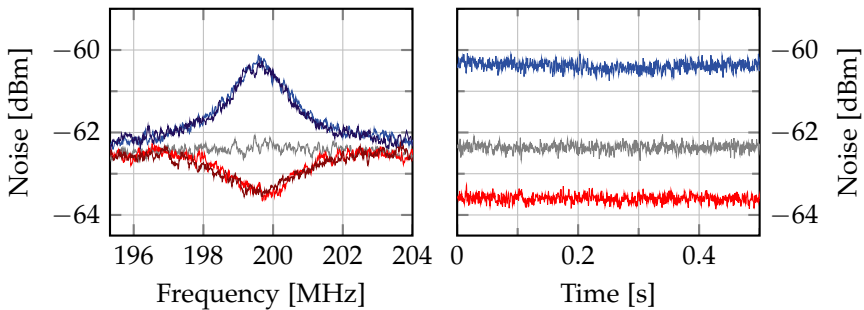
FIGURE 4.24: Squeezing measurement with both, pump and local oscillator phases locked. Left: Squeezing and anti-squeezing around the first FSR. Right: Squeezing and anti-squeezing at the first FSR over time. Measurements show 1.24 dB squeezing and 2.03 dB anti-squeezing, corresponding (in the single-mode case) to initial squeezing of 3.8 dB, a pump parameter $x = 0.22$, threshold power $P_{\mathrm{th}} = 3.7\,\mathrm{W}$ and overall efficiency $\eta = 0.43$. Both spectra are taken with both, pump phase and local oscillator locked (pump phase locked on de-amplification for squeezing and on amplification for anti-squeezing, local oscillator locked on mid-fringe). Pump power was 170 mW. RBW 300 kHz, VBW 300 Hz for both. All traces were averaged over two sweeps. In the left plot, two traces are displayed for each, squeezing and anti-squeezing.
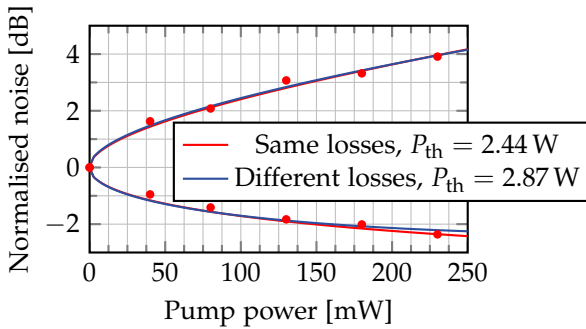
FIGURE 4.25: Squeezing and anti-squeezing at different pump powers. The data was fitted assuming same losses for both modes, which corresponds to the single-mode case (Eqs. 4.29 and 4.51), and assuming different losses for the two modes (Eq. 4.50). Fit results of efficiencies were $\eta = 0.58$ for same losses and $\eta_a = 1$, $\eta_c = 0.42$ for different losses. The single-mode case fits to other measurements presented in this chapter regarding threshold power and efficiency. In case of different losses, the best fit was reached assuming one lossless and one lossy mode, which is not realistic. Fixing one of the efficiencies to a value between 0.58 and 1 leads to threshold powers between those obtained from the two fits above and efficiencies between 0.58 and 0.42.

Discussion

Contrary to earlier belief,[243] the coupling strength realised with this set-up is measured to lie indeed in the expected range of 150 kHz. All three ways to determine the threshold power P_{th}[244] and with it the coupling strengths g_{DC} were done independently from each other and conducted days to months apart. This explains variations, still they agree rather well and are compatible with the theoretically expected value. The higher threshold power obtained from amplification/de-amplification measurements and from squeezing/anti-squeezing measurements could be explained by non-optimal mode matching of pump beam to infra-red beam – this mode-matching is not needed when measuring the single-pass second harmonic generation gain E_{NL}.

Both, amplification/de-amplification and squeezing measurements, show some instabilities at higher pump powers. This might be due to pump beam alignment, thermal lensing and/or phase noise. Assuming that these instabilities can be controlled in the future,[245] pump powers of up to 400 mW just below the damage threshold could result in a coupling strength of more than 400 kHz.

Making the cavity resonant for both polarisations at the crystal's optimal phase matching temperature can bring the pump threshold down to 1.9 W and thus the coupling strength up to more than 450 kHz – a factor three above the initial requirements.

For even higher coupling strengths, either the beam shapes can be changed as to use even more pump power, cf. Fig. 4.13, or other wavelengths, materials, or phase-matching processes need to be used. A different beam shape and a larger region of high intensity might additionally mitigate thermal lensing problems. KTP allows for non-critical (temperature) phase matching at a wavelength of 1080 nm, which would improve the effective nonlinear coefficient d_{eff} and thus the coupling strength by a factor of $\pi/2$ compared to quasi-phase-matching.

---

[243] Wimmer, PhD thesis (2016), pp. 98, 112.

[244] Note that two of them rely on the fact that the here presented two-mode squeezing experiment can equally be described as a single-mode squeezing experiment because to a good approximation nothing in the experiment distinguishes between the two polarisation modes.

[245] A possible ansatz regarding alignment and phase noise would be to use a cavity resonant also for the pump beam. This comes at the cost of needing a triply resonant cavity, which is a lot more difficult to realise.

Works referenced in the preceding chapter

Andersen, U. L., T. Gehring, C. Marquardt and G. Leuchs, '30 Years of Squeezed Light Generation', *Phys. Scr.* **91** (2016), 053001, DOI: 10.1088/0031-8949/91/5/053001, arXiv: 1511.03250.

Aoki, T., G. Takahashi and A. Furusawa, 'Squeezing at 946nm with periodically poled KTiOPO$_4$', *Opt. Express* **14** (2006), 6930, DOI: 10.1364/oe.14.006930.

Bachor, H.-A. and T. C. Ralph, *A Guide to Experiments in Quantum Optics*, Weinheim: Wiley, 2004, DOI: 10.1002/9783527619238.

Bauchrowitz, J., T. Westphal and R. Schnabel, 'A graphical description of optical parametric generation of squeezed states of light', *Am. J. Phys.* **81** (2013), 767–771, DOI: 10.1119/1.4819195.

Bloembergen, N., 'Conservation laws in nonlinear optics', *J. Opt. Soc. Am.* **70** (1980), 1429, DOI: 10.1364/JOSA.70.001429.

Boyd, G. D. and D. A. Kleinman, 'Parametric interaction of focused Gaussian light beams', *J. Appl. Phys.* **39** (1968), 3597–3639, DOI: 10.1063/1.1656831.

Boyd, R. W., *Nonlinear Optics*, Amsterdam et al.: Acad. Press, 2008.

Braunstein, L. S. and P. Van Loock, 'Quantum information with continuous variables', *Rev. Mod. Phys.* **77** (2005), 513–577, DOI: 10.1103/RevModPhys.77.513.

Chelkowski, S., 'Squeezed light and laser interferometric gravitational wave detectors', PhD thesis, Leibniz Universität Hannover, 2007, URL: https://edocs.tib.eu/files/e01dh07/537859527.pdf.

Collett, M. J. and C. W. Gardiner, 'Squeezing of intracavity and traveling-wave light fields produced in parametric amplification', *Phys. Rev. A* **30** (1984), 1386–1391, DOI: 10.1103/PhysRevA.30.1386.

Collett, M. J. and D. F. Walls, 'Squeezing spectra for nonlinear optical systems', *Phys. Rev. A* **32** (1985), 2887–2892, DOI: 10.1103/PhysRevA.32.2887.

D'Auria, V., S. Fornaro, A. Porzio, S. Solimeno, S. Olivares and M. G. A. Paris, 'Full characterization of Gaussian bipartite entangled states by a single homodyne detector', *Phys. Rev. Lett.* **102** (2009), DOI: 10.1103/PhysRevLett.102.020502, arXiv: 0805.1993.

D'Auria, V., A. Porzio, S. Solimeno, S. Olivares and M. G. Paris, 'Characterization of bipartite states using a single homodyne detector', *J. Opt. B* **7** (2005), S750–S753, DOI: 10.1088/1464-4266/7/12/044, arXiv: 0509180 [quant-ph] .

Datasheet Mephisto, Coherent, URL: https://edge.coherent.com/assets/pdf/COHR%7B%5C_%7DMephisto%7B%5C_%7DDS%7B%5C_%7D0417%7B%5C_%7D2.pdf.

Datasheet Newport 4004 Broadband Phase Modulator, Newport, URL: https://www.newport.com/medias/sys_master/images/images/h65/hcc/8797007839262/400X-and-406X-User-Manual-Rev-J.pdf.

Denker, T., 'High-precision metrology with high-frequency nonclassical light sources', PhD thesis, Leibniz Universität Hannover, 2016, URL: http://edok01.tib.uni-hannover.de/edoks/e01dh16/862559057.pdf.

Einstein, A., B. Podolsky and N. Rosen, 'Can Quantum-Mechanical Description of Physical Reality Be Considered Complete?', *Phys. Rev.* **47** (1935), 777–780, DOI: 10.1103/PhysRev.47.777.

Gardiner, C. W. and P. Zoller, *Quantum noise : a handbook of Markovian and non-Markovian quantum stochastic methods with applications to quantum optics*, Berlin et al.: Springer, 2000.

Gerry, C. C. and P. L. Knight, *Introductory Quantum Optics*, Cambridge et al.: Cambridge University Press, 2005.

Guha, S., 'Focusing dependence of the efficiency of a singly resonant optical parametric oscillator', *Appl. Phys. B* **66** (1998), 663–675, DOI: 10.1007/s003400050453.

Guha, S., F. J. Wu and J. Falk, 'The Effects of Focusing on Parametric Oscillation', *IEEE J. Quantum Electron.* **18** (1982), 907–912, DOI: 10.1109/JQE.1982.1071624.

Heurs, M., I. R. Petersen, M. R. James and E. H. Huntington, 'Homodyne locking of a squeezer', *Opt. Lett.* **34** (2009), 2465, DOI: 10.1364/OL.34.002465, arXiv: 0907.3323.

Lastzka, N., 'Numerical modelling of classical and quantum effects in non-linear optical systems', PhD thesis, Leibniz Universität Hannover, 2010, URL: http://edok01.tib.uni-hannover.de/edoks/e01dh11/643368353.pdf.

Louisell, W. H., A. Yariv and A. E. Siegman, 'Quantum fluctuations and noise in parametric processes. I.', *Phys. Rev.* **124** (1961), 1646–1654, DOI: 10.1103/PhysRev.124.1646.

Masada, G., T. Suzudo, Y. Satoh, H. Ishizuki, T. Taira and A. Furusawa, 'Efficient generation of highly squeezed light with periodically poled MgO:LiNbO$_3$', *Opt. Express* **18** (2010), 13114, DOI: 10.1364/OE.18.013114.

Milburn, G. and D. Walls, 'Production of squeezed states in a degenerate parametric amplifier', *Opt. Commun.* **39** (1981), 401–404, DOI: 10.1016/0030-4018(81)90232-7.

Nikogosyan, D. N., *Nonlinear Optical Crystals: A Complete Survey*, New York: Springer, 2005, DOI: 10.1007/b138685, URL: http://link.springer.com/10.1007/b138685.

Ou, Z. Y., S. F. Pereira and H. J. Kimble, 'Realization of the Einstein-Podolsky-Rosen paradox for continuous variables in nondegenerate parametric amplification', *Appl. Phys. B* **55** (1992), 265–278, DOI: 10.1007/BF00325015.

Schnabel, R., 'Squeezed states of light and their applications in laser interferometers', *Phys. Rep.* **684** (2017), 1–51, DOI: 10.1016/j.physrep.2017.04.001, arXiv: 1611.03986.

Schori, C., J. L. Sørensen and E. S. Polzik, 'Narrow-band frequency tunable light source of continuous quadrature entanglement', *Phys. Rev. A* **66** (2002), 10, DOI: 10.1103/PhysRevA.66.033802, arXiv: 0205015 [quant-ph].

Skorupka, S., 'Rauschuntersuchungen an hochstabilen Lasersystemen für die wissenschaftliche Weltraummission LISA', PhD thesis, Leibniz Universität Hannover, 2007, URL: https://edocs.tib.eu/files/e01dh07/551342838.pdf.

Smith, A., *SNLO*, URL: http://www.as-photonics.com/snlo.

Vahlbruch, H., M. Mehmet, K. Danzmann and R. Schnabel, 'Detection of 15 dB Squeezed States of Light and their Application for the Absolute Calibration of Photoelectric Quantum Efficiency', *Phys. Rev. Lett.* **117** (2016), 110801, DOI: 10.1103/PhysRevLett.117.110801.

Walls, D. F. and G. J. Milburn, *Quantum Optics*, Berlin, Heidelberg: Springer, 2008, DOI: 10.1007/978-3-540-28574-8.

Wimmer, M. H., 'Coupled nonclassical systems for coherent backaction noise cancellation', PhD thesis, Leibniz Universität Hannover, 2016, URL: http://edok01.tib.uni-hannover.de/edoks/e01dh16/863136931.pdf.

Wimmer, M. H., D. Steinmeyer, K. Hammerer and M. Heurs, 'Coherent cancellation of backaction noise in optomechanical force measurements', *Phys. Rev. A* **89** (2014), 053836, DOI: 10.1103/PhysRevA.89.053836, arXiv: 1403.2992.

Wu, L.-A., M. Xiao and H. J. Kimble, 'Squeezed states of light from an optical parametric oscillator', *J. Opt. Soc. Am. B* **4** (2008), 1465, DOI: 10.1364/josab.4.001465, URL: https://authors.library.caltech.edu/4725/1/WULjosab87.pdf.

Yariv, A., *Quantum Electronics*, New York et al., 1989.

Zhang, T. C., K. W. Goh, C. W. Chou, P. Lodahl and H. J. Kimble, 'Quantum teleportation of light beams', *Phys. Rev. A* **67** (2003), 16, DOI: 10.1103/PhysRevA.67.033802, arXiv: 0207076 [quant-ph] .

Zondy, J.-J., D. Touahri and O. Acef, 'Absolute value of the d_{36} nonlinear coefficient of AgGaS$_2$: prospect for a low-threshold doubly resonant oscillator-based 3:1 frequency divider', *J. Opt. Soc. Am. B* **14** (2008), 2481, DOI: 10.1364/josab.14.002481.

<div align="right">

5

</div>

<div align="center">

Coupled cavities and
beam-splitterlike interaction

</div>

At the heart of all-optical CQNC lies an optical cavity realising the negative-mass harmonic oscillator, the *ancilla* cavity. The ancilla cavity will be coupled to the incoming light via a down-conversion and a beam-splitter process. Another cavity will be built around the ancilla cavity to enhance the coupling interactions. This chapter deals with the effects of coupling the two cavities with a beam-splitterlike process. Section 5.1 shows how two coupled cavities influence each other. Here, they are modelled as two coupled harmonic oscillators showing effects known from coupled mode theory.[246] Section 5.2 shows how a wave plate is equivalent to a beam splitter and can be utilised to couple two modes in a beam-splitterlike fashion. Section 5.3 presents an experiment realising beam-splitter coupling with a wave plate. The theoretical model from Sec. 5.1.2 accurately describes the two coupled cavities, and the beam-splitter coupling strength required for all-optical CQNC as in Sec. 2.4.1 can be realised with a wave plate.

Parts of the assembly and of the measurements were done together with Elisabeth von Känel.[247]

5.1 Coupled cavities

This section explores coupled optical cavities without specifying the concrete realisation of the coupling interaction. First, the difficulties when trying to stabilise coupled cavities are explained phenomenologically and approaches

---

[246]Cf. H. Haus and W. Huang, 'Coupled-mode theory', *Proc. IEEE* **79** (1991), 1505–1518.
[247]E. von Känel, *To be published*, Master thesis, Leibniz Universität Hannover.
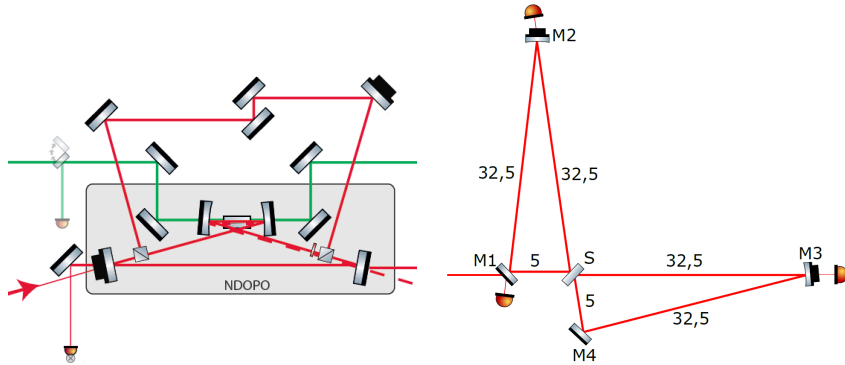
FIGURE 5.1: Previously realised coupled-cavity set-ups. Left: Cavities coupled via a wave plate, figure from Wimmer, PhD thesis (2016), p. 99. Right: Cavities coupled via a beam splitter, figure from Weißbrich, Master thesis (2017), p. 55.

to solve the difficulties are presented. Then, the Hamiltonian formalism is used to derive effects caused by coupling two cavity modes to each other.

5.1.1 Stabilisation issues with coupled cavities

When coupled cavities were first set up within this group as in the schemes shown in Fig. 5.1, they proved difficult to stabilise.[248] In hindsight, this makes sense because the two cavities are not independent of one another due to their coupling. The second cavity can be viewed as a compound mirror for the first cavity.[249] The reflection coefficient of this compound mirror is frequency-dependent and complex. It is a function of the detuning and the impedance matching of the second cavity. Whenever the length of this second cavity changes, the light inside the first cavity reflected from the compound mirror, which represents the second cavity, experiences a phase change, which in turn changes the resonance condition of the first cavity. A change in the error

---

[248]M. H. Wimmer, 'Coupled nonclassical systems for coherent backaction noise cancellation', PhD thesis, Leibniz Universität Hannover, 2016; H. Weißbrich, 'Untersuchungen zur Frequenzstabilisierung gekoppelter optischer Resonatoren', Master thesis, Leibniz Universität Hannover, 2017.

[249]A. Thüring, R. Schnabel, H. Lück and K. Danzmann, 'Detuned Twin-Signal-Recycling for ultrahigh-precision interferometers', *Opt. Lett.* **32** (2007), 985; A. Thüring, 'Investigations of coupled and Kerr non-linear optical resonators', PhD thesis, Leibniz Universität Hannover, 2009; Wimmer, PhD thesis (2016); Weißbrich, Master thesis (2017).

signal of one cavity cannot be attributed to a phase change in said cavity but could also be caused by the other cavity.

While this view is more general and somewhat more correct,[250] another, more abstract way of looking at it yields further understanding of the observed effects. The two coupled cavities can be described as two coupled harmonic oscillators, cf. Sec. 1.1. If the coupling between two harmonic oscillators is strong enough, they *hybridise* and can not be seen as two individual systems any more, but as one new system. The resonances of the new system as well as their linewidths are different from the resonance frequencies of the single (sub-)systems and their respective linewidths. Common in different fields in physics, e.g. opto-mechanics,[251] atomic physics,[252] classical mechanics,[253] this approach is used to calculate coupling effects in the following Sec. 5.1.2. It is compared to a transfer-matrix description closer to the experiment in Sec. 5.2.2.

The question still remains how the two coupled cavities can be stabilised. There are three options, explained in the following paragraphs.

Make cavities distinguishable.   The two main characteristics of a cavity seen as a harmonic oscillator are its resonance frequency and its linewidth. The resonance frequency is the parameter to be controlled, leaving the linewidth to distinguish between the two cavities. If the linewidths are different, suitable side-bands for a Pound-Drever-Hall lock are reflected off the cavity with smaller linewidth, but enter the cavity with bigger linewidth. Demodulation of the beat signal delivers an error signal only for one cavity, which can be stabilised first. Once this cavity is stably locked, the other one can also be locked. The stabilisation scheme of coupled cavities in the aLIGO detectors makes use of their difference in linewidths.[254] This does not work if the linewidths of the two cavities are similar, as was the case in the schemes previously tried in this group, see Fig. 5.1. If the cavities are travelling wave

---

[250]It does not rely on the single-mode approximation made when using the Hamiltonian formalism, cf. also Sec. 5.2.2.

[251]S. Gröblacher, K. Hammerer, M. R. Vanner and M. Aspelmeyer, 'Observation of strong coupling between a micromechanical resonator and an optical cavity field', *Nature* **460** (2009), 724–727.

[252]R. J. Thompson, G. Rempe and H. J. Kimble, 'Observation of normal-mode splitting for an atom in an optical cavity', *Phys. Rev. Lett.* **68** (1992), 1132–1135.

[253]L. Novotny, 'Strong coupling, energy splitting, and level crossings: A classical perspective', *Am. J. Phys.* **78** (2010), 1199–1202.

[254]A. Staley et al., 'Achieving resonance in the Advanced LIGO gravitational-wave interferometer', *Class. Quantum Gravity* **31** (2014), 245010.

resonators, they can be made different by inserting an optical diode (e.g., a Faraday rotator) into one cavity and use counter-propagating locking beams. This comes, however, at the cost of introducing additional losses. Another option also used in the aLIGO detectors[255] is to make one cavity resonant for light of a different colour. This approach requires optical coatings for multiple wavelengths and an additional light source.

KNOW SYSTEM DYNAMICS.   Coupled cavities have two degrees of freedom – the phase (or length or detuning) of cavity one and the phase of cavity two. These are the quantities to be stabilised. It should in principle be possible to gather enough information from two independent measurements to trace back which of the two phases changed, and correct for that change. This might be done with measurements of amplitudes and phases of the outgoing beams. If the system can be modelled well enough, a change in the measurements can be attributed to a change in either cavity one or cavity two. The challenge of this approach lies in the quality of the model and the quality and amount of data. As much as four homodyne detectors measuring amplitudes and phases of two outgoing beams might be necessary for a reliable state estimation.

USE TWO CAVITIES IN ONE.   Another option is to simplify the set-up, a solution in anticipation of Sec. 5.2's results: If a wave plate is used as a beam splitter, and there is no need to spatially separate the two coupled modes, they can use the same beam path and the same set of mirrors. As a result, occurring phase changes caused by environmental disturbances always affect both modes equally. Additionally, only one beam path needs to be stabilised instead of two. None of the disadvantages of the other two options applies here. Instead, this approach simplifies the set-up. Its successful implementation is shown in Sec. 5.3.

5.1.2 THEORETICAL DESCRIPTION OF COUPLED CAVITIES

A system of two coupled harmonic oscillators with modes $\hat{a}$ and $\hat{c}$ can be described using the Hamiltonian formalism as introduced in Sec. 2.3. With resonance frequencies ω_a and ω_c detuned from a reference frequency ω_0 such that $\Delta_a = \omega_0 - \omega_a$ and $\Delta_c = \omega_0 - \omega_c$, the Hamiltonian $\hat{H}_{sys}$ in a frame

---

[255]Staley et al. (2014).

rotating with ω_0 is

$$\hat{H}_{\text{sys}} = \Delta_a \hat{a}^\dagger \hat{a} + \Delta_c \hat{c}^\dagger \hat{c} - g_{\text{BS}}(\hat{a}^\dagger \hat{c} + \hat{a}\hat{c}^\dagger) \tag{5.1}$$

with a coupling strength g_{BS} coupling the $\hat{a}$ and $\hat{c}$. The Hamiltonian, together with damping and driving terms quantified by the linewidths κ_a and κ_c, gives rise to the coupled equations of motion

$$\dot{a} = -\frac{\kappa_a}{2}a - i\Delta_a a + ig_{\text{BS}}c + \sqrt{\kappa_a}a_{\text{in}}, \tag{5.2a}$$

$$\dot{c} = -\frac{\kappa_c}{2}c - i\Delta_c c + ig_{\text{BS}}a + \sqrt{\kappa_c}c_{\text{in}}, \tag{5.2b}$$

or, in matrix form,

$$\dot{\mathbf{a}} = \begin{pmatrix} -\kappa_a/2 - i\Delta_a & ig_{\text{BS}} \\ ig_{\text{BS}} & -\kappa_c/2 - i\Delta_c \end{pmatrix} \mathbf{a} + K_{\text{in}}\mathbf{a}_{\text{in}},$$

$$\mathbf{a} = \begin{pmatrix} a \\ c \end{pmatrix}, \qquad \mathbf{a}_{\text{in}} = \begin{pmatrix} a_{\text{in}} \\ c_{\text{in}} \end{pmatrix}, \qquad K_{\text{in}} = \text{diag}(\sqrt{\kappa_a}, \sqrt{\kappa_c}), \tag{5.3}$$

where, taking the classical limit, hats are omitted.

This system can easily be diagonalised (discarding the driving terms), with eigenvalues $\lambda_\pm$ and eigenvectors $d_\pm$

$$\lambda_\pm = -\kappa_+/2 - i\left(\Delta_+ \pm \sqrt{g_{\text{BS}}^2 + (\Delta_- - i\kappa_-/2)^2}\right), \tag{5.4}$$

$$d_\pm = \frac{-\Delta_- + i\kappa_-/2 \pm \sqrt{g_{\text{BS}}^2 + (\Delta_- - i\kappa_-/2)^2}}{g_{\text{BS}}}a + c, \tag{5.5}$$

with

$$\kappa_\pm = \frac{\kappa_a \pm \kappa_c}{2}, \qquad \Delta_\pm = \frac{\Delta_a \pm \Delta_c}{2}, \tag{5.6}$$

such that

$$\dot{\mathbf{d}} = \begin{pmatrix} \lambda_+ & 0 \\ 0 & \lambda_- \end{pmatrix} \mathbf{d} \quad \text{with} \quad \mathbf{d} = \begin{pmatrix} d_+ \\ d_- \end{pmatrix}. \tag{5.7}$$

The diagonalised equations of motion are easily solved, $d_\pm(t) = d_{0\pm} \exp \lambda_\pm t$.

Effects typical for coupled oscillators can be seen in Eqs. 5.4 and 5.5: The new eigenmodes, also called *normal modes*[256] are superpositions of the modes

---

[256]See, e.g., Haus and Huang (1991), another term, especially in the context of exceptional points, is *super modes*.
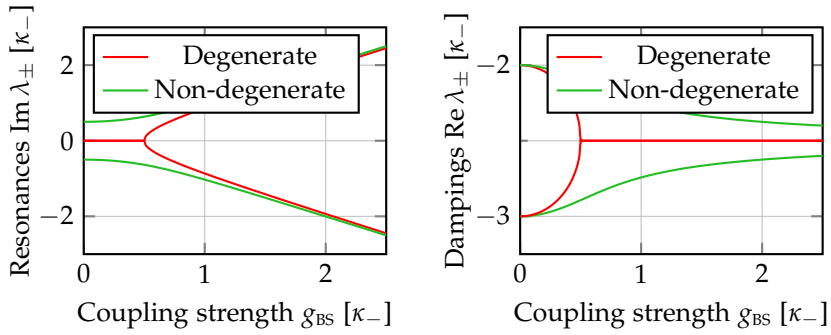
FIGURE 5.2: Normal-mode splitting and effective linewidths. Left: Coupling the modes shifts the resonance frequencies $\mathrm{Im}\,\lambda_\pm$ of the coupled system, leading to a splitting of degenerate modes. Right: Whereas the resonances split, the coupling causes the dampings $\mathrm{Re}\,\lambda_\pm$ to synthesise. Plotted from Eq. 5.4.

of the uncoupled systems. The new resonance frequencies $\mathrm{Im}\,\lambda_\pm$ depend on the uncoupled resonance frequencies ω_i and Δ_i, respectively, on the coupling strength g_{BS}, and on the difference of uncoupled linewidths κ_-. The damping of the new modes has become $\mathrm{Re}\,\lambda_\pm$. The coupling effects are strongest in the degenerate case $\Delta_- = 0$.

$\lambda_\pm$ warrants more attention as it contains normal-mode resonance frequencies and dampings. With strong enough coupling, a phenomenon called *normal-mode splitting* occurs. Starting with degenerate modes, $\omega_{\mathrm{a}} = \omega_{\mathrm{c}}$, the coupling causes energy shifts and the normal mode resonances become non-degenerate, as can be seen in Fig. 5.2. The splitting distance $\delta\omega$ is two times the coupling strength g_{BS} in the limit of strong coupling or when the linewidths are equal ($\kappa_- = 0$). In the decoupled system, it was possible to change the detuning of one mode to match its resonance frequency to the other mode's resonance (see dashed lines in Fig. 5.3). With coupling, the crossing of resonances is *avoided*. The system cannot be made degenerate any more by changing the relative detuning Δ_-, see again Fig. 5.3.

The minimum splitting $\delta\omega$ can be found by trying to minimise $\delta\omega^2 = (\mathrm{Im}\,\lambda_+ - \mathrm{Im}\,\lambda_-)^2$ over the relative detuning Δ_-, which is the same as minim-
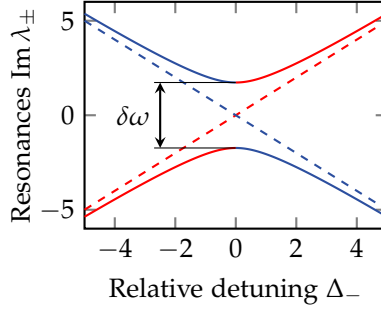
Figure 5.3: Avoided crossing. With strongly coupled modes, their resonances cannot be made degenerate any more, the minimum splitting distance is $\delta\omega$. For an experimental demonstration, see Fig. 5.15. Plotted from Eq. 5.4.

ising $\left[\text{Re}\,\sqrt{g_{\text{BS}}^2 + (\Delta_- - i\kappa_-/2)^2}\right]^2$:

$$
\left[\text{Re}\,\sqrt{g_{\text{BS}}^2 + (\Delta_- - i\kappa_-/2)^2}\right]^2
$$
$$
= \tfrac{1}{4}\left(\sqrt{g_{\text{BS}}^2 - \kappa_-^2/4 + \Delta_-^2 - i\Delta_-\kappa_-} + \sqrt{g_{\text{BS}}^2 - \kappa_-^2/4 + \Delta_-^2 + i\Delta_-\kappa_-}\right)^2
$$
$$
= \tfrac{1}{2}\left(g_{\text{BS}}^2 - \kappa_-^2/4 + \Delta_-^2\right) + \tfrac{1}{2}\sqrt{(g_{\text{BS}}^2 - \kappa_-^2/4 + \Delta_-^2)^2 + \Delta_-^2\kappa_-^2}. \tag{5.8}
$$

The expression is positive. For $g_{\text{BS}}^2 - \kappa_-^2/4 > 0$ it becomes minimal for $\Delta_- = 0$. For $g_{\text{BS}}^2 - \kappa_-^2/4 \leq 0$ it becomes zero if $\Delta_- = 0$.

The minimum distance of the resonance frequencies is given by

$$
\delta\omega = 2\sqrt{g_{\text{BS}}^2 - \kappa_-^2/4} = 2\sqrt{g_{\text{BS}}^2 - (\kappa_{\text{a}} - \kappa_{\text{c}})^2/16} \tag{5.9}
$$

for $|g_{\text{BS}}| > |\kappa_-/2|$ and zero for $|g_{\text{BS}}| \leq |\kappa_-/2|$. In an experiment, where the resonance frequencies can be tuned with respect to each other, $\Delta_- = 0$ is reached when the normal-mode splitting is minimal. This is an important indicator to find the degenerate point $\Delta_- = 0$.

Similar arguments as for the imaginary part hold for the real part of the eigenvalues, the damping:

$$
\text{Re}\,\lambda_\pm = -\kappa_+/2 \pm \text{Im}\,\sqrt{g_{\text{BS}}^2 + (\Delta_- - i\kappa_-/2)^2}. \tag{5.10}
$$
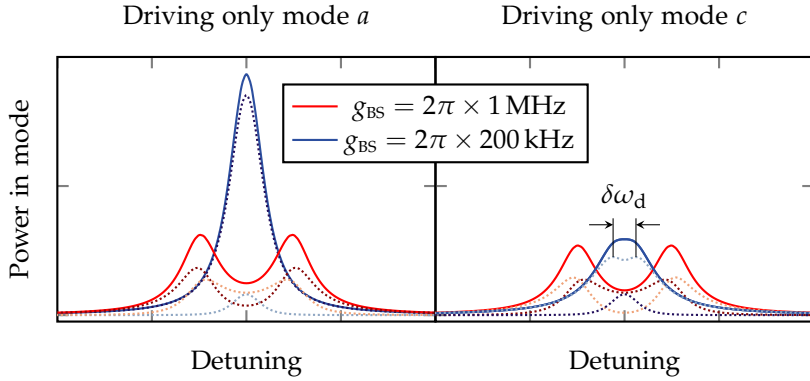
FIGURE 5.4: Normal modes decomposed into original components. The total intracavity power $|\mathbf{a}|^2$ is represented by solid lines and equal to the sum of dotted lines, $|a|^2 + |c|^2$, where the dark dotted lines are $|a|^2$ and the light dotted lines are $|c|^2$. In the limit of strong coupling (red), it does not matter whether one or the other mode is driven. Driving the smaller linewidth mode (mode a) results in higher intracavity power in the case of smaller coupling (compare blue solid lines in left and right plot). Also for smaller coupling, a splitting can be observed in one of the modes even if normal-mode splitting does not occur, see right plot and Fig. 5.5. Plotted from Eq. 5.11, plot parameters are: $\kappa_a = 2\pi \times 650\,\text{kHz}$, $\kappa_c = 2\pi \times 1.3\,\text{MHz}$, $\Delta_a = \Delta_c$. It follows that $\delta\omega_d = 2\pi \times 484\,\text{kHz}$ for $g_{BS} = 2\pi \times 200\,\text{kHz}$.

The normal-mode linewidths converge towards higher coupling strengths. Their difference is minimal when $\Delta_- = 0$ and given by $2\sqrt{g_{BS}^2 - \kappa_-^2/4}$ at $\Delta_- = 0$. It becomes zero for $\kappa_-^2/4 < g_{BS}^2$.

Now, the the cavity output spectrum, obtained by solving the equations of motion including the driving fields, Eq. 5.3, can be studied. In an experiment, this would be accomplished by photodetection in transmission of the coupled cavities, see Sec. 5.3 and Fig. 5.12. In Fourier space, the solution for the intracavity field $\mathbf{a}$ is

$$\mathbf{a} = i\left[g_{BS}^2 - (\omega + \Delta_a - i\kappa_a/2)(\omega + \Delta_c - i\kappa_c/2)\right]^{-1}$$
$$\times \begin{pmatrix} \omega + \Delta_c - i\kappa_c/2 & g_{BS} \\ g_{BS} & \omega + \Delta_a - i\kappa_a/2 \end{pmatrix} \begin{pmatrix} \sqrt{\kappa_a}a_{in} \\ \sqrt{\kappa_c}c_{in} \end{pmatrix}. \qquad (5.11)$$

The absolute squared of the intracavity field $\mathbf{a}$ is proportional to the intracavity

power.

Two coupled damped and driven harmonic oscillators show peculiar behaviour which depends on driving details. For example, if driven with a suitable combination of input modes, it is possible to excite only one of the normal modes. As the other is not excited at all, normal mode splitting cannot be observed. To obtain simple and experimentally verifiable expressions, two assumptions are made. First, only one of the system modes is driven. Second, the system is tuned to minimum splitting, where Δ_- is zero.[257]

Taking only one of $\mathbf{a}$'s entries means a decomposition of the normal modes back into their original components a and c. The total intracavity power, $|\mathbf{a}|^2$, and the powers in the two parts, $|a|^2$ and $|c|^2$, are plotted in Fig. 5.4 for different coupling strengths g_{BS}. Peaks in the decomposed spectrum do not necessarily coincide with normal mode resonances. This is especially true for small coupling strengths close to the difference in linewidth. In fact, if only the mode with bigger linewidth (here, mode c) is driven, a splitting can be resolved in this mode even if the normal mode splitting cannot be observed due to the not sufficient coupling strength. Conversely, the splitting in the mode with smaller linewidth (here, mode a) is smaller than the normal-mode splitting. The different splittings can be expressed as follows, where only one of the original modes, here chosen to be mode c, is driven:[258]

- Normal-mode resonance splitting (as before):

$$\delta\omega = 2\sqrt{g_{\text{BS}}^2 - \kappa_-^2/4} \tag{5.12}$$

- Splitting of undriven mode:

$$\delta\omega_{\text{u}} = 2\sqrt{g_{\text{BS}}^2 - \kappa_+^2/4 - \kappa_-^2/4} \tag{5.13}$$

- Splitting of driven mode c:

$$\delta\omega_{\text{d}} = 2\sqrt{g_{\text{BS}}\sqrt{g_{\text{BS}}^2 + \kappa_a\kappa_+} - \kappa_a^2/4} \tag{5.14}$$

The normal-mode resonances do not depend on which of the two modes is driven. Neither does the splitting in the undriven mode, but for a splitting

---

[257]Experimentally, the conditions can be realised by driving either only with s- or only with p-polarised light, and by changing the crystal temperature to tune the relative phase between s- and p-polarised mode, see Sec. 5.3.

[258]These are obtained by analytically finding maxima in Eq. 5.11 if driven with only one mode.
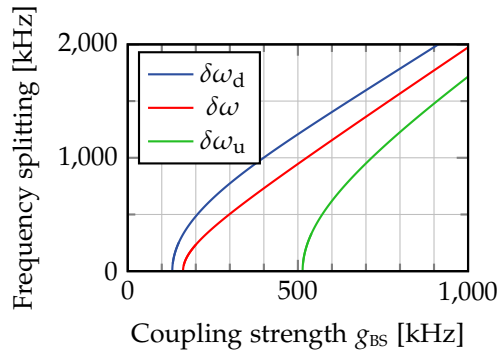
FIGURE 5.5: Splittings over coupling strength while driving only mode c, obtained from Eqs. 5.12–5.14. Splitting in the driven mode is the earliest to occur. Compare this plot with the experimentally obtained Fig. 5.17. Plot parameters are $\kappa_a = 2\pi \times 650\,\text{kHz}$, $\kappa_c = 2\pi \times 1.3\,\text{MHz}$.

to occur here, larger coupling strengths are needed than for normal-mode splitting. Not so for the driven mode: Here, a splitting can be observed even before the normal-mode splitting condition $g_{BS} > \kappa_-/2$ is fulfilled (if the mode with larger linewidth is driven). With observing the decomposed intracavity power, $|a|^2$ and $|c|^2$, and the knowledge of the linewidths κ_a and κ_c, the coupling strength g_{BS} can be determined even if the normal-mode splitting $\delta\omega$ cannot be observed, see Fig. 5.5 for the onset of splittings over coupling strengths and for the splitting sizes.

If the system is driven with both polarisations while keeping an equal detuning $\Delta_c = \Delta_a$ resulting in $\Delta_- = 0$, the intracavity power for one polarisation can be minimised at $\omega = -\Delta_{a,c}$. It becomes zero for a suitable ratio of driving fields,

$$i\frac{\kappa_c}{2}\sqrt{\kappa_{a,\text{in}}}a_{\text{in}} = g_{BS}\sqrt{\kappa_{c,\text{in}}}c_{\text{in}} \quad \Rightarrow \quad a = 0, \tag{5.15a}$$

$$g_{BS}\sqrt{\kappa_{a,\text{in}}}a_{\text{in}} = i\frac{\kappa_a}{2}\sqrt{\kappa_{c,\text{in}}}c_{\text{in}} \quad \Rightarrow \quad c = 0, \tag{5.15b}$$

which can be seen in Fig. 5.6. This is because, under these conditions, the power coupled into one mode from the other mode via the beam-splitter interaction is exactly the same as the power coupled into said mode via driving, but phase-shifted for complete destructive interference.[259] The maxima of that

[259] T. Oishi and M. Tomita, 'Inverted coupled-resonator-induced transparency', *Phys. Rev. A* **88**

$g_{BS} = 2\pi \times 1\,\mathrm{MHz}$ $g_{BS} = 2\pi \times 100\,\mathrm{kHz}$
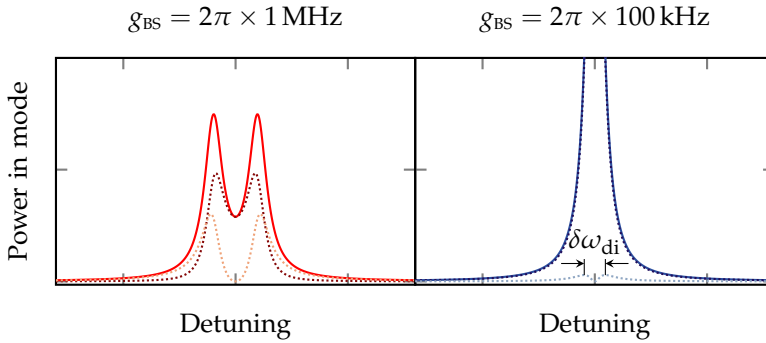
FIGURE 5.6: Destructive interference in coupled cavities. Similar to Fig. 5.4, the total intracavity power $|\mathbf{a}|^2$ is represented by solid lines and equal to the sum of dotted lines, $|a|^2 + |c|^2$, where the dark dotted lines are $|a|^2$ and the light dotted lines are $|c|^2$. Plot parameters are $\kappa_a = 2\pi \times 650\,\mathrm{kHz}$, $\kappa_c = 2\pi \times 1.3\,\mathrm{MHz}$, $\Delta_a = \Delta_c$, $c_{\mathrm{in}} = -i(1-k)a_{\mathrm{in}}$, where $k = 0.25$ and $k = 0.77$ for stronger and weaker coupling, respectively, resulting in no power in mode c at resonance. It follows that $\delta\omega_{\mathrm{di}} = 2\pi \times 940\,\mathrm{kHz}$. Plotted from Eq. 5.11. See Fig. 5.16 for experimental realisation.

mode show a frequency splitting of[260]

$$\delta\omega_{\mathrm{di}} = 2\sqrt{g_{BS}^2 + \kappa_a\kappa_c/4}. \tag{5.16}$$

If the linewidths κ_a and κ_c are known well enough and the driving powers a_{in} and c_{in} and the relative detuning Δ_- as well as the relative phase between a_{in} and c_{in} can be controlled appropriately, even very small coupling strength could be measured this way.[261]

Note that up to now, no assumptions about the nature of the two cavity modes is made – in principle, they can be spatial modes, polarisation modes, or transverse electromagnetic modes. The same is true for the kind of the coupling, be it realised by a beam splitter, by a wave plate or by something else. The results presented here are very general and apply to all kinds of

---

(2013), 063804.

[260] For modes different in their polarisation, the necessary phase shift of $\pi/2$ can be realised with a quarter-wave plate, the ratio between a_{in} and c_{in} can be tuned with a half-wave plate.

[261] Eq. 5.16 seems to suggest that destructive interference and a splitting is visible even without coupling ($g_{BS} = 0$). This is not true because in this case, Eqs. 5.15, which are a prerequisite for Eq. 5.16, cannot be fulfilled. Note also that the experimental realisation turns out to be rather difficult for very small coupling strengths g_{BS}, see Sec. 5.3.
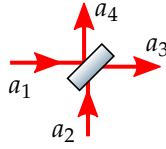
Figure 5.7: Inputs and outputs of a beam splitter.

couplings between two modes (as long as the single-mode approximation inherent in the Hamiltonian method is justified).

5.2 Wave plate as beam splitter

In this section, the use of a wave plate as a beam splitter is studied theoretically, using first a Hamiltonian model and then a transfer-matrix approach. The latter approach does not rely on the single-mode approximation and is thus more general.

5.2.1 Coupling strength of a wave plate

In the following paragraphs, the equivalence between a wave plate and a beam splitter is shown. A beam splitter is a two-port device, coupling two input modes to two output modes and in the process mixing the two input modes. This can be depicted with the following relation:

$$\begin{pmatrix} a_3 \\ a_4 \end{pmatrix} = M_{\mathrm{BS}} \begin{pmatrix} a_1 \\ a_2 \end{pmatrix} \tag{5.17}$$

with inputs and outputs as in Fig. 5.7 and the coupling matrix M_{BS},

$$M_{\mathrm{BS}} = \begin{pmatrix} t & r' \\ r & t' \end{pmatrix} \tag{5.18}$$

where the coupling coefficients need to fulfil the following relations due to energy conservation (or, quantum-mechanically, conservation of commutation

relations):[262]

$$|r| = |r'|, \quad |t| = |t'|, \tag{5.19a}$$

$$|r|^2 + |t|^2 = 1, \tag{5.19b}$$

$$r^*t' + r't^* = 0. \tag{5.19c}$$

Usually, the absolute phase shifts do not matter because the modes are spatially separated and acquire different phases anyway. To make the theory self-consistent, either a phase of $\pi/2$ (a factor of i) is added to the off-diagonal elements or a phase of π (a factor of -1) is added to one diagonal element.[263]

A wave plate is a birefringent medium which shifts the phase of the polarisation component perpendicular to its optical axis compared to the component parallel to its optical axis. In the following, the relative phase shift is called θ, whereas the angle of the optical axis towards s-polarised light is denoted as δ. With two input modes being of orthogonal polarisation and two output modes in the basis of the input modes, the effect of a wave plate can be written as[264]

$$
\begin{aligned}
M_{\text{wp}} &= M_{\text{rot}}(-\delta) M_{\text{delay}}(\theta) M_{\text{rot}}(\delta) \\
&= \begin{pmatrix} \cos\delta & \sin\delta \\ -\sin\delta & \cos\delta \end{pmatrix} \begin{pmatrix} 1 & 0 \\ 0 & e^{-i\theta} \end{pmatrix} \begin{pmatrix} \cos\delta & -\sin\delta \\ \sin\delta & \cos\delta \end{pmatrix} \\
&= \begin{pmatrix} \cos^2\delta + e^{-i\theta}\sin^2\delta & -(1-e^{-i\theta})\sin\delta\cos\delta \\ -(1-e^{-i\theta})\sin\delta\cos\delta & e^{-i\theta}\cos^2\delta + \sin^2\delta \end{pmatrix} \\
&= \begin{pmatrix} t_{\text{wp}} & r'_{\text{wp}} \\ r_{\text{wp}} & t'_{\text{wp}} \end{pmatrix},
\end{aligned}
\tag{5.20}
$$

where the wave plate coefficients also fulfil the conditions in Eqs. 5.19a–5.19c. Thus, a wave plate coupling two polarisation components to each other is equivalent to a beam splitter coupling two spatial modes to each other. As the output modes are not spatially separated any more, the wave plate coupling introduces noticeable phase shifts, which depend on the wave plate angle δ and delay θ.

---

[262] C. C. Gerry and P. L. Knight, *Introductory Quantum Optics*, Cambridge et al.: Cambridge University Press, 2005, Sec. 6.2.

[263] For a discussion of phase relations at a beam splitter see also C. Bond, D. Brown, A. Freise and K. A. Strain, 'Interferometer techniques for gravitational-wave detection', *Living Rev. Relativ.* **19** (2016), 1–221, Sec. 2.4.

[264] Actually, this is true for any birefringent medium if the angle of incidence is chosen such that the medium does not exhibit double refraction.

Seeing that the wave plate is equivalent to a beam splitter, a closer look at the Hamiltonian description of such an interaction is warranted. In the remainder of this section, an effective wave plate Hamiltonian is derived following Leonhardt and Neumaier.[265] Quantum-mechanically, a unitary operator $\hat{S}$ of the form $\hat{S} = e^{-i\hat{H}t}$ is needed, such that $\hat{\mathbf{a}}$ is transformed as

$$\hat{\mathbf{a}} \to \hat{\mathbf{a}}_{\text{out}} = M'_{\text{wp}}\hat{\mathbf{a}} \stackrel{!}{=} \hat{S}^\dagger \hat{\mathbf{a}} \hat{S}, \tag{5.21}$$

where

$$\hat{\mathbf{a}} = \begin{pmatrix} \hat{a}_1 \\ \hat{a}_2 \\ \hat{a}_1^\dagger \\ \hat{a}_2^\dagger \end{pmatrix}, \quad \hat{\mathbf{a}}_{\text{out}} = \begin{pmatrix} \hat{a}_3 \\ \hat{a}_4 \\ \hat{a}_3^\dagger \\ \hat{a}_4^\dagger \end{pmatrix}, \quad M'_{\text{wp}} = \begin{pmatrix} M_{\text{wp}} & 0 \\ 0 & M_{\text{wp}}^\dagger \end{pmatrix} \tag{5.22}$$

and $\hat{S}$ acts individually on each operator. The matrix M'_{wp} is diagonalisable and can be written as $M'_{\text{wp}} = e^K$ with

$$K = M'^{-1}_{\text{rot}} \ln(M'_{\text{delay}}) M'_{\text{rot}}, \tag{5.23}$$

where $M'_{\text{rot}} = \begin{pmatrix} M_{\text{rot}} & 0 \\ 0 & M_{\text{rot}} \end{pmatrix}$, $M'_{\text{delay}} = \begin{pmatrix} M_{\text{delay}} & 0 \\ 0 & M_{\text{delay}}^\dagger \end{pmatrix}$, and M_{delay}, M_{rot} as in Eq. 5.20. Now, an effective Hamiltonian for the wave plate interaction can be constructed as

$$\hat{H}_{\text{eff}} = \frac{1}{2}\hat{\mathbf{a}}^\dagger(-iGK)\hat{\mathbf{a}} \tag{5.24}$$

with the G specifying commutation relations, $G = \begin{pmatrix} \mathbb{1} & 0 \\ 0 & -\mathbb{1} \end{pmatrix}$, leading to

$$\hat{S} = e^{-i\hat{H}_{\text{eff}}}, \tag{5.25}$$

$$\hat{H}_{\text{eff}} = -\theta \sin^2\delta\, \hat{a}_1^\dagger \hat{a}_1 - \theta \cos^2\delta\, \hat{a}_2^\dagger \hat{a}_2 - \theta \cos\delta \sin\delta \left(\hat{a}_1^\dagger \hat{a}_2 + \hat{a}_1 \hat{a}_2^\dagger \right). \tag{5.26}$$

Introducing a time-dependency, such that $\hat{H}_{\text{eff}} = \hat{H}_{\text{wp}}t$, the wave plate Hamiltonian $\hat{H}_{\text{wp}}$ becomes $\hat{H}_{\text{wp}} = \hat{H}_{\text{eff}}/t = c\hat{H}_{\text{eff}}/L$ with $t = L/c$, the cavity round-trip time. Then, $\hat{S} = e^{-i\hat{H}_{\text{wp}}t}$ transforms to the familiar form for time-evolution Hamiltonians.

Equation 5.26 can be compared with the formulation in Sec. 5.1.2, Eq. 5.1. In addition to the beam-splitter interaction $\propto \hat{a}_1^\dagger \hat{a}_2 + \hat{a}_1 \hat{a}_2^\dagger$, the wave plate interaction shifts the phase of each mode, specified by the terms $\propto \hat{a}_i^\dagger \hat{a}_i$. A

[265]U. Leonhardt and A. Neumaier, 'Explicit effective Hamiltonians for general linear quantum-optical networks', *J. Opt. B* **6** (2003), L1–L4.
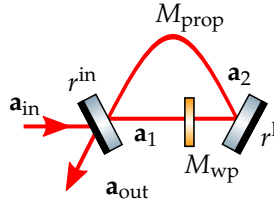
FIGURE 5.8: Simplified scheme for cavities coupled with a wave plate.

shift in resonance frequencies induced by a wave plate coupling two cavity modes does not only occur due to the coupling, but also due to this phase shift. In the experiment, the latter effect can be undone with an additional phase shifter, realised by a temperature-controlled birefringent crystal, see Sec. 5.3.

The beam-splitter coupling strength, realised with a wave plate, resulting from the formalism above by again comparing Eq. 5.26 with Eq. 5.1 amounts to[266]

$$g_{\mathrm{BS}} = \frac{c}{L}\theta \cos\delta \sin\delta = \frac{c}{L}\frac{\theta}{2}\sin 2\delta. \tag{5.27}$$

Although a quantum-mechanical formalism was used in this section, the effects presented are not quantum-mechancial, but classical. They can also be studied with a classical transfer matrix approach, which will be done in the following Sec. 5.2.2.

5.2.2 SIMULATING WAVE-PLATE COUPLING WITH TRANSFER-MATRIX APPROACH

As the wave plate coupling is a classical effect, it can be written solely in classical terms. This is done in this section by using the transfer-matrix approach. Light is coupled into the cavity and passes several optical elements. In a stable cavity on resonance, the field has to replicate after one round-trip. A vector description is used where $\mathbf{a} = (a_{\mathrm{s}}, a_{\mathrm{p}})$ contains amplitudes for s- and p-polarised light. Further elements of the simplified system as in Fig. 5.8 are:

- an input coupling mirror with amplitude reflectivities and transmissivities $r_{\mathrm{s}}^{\mathrm{in}}, t_{\mathrm{s}}^{\mathrm{in}}, r_{\mathrm{p}}^{\mathrm{in}}, t_{\mathrm{p}}^{\mathrm{in}}$ for the s-polarised and the p-polarised mode,

---

[266]It turns out that the prefactor $\theta/2$ seems to be an approximation for $\sin\theta/2$, cf. the following Sec. 5.2.2, especially Fig. 5.9.

- a wave plate with a relative delay θ ($\theta = \pi$ for half-wave plate and $\theta = \pi/2$ for quarter-wave plate) between s- and p-polarised modes and an angle δ of its optical axis towards the s-polarised mode,

- a mirror with coefficients $r_s^1, t_s^1, r_p^1, t_p^1$ to model losses inside the cavity,

- propagation lengths of L_s, L_p of s- and p-polarised modes which lead to detunings of the cavity.

The system of equations is then

$$\mathbf{a}_{in} = \mathbf{a}_{in}, \tag{5.28a}$$

$$\mathbf{a}_1 = t^{in}\mathbf{a}_{in} + r^{in}M_{prop}\mathbf{a}_2, \tag{5.28b}$$

$$\mathbf{a}_2 = r^1 M_{wp}\mathbf{a}_1, \tag{5.28c}$$

$$\mathbf{a}_{out} = -r^{in}\mathbf{a}_{in} + t^{in}M_{prop}\mathbf{a}_2, \tag{5.28d}$$

with the matrices

$$M_{wp} = M_{rot}(-\delta) \times M_{delay}(\theta) \times M_{rot}(\delta), \tag{5.29a}$$

$$M_{rot} = \begin{pmatrix} \cos\delta & -\sin\delta \\ \sin\delta & \cos\delta \end{pmatrix}, \tag{5.29b}$$

$$M_{delay} = \text{diag}(1, e^{-i\theta}), \tag{5.29c}$$

$$M_{prop} = \text{diag}(e^{ikL_s}, e^{ikL_p}), \tag{5.29d}$$

$$t^{in} = \text{diag}(t_s^{in}, t_p^{in}), \tag{5.29e}$$

$$r^{in} = \text{diag}(r_s^{in}, r_p^{in}), \tag{5.29f}$$

$$r^1 = \text{diag}(r_s^1, r_p^1). \tag{5.29g}$$

The system of equations 5.28 can be solved. The intracavity field $\mathbf{a}_1$ becomes

$$\mathbf{a}_1 = \left(\mathbb{1} - r^{in}M_{prop}r^1 M_{wp}\right)^{-1} t^{in}\mathbf{a}_{in}. \tag{5.30}$$

Taking the absolute square of $\mathbf{a}_1$ gives information about the intracavity power, which depends on the wave plate coupling. This can be used to get a mode spectrum for comparison of this ansatz to the Hamiltonian one, see Fig. 5.9. In the single-mode approximation, far away from other resonances, which translates to an FSR much bigger than the linewidths, FSR $\gg \kappa_{a,c}$, and a small coupling strength g_{BS} such that the shifted resonances are still far away
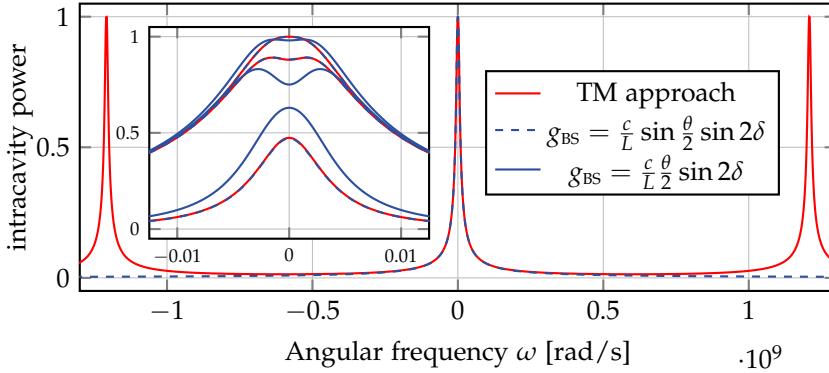
FIGURE 5.9: Coupled cavities mode spectrum with small coupling while driving only mode c as in Fig. 5.4. Note how the Hamiltonian formalism only grasps one resonance. The main figure shows only the normal modes, the inset additionally includes the intracavity field decomposed into s- and p-polarised parts as in Fig. 5.4. Plot parameters are similar to the actual experiment: $L = 1.56\,\text{m}$, $\delta = 0.2°$, $\theta = \pi$, $\Delta_- = 0$, $\kappa_c = 2\pi \times 1.7\,\text{MHz}$, $\kappa_a = 2\pi \times 800\,\text{kHz}$, where the linewidths correspond to total mirror reflectivities of $R_c = 0.946$, $R_a = 0.974$.

from other resonances, $\text{FSR} \gg \delta\omega$, the Hamiltonian approach is an excellent approximation. It should be noted that the proper coupling strength is not as derived in the preceding section. Rather, the correct prefactor seems to be $\sin\theta/2$ instead of $\theta/2$, which is confirmed by the experiment in the following Sec. 5.3.[267]

5.3 MEASURING g_{BS}

The beam-splitter coupling strength of a birefringent medium depends only on the relative delay θ it causes, determined by its birefringence and its length, on the angle of its optical axis δ, and on the cavity length. To determine the coupling strength, the splitting in resonance frequencies caused by the coupling device can be used according to Eqs. 5.12–5.14. In the presented experiment, the two polarisation modes of a cavity are coupled with a wave

---

[267]The reason for this is not really clear to me. My guess is that in the course of the Hamiltonian formalism, at some point the implicit assumption of small delays was made, but discussions with a quantum optics theorist could not clarify this. Another reason might be a wrong use of the Fourier transform.

plate.[268] To find the minimum distance of the splitting, the modes are shifted relatively to each other with a temperature-dependent birefringent crystal. This is necessary because a cavity in practice is inherently birefringent due to the mirrors' coatings, and to account for the additional phase shift caused by a wave plate as seen in Eq. 5.26.

A set-up like that, detailed further in the next Sec. 5.3.1, proves to offer several advantages not only for CQNC but for general studies of coupled optical resonators. First, the coupling strength is easily tunable via rotating the wave plate. Second, the resonance frequencies of the two modes are easily shifted with the crystal temperature. And third, the normal modes can be decomposed back into the original modes easily with a polarising beam splitter. The latter is a characteristic usually not present in coupled optical resonators.[269]

5.3.1 Experimental set-up

To compare experimental results with above theory, and to find a suitable design for future CQNC experiments, attention has to be paid to some requirements:

- The cavity linewidth should be different for the two polarisation modes for several of reasons. First, CQNC requires that the ancilla cavity's linewidth be as small as possible, whereas the other mode should be efficiently coupled into the cavity. Second, the other mode's linewidth determines the measurement strength G_{anc} which in the cascaded set-up needs to be matched to the opto-mechanical measurement strength G, see Sec. 2.3.3. Third, a small linewidth for one polarisation eases resolving the transmission peaks and mode splitting. Fourth, if the linewidths are different, it is possible to also reach the regime below the normal-mode splitting. Additionally, with different linewidths, the convergence of the normal-mode linewidths when coupling the modes could be observed.

---

[268]Other unwanted coupling was caused by a not perfectly aligned birefringent nonlinear crystal, see Fig. 5.18.

[269]Incidentally, this set-up shows exceptional points. It also makes it possible to realise a parity-time symmetric non-Hermitian Hamiltonian. There has been a lot of interest in these recently, see, e.g., M.-A. Miri and A. Alù, 'Exceptional points in optics and photonics', *Science* **363** (2019), eaar7709, S. K. Özdemir, S. Rotter, F. Nori and L. Yang, 'Parity–time symmetry and exceptional points in photonics', *Nat. Mater.* (2019), and references therein.

- For CQNC, a nonlinear crystal inside the cavity will require a small beam waist. To show coupled cavity theory, an element to detune the mode resonances relative to each other is required. Conveniently, a nonlinear crystal[270] is used whose temperature can be changed and with it the difference in resonance frequencies of the polarisation modes. Again, a small waist is required.

- The cavity needs to be a travelling-wave cavity.[271] In order to keep astigmatic effects small, small angles of incidence on all focussing elements are required.

A non-zero angle of incidence of a mirror breaks the degeneracy of its reflection coefficient between the orthogonally polarised modes – the larger the angle, the larger the difference in reflectivity and thus the difference in linewidths.[272] All other mirrors should be highly reflective for both polarisations to not induce additional losses, which requires small angles of incidence. One mirror with a large angle of incidence and small angles of incidence on all other mirrors results in an odd number of cavity mirrors if the number of mirrors is kept small.

Focussing elements are needed for the crystal inside the cavity. The NDOPO-design from Sec. 4.4.1 serves as a starting point. The angles of incidence of the flat mirrors M_2 and M_4 are changed slightly and a fifth mirror M_1 is introduced as an input coupler. The basic design thus is as in Fig. 5.10.

The cavity has several geometric degrees of freedom, see Fig. 5.11. First, two angles are fixed, which determines the third one according to

$$\alpha + \beta + \gamma = 90°. \tag{5.31}$$

---

[270] The crystal used here is a PPKTP crystal with a poling period of 9.2 nm, made by Raicol and earlier used for SHG/down-conversion interaction. It couples infra-red light polarised along its z-axis to green light of the same polarisation leading to (in this experiment unwanted) creation of green light from s-polarised light. When possible, the temperature was chosen such that phase-matching condition for this process was not fulfilled, which was the case especially at temperatures below 20 °C.

[271] One reason is the ease of separating input and output beams. Another reason is that in a linear cavity, a half-wave plate would be traversed twice per round-trip and thus would not have an effect.

[272] After finishing this thesis, another method of breaking the degeneracy became available. Microstructuring membranes can lead to different reflectivities for orthogonal polarisations, even under normal incidence (private communication with Johannes Dickmann, PTB Braunschweig).
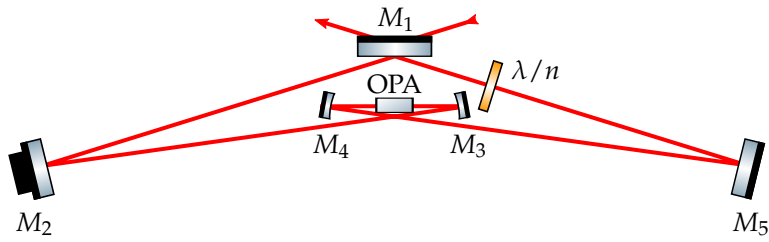
FIGURE 5.10: 5-mirror coupled cavities scheme. Flat mirror M_1 breaks the symmetry between s- and p-polarised light and causes different linewidths for the two polarisations. It additionally serves as input coupler. Flat mirrors M_2 and M_5 are highly reflective and are hit under a small angle of incidence to avoid polarisation-dependent losses. Curved mirrors M_3 and M_4 are hit under a small angle of incidence for the same reason and to additionally avoid astigmatism. They focus the beam into the crystal. A wave plate λ/n couples the polarisation modes.

$$d = 2\overline{AB}, \quad y_1 = \overline{AE},$$
$$x = \overline{OD}, \quad y_2 = \overline{OA}$$
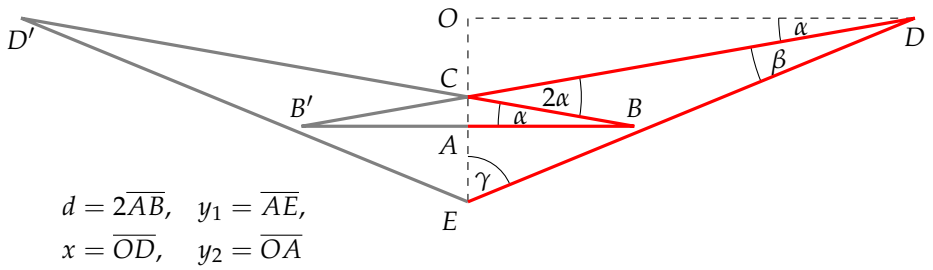
FIGURE 5.11: Geometry of 5-mirror coupled cavities. Parameters are given in Tab. 5.1.

In a symmetrical configuration as in Fig. 5.11, two more parameters determine the geometrical layout. The distance between the two curved mirrors M_3 and M_4 at points B, B' and the total cavity length are chosen. Together with the radius of curvature of the mirrors, these also determine the geometric eigenmode, cf. Sec. 1.2.2. The geometrical layout is thus determined by four parameters, namely two angles, α and β and two distances, d and L. The eigenmode is determined by the distances d and L, and the effective radius of curvature of the mirror, R_{eff}, which depends on the radius of curvature R and the angle of incidence α and is different in horizontal and vertical direction.

Of course, four different parameters could be chosen for the geometrical layout, as for example, again the distance $d = 2\overline{AB} = \overline{BB'}$ between the curved mirrors, and then the distance $2x = 2\overline{OD} = \overline{DD'}$ between the flat mirrors M_2 and M_4, the vertical distance $y_1 = \overline{OA}$ between the incoupler M_1 and the curved mirrors, and the vertical distance $y_2 = \overline{AE}$ between the curved mirrors and the flat mirrors, as in Fig. 5.11. For the final design, first the critical angles α and β were chosen to be as small as possible. Then, the distances d and L were chosen for an appropriate eigenmode with given radii of curvature $R = 100\,\text{mm}$. Next, the parameters y_1, y_2, x were calculated and for ease of assembly changed to multiples of $2.5\,\text{cm}$, the optical table's grid distance. This did not result in big changes of angles and distances. The final set of parameters is listed in Tab. 5.1.

The set-up as assembled on the optical table is shown in Fig. 5.12 and allows observation of the total intracavity power and the s-polarised and p-polarised parts of the intracavity modes separately.

5.3.2 Inferring g_{BS}

For coupling strength measurements, the frequency distances between the various splittings calculated in Sec. 5.1.2 need to be measured. As in Sec. 4.4.1, it is necessary to calibrate the oscilloscope's time axis. This is done as shown in Fig. 5.14. Misaligning the input beam vertically causes an equally spaced comb of higher-order modes to show up. Utilising the spacing to linearise the nonlinear piezo movement, the cavity's free spectral range calculated from its length can be used to convert the time axis into frequencies.

Introducing a wave plate into the set-up couples the two polarisation modes, resulting in normal-mode splitting. Changing the relative detuning between s- and p-polarised mode in the cavity driven only with p-polarised light leads to the observation of an avoided crossing as in Fig. 5.15. At the point

Table 5.1: Design parameters of 5-mirror coupled cavities. For both, the geometrical layout and the eigenmode, shaded parameters are fixed beforehand and determine the remaining parameters. Waists w_0 in the crystal and w_1 on input coupler M_1 result from geometrical layout and radius of curvature R.

	Parameter	in Fig. 5.11	Value
Geometrical layout	x	$\overline{OD}$	32.5 cm
	d	$2\overline{AB}$	11 cm
	y_1	$\overline{OA}$	5 cm
	y_2	$\overline{AE}$	5 cm
	L	$2\overline{ABCDE}$	1.56 m
		α	7.5°
		β	9.6°
		2γ	145.8°
Eigenmode	R		100 mm
	w_0		22 µm
	w_1		380 µm
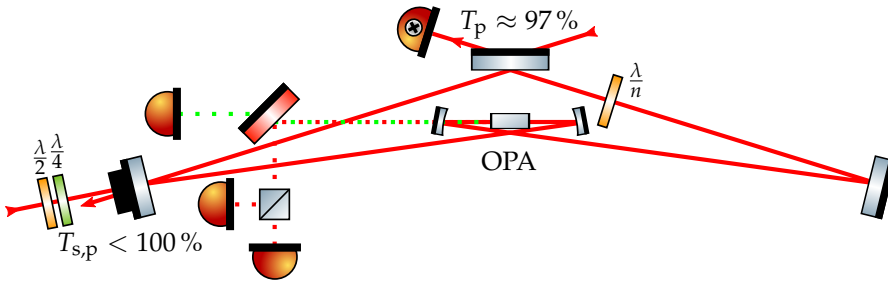
FIGURE 5.12: Experimental set-up of 5-mirror coupled cavities. Light can be coupled into the cavity via the front mirror with $T_p \approx 97\%$ (only p-polarised light) or via the not quite highly-reflective rear piezo-mirror with $T_{s,p} < 100\%$. The intracavity power is observed in transmission of a highly-reflective curved mirror. This mirror also transmits (accidentally) created green light, separated from the infra-red light with a dichroic mirror. The infra-red light is then separated into orthogonal polarisations with a polarising beam splitter and sent onto two photodetectors. See also picture of experimental set-up, Fig. 5.13.
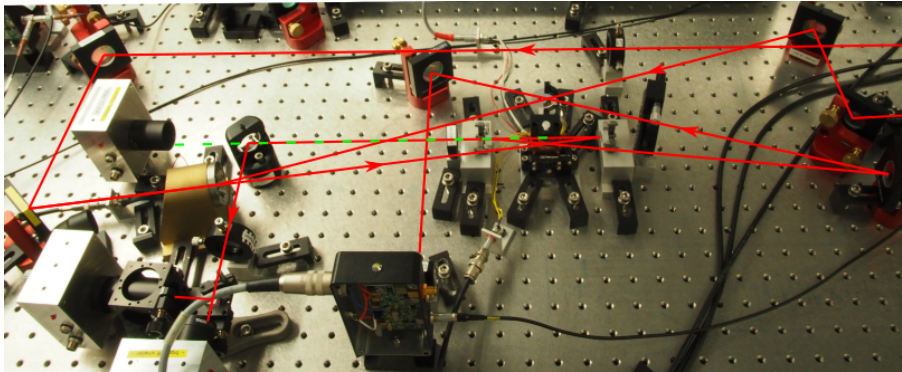
FIGURE 5.13: Picture of 5-mirror coupled cavities as set up on the optical table. Compare to schematic in Fig. 5.12.
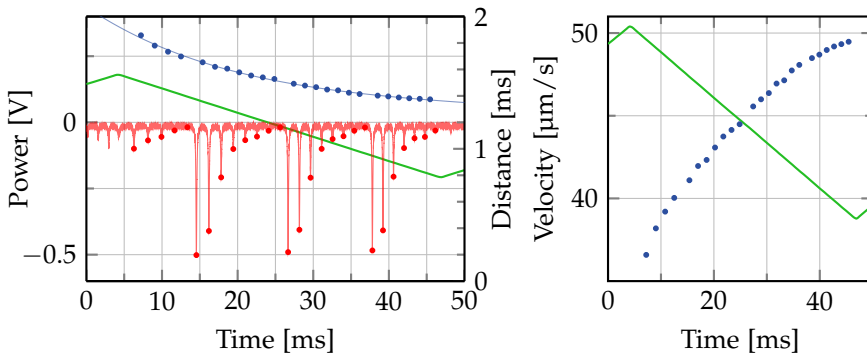
FIGURE 5.14: Calibrating time axis with higher-order mode spacing. Left: Transmission of vertical higher-order modes (red), time it took the piezo to cover the distance between adjacent higher order modes (blue), voltage applied to the piezo (green). Right: Velocity of piezo at different points in time (blue), calculated from distances between higher-order modes in space (vertical Gouy phase over wave vector, divided by two) and time (measured); voltage on piezo for reference. Cf. Fig 3.7 for nonlinear piezo behaviour and Fig. 1.12 for Gouy phase.

of minimal splitting, where $\Delta_- = 0$, both normal mode resonances contain both polarisations as expected from Eq. 5.5 and from simulations, cf. Fig. 5.9. There is an intuitive explanation for that: Modes are those excitations of a system which do not change over time into other modes or change their form. Coupling of p-polarised light to s-polarised light means the conversion of a part of the p-polarised light into s-polarised light. Contrary to a free-running beam, the cavity field's p-polarised part alone does not constitute a mode. A mode, which does not change over time, has to be in a 'conversion equilibrium' and thus needs to consist of p- as well as s-polarised light.

Driving the system with a suitable combination of s- and p-polarised light as given by Eq. 5.15 leads to destructive interference in one mode. This could be used to measure the coupling strength according to Eq. 5.16. Very small coupling strengths require a high, but still perfectly matched, ratio between the amplitudes of the input modes for complete destructive interference. Only for complete destructive interference, Eq. 5.16 for the coupling strength is valid. Unfortunately, in this experiment, it was not possible to obtain complete destructive interference for very small couplings. This is probably due to mode matching differences between s- and p-polarised modes, and coupling
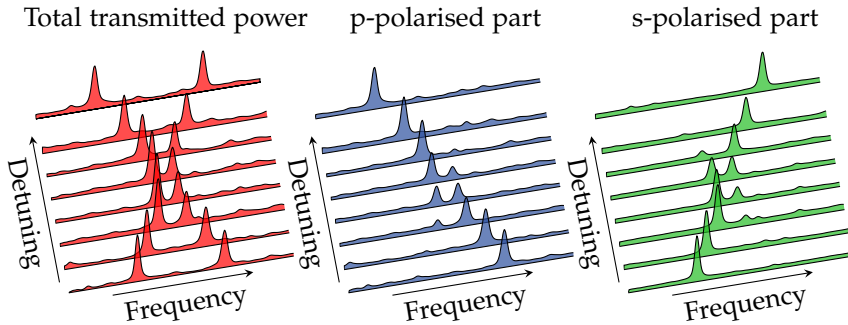
FIGURE 5.15: Experimental observation of avoided crossing. This measurement corresponds to the theoretical plot in Fig. 5.3. The wave plate was set under an angle of roughly 5° leading to strong coupling between the two polarisation modes. The avoided crossing is observed by varying the relative detuning via changing the crystal's temperature. The two resonances 'repel' each other with a minimal splitting of ca. 5 MHz and avoid a crossing. When the relative detuning approaches zero, the normal modes entail both original modes as can be seen by breaking the transmitted light into its polarisation components. A thermistor is used to monitor temperature changes. Its resistance is tuned from 66 kΩ to 106 kΩ by changing the temperature from 33 °C to 19 °C.
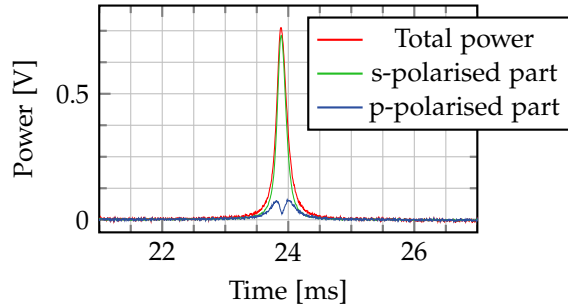
Figure 5.16: Coupling-induced destructive interference. The polarisation modes were coupled by a misaligned crystal, see also Fig. 5.18. Destructive interference around $\Delta_- = 0$ is observed in the p-polarised part with a suitable driving field. But only with *complete* destructive interference, the distance between the peaks can be used to extract the coupling strength. This figure corresponds to the theoretical plot in Fig. 5.6.

to higher-order modes.

Instead, the coupling strength can be estimated from splittings of normal, driven, and undriven modes as in Eqs. 5.12–5.14. The cavity is driven only with p-polarised light, which is the mode with a larger linewidth. Linewidths were measured to be $\kappa_s = 2\pi \times 900 \, \text{kHz}$ and $\kappa_p = 2\pi \times 1.95 \, \text{MHz}$, corresponding to intracavity losses of ca. 2.9 % in addition to the transmission of the front mirror. Changes in the coupling strength due to rotating a half-wave plate[273] in a precision rotation mount[274] at the degeneracy point ($\Delta_- = 0$) caused splittings in the resonances. Minimum coupling is realised by minimising the intracavity power of s-polarised light at the degeneracy point over the wave plate angle δ. At this point, no splitting occurs. By changing the wave plate angle δ, the onset of the three splittings as in Fig. 5.17 can be observed. From this measurement, a smallest observed coupling strength of $g_{\text{BS}} = 2\pi \times 235 \, \text{kHz}$ was obtained. The precise handling of the wave plate rotation makes it possible to go to even smaller coupling strengths, in theory down to zero coupling. In practice, some p-polarised light is converted into s-polarised light even at the point of smallest coupling. Comparing peak heights with the simulation in Sec. 5.2.2 suggests a minimum coupling strength of $g_{\text{BS}} = 2\pi \times 500 \, \text{Hz}$ due to imperfections in the alignment of the wave plate's optical axis or residual misalignment of the

---

[273] Union Optic WPZ2320-1064nm.
[274] High-precision rotation mount PRM1/M by Thorlabs.
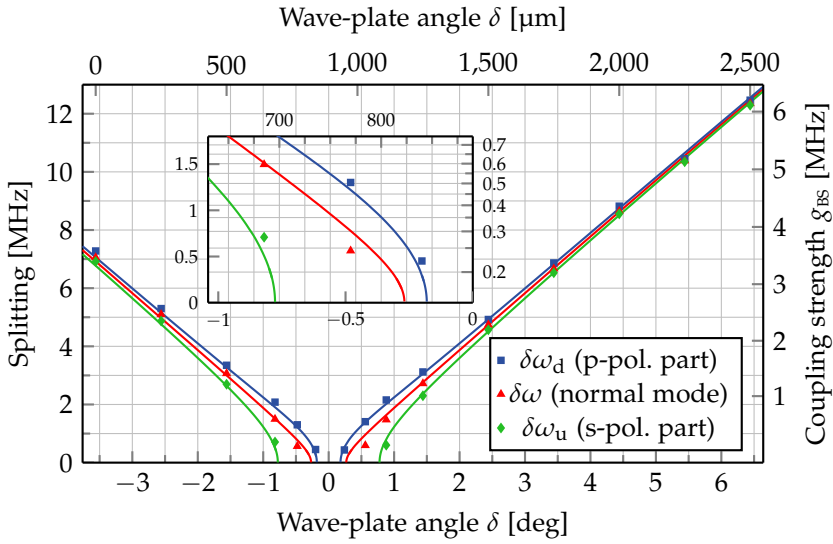
FIGURE 5.17: Mode splitting and beam-splitter coupling strength measurement (compare with Fig. 5.5). The cavity was driven with p-polarised light, the swept transmitted spectrum was calibrated as in Fig. 5.14 and used to determine the distance of split modes. Linewidths were independently measured to be $\kappa_s = 2\pi \times 900\,\text{kHz}$, $\kappa_p = 2\pi \times 1.95\,\text{MHz}$. The offset from the micrometre scale's zero to minimal coupling was determined to be 890 µm. The coupling strength was modelled as $g_{BS} = A \times \sin 2\delta$. Then, Eqs. 5.12–5.14 were all three fitted to the data points simultaneously with the single remaining fit constant A, which resulted in $A = 2\pi \times 28.0\,\text{MHz}$ roughly in agreement with the expected value of $A = \frac{c}{L}\sin\frac{\theta}{2} = 2\pi \times 30.6\,\text{MHz}$ for a half-wave plate. This leads to a smallest measured coupling strength of $g_{BS} = 2\pi \times 235\,\text{kHz}$. Smaller coupling strengths can be realised but not seen in this experiment as then the splitting is not visible any more. Including offset and linewidths as fit parameters has a negligible effect on A but prefers a smaller linewidth $\kappa_s = 2\pi \times 800\,\text{kHz}$, a bigger linewidth $\kappa_p = 2\pi \times 2.05\,\text{MHz}$ and a slight offset of 0.034°. This results in an even smaller measured coupling strength of $g_{BS} = 2\pi \times 205\,\text{kHz}$. The right-hand y-axis corresponds to the coupling strength needed for a splitting in the p-polarised mode of size of the left-hand y-axis.

193
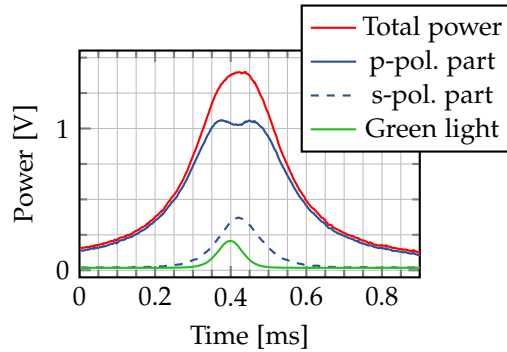
Figure 5.18: Observed mode splitting due to misaligned crystal. Note the splitting in the p-polarised mode part due to a misaligned crystal in an otherwise empty cavity. Note also that the maximum in conversion to green light does not coincide with the maximum of intracavity s-polarised light, which hints at different polarisation bases for crystal and cavity.

crystal. However, this method would need further investigation if utilised for reliable measurements of the coupling strength.

Note that the experimental set-up defines three potentially different polarisation bases.[275] The incoupling mirror hit under a large angle of incidence defines the two cavity polarisation modes. The wave plate couples the two cavity modes according to the angle of its optical axis to the cavity polarisation basis. A third basis is defined by the birefringent crystal. In an earlier set-up with a mount which could not be rotated around the light's direction of propagation, the crystal's birefringence visibly coupled the cavity polarisation modes, see Fig. 5.18. Mode splitting was observed even without a wave plate inside the cavity. With a better aligned crystal, a difference between the cavity basis and the crystal basis can still be observed by the fact that the peak in converted green light does not coincide perfectly with a peak in s-polarised light, although the effect is much less pronounced than in Fig. 5.18.

From Sec. 5.1.1, it remains to be shown that the cavities can be stabilised in spite of their coupling. With very small coupling as well as with strong coupling, a typical Pound-Drever-Hall error signal can be obtained as seen in Fig. 5.19. For small coupling strengths causing normal-mode splitting, locking

---

[275]More for each additional mirror hit under an angle of incidence. The other four cavity mirrors omitted due to their small angle of incidence.
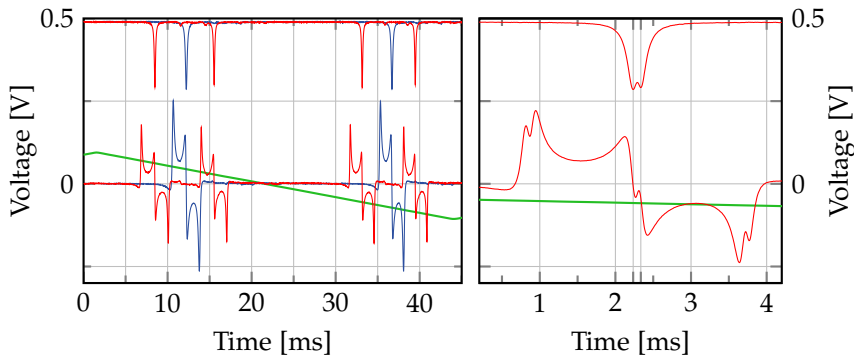
FIGURE 5.19: Error signal of coupled cavities. Left: Very small coupling such that *no* splitting occurs (blue trace) and strong coupling with *distinct* split modes (red trace). Power in reflection are upper traces, demodulated error signal lower traces. The usual Pound-Drever-Hall signal makes it easy to lock on (normal-mode) resonances. Off-resonance locking could be achieved with locking to one of the side-bands or with changing the error signal's offset. Right: Small coupling, which causes *small* splitting. Here, the error signal is not as pronounced. Still, on (normal-mode) resonances and right in between, a slope in the error signal is found, which could be used for locking.

to the resonances becomes more difficult but is still possible. In Sec. 2.4.1, requirements for CQNC were determined. It follows from Tab. 2.3 that the required coupling strength g_{BS} will be too small to cause a normal mode splitting. The detuning Δ_{a} will lie within the meter cavity's linewidth κ_{c}. This ensures that, in the cascaded set-up, the negative-mass oscillator consisting of coupled cavities can be locked with a Pound-Drever-Hall lock as shown above.

The main results of this chapter are summarised as follows: wave plates can be used to realise beam-splitter coupling. Their coupling strength g_{BS} depends on the phase delay θ specific to the wave plate and on the angle δ between the wave plate's optical axis and the incoming light's polarisation. The smallest measured coupling strength $g_{\text{BS}} = 2\pi \times 235\,\text{kHz}$ lies above the coupling strength required in Tab. 2.3. The smallest actually realised coupling strength, however, is much smaller and believed to be of the order of $1\,\text{kHz}$. In a cascaded set-up, where there is no need to spatially separate the coupled cavity modes, both polarisation modes use the same set of cavity mirrors. The cavity can then be stabilised with the well-known Pound-Drever-Hall lock. The 5-mirror coupled cavities still have to be improved in terms of losses, as the measured ancilla cavity linewidth $\kappa_{\text{a}} \hat{=} \kappa_{\text{s}} = 2\pi \times 900\,\text{kHz}$ corresponding to $2.9\,\%$ intracavity losses is higher than required.

Works referenced in the preceding chapter

Bond, C., D. Brown, A. Freise and K. A. Strain, 'Interferometer techniques for gravitational-wave detection', *Living Rev. Relativ.* **19** (2016), 1–221, DOI: 10.1007/s41114-016-0002-8.

Gerry, C. C. and P. L. Knight, *Introductory Quantum Optics*, Cambridge et al.: Cambridge University Press, 2005.

Gröblacher, S., K. Hammerer, M. R. Vanner and M. Aspelmeyer, 'Observation of strong coupling between a micromechanical resonator and an optical cavity field', *Nature* **460** (2009), 724–727, DOI: 10.1038/nature08171, arXiv: 0903.5293.

Haus, H. and W. Huang, 'Coupled-mode theory', *Proc. IEEE* **79** (1991), 1505–1518, DOI: 10.1109/5.104225.

Känel, E. von, *To be published*, Master thesis, Leibniz Universität Hannover.

Leonhardt, U. and A. Neumaier, 'Explicit effective Hamiltonians for general linear quantum-optical networks', *J. Opt. B* **6** (2003), L1–L4, DOI: 10.1088/1464-4266/6/1/L01, arXiv: 0306123 [quant-ph] .

Miri, M.-A. and A. Alù, 'Exceptional points in optics and photonics', *Science* **363** (2019), eaar7709, DOI: 10.1126/science.aar7709.

Novotny, L., 'Strong coupling, energy splitting, and level crossings: A classical perspective', *Am. J. Phys.* **78** (2010), 1199–1202, DOI: 10.1119/1.3471177, URL: https://www.photonics.ethz.ch/fileadmin/user%7B%5C_%7Dupload/novotny10a.pdf.

Oishi, T. and M. Tomita, 'Inverted coupled-resonator-induced transparency', *Phys. Rev. A* **88** (2013), 063804, DOI: 10.1103/PhysRevA.88.013813.

Özdemir, S. K., S. Rotter, F. Nori and L. Yang, 'Parity–time symmetry and exceptional points in photonics', *Nat. Mater.* (2019), DOI: 10.1038/s41563-019-0304-9, URL: http://www.nature.com/articles/s41563-019-0304-9.

Staley, A. et al., 'Achieving resonance in the Advanced LIGO gravitational-wave interferometer', *Class. Quantum Gravity* **31** (2014), 245010, DOI: 10.1088/0264-9381/31/24/245010.

Thompson, R. J., G. Rempe and H. J. Kimble, 'Observation of normal-mode splitting for an atom in an optical cavity', *Phys. Rev. Lett.* **68** (1992), 1132–1135, DOI: 10.1103/PhysRevLett.68.1132, arXiv: 1203.0743.

Thüring, A., 'Investigations of coupled and Kerr non-linear optical resonators', PhD thesis, Leibniz Universität Hannover, 2009, URL: https://edocs.tib.eu/files/e01dh09/607882433.pdf.

Thüring, A., R. Schnabel, H. Lück and K. Danzmann, 'Detuned Twin-Signal-Recycling for ultrahigh-precision interferometers', *Opt. Lett.* **32** (2007), 985, DOI: 10.1364/ol.32.000985.

Weißbrich, H., 'Untersuchungen zur Frequenzstabilisierung gekoppelter optischer Resonatoren', Master thesis, Leibniz Universität Hannover, 2017.

Wimmer, M. H., 'Coupled nonclassical systems for coherent backaction noise cancellation', PhD thesis, Leibniz Universität Hannover, 2016, URL: http://edok01.tib.uni-hannover.de/edoks/e01dh16/863136931.pdf.

Conclusion

The aim of this thesis was to develop a comprehensive understanding of coherent quantum-noise cancellation to determine the specifics of an all-optical experimental realisation. The starting point was an initial set of parameters for the three subsystems, the opto-mechanical, the down-conversion and the beam-splitter interaction, which in principle should enable reduction of back-action noise.[276] These subsystems, together with the theoretical underpinnings of CQNC, have been studied further, which has resulted in an updated set of parameters, here backed by experimental evidence.

This conclusion is divided into three parts. The first part recapitulates the theoretical and experimental results of this thesis. The second part is devoted to updating the parameters and the experimentally feasible reduction of quantum noise, using the knowledge gained through this work. The third part sums up work proposed as sensible next steps.

What has been done

CQNC.   Intuitive ways of understanding coherent quantum-noise cancellation were presented from four different viewpoints, namely as entanglement of a positive- with a negative-mass oscillator, as destructive interference of radiation-pressure noise, as undoing ponderomotive squeezing, and as non-measurement-based feed-forward control. The formal equivalence of negative- and positive-mass oscillators was shown. They differ only in the description of mechanical damping and optical damping in the limit of small quality factors. The motivation behind using a detuned cavity as an effective negative-mass oscillator was given, as well as an explanation for it being coupled with a

---

[276]M. H. Wimmer, D. Steinmeyer, K. Hammerer and M. Heurs, 'Coherent cancellation of backaction noise in optomechanical force measurements', *Phys. Rev. A* **89** (2014), 053836.

beam splitter and a down-conversion process to the incoming light field. An important design decision, namely using optical modes non-degenerate in their polarisation, was motivated.

Two possible experimental set-ups of all-optical CQNC were presented, an integrated set-up, where negative- and positive-mass oscillator reside in the same cavity, and a cascaded set-up, where the cavities containing the two oscillators are spatially separated. Calculations for the cascaded set-up were done and compared to earlier calculations of the integrated set-up. Where for the integrated set-up coupling strengths have to be matched, for the cascaded set-up it is measurement strengths which have to coincide. They are frequency-dependent and additionally depend on cavity linewidths. Additionally, in case of the cascaded set-up, the potential propagation loss from one oscillator to the other might become problematic. However, under similar conditions the integrated and the cascaded set-up lead to similar results.

OPTO-MECHANICAL INTERACTION. Two different micro-mechanical systems, photonic-crystal membranes and Bragg mirrors on a cantilever, were characterised with regard to resonance frequency, linewidth and effective mass. The effective mass determines the opto-mechanical coupling strength. Coupling strength, resonance frequency and potentially linewidth of the micro-mechanical system will have to be matched by the negative-mass oscillator. A first experiment, set up before the lab was closed for construction work, consisted of a Michelson interferometer at 2×10^{-2} mbar with the optical device as end mirror of one arm. It confirmed that the devices under test roughly agree with initially suggested parameters with their resonance frequencies lying in the range of 100 kHz to 1 MHz, and an effective mass of the membranes of the order of nanograms. The linewidths around 10 Hz were limited by residual pressure.

DOWN-CONVERSION INTERACTION. A detailed theoretical analysis of differences and similarities of single- and two-mode squeezing helped gain a better understanding of the role of different losses for different modes in two-mode squeezing. Based on these insights, a simplified detection scheme was set-up, proving that measuring two-mode squeezed light is indeed possible with a single homodyne detector. This enabled measuring more than 2.3 dB of squeezing in the newly built experiment, compared to 0.4 dB in the old lab. Full Gaussian state estimation of bipartite states with a single homodyne

detector should be possible as well.

The relationship between the down-conversion coupling strength for CQNC and squeezing was clearly defined. Different ways of measuring the coupling strength were devised. Several suggestions of how to improve one or the other were made. The installation of a new input coupling mirror with lower transmission led to an improved trade-off between pump parameter and escape efficiency. In our set-up, the nonlinear crystal's damage threshold sets a limit to the usable pump power. It was shown that changing the beam parameters of the participating beams towards larger waists in order to pump harder can lead to stronger coupling and outweigh the resulting less optimal focusing. Three different approaches to measure the down-conversion coupling strength were conducted. All led to a similar down-conversion coupling strength of $g_{\mathrm{DC}} \approx 2\pi \times 200\,\mathrm{kHz}$ at $100\,\mathrm{mW}$ pump power, well within the initially required range for this parameter.

BEAM-SPLITTERLIKE INTERACTION. Two coupled optical resonators were appropriately described as coupled harmonic oscillators. Their Hamiltonian description, valid in the single-mode approximation, predicted effects such as normal-mode splitting, different onsets of splittings in the decomposed modes, and avoided crossing. The splittings are determined by the beam-splitter coupling strength and the linewidths of the coupled resonators. It was shown that a birefringent medium is equivalent to a beam splitter; its corresponding coupling strength was derived. A comparison of the Hamiltonian formalism with a transfer matrix approach shows the validity of the Hamiltonian formulation close to the cavity resonance and determines the beam-splitter coupling strength.

With this knowledge, it is possible to simplify the set-up of coupled cavities. If the cavity modes do not have to be separated spatially, both modes can use the same set of mirrors and travel along the same path. An experiment was set up in this fashion, the observed effects were in excellent agreement with the predictions. Using observed mode splittings, the smallest measured beam-splitter coupling strength was $g_{\mathrm{BS}} \approx 2\pi \times 235\,\mathrm{kHz}$, realised by a half-wave plate inside the cavity. The wave plate can easily be adjusted for smaller coupling strengths, but these are difficult to measure. The minimum coupling realised with a wave plate is estimated to have been of a strength of ca. $500\,\mathrm{Hz}$.

The simplified set-up of coupled cavities enabled locking the cavities with a Pound-Drever-Hall lock, even when strongly coupled. A stabilisation of

coupled cavities has been proved difficult before, but is of importance for CQNC.

CQNC PARAMETERS REVISED

With the knowledge gained in the course of this work, the set of required experimental parameters is updated with two new sets of parameters, an optimistic case and a less optimistic one, see Tab. 6.1. Of special interest are the coupling strengths. The down-conversion coupling has been shown to be stronger than expected. A coupling strength of $g_{DC} = 2\pi \times 250\,\text{kHz}$ has been reliably realised in this thesis. The limit with the current set-up at about $g_{DC} = 2\pi \times 450\,\text{kHz}$, caused by usable pump power, results in both, the optimistic and the less optimistic parameter estimate in Tab. 6.1, being feasible.

The smallest beam-splitter coupling strength was measured to be $g_{BS} = 2\pi \times 235\,\text{kHz}$, but smaller coupling strengths as well as couplings of several MHz can easily be realised. This seems to be the least critical of the parameters.

Opto-mechanical coupling strengths of $g = 2\pi \times 440\,\text{kHz}$ in similar micro-mechanical set-ups have been reported,[277] higher couplings in the order of MHz should be possible.[278] Hence, both assumed parameters for g should be achievable.

The beam-splitter coupling strength in the CQNC experiment will be too small to cause normal-mode splitting. It has been shown here that in this case stabilising the coupled cavities with a Pound-Drever-Hall lock is possible. The required detuning of the ancilla cavity lies within the meter cavity's linewidth. It should not be too difficult to realise this by adjusting the crystal temperature, without negatively affecting phase matching and thus the coupling strength too much.

The linewidth of the ancilla cavity was measured to be $\kappa_a = 2\pi \times 900\,\text{kHz}$, corresponding to 2.9 % intracavity loss, a value larger than expected and required. Appropriately coated wave plate and crystal inside the cavity are expected to introduce 0.1 % loss per surface, corresponding to a linewidth of $\kappa_a = 2\pi \times 120\,\text{kHz}$. A different experiment in the group showed intracavity losses of 0.3 % with a crystal inside the cavity. This corresponds to a linewidth

---

[277] C. B. Møller et al., 'Quantum back-action-evading measurement of motion in a negative mass reference frame', *Nature* **547** (2017), 191–195.

[278] Cf. R. A. Norte, J. P. Moura and S. Gröblacher, 'Mechanical Resonators for Quantum Optomechanics Experiments at Room Temperature', *Phys. Rev. Lett.* **116** (2016), 147202.

Table 6.1: CQNC parameters revised. The main critical parameters are losses/efficiencies and measurement strength. Only with a large enough measurement strength is one limited by radiation-pressure noise and only then, CQNC is advantageous. Matching the oscillators and the coupling rates is not as important while losses are still limiting.

	Parameter	Optimistic		Less optimistic	
		Given by	Value	Given by	Value
Common parameters	ω_m		500 kHz		500 kHz
	γ_m	ω_m/Q	500 Hz		50 mHz
	Q		10^3		10^7
	Δ_a	$-0.99\omega_\mathrm{m}$	-495 kHz	$-0.9\omega_\mathrm{m}$	-450 kHz
	κ_a	$400\gamma_\mathrm{m}$	200 kHz	$8\times10^6\gamma_\mathrm{m}$	400 kHz
	Δ_c		0		0
	κ_c		2 MHz		2 MHz
	$\kappa_\mathrm{c}^\mathrm{bath}$		30 kHz		100 kHz
	g		800 kHz		500 kHz
	g_BS	$1.01\frac{g}{2}$	404 kHz	$1.1\frac{g}{2}$	275 kHz
	g_DC	$0.97\frac{g}{2}$	388 kHz	$0.7\frac{g}{2}$	175 kHz
Cascaded set-up	Δ_om		0		0
	κ_om	$0.99\kappa_\mathrm{c}$	1.98 MHz	$0.9\kappa_\mathrm{c}$	1.8 MHz
	$\kappa_\mathrm{om}^\mathrm{bath}$		30 kHz		100 kHz
	η_1		0.95		0.9
	η_2		0.95		0.9
Integrated set-up	η		0.95		0.9
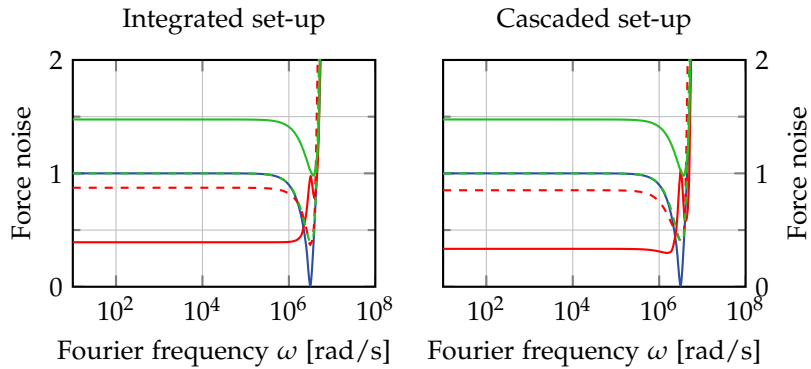
FIGURE 6.1: CQNC sensitivity revised. Blue trace: SQL, red traces: with CQNC, green traces: classical. Solid: Optimistic set of parameters, Dashed: Less optimistic set of parameters. Force noise normalised to Q. In the optimistic case, classical noise is a lot higher, with CQNC, the sensitivity becomes a lot smaller than in the less optimistic case. Both effects are due to the sensitivity being actually limited by radiation-pressure noise in the optimistic case. Plot parameters as in Tab. 6.1.

of $\kappa_a = 2\pi \times 190\,\text{kHz}$ when assuming the same amount of losses for an additional wave plate. The required ancilla cavity linewidth is thus in reach.

The propagation losses η_i mainly stem from mode mismatches, escape efficiency and detection efficiency. Detection efficiencies in excess of 97.5 % have been realised.[279] Mode matching and escape efficiencies of 95 % up to 99 % have been measured in our lab. Thus, the assumed parameters in Tab. 6.1 should be well within reach. To me, however, they seem to be one of the more challenging requirements.

With the parameters from Tab. 6.1, which realistically already assume most of the requirements not to be met perfectly, sensitivities as in Fig. 6.1 can be achieved. At low frequencies, the plots show reduction of 61 %/67 % (4.1 dB/4.8 dB) below the SQL and 73 %/77 % (5.8 dB/6.4 dB) below the classical case for integrated and cascaded set-up in the optimistic case, and 13 %/15 % (0.6 dB/0.7 dB) below the SQL and the classical case in the less optimistic case.

[279]H. Vahlbruch, M. Mehmet, K. Danzmann and R. Schnabel, 'Detection of 15 dB Squeezed States of Light and their Application for the Absolute Calibration of Photoelectric Quantum Efficiency', *Phys. Rev. Lett.* **117** (2016), 110801.

The limiting factor will actually *not* necessarily be the matching of oscillators. Rather, losses limit the amount of noise reduction. The other main difficulty will be to actually reach the point where back-action noise becomes limiting. Without being limited by back-action noise, there will be no noise reduction by back-action evasion. A high measurement strength as well as low thermal noise levels are required for that. These two factors will also be limiting the quantum-noise cancellation.

Future work

CQNC.   A quantum-noise experiment in Copenhagen[280] showed that it might be advantageous to detune the opto-mechanical cavity from resonance. The effect of detuning the main cavities has not been studied for all-optical CQNC, neither has the effect of using different squeezing angles. Within this thesis, thermal noise has been neglected, an unrealistic assumption. Rather, coupling to a thermal bath will be a limiting factor in an experiment, which suggests a trade-off between isolation from thermal bath (small mechanical linewidth) and matching of oscillator linewidths (big mechanical linewidth). The parameters in Tab. 6.1 and the resulting sensitivities suggest that matching the linewidths is not as important. Further studies in this direction are needed.

In the micro-mechanical set-up studied in this work (with resonance frequencies in the hundreds-of-kilohertz range and parameters as in Tab. 6.1), quantum noise will be reduced below the mechanical resonance. It would be interesting to obtain a set of parameters which enables CQNC for frequencies *above* the mechanical resonance. This is the region where quantum-noise reduction is needed for gravitational-wave detection, where mechanical resonance frequencies lie around one hertz. Precondition for this is a high measurement strength in order to be limited by radiation-pressure noise at these frequencies. Injecting phase-quadrature squeezed light might help here and deserves an investigation.

Preliminary investigations have shown that back-action evasion should also be possible by reflection of light containing radiation-pressure noise off a detuned single-mode squeezer, at least in a limited frequency range. The advantage here would be that a substantially higher down-conversion coupling strength is possible due to a higher effective nonlinear coefficient. This set-up, which shows similarities to CQNC, requires further research.

---

[280]Møller et al. (2017).

Opto-mechanical interaction.   The opto-mechanical subsystem is the one that still requires the most work in terms of experimental realisation. An opto-mechanical cavity needs to be set up in high vacuum in order to reliably determine the opto-mechanical coupling strength, for example from ponderomotive squeezing or opto-mechanically induced transparency measurements. Then, artificial radiation-pressure noise can be produced by sending an amplitude-modulated light field into the opto-mechanical cavity. The evasion of this *classical* noise should be possible with current realisable parameters. For *quantum* radiation-pressure noise cancellation, a significant reduction of thermal noise will be necessary by transferring the set-up to a cryogenic environment.

Down-conversion interaction. The down-conversion interaction already shows the required coupling strength. However, improvements are needed regarding the pump beam. The behaviour at higher pump powers shows power-dependent losses, probably due to thermal lensing. The pump beam alignment is not very stable, nor is the pump phase lock. With a reliable pump phase lock, full estimation of a bipartite Gaussian state could be performed. The cavity stability should further be improved. Additionally, losses will become very important, even potentially limiting, and hence need to be mitigated. All of these are technical, not principal problems.

Beam-splitter interaction.   The main limiting factor for the beam-splitter interaction are losses. A different crystal, which is needed anyway to provide the down-conversion interaction, will improve on that. Locking the coupled cavities with a defined detuning has not yet been done, but there should be no show-stopper to that.

An interesting aspect of the experiment as it is currently set up on the optical table is that it shows exceptional points and can realise a parity-time (PT) symmetric Hamiltonian.[281] Under certain conditions, eigenvalues as well as eigenvectors of a system are degenerate. These points are called *exceptional points* and have recently attracted a lot of interest due to their topological characteristics and potentially enhanced sensitivities.[282] PT-symmetric systems

[281] M.-A. Miri and A. Alù, 'Exceptional points in optics and photonics', *Science* **363** (2019), eaar7709; S. K. Özdemir, S. Rotter, F. Nori and L. Yang, 'Parity–time symmetry and exceptional points in photonics', *Nat. Mater.* (2019).

[282] H.-K. Lau and A. A. Clerk, 'Fundamental limits and non-reciprocal approaches in non-Hermitian quantum sensing', *Nat. Commun.* **9** (2018), 4320.

are symmetric under swapping of parity, here the two modes, and time, here corresponding to exchanging gain with loss. An additional pump beam would turn the ancilla cavity mode into a mode with gain. Tuning the pump power such that the gain is of the same size as the loss in the other mode renders the system parity-time symmetric. These types of systems are interesting as a means to study non-Hermitian Hamiltonians. Per se, the system has not a lot to do with coherent quantum-noise cancellation, but this might still be an interesting avenue to pursue.

The effective negative-mass oscillator with the ancilla cavity on resonance resembles another system termed *direct coupling coherent observer*,[283] which has been proposed in the field of control theory and engineering. A similar idea with essentially the same set-up as for the direct observer (and as for CQNC) comes from the quantum optics context, where two modes coupled with a beam splitter or frequency converter and a down-conversion interaction create a QND variable.[284] As the system is very similar to the one studied here, it makes sense to look into similarities and differences in the future.

After finishing this thesis, a new method to break the degeneracy between the two polarisations inside the cavity became available: Instead of a very shallow angle of incidence on the incoupling mirror, a conventional four-mirror bow-tie cavity with a micro-structured input mirror could be used.[285]

WORKS REFERENCED IN THE PRECEDING CHAPTER

Kimble, H. J., 'Course 10: Quantum Fluctuations in Quantum Optics – Squeezing and Related Phenomena', in: *Systèmes Fondamentaux en Optique Quantique, Les Houches, Session LIII, 1990*, ed. by J. Dalibard, J. M. Raimond and J. Zinn-Justin, Amsterdam: Elsevier, 1992.

Lau, H.-K. and A. A. Clerk, 'Fundamental limits and non-reciprocal approaches in non-Hermitian quantum sensing', *Nat. Commun.* **9** (2018), 4320, DOI: 10.1038/s41467-018-06477-7.

Miri, M.-A. and A. Alù, 'Exceptional points in optics and photonics', *Science* **363** (2019), eaar7709, DOI: 10.1126/science.aar7709.

---

[283] I. R. Petersen and E. H. Huntington, 'Implementation of a direct coupling coherent quantum observer including observer measurements', in: *Proc. 2016 Am. Control Conf.* 2016, pp. 4765–4768, DOI: 10.1109/ACC.2016.7526107.

[284] See H. J. Kimble, 'Course 10: Quantum Fluctuations in Quantum Optics – Squeezing and Related Phenomena', in: *Systèmes Fondamentaux en Optique Quantique, Les Houches, Session LIII, 1990*, Amsterdam: Elsevier, 1992, Sec. 8.2, who himself references B. Yurke, 'Optical back-action-evading amplifiers', *J. Opt. Soc. Am. B* **2** (1985), 732.

[285] Personal communication with Johannes Dickmann, PTB Braunschweig.

Møller, C. B., R. A. Thomas, G. Vasilakis, E. Zeuthen, Y. Tsaturyan, M. Balabas, K. Jensen, A. Schliesser, K. Hammerer and E. S. Polzik, 'Quantum back-action-evading measurement of motion in a negative mass reference frame', *Nature* **547** (2017), 191–195, DOI: 10.1038/nature22980, arXiv: 1608.03613.

Norte, R. A., J. P. Moura and S. Gröblacher, 'Mechanical Resonators for Quantum Optomechanics Experiments at Room Temperature', *Phys. Rev. Lett.* **116** (2016), 147202, DOI: 10.1103/PhysRevLett.116.147202, arXiv: 1511.06235.

Özdemir, S. K., S. Rotter, F. Nori and L. Yang, 'Parity–time symmetry and exceptional points in photonics', *Nat. Mater.* (2019), DOI: 10.1038/s41563-019-0304-9, URL: http://www.nature.com/articles/s41563-019-0304-9.

Petersen, I. R. and E. H. Huntington, 'Implementation of a direct coupling coherent quantum observer including observer measurements', in: *Proc. 2016 Am. Control Conf.* 2016, pp. 4765–4768, DOI: 10.1109/ACC.2016.7526107.

Vahlbruch, H., M. Mehmet, K. Danzmann and R. Schnabel, 'Detection of 15 dB Squeezed States of Light and their Application for the Absolute Calibration of Photoelectric Quantum Efficiency', *Phys. Rev. Lett.* **117** (2016), 110801, DOI: 10.1103/PhysRevLett.117.110801.

Wimmer, M. H., D. Steinmeyer, K. Hammerer and M. Heurs, 'Coherent cancellation of backaction noise in optomechanical force measurements', *Phys. Rev. A* **89** (2014), 053836, DOI: 10.1103/PhysRevA.89.053836, arXiv: 1403.2992.

Yurke, B., 'Optical back-action-evading amplifiers', *J. Opt. Soc. Am. B* **2** (1985), 732, DOI: 10.1364/JOSAB.2.000732.

Appendix

A Electrodynamics

Maxwell's equations describing the whole classical world of electrodynamics are

$$\nabla \cdot \mathbf{D} = \rho \tag{A.1a}$$

$$\nabla \cdot \mathbf{B} = 0 \tag{A.1b}$$

$$\nabla \times \mathbf{E} = -\frac{\partial}{\partial t}\mathbf{B} \tag{A.1c}$$

$$\nabla \times \mathbf{H} = \mathbf{j} + \frac{\partial}{\partial t}\mathbf{D}. \tag{A.1d}$$

with

$$\mathbf{D} = \epsilon_0\mathbf{E} + \mathbf{P}, \qquad \mathbf{B} = \mu_0(\mathbf{H} + \mathbf{M}), \tag{A.2}$$

and *free* charge densities and currents ρ and $\mathbf{j}$.

A.1 Maxwell's equations in free space

In free space, where there is no matter, they simplify to

$$\nabla \cdot \mathbf{E} = 0, \tag{A.3a}$$

$$\nabla \cdot \mathbf{H} = 0, \tag{A.3b}$$

$$\nabla \times \mathbf{E} = -\frac{\partial}{\partial t}\mu_0\mathbf{H}, \tag{A.3c}$$

$$\nabla \times \mathbf{H} = \frac{\partial}{\partial t}\epsilon_0\mathbf{E} \tag{A.3d}$$

A.1.1 Wave equation

With the vector identity $\nabla \times (\nabla \times \mathbf{V}) = \nabla(\nabla \cdot \mathbf{V}) - \nabla \cdot (\nabla \mathbf{V})$ and because $\mathbf{E}$ is divergence free, from $\nabla \times (\nabla \times \mathbf{E})$ one arrives at the wave equation

$$\nabla^2 \mathbf{E} - \frac{1}{c^2} \frac{\partial^2}{\partial t^2} \mathbf{E} = 0. \tag{A.4}$$

General solutions to the wave equation are of the form

$$\mathbf{E}(\mathbf{r}, t) = g(\omega t - \mathbf{kr}) \tag{A.5}$$

with the dispersion relation $|k| = \frac{\omega}{c}$.

A.1.2 Paraxial approximation

Monochromatic electromagnetic waves can be written as (assuming propagation in z-direction and an amplitude constant in time)

$$\mathbf{E}(\mathbf{r}, t) = \operatorname{Re} \mathbf{A}(\mathbf{r}) e^{i(\omega t - kz)}, \tag{A.6}$$

the wave equation becomes

$$\nabla^2 \mathbf{A} + 2ik \frac{\mathrm{d}}{\mathrm{d}z} \mathbf{A} - \left(k^2 - \frac{\omega^2}{c^2} \right) \mathbf{A} = 0. \tag{A.7}$$

The last term is equal to zero because of the dispersion relation. The paraxial approximation, also known as slowly varying envelope approximation, assumes $\mathbf{A}$ to vary slowly with z. The second-order derivative in z is neglected in comparison with the first one, the equation becomes

$$\left(\frac{\mathrm{d}^2}{\mathrm{d}x^2} + \frac{\mathrm{d}^2}{\mathrm{d}y^2} + 2ik \frac{\mathrm{d}}{\mathrm{d}z} \right) \mathbf{A} = 0. \tag{A.8}$$

A family of solutions to this equation are Gaussian beams.

A.2 Maxwell's equations in dielectric media

In dielectric media, there are no free charges, $\rho = 0$, no free currents, $\mathbf{j} = 0$. Furthermore, a linear magnetisation is assumed, such that $\mathbf{H} + \mathbf{M} = \mu_r \mathbf{H}$. The polarisation $\mathbf{P}$ is developed in a Taylor series with the linear part included

into ϵ_r and the nonlinear part $\mathcal{P}$ kept so that $\epsilon_0\mathbf{E} + \mathbf{P} = \epsilon_0\epsilon_r\mathbf{E} + \mathcal{P}$. Now, with $\mu = \mu_0\mu_r$ and $\epsilon = \epsilon_0\epsilon_r$, the Maxwell equations can be written as

$$\nabla \cdot (\epsilon\mathbf{E} + \mathcal{P}) = 0, \tag{A.9a}$$

$$\nabla \cdot \mu_r\mathbf{H} = 0, \tag{A.9b}$$

$$\nabla \times \mathbf{E} = -\frac{\partial}{\partial t}\mu_0\mu_r\mathbf{H}, \tag{A.9c}$$

$$\nabla \times \mathbf{H} = \frac{\partial}{\partial t}(\epsilon\mathbf{E} + \mathcal{P}) \tag{A.9d}$$

A.2.1 THE WAVE EQUATION

Similar as above, the wave equation can be obtained (c is the speed of light within the medium),

$$\nabla^2\mathbf{E} - \frac{1}{c^2}\frac{\partial^2}{\partial t^2}\mathbf{E} = \frac{1}{\epsilon c^2}\frac{\partial^2}{\partial t^2}\mathcal{P}. \tag{A.10}$$

The nonlinear polarisation $\mathcal{P}$ now acts as a driving term for the electric field.

A.2.2 THE NONLINEAR POLARISATION

Phenomenologically, the polarisation of a medium can be seen as its response to an incoming electrical field. It can be series-expanded in terms of the electrical field, so that we assume the polarisation to consist of several parts:

$$\mathbf{P}(\mathbf{r}, t) = \mathbf{P}^{(1)}(\mathbf{r}, t) + \mathbf{P}^{(2)}(\mathbf{r}, t) + \mathbf{P}^{(3)}(\mathbf{r}, t) + \dots, \tag{A.11}$$

where $\mathbf{P}^{(1)}(\mathbf{r}, t)$ is linear in the electric field, $\mathbf{P}^{(2)}(\mathbf{r}, t)$ quadratic and so on. The electric field $\mathbf{E}(\mathbf{r}, t)$ is assumed to be a superposition of several monochromatic electric fields of frequency ω_n:

$$\mathbf{E}(\mathbf{r}, t) = \tfrac{1}{2}\sum_{\omega_n}\mathbf{E}^{\omega_n}(\mathbf{r})e^{-i\omega_n t} + \text{c.c.} \tag{A.12}$$

Here, we take the sum over positive frequencies, and $\mathbf{E}^{-\omega_n}(\mathbf{r}) = \mathbf{E}^{*\omega_n}(\mathbf{r})$.

We expect the second-order polarisation (which, in the following we write as $\mathbf{P}^{(2)} = \mathcal{P}$) to be connected to the square of the electric field. This is realised by a tensor χ, a material characteristic in general dependent on the participating frequencies, the beam directions and the polarisations of the electric fields. Squaring the electrical field yields contributions of frequencies $\pm\omega_m \pm \omega_n$

including $m = n$. This justifies to also split the polarisation into frequency components,

$$\mathcal{P}(\mathbf{r}, t) = \tfrac{1}{2} \sum_{\omega_n} \mathcal{P}^{\omega_n}(\mathbf{r}) e^{-i\omega_n t} + \text{c.\,c.} \tag{A.13}$$

Now we restrict number of frequencies to three, ω_1, ω_2, and $\omega_3 = \omega_1 + \omega_2$. We can write the frequency components of the nonlinear polarisation as

$$\mathcal{P}^{\omega_{m+n}}(\mathbf{r}) = \epsilon_0 \sum_{(nm)} \chi(\omega_{m+n}; \omega_m, \omega_n) \mathbf{E}^{\omega_m}(\mathbf{r}) \mathbf{E}^{\omega_n}(\mathbf{r}) \tag{A.14}$$

where ω_{n+m} is short for $\omega_n + \omega_m$. E.g.:

$$\omega_{m+n} = \omega_3, \quad \omega_m = \omega_1, \quad \omega_n = \omega_2 \tag{A.15}$$

$$\text{or}$$

$$\omega_{m+n} = -\omega_1, \quad \omega_m = -\omega_3, \quad \omega_n = \omega_2. \tag{A.16}$$

Here, (nm) means that we take the sum over different ω_n and ω_m, but such that $\omega_n + \omega_m$ stays constant. We can write this shorter by using a degeneracy factor D:[286]

$$\mathcal{P}^{\omega_{m+n}}(\mathbf{r}) = \epsilon_0 \frac{D}{2} \chi(\omega_{m+n}; \omega_m, \omega_n) \mathbf{E}^{\omega_m}(\mathbf{r}) \mathbf{E}^{\omega_n}(\mathbf{r}) \tag{A.17}$$

where D is the number of distinct permutations of ω_n and ω_m. The same can be written in index notation (summing over doubly appearing indices j and k where ijk stand for the spatial (crystallographic) directions xyz):

$$\mathcal{P}_i^{\omega_{m+n}}(\mathbf{r}) = \epsilon_0 \frac{D}{2} \chi_{ijk}(\omega_{m+n}; \omega_m, \omega_n) E_j^{\omega_m}(\mathbf{r}) E_k^{\omega_n}(\mathbf{r}).^{[287]} \tag{A.18}$$

For SHG, we have $\chi(\omega_{m+n}; \omega_m, \omega_n) = \chi(2\omega; \omega, \omega)$ and thus only one distinct permutation of ω_n and ω_m ($D = 1$), whereas for down conversion, $D = 2$ due to two permutations $\chi(\omega_{m+n}; \omega_m, \omega_n) = \chi(\omega; 2\omega, -\omega) = \chi(\omega; -\omega, 2\omega)$.

In the case of parametric down conversion, we are interested in the creation of signal and idler, i.e. beams at frequencies ω_1 and ω_2 and a pump beam at frequency $\omega_3 = \omega_1 + \omega_2$. With all kinds of symmetries, especially using Kleinman's symmetry, we can make χ frequency-independent. For historical

---

[286]Cf. R. W. Boyd, *Nonlinear Optics*, Amsterdam et al.: Acad. Press, 2008, Eq. 1.3.19.
[287]This formula differs by a factor $1/2$ from Eq. 1.3.19 given by Boyd (2008) due different definitions of the fields in our Eqs. A.12 and A.13 and their Eqs. 1.3.7 and 1.3.11.

reasons χ_{ijk} is often substituted by the tensor $d_{ijk} = \frac{1}{2}\chi_{ijk}$ so that we have

$$\mathcal{P}_i^{\omega_1}(\mathbf{r}) = 2\epsilon_0 d_{ijk} E_j^{\omega_3}(\mathbf{r},t) E_k^{-\omega_2}(\mathbf{r},t) \tag{A.19}$$

$$= 2\epsilon_0 d_{ijk} E_j^{\omega_3}(\mathbf{r},t) E_k^{*\omega_2}(\mathbf{r},t) \tag{A.20}$$

and correspondingly

$$\mathcal{P}_i^{\omega_2}(\mathbf{r}) = 2\epsilon_0 d_{ijk} E_j^{\omega_3}(\mathbf{r},t) E_k^{*\omega_1}(\mathbf{r},t), \tag{A.21}$$

$$\mathcal{P}_i^{\omega_3}(\mathbf{r}) = \epsilon_0 d_{ijk} E_j^{\omega_1}(\mathbf{r},t) E_k^{\omega_2}(\mathbf{r},t). \tag{A.22}$$

Usually d_{ijk} is contracted to d_{il}.[288] In our NDOPO, we use the tensor component $d_{yzy} = d_{24} = d_{32} \approx 3.7\,\mathrm{pm/V}$ of KTP which yields an effective nonlinear coefficient due to quasi phase matching[289]

$$d_\mathrm{eff} = \frac{2}{\pi} d_{24} \approx 2.4\,\mathrm{pm/V} \tag{A.23}$$

for the conversion involving wavelengths of 532 nm and 1064 nm. Note that using the d_{33}-coefficient to couple three waves of the same polarisation results in an effective nonlinearity $d_\mathrm{eff} = \frac{2}{\pi} 17\,\mathrm{pm/V} = 11\,\mathrm{pm/V}$ – a factor 5 higher.

Two fundamental waves of orthogonal polarisation (y and z in the crystal's coordinate system) travelling in the same direction (x) are coupled to a harmonic wave polarised in one direction (y) travelling in the same direction by the nonlinear coefficient d_{24}. For a specific set of beams like these, the following scalar equation suffice to describe the interaction:

$$\mathcal{P}^{\omega_2}(\mathbf{r}) = 2\epsilon_0 d_\mathrm{eff} E^{\omega_3}(\mathbf{r},t) E^{*\omega_1}(\mathbf{r},t) \tag{A.24}$$

$$\mathcal{P}^{\omega_1}(\mathbf{r}) = 2\epsilon_0 d_\mathrm{eff} E^{\omega_3}(\mathbf{r},t) E^{*\omega_2}(\mathbf{r},t) \tag{A.25}$$

$$\mathcal{P}^{\omega_3}(\mathbf{r}) = \epsilon_0 d_\mathrm{eff} E^{\omega_1}(\mathbf{r},t) E^{\omega_2}(\mathbf{r},t). \tag{A.26}$$

A.2.3 ENERGY CONSIDERATIONS

Because of the BAC-CAB formula,

$$(\nabla \times \mathbf{E})\mathbf{H} - (\nabla \times \mathbf{H})\mathbf{E} = \nabla(\mathbf{E} \times \mathbf{H}) \tag{A.27}$$

---

[288] Cf. Boyd (2008), Eqs. 1.5.26 and 27.
[289] Cf. Boyd (2008), Sec. 2.4.

and with the Gaussian theorem and the Poynting vector $\mathbf{S} = \mathbf{E} \times \mathbf{H}$ defining the flow of energy through a surface,

$$\oint d\mathbf{a} \, \mathbf{S} = \int d\mathbf{V} \, \nabla \mathbf{S} \tag{A.28}$$

$$= \int d\mathbf{V} \, \nabla(\mathbf{E} \times \mathbf{H}), \tag{A.29}$$

the net power deposited in a volume V per unit volume from Maxwell's equations is

$$-\nabla(\mathbf{E} \times \mathbf{H}) = \frac{\partial}{\partial t} \left(\tfrac{1}{2}\epsilon\mathbf{EE} + \tfrac{1}{2}\mu\mathbf{HH} \right) + \mathbf{E}\frac{\partial \mathbf{P}}{\partial t}. \tag{A.30}$$

The first corresponds to the change of storage of energy in the vacuum electromagnetic field and in the linear polarisation, the second term is the work done on the nonlinear polarisation by the electric field. Integrating the Poynting vector over the closed surface S of the crystal leads to

$$\oint_{A_{\text{crystal}}} d\mathbf{a} \, \mathbf{S} = \int_{V_{\text{crystal}}} d\mathbf{V} \left[\frac{\partial}{\partial t} \left(\tfrac{1}{2}\epsilon\mathbf{EE} + \tfrac{1}{2}\mu\mathbf{HH} \right) + \mathbf{E}\frac{\partial \mathbf{P}}{\partial t} \right]. \tag{A.31}$$

For a lossless medium, this is zero, but it does not need to be zero if one only takes into account a specific frequency. Then, the last term gives the power from the nonlinear polarisation converted into the new frequency. Its calculation is shown in the next section, Sec. A.2.4.

A.2.4 Average power transfer

From Sec. A.2.3 above, one derives the average power per unit volume in the second-order nonlinear polarisation $\mathcal{P}$, Eq. 4.57, which in the following will

be calculated for a specific beam i and volume V.

$$\overline{P_i} = \frac{1}{2T} \int\limits_{-T}^{T} dt \int\limits_{V} d\mathbf{r} \, \mathbf{E}_i(\mathbf{r}, t) \frac{\partial \mathcal{P}_i(\mathbf{r}, t)}{\partial t} \tag{A.32}$$

$$= \frac{1}{2T} \int\limits_{-T}^{T} dt \int\limits_{V} d\mathbf{r} \, \tfrac{1}{2} \left(\mathbf{E}_i(\mathbf{r})e^{-i\omega_i t} + \mathbf{E}_i^*(\mathbf{r})e^{i\omega_i t} \right) \frac{\partial}{\partial t} \tfrac{1}{2} \left(\mathcal{P}_i(\mathbf{r})e^{-i\omega_i t} + \mathcal{P}_i^*(\mathbf{r})e^{i\omega_i t} \right) \tag{A.33}$$

$$= \frac{i\omega_i}{8T} \int\limits_{V} d\mathbf{r} \int\limits_{-T}^{T} dt \left[\mathbf{E}_i^*(\mathbf{r})\mathcal{P}_i(\mathbf{r}) - \mathbf{E}_i(\mathbf{r})\mathcal{P}_i^*(\mathbf{r}) + \mathbf{E}_i(\mathbf{r})\mathcal{P}_i(\mathbf{r})e^{-i2\omega_i t} - \mathbf{E}_i^*(\mathbf{r})\mathcal{P}_i^*(\mathbf{r})e^{i2\omega_i t} \right] \tag{A.34}$$

$$= -\mathrm{Im} \left[\frac{\omega_i}{2} \int\limits_{V} d\mathbf{r} \, \mathbf{E}_i^*(\mathbf{r})\mathcal{P}_i(\mathbf{r}) \right]. \tag{A.35}$$

B FULL GAUSSIAN STATE ESTIMATION WITH SINGLE HOMODYNE DETECTOR

For a complete state estimation of a Gaussian state with two modes, we need to measure variances and correlations of all involved degrees of freedom, which are amplitude and phase quadratures of both involved modes. The covariance matrix C of the four quadratures of the two modes $\hat{a}$ and $\hat{c}$ looks like

$$C(\hat{a}, \hat{c}) = \begin{pmatrix} \mathrm{var}\,\hat{x}_a & \mathrm{cov}\,\hat{x}_a, \hat{p}_a & \mathrm{cov}\,\hat{x}_a, \hat{x}_c & \mathrm{cov}\,\hat{x}_a, \hat{p}_c \\ \mathrm{cov}\,\hat{p}_a, \hat{x}_a & \mathrm{var}\,\hat{p}_a & \mathrm{cov}\,\hat{p}_a, \hat{x}_c & \mathrm{cov}\,\hat{p}_a, \hat{p}_c \\ \mathrm{cov}\,\hat{x}_c, \hat{x}_a & \mathrm{cov}\,\hat{x}_c, \hat{p}_a & \mathrm{var}\,\hat{x}_c & \mathrm{cov}\,\hat{x}_c, \hat{p}_c \\ \mathrm{cov}\,\hat{p}_c, \hat{x}_a & \mathrm{cov}\,\hat{p}_c, \hat{p}_a & \mathrm{cov}\,\hat{p}_c, \hat{x}_c & \mathrm{var}\,\hat{p}_c \end{pmatrix}$$

$$= \begin{pmatrix} \bullet & \star & \circ & * \\ & \bullet & * & \circ \\ & & \bullet & \star \\ & & & \bullet \end{pmatrix}, \tag{B.1}$$

where C is symmetric (meaning only 10 independent entries) and different symbols refer to different measurement methods.[290] The whole covariance matrix can be measured with a single homodyne detector by shaping the local oscillator:[291] The variances of the single quadratures (●) are easily measured by using a local oscillator only interfering with mode $\hat{a}$ (or mode $\hat{c}$) and adjusting the local oscillator's phase as to measure either the phase or the amplitude quadrature. Correlations between amplitude quadratures (phase quadratures) of both modes (○) can be measured by using a diagonally polarised local oscillator with the respective phase to the signal beam, see Eq. 4.17.[292] To measure correlations between the amplitude quadrature of one mode and the phase quadrature of the other mode (∗), the local oscillator of one mode has to be $\pi/2$-phase-shifted with respect to the other mode. This can be accomplished with a quarter-wave plate. The tricky part is measuring correlations between amplitude and phase quadratures of the same mode (⋆). Here, a trick helps:[293] One can measure a linear combination of amplitude and phase quadrature of the same mode. In an experiment, it means locking the local oscillator's phase not to measure the phase or the amplitude quadrature, but something in between, e.g. to $\phi = \pi/4$. From here, one can calculate the internal quadrature correlations with the help of earlier measurements of single-quadrature variances:

$$\mathrm{var}\,\hat{x}_c^{\pi/4} = \frac{1}{2}\left(\mathrm{var}\,\hat{x}_c + \mathrm{var}\,\hat{p}_c + 2\,\mathrm{cov}\,\hat{x}_c, \hat{p}_c\right). \tag{B.2}$$

C Maximum a-posteriori estimation for cavity characterisation

The eigenmode of a symmetric two-waist cavity, e.g. a bow-tie cavity, is determined by three out of five of the following parameters:

[290] Notation inspired by A. Samblowski, 'State Preparation for Quantum Information Science and Metrology', PhD thesis, Leibniz Universität Hannover, 2012, Eq. 3.8.

[291] One could also shape the signal beam as is suggested by V. D'Auria et al., 'Characterization of bipartite states using a single homodyne detector', *J. Opt. B* **7** (2005), S750–S753 and done by V. D'Auria et al., 'Full characterization of Gaussian bipartite entangled states by a single homodyne detector', *Phys. Rev. Lett.* **102** (2009), but that might be detrimental to the quantum state under test.

[292] This is where later the squeezing will be visible.

[293] See V. Händchen, 'Experimental analysis of Einstein-Podolsky-Rosen steering for quantum information applications', PhD thesis, Leibniz Universität Hannover, 2016, Sec. 3.5 and Samblowski, PhD thesis (2012), Sec. 3.3.

- (effective) radius of curvature of the mirrors, R_{eff},

- shorter distance between the two curved mirrors, d_1,

- longer distance between the two curved mirrors, d_2,

- (smaller) waist w_1 centred between the two curved mirrors,

- (bigger) waist w_2, also centred between the two curved mirrors.

Often and in our bow-tie cavities, the eigenmode and thus the waist (particularly the small waist) is *very* sensitive to the short distance between the curved mirrors and to the radii of curvature of the focusing mirrors. One characteristic of the eigenmode can be measured, though: the Gouy phase acquired over one round-trip, which is determined by the cavity elements, i.e. the propagations and the effective radii of curvature.

A non-normal angle of incidence on the curved mirrors leads to a second Gouy phase in the opposite plane of the first, but also to a new parameter, angle θ. I now have two equations of motion for the two Gouy phases, see Eq. 1.26, depending on the total of four parameters, d_1, d_2, R, and $\theta = \alpha/2$ as in Fig. 5.11.

The idea now to incorporate a prior belief on the parameters into the analysis. The *exact* value of d_1 is not known, but the error bar is also not too high. With priors for all parameters, and assumptions on the accurateness of the Gouy phase measurements, a most likely set of parameters causing the measurements can be devised. This is called *maximum a posteriori estimation* (MAP).

MAP tries to maximise the probability $P(\mathbf{p}|\mathbf{x})$ that the set of four parameters $\mathbf{p} = (p_1, p_2, p_3, p_4)$ caused the two measurements $\mathbf{x} = (x_1, x_2)$. According to Bayes' rule,

$$P(\mathbf{p}|\mathbf{x}) = \frac{P(\mathbf{x}|\mathbf{p})P(\mathbf{p})}{P(\mathbf{x})}. \tag{C.1}$$

When maximising $P(\mathbf{p}|\mathbf{x})$, the constant denominator $P(\mathbf{x})$ is not needed. Instead, models for probabilities $P(\mathbf{p}) = \prod_i P(p_i)$, here with the assumption of independent parameters, and a model connecting the measurement results with the parameter in order to obtain $P(\mathbf{x}|\mathbf{p})$ is needed. The latter is given by Eq. 1.26 and the additional assumption that the measurement results are normally distributed, with some standard deviation. Now, priors

Table C.1: Parameters for MAP. Note that length d_1 is corrected for the crystal's refractive index.

Parameter	in Fig. 5.11	μ	σ	measured/fit result
ψ_{vert}			6°	46°
ψ_{hor}			6°	35°
d_1	$2\overline{AB}$	10.2 cm	2 cm	10.67 cm
d_2	$2\overline{BCDE}$	1.45 m	0.2 m	1.449 m
R		100 mm	20 mm	100.1 mm
θ	$\alpha/2$	3.75°	2°	3.81°

for the parameters are needed, also normal distribution with some standard deviation:

$$\mathcal{N}(x - \mu, \sigma_x) = \frac{1}{\sqrt{2\pi\sigma_x^2}} e^{-\frac{(x-\mu)^2}{2\sigma_x^2}}. \tag{C.2}$$

The round-trip Gouy phases for the system described above is given by

$$\cos\psi_{\text{vert}}(d_1, d_2, R, \theta) = 1 - 2(d_1 + d_2)\frac{\cos\theta}{R} + 2d_1 d_2 \frac{\cos^2\theta}{R^2}, \tag{C.3}$$

$$\cos\psi_{\text{hor}}(d_1, d_2, R, \theta) = 1 - 2(d_1 + d_2)\frac{1}{R\cos\theta} + 2d_1 d_2 \frac{1}{R^2 \cos^2\theta}, \tag{C.4}$$

from Eq. 1.26 and Eqs. 1.25. The assumed mean and standard deviations from Tab. C.1 lead to priors. With them and assuming independent and identically distributed measurements, the quantity to be maximised over the parameters $\mathbf{p} = (d_1, d_2, R, \theta)$ is

$$P(\mathbf{p}|\mathbf{x}) = \mathcal{N}\left(\psi_{\text{vert}}(d_1, d_2, R, \theta) - \psi_{\text{vert}}, \sigma_\psi\right) \mathcal{N}\left(\psi_{\text{hor}}(d_1, d_2, R, \theta) - \psi_{\text{hor}}, \sigma_\psi\right)$$
$$\times \mathcal{N}(d_1 - \mu_{d_1}, \sigma_{d_1}) \mathcal{N}(d_2 - \mu_{d_2}, \sigma_{d_2}) \mathcal{N}(R - \mu_R, \sigma_R) \mathcal{N}(\theta - \mu_\theta, \sigma_\theta) \tag{C.5}$$

with measurements $\mathbf{x} = (\psi_{\text{vert}}, \psi_{\text{hor}})$. Because of big numbers and procedure, actually the negative logarithm of $P(\mathbf{p}|\mathbf{x})$ is numerically minimised with Matlab. The results are also displayed in Tab. C.1. The whole procedure

is quite sensitive to the priors. If one of the standard deviations becomes too big relative to the others, this will be the only parameter affected by the optimisation, so some trial and error is necessary.

D Picture of complete set-up on optical table

In the picture on pp. 220–221, the status of the optical table shortly before finishing this thesis is recorded. Beam paths of the experiments from Secs. 4 and 5 are drawn, except for the intracavity paths of the monolithic cavities (the silvery blocks) and dumped beams. Whenever beams seem to end nowhere, they hit a photodetector (or leave a monolithic cavity). Starting with the laser in the lower left corner, the beam traverses the beam preparation stage from laser to mode-cleaning cavity including polarisation homodyne lock (lower left) and second harmonic generator (SHG, lower centre), compare this to scheme in Fig. 4.15, followed by the non-degenerate optical parametric oscillator with the mode-matching cavity for green (lower right), the homodyne detection scheme and the mode-matching cavity for the homodyne detection (lower centre), compare this to scheme in Fig. 4.17. In the upper right, the 5-mirror coupled cavities can be seen (compare to Fig. 5.12). The assembly of the first components (laser, Faraday isolator) was done together with Bernd Schulte.

Works referenced in the Appendix

Boyd, R. W., *Nonlinear Optics*, Amsterdam et al.: Acad. Press, 2008.

D'Auria, V., S. Fornaro, A. Porzio, S. Solimeno, S. Olivares and M. G. A. Paris, 'Full characterization of Gaussian bipartite entangled states by a single homodyne detector', *Phys. Rev. Lett.* **102** (2009), DOI: 10.1103/PhysRevLett.102.020502, arXiv: 0805.1993.

D'Auria, V., A. Porzio, S. Solimeno, S. Olivares and M. G. Paris, 'Characterization of bipartite states using a single homodyne detector', *J. Opt. B* **7** (2005), S750–S753, DOI: 10.1088/1464-4266/7/12/044, arXiv: 0509180 [quant-ph] .

Händchen, V., 'Experimental analysis of Einstein-Podolsky-Rosen steering for quantum information applications', PhD thesis, Leibniz Universität Hannover, 2016, URL: http://edok01.tib.uni-hannover.de/edoks/e01dh16/857300237.pdf.

Samblowski, A., 'State Preparation for Quantum Information Science and Metrology', PhD thesis, Leibniz Universität Hannover, 2012, URL: http://edok01.tib.uni-hannover.de/edoks/e01dh12/717970612.pdf.
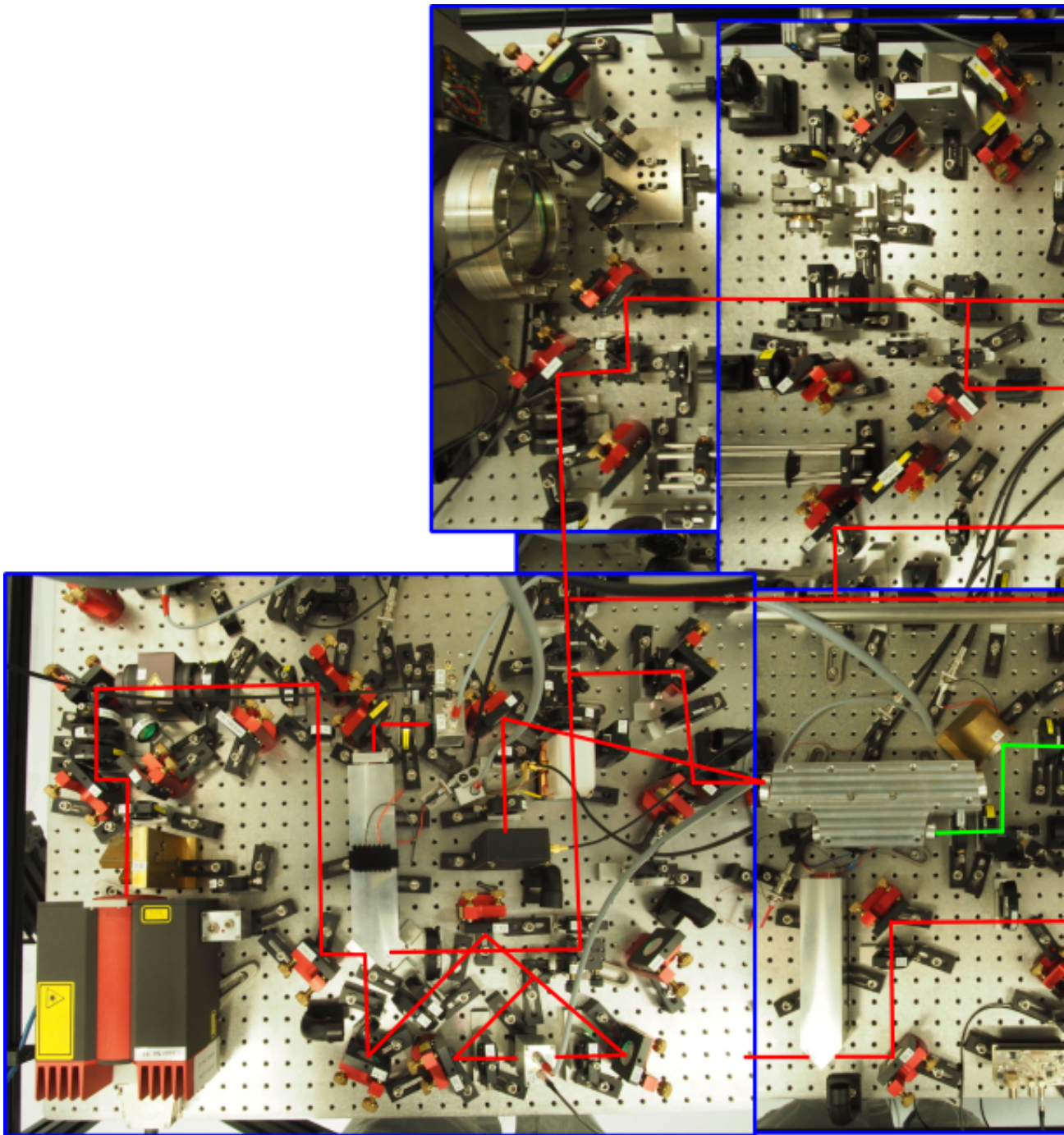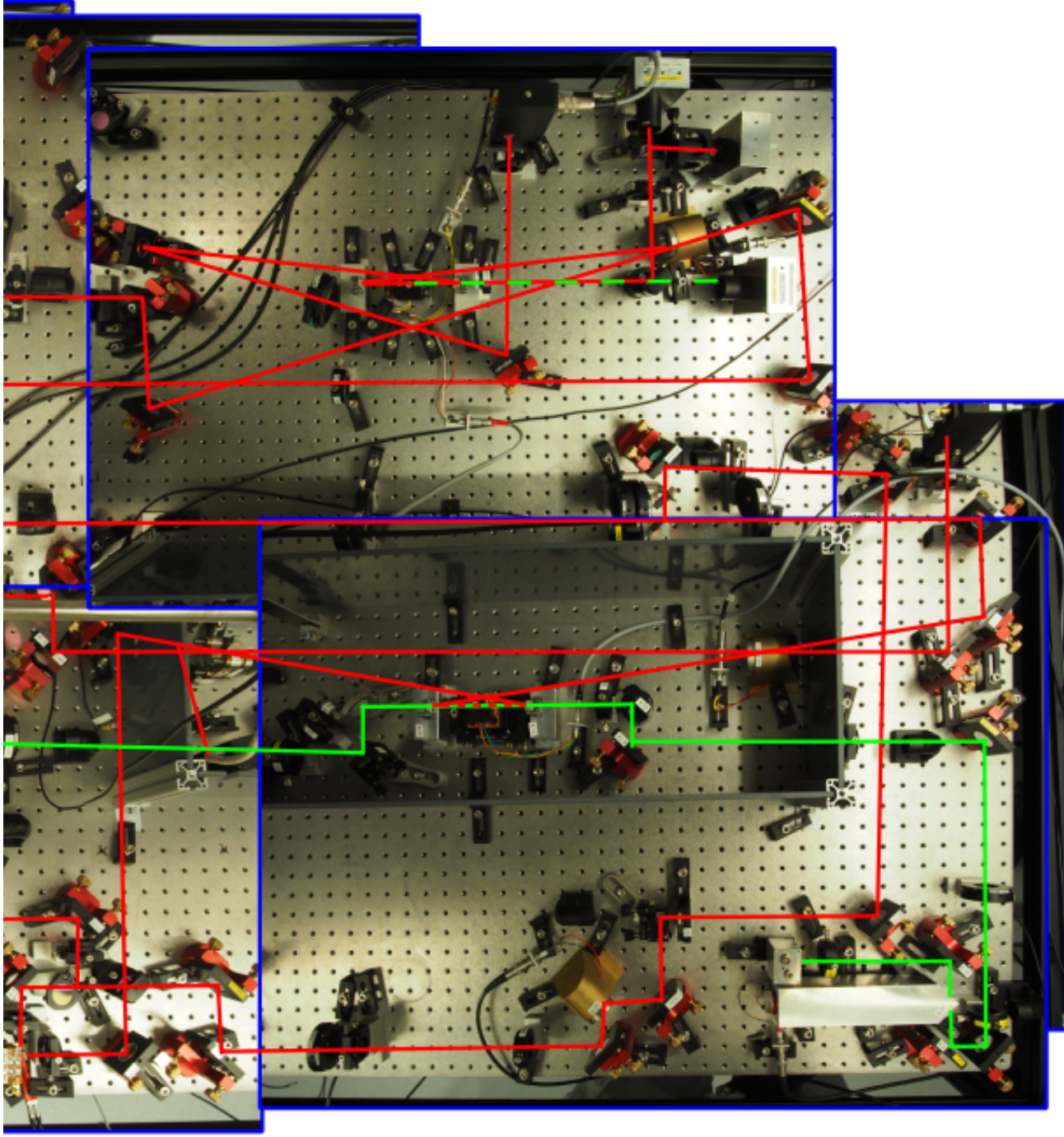
Bibliography

Aasi, J. et al., 'Advanced LIGO', *Class. Quantum Gravity* **32** (2015), 074001, DOI: 10.1088/0264-9381/32/7/074001.

Abramochkin, E. and V. Volostnikov, 'Beam transformations and nontransformed beams', *Opt. Commun.* **83** (1991), 123–135, DOI: 10.1016/0030-4018(91)90534-K.

Abramowitz, M. and I. A. Stegun, eds., *Handbook of Mathematical Functions: With Formulas, Graphs, and Mathematical Tables*, New York: Dover, 1972, URL: http://people.math.sfu.ca/%7B~%7Dcbm/aands/abramowitz%7B%5C_%7Dand%7B%5C_%7Dstegun.pdf.

Andersen, U. L., T. Gehring, C. Marquardt and G. Leuchs, '30 Years of Squeezed Light Generation', *Phys. Scr.* **91** (2016), 053001, DOI: 10.1088/0031-8949/91/5/053001, arXiv: 1511.03250.

Anderson, D. Z., 'Alignment of resonant optical cavities.', *Appl. Opt.* **23** (1984), 2944, DOI: 10.1364/AO.23.002944.

Andrews, R. W., R. W. Peterson, T. P. Purdy, K. Cicak, R. W. Simmonds, C. A. Regal and K. W. Lehnert, 'Bidirectional and efficient conversion between microwave and optical light', *Nat. Phys.* **10** (2014), 321–326, DOI: 10.1038/nphys2911.

Aoki, T., G. Takahashi and A. Furusawa, 'Squeezing at 946nm with periodically poled KTiOPO$_4$', *Opt. Express* **14** (2006), 6930, DOI: 10.1364/oe.14.006930.

Arai, K., *On the accumulated round-trip Gouy phase shift for a general optical cavity*, tech. rep., LIGO-T1300189, 2013, URL: https://dcc.ligo.org/LIGO-T1300189/public.

Aspelmeyer, M., T. J. Kippenberg and F. Marquardt, 'Cavity optomechanics', *Rev. Mod. Phys.* **86** (2014), 1391–1452, DOI: 10.1103/RevModPhys.86.1391, arXiv: 1303.0733.

Bachor, H.-A. and T. C. Ralph, *A Guide to Experiments in Quantum Optics*, Weinheim: Wiley, 2004, DOI: 10.1002/9783527619238.

Baker, C. G. and W. P. Bowen, 'Precision measurement: Sensing past the quantum limit', *Nature* **547** (2017), 164–165, DOI: 10.1038/547164a.

Bauchrowitz, J., T. Westphal and R. Schnabel, 'A graphical description of optical parametric generation of squeezed states of light', *Am. J. Phys.* **81** (2013), 767–771, DOI: 10.1119/1.4819195.

Bayer-Helms, F., 'Coupling coefficients of an incident wave and the modes of a spherical optical resonator in the case of mismatching and misalignment.', *Appl. Opt.* **23** (1984), 1369, DOI: 10.1364/AO.23.001369.

Black, E. D., 'An introduction to Pound–Drever–Hall laser frequency stabilization', *Am. J. Phys.* **69** (2001), 79–87, DOI: 10.1119/1.1286663, arXiv: 1309.7933.

Bloembergen, N., 'Conservation laws in nonlinear optics', *J. Opt. Soc. Am.* **70** (1980), 1429, DOI: 10.1364/JOSA.70.001429.

Bond, C., D. Brown, A. Freise and K. A. Strain, 'Interferometer techniques for gravitational-wave detection', *Living Rev. Relativ.* **19** (2016), 1–221, DOI: 10.1007/s41114-016-0002-8.

Boyd, G. D. and D. A. Kleinman, 'Parametric interaction of focused Gaussian light beams', *J. Appl. Phys.* **39** (1968), 3597–3639, DOI: 10.1063/1.1656831.

Boyd, R. W., *Nonlinear Optics*, Amsterdam et al.: Acad. Press, 2008.

Braginsky, V. and F. Khalili, 'Gravitational wave antenna with QND speed meter', *Phys. Lett. A* **147** (1990), 251–256, DOI: 10.1016/0375-9601(90)90442-Q.

Braginsky, V. B., Y. I. Vorontsov and K. S. Thorne, 'Quantum Nondemolition Measurements', *Science* **209** (1980), 547–557, DOI: 10.1126/science.209.4456.547.

Braunstein, L. S. and P. Van Loock, 'Quantum information with continuous variables', *Rev. Mod. Phys.* **77** (2005), 513–577, DOI: 10.1103/RevModPhys.77.513.

Buonanno, A. and Y. Chen, 'Optical noise correlations and beating the standard quantum limit in advanced gravitational-wave detectors', *Class. Quantum Gravity* **18** (2001), L95–L101, DOI: 10.1088/0264-9381/18/15/102.

Camerer, S., M. Korppi, A. Jöckel, D. Hunger, T. W. Hänsch and P. Treutlein, 'Realization of an optomechanical interface between ultracold atoms and a membrane', *Phys. Rev. Lett.* **107** (2011), DOI: 10.1103/PhysRevLett.107.223001.

Caves, C. M., 'Quantum-mechanical radiation-pressure fluctuations in an interferometer', *Phys. Rev. Lett.* **45** (1980), 75–79, DOI: 10.1103/PhysRevLett.45.75.

Caves, C. M., K. S. Thorne, R. W. Drever, V. D. Sandberg and M. Zimmermann, 'On the measurement of a weak classical force coupled to a quantum-

mechanical oscillator. I. Issues of principle', *Rev. Mod. Phys.* **52** (1980), 341–392, DOI: 10.1103/RevModPhys.52.341.

Chelkowski, S., 'Squeezed light and laser interferometric gravitational wave detectors', PhD thesis, Leibniz Universität Hannover, 2007, URL: https://edocs.tib.eu/files/e01dh07/537859527.pdf.

Clerk, A. A., M. H. Devoret, S. M. Girvin, F. Marquardt and R. J. Schoelkopf, 'Introduction to quantum noise, measurement, and amplification', *Rev. Mod. Phys.* **82** (2010), 1155–1208, DOI: 10.1103/RevModPhys.82.1155.

Collett, M. J. and C. W. Gardiner, 'Squeezing of intracavity and traveling-wave light fields produced in parametric amplification', *Phys. Rev. A* **30** (1984), 1386–1391, DOI: 10.1103/PhysRevA.30.1386.

Collett, M. J. and D. F. Walls, 'Squeezing spectra for nonlinear optical systems', *Phys. Rev. A* **32** (1985), 2887–2892, DOI: 10.1103/PhysRevA.32.2887.

Cripe, J., N. Aggarwal, R. Lanza, A. Libson, R. Singh, P. Heu, D. Follman, G. D. Cole, N. Mavalvala and T. Corbitt, 'Observation of a room-temperature oscillator's motion dominated by quantum fluctuations over a broad audio-frequency band' (2018), arXiv: 1802.10069.

D'Auria, V., S. Fornaro, A. Porzio, S. Solimeno, S. Olivares and M. G. A. Paris, 'Full characterization of Gaussian bipartite entangled states by a single homodyne detector', *Phys. Rev. Lett.* **102** (2009), DOI: 10.1103/PhysRevLett.102.020502, arXiv: 0805.1993.

D'Auria, V., A. Porzio, S. Solimeno, S. Olivares and M. G. Paris, 'Characterization of bipartite states using a single homodyne detector', *J. Opt. B* **7** (2005), S750–S753, DOI: 10.1088/1464-4266/7/12/044, arXiv: 0509180 [quant-ph].

Danilishin, S. L. and F. Y. Khalili, 'Quantum Measurement Theory in Gravitational-Wave Detectors', *Living Rev. Relativ.* **15** (2012), 5–147, DOI: 10.12942/lrr-2012-5.

Danilishin, S. L., F. Y. Khalili and H. Miao, 'Advanced quantum techniques for future gravitational-wave detectors', *Living Rev. Relativ.* **22** (2019), 2–89, DOI: 10.1007/s41114-019-0018-y.

Datasheet Agilent IDP-15 Dry Scroll Vacuum Pump, Agilent, URL: https://www.agilent.com/cs/library/datasheets/public/IDP-15_5991-7604EN_DataSheet_LR.pdf.

Datasheet Mephisto, Coherent, URL: https://edge.coherent.com/assets/pdf/COHR%7B%5C_%7DMephisto%7B%5C_%7DDS%7B%5C_%7D0417%7B%5C_%7D2.pdf.

Datasheet Newport 4004 Broadband Phase Modulator, Newport, URL: https://www.newport.com/medias/sys_master/images/images/h65/hcc/8797007839262/400X-and-406X-User-Manual-Rev-J.pdf.

Denker, T., 'High-precision metrology with high-frequency nonclassical light sources', PhD thesis, Leibniz Universität Hannover, 2016, URL: http://edok01.tib.uni-hannover.de/edoks/e01dh16/862559057.pdf.

Drever, R. W., J. L. Hall, F. V. Kowalski, J. Hough, G. M. Ford, A. J. Munley and H. Ward, 'Laser phase and frequency stabilization using an optical resonator', *Appl. Phys. B* **31** (1983), 97–105, DOI: 10.1007/BF00702605, arXiv: 1602.03504.

Eiermann, B., P. Treutlein, T. Anker, M. Albiez, M. Taglieber, K. P. Marzlin and M. K. Oberthaler, 'Dispersion Management for Atomic Matter Waves', *Phys. Rev. Lett.* **91** (2003), 060402, DOI: 10.1103/PhysRevLett.91.060402.

Einstein, A., B. Podolsky and N. Rosen, 'Can Quantum-Mechanical Description of Physical Reality Be Considered Complete?', *Phys. Rev.* **47** (1935), 777–780, DOI: 10.1103/PhysRev.47.777.

Erden, M. F. and H. M. Ozaktas, 'Accumulated Gouy phase shift in Gaussian beam propagation through first-order optical systems', *J. Opt. Soc. Am. A* **14** (2008), 2190, DOI: 10.1364/josaa.14.002190.

Gardiner, C. W. and P. Zoller, *Quantum noise : a handbook of Markovian and non-Markovian quantum stochastic methods with applications to quantum optics*, Berlin et al.: Springer, 2000.

Gerry, C. C. and P. L. Knight, *Introductory Quantum Optics*, Cambridge et al.: Cambridge University Press, 2005.

Gröblacher, S., 'Quantum opto-mechanics with micromirrors: combining nano-mechanics with quantum optics', PhD thesis, Universität Wien, 2010.

Gröblacher, S., K. Hammerer, M. R. Vanner and M. Aspelmeyer, 'Observation of strong coupling between a micromechanical resonator and an optical cavity field', *Nature* **460** (2009), 724–727, DOI: 10.1038/nature08171, arXiv: 0903.5293.

Guha, S., 'Focusing dependence of the efficiency of a singly resonant optical parametric oscillator', *Appl. Phys. B* **66** (1998), 663–675, DOI: 10.1007/s003400050453.

Guha, S., F. J. Wu and J. Falk, 'The Effects of Focusing on Parametric Oscillation', *IEEE J. Quantum Electron.* **18** (1982), 907–912, DOI: 10.1109/JQE.1982.1071624.

Hammerer, K., M. Aspelmeyer, E. S. Polzik and P. Zoller, 'Establishing Einstein-Poldosky-Rosen Channels between Nanomechanics and Atomic Ensembles',

Phys. Rev. Lett. **102** (2009), 020501, DOI: 10.1103/PhysRevLett.102.020501, arXiv: 0804.3005.

Hammerer, K., A. S. Sørensen and E. S. Polzik, 'Quantum interface between light and atomic ensembles', *Rev. Mod. Phys.* **82** (2010), 1041–1093, DOI: 10.1103/RevModPhys.82.1041.

Händchen, V., 'Experimental analysis of Einstein-Podolsky-Rosen steering for quantum information applications', PhD thesis, Leibniz Universität Hannover, 2016, URL: http://edok01.tib.uni-hannover.de/edoks/e01dh16/857300237.pdf.

Hansch, T. and B. Couillaud, 'Laser frequency stabilization by polarization spectroscopy of a reflecting reference cavity', *Opt. Commun.* **35** (1980), 441–444, DOI: 10.1016/0030-4018(80)90069-3.

Haus, H. and W. Huang, 'Coupled-mode theory', *Proc. IEEE* **79** (1991), 1505–1518, DOI: 10.1109/5.104225.

Heurs, M., I. R. Petersen, M. R. James and E. H. Huntington, 'Homodyne locking of a squeezer', *Opt. Lett.* **34** (2009), 2465, DOI: 10.1364/OL.34.002465, arXiv: 0907.3323.

Ismail, N., C. C. Kores, D. Geskus and M. Pollnau, 'Fabry-Pérot resonator: spectral line shapes, generic and related Airy distributions, linewidths, finesses, and performance at low or frequency-dependent reflectivity', *Opt. Express* **24** (2016), 16366, DOI: 10.1364/OE.24.016366.

Jayich, A. M., J. C. Sankey, B. M. Zwickl, C. Yang, J. D. Thompson, S. M. Girvin, A. A. Clerk, F. Marquardt and J. G. Harris, 'Dispersive optomechanics: A membrane inside a cavity', *New J. Phys.* **10** (2008), 095008, DOI: 10.1088/1367-2630/10/9/095008.

Känel, E. von, *To be published*, Master thesis, Leibniz Universität Hannover.

Khalili, F. Y. and E. S. Polzik, 'Overcoming the Standard Quantum Limit in Gravitational Wave Detectors Using Spin Systems with a Negative Effective Mass', *Phys. Rev. Lett.* **121** (2018), 031101, DOI: 10.1103/PhysRevLett.121.031101, arXiv: 1710.10405.

Kimble, H. J., Y. Levin, A. B. Matsko, K. S. Thorne and S. P. Vyatchanin, 'Conversion of conventional gravitational-wave interferometers into quantum nondemolition interferometers by modifying their input and/or output optics', *Phys. Rev. D* **65** (2001), 022002, DOI: 10.1103/PhysRevD.65.022002.

Kimble, H. J., 'Course 10: Quantum Fluctuations in Quantum Optics – Squeezing and Related Phenomena', in: *Systèmes Fondamentaux en Optique Quantique, Les Houches, Session LIII, 1990*, ed. by J. Dalibard, J. M. Raimond and J. Zinn-Justin, Amsterdam: Elsevier, 1992.

Kogelnik, H. and T. Li, 'Laser Beams and Resonators', *Proc. IEEE* **54** (1966), 1312–1329, DOI: 10.1109/PROC.1966.5119.

Kohler, J., J. A. Gerber, E. Dowd and D. M. Stamper-Kurn, 'Negative-Mass Instability of the Spin and Motion of an Atomic Gas Driven by Optical Cavity Backaction', *Phys. Rev. Lett.* **120** (2018), 013601, DOI: 10.1103/PhysRevLett.120.013601.

Lastzka, N., 'Numerical modelling of classical and quantum effects in nonlinear optical systems', PhD thesis, Leibniz Universität Hannover, 2010, URL: http://edok01.tib.uni-hannover.de/edoks/e01dh11/643368353.pdf.

Lau, H.-K. and A. A. Clerk, 'Fundamental limits and non-reciprocal approaches in non-Hermitian quantum sensing', *Nat. Commun.* **9** (2018), 4320, DOI: 10.1038/s41467-018-06477-7.

Law, C. K., 'Interaction between a moving mirror and radiation pressure: A Hamiltonian formulation', *Phys. Rev. A* **51** (1995), 2537–2541, DOI: 10.1103/PhysRevA.51.2537.

Leonhardt, U. and A. Neumaier, 'Explicit effective Hamiltonians for general linear quantum-optical networks', *J. Opt. B* **6** (2003), L1–L4, DOI: 10.1088/1464-4266/6/1/L01, arXiv: 0306123 [quant-ph] .

Louisell, W. H., A. Yariv and A. E. Siegman, 'Quantum fluctuations and noise in parametric processes. I.', *Phys. Rev.* **124** (1961), 1646–1654, DOI: 10.1103/PhysRev.124.1646.

Masada, G., T. Suzudo, Y. Satoh, H. Ishizuki, T. Taira and A. Furusawa, 'Efficient generation of highly squeezed light with periodically poled MgO:LiNbO$_3$', *Opt. Express* **18** (2010), 13114, DOI: 10.1364/OE.18.013114.

Mathis, C., C. Taggiasco, L. Bertarelli, I. Boscolo and J. R. Tredicce, 'Resonances and instabilities in a bidirectional ring laser', *Phys. D Nonlinear Phenom.* **96** (1996), 242–250, DOI: 10.1016/0167-2789(96)00024-3.

Maxwell, J. C., *A Treatise on Electricity and Magnetism*, Oxford: Clarendon, 1873, URL: https://gallica.bnf.fr/ark:/12148/bpt6k95176j/.

Meers, B. J., 'Recycling in laser-interferometric gravitational-wave detectors', *Phys. Rev. D* **38** (1988), 2317–2326, DOI: 10.1103/PhysRevD.38.2317.

Milburn, G. and D. Walls, 'Production of squeezed states in a degenerate parametric amplifier', *Opt. Commun.* **39** (1981), 401–404, DOI: 10.1016/0030-4018(81)90232-7.

Miri, M.-A. and A. Alù, 'Exceptional points in optics and photonics', *Science* **363** (2019), eaar7709, DOI: 10.1126/science.aar7709.

Mizuno, J., 'Comparison of optical configurations for laser-interferometric gravitational-wave detectors', PhD thesis, Universität Hannover and Max-Planck-Institut für Quantenoptik, Garching, 1995.

Møller, C. B., R. A. Thomas, G. Vasilakis, E. Zeuthen, Y. Tsaturyan, M. Balabas, K. Jensen, A. Schliesser, K. Hammerer and E. S. Polzik, 'Quantum backaction-evading measurement of motion in a negative mass reference frame', *Nature* **547** (2017), 191–195, DOI: 10.1038/nature22980, arXiv: 1608.03613.

Murch, K. W., K. L. Moore, S. Gupta and D. M. Stamper-Kurn, 'Observation of quantum-measurement backaction with an ultracold atomic gas', *Nat. Phys.* **4** (2008), 561–564, DOI: 10.1038/nphys965.

Nikogosyan, D. N., *Nonlinear Optical Crystals: A Complete Survey*, New York: Springer, 2005, DOI: 10.1007/b138685, URL: http://link.springer.com/10.1007/b138685.

Norte, R. A., J. P. Moura and S. Gröblacher, 'Mechanical Resonators for Quantum Optomechanics Experiments at Room Temperature', *Phys. Rev. Lett.* **116** (2016), 147202, DOI: 10.1103/PhysRevLett.116.147202, arXiv: 1511.06235.

Novotny, L., 'Strong coupling, energy splitting, and level crossings: A classical perspective', *Am. J. Phys.* **78** (2010), 1199–1202, DOI: 10.1119/1.3471177, URL: https://www.photonics.ethz.ch/fileadmin/user%7B%5C_%7Dupload/novotny10a.pdf.

Ockeloen-Korppi, C. F., E. Damskägg, J. M. Pirkkalainen, A. A. Clerk, M. J. Woolley and M. A. Sillanpää, 'Quantum Backaction Evading Measurement of Collective Mechanical Modes', *Phys. Rev. Lett.* **117** (2016), 140401, DOI: 10.1103/PhysRevLett.117.140401.

Ogata, K., *Modern Control Engineering*, 5th ed., Upper Saddle River, NJ: Pearson, 2010.

Oishi, T. and M. Tomita, 'Inverted coupled-resonator-induced transparency', *Phys. Rev. A* **88** (2013), 063804, DOI: 10.1103/PhysRevA.88.013813.

Ou, Z. Y., S. F. Pereira and H. J. Kimble, 'Realization of the Einstein-Podolsky-Rosen paradox for continuous variables in nondegenerate parametric amplification', *Appl. Phys. B* **55** (1992), 265–278, DOI: 10.1007/BF00325015.

Özdemir, S. K., S. Rotter, F. Nori and L. Yang, 'Parity–time symmetry and exceptional points in photonics', *Nat. Mater.* (2019), DOI: 10.1038/s41563-019-0304-9, URL: http://www.nature.com/articles/s41563-019-0304-9.

Petersen, I. R. and E. H. Huntington, 'Implementation of a direct coupling coherent quantum observer including observer measurements', in: *Proc. 2016 Am. Control Conf.* 2016, pp. 4765–4768, DOI: 10.1109/ACC.2016.7526107.

Pinard, M., Y. Hadjar and A. Heidmann, 'Effective mass in quantum effects of radiation pressure', *Eur. Phys. J. C* **7** (1999), 107–111, DOI: 10.1007/s100530050354.

Polzik, E. S. and K. Hammerer, 'Trajectories without quantum uncertainties', *Ann. Phys.* **527** (2015), A15–A20, DOI: 10.1002/andp.201400099, arXiv: 1405.3067.

Purdy, T. P., R. W. Peterson and C. A. Regal, 'Observation of Radiation Pressure Shot Noise on a Macroscopic Object', *Science* **339** (2013), 801–804, DOI: 10.1126/science.1231282.

Riedinger, R., A. Wallucks, I. Marinković, C. Löschnauer, M. Aspelmeyer, S. Hong and S. Gröblacher, 'Remote quantum entanglement between two micromechanical oscillators', *Nature* **556** (2018), 473–477, DOI: 10.1038/s41586-018-0036-z.

Saleh, B. E. A. and M. C. Teich, *Fundamentals of Photonics*, 2nd, Hoboken, NJ: Wiley, 2007.

Samblowski, A., 'State Preparation for Quantum Information Science and Metrology', PhD thesis, Leibniz Universität Hannover, 2012, URL: http://edok01.tib.uni-hannover.de/edoks/e01dh12/717970612.pdf.

Schnabel, R., 'Squeezed states of light and their applications in laser interferometers', *Phys. Rep.* **684** (2017), 1–51, DOI: 10.1016/j.physrep.2017.04.001, arXiv: 1611.03986.

Schori, C., J. L. Sørensen and E. S. Polzik, 'Narrow-band frequency tunable light source of continuous quadrature entanglement', *Phys. Rev. A* **66** (2002), 10, DOI: 10.1103/PhysRevA.66.033802, arXiv: 0205015 [quant-ph].

Shaddock, D. A., M. B. Gray and D. E. McClelland, 'Frequency locking a laser to an optical cavity by use of spatial mode interference', *Opt. Lett.* **24** (1999), 1499, DOI: 10.1364/OL.24.001499, arXiv: 0809.0545.

Siegman, A. E., *Lasers*, Sausalito, CA: University Science Books, 1986.

Skorupka, S., 'Rauschuntersuchungen an hochstabilen Lasersystemen für die wissenschaftliche Weltraummission LISA', PhD thesis, Leibniz Universität Hannover, 2007, URL: https://edocs.tib.eu/files/e01dh07/551342838.pdf.

Smith, A., *SNLO*, URL: http://www.as-photonics.com/snlo.

Staley, A. et al., 'Achieving resonance in the Advanced LIGO gravitational-wave interferometer', *Class. Quantum Gravity* **31** (2014), 245010, DOI: 10.1088/0264-9381/31/24/245010.

Steinmeyer, D., 'Towards Coherent Quantum Noise Cancellation. Untersuchungen zur kohärenten Unterdrückung von Quantenrauschen in Interferometern', Master thesis, Leibniz Universität Hannover, 2014.

Thompson, R. J., G. Rempe and H. J. Kimble, 'Observation of normal-mode splitting for an atom in an optical cavity', *Phys. Rev. Lett.* **68** (1992), 1132–1135, DOI: 10.1103/PhysRevLett.68.1132, arXiv: 1203.0743.

Thüring, A., 'Investigations of coupled and Kerr non-linear optical resonators', PhD thesis, Leibniz Universität Hannover, 2009, URL: https://edocs.tib.eu/files/e01dh09/607882433.pdf.

Thüring, A., R. Schnabel, H. Lück and K. Danzmann, 'Detuned Twin-Signal-Recycling for ultrahigh-precision interferometers', *Opt. Lett.* **32** (2007), 985, DOI: 10.1364/ol.32.000985.

Tsang, M. and C. M. Caves, 'Coherent quantum-noise cancellation for optomechanical sensors', *Phys. Rev. Lett.* **105** (2010), 123601, DOI: 10.1103/PhysRevLett.105.123601, arXiv: 1006.1005.

Tsang, M. and C. M. Caves, 'Evading quantum mechanics: Engineering a classical subsystem within a quantum environment', *Phys. Rev. X* **2** (2012), 031016, DOI: 10.1103/PhysRevX.2.031016, arXiv: 1203.2317.

Tsaturyan, Y., A. Barg, E. S. Polzik and A. Schliesser, 'Ultracoherent nanomechanical resonators via soft clamping and dissipation dilution', *Nat. Nanotechnol.* **12** (2017), 776–783, DOI: 10.1038/nnano.2017.101, arXiv: 1608.00937.

Vahlbruch, H., M. Mehmet, K. Danzmann and R. Schnabel, 'Detection of 15 dB Squeezed States of Light and their Application for the Absolute Calibration of Photoelectric Quantum Efficiency', *Phys. Rev. Lett.* **117** (2016), 110801, DOI: 10.1103/PhysRevLett.117.110801.

Vasilakis, G., V. Shah and M. V. Romalis, 'Stroboscopic Backaction Evasion in a Dense Alkali-Metal Vapor', *Phys. Rev. Lett.* **106** (2011), 143601, DOI: 10.1103/PhysRevLett.106.143601.

Walls, D. F. and G. J. Milburn, *Quantum Optics*, Berlin, Heidelberg: Springer, 2008, DOI: 10.1007/978-3-540-28574-8.

Weis, S., R. Rivière, S. Deléglise, E. Gavartin, O. Arcizet, A. Schliesser and T. J. Kippenberg, 'Optomechanically Induced Transparency', *Science* **330** (2010), 1520–1523, DOI: 10.1126/science.1195596.

Weiss, R., 'Electromagnetically coupled broadband gravitational wave antenna', *Q. Prog. Rep. Research Lab. Electronics, Massachusetts Inst. Technol.* **105**

(1972), 54, URL: https://dcc.ligo.org/public/0038/P720002/001/P720002-00.pdf.

Weißbrich, H., 'Untersuchungen zur Frequenzstabilisierung gekoppelter optischer Resonatoren', Master thesis, Leibniz Universität Hannover, 2017.

Wimmer, M. H., 'Coupled nonclassical systems for coherent backaction noise cancellation', PhD thesis, Leibniz Universität Hannover, 2016, URL: http://edok01.tib.uni-hannover.de/edoks/e01dh16/863136931.pdf.

Wimmer, M. H., D. Steinmeyer, K. Hammerer and M. Heurs, 'Coherent cancellation of backaction noise in optomechanical force measurements', *Phys. Rev. A* **89** (2014), 053836, DOI: 10.1103/PhysRevA.89.053836, arXiv: 1403.2992.

Woolley, M. J. and A. A. Clerk, 'Two-mode back-action-evading measurements in cavity optomechanics', *Phys. Rev. A* **87** (2013), 063846, DOI: 10.1103/PhysRevA.87.063846.

Wu, L.-A., M. Xiao and H. J. Kimble, 'Squeezed states of light from an optical parametric oscillator', *J. Opt. Soc. Am. B* **4** (2008), 1465, DOI: 10.1364/josab.4.001465, URL: https://authors.library.caltech.edu/4725/1/WULjosab87.pdf.

Wysin, G. M., 'Quantization of the Free Electromagnetic Field: Photons and Operators', 2011, URL: https://www.phys.ksu.edu/personal/wysin/notes/quantumEM.pdf.

Yamamoto, N., 'Coherent versus Measurement Feedback: Linear Systems Theory for Quantum Information', *Phys. Rev. X* **4** (2014), 041029, DOI: 10.1103/PhysRevX.4.041029.

Yariv, A., *Quantum Electronics*, New York et al., 1989.

Yurke, B., 'Optical back-action-evading amplifiers', *J. Opt. Soc. Am. B* **2** (1985), 732, DOI: 10.1364/JOSAB.2.000732.

Zhang, K., P. Meystre and W. Zhang, 'Back-action-free quantum optomechanics with negative-mass Bose-Einstein condensates', *Phys. Rev. A* **88** (2013), 043632, DOI: 10.1103/PhysRevA.88.043632.

Zhang, T. C., K. W. Goh, C. W. Chou, P. Lodahl and H. J. Kimble, 'Quantum teleportation of light beams', *Phys. Rev. A* **67** (2003), 16, DOI: 10.1103/PhysRevA.67.033802, arXiv: 0207076 [quant-ph].

Zondy, J.-J., D. Touahri and O. Acef, 'Absolute value of the d_{36} nonlinear coefficient of AgGaS$_2$: prospect for a low-threshold doubly resonant oscillator-based 3:1 frequency divider', *J. Opt. Soc. Am. B* **14** (2008), 2481, DOI: 10.1364/josab.14.002481.

Acknowledgements

The institute has been a fabulous place to work. So many different fields coming together on a regular basis – cosmology, astronomy, GR, space missions, large-scale experiments, optics, quantum mechanics, ... there was always something interesting going on, an interesting talk to hear. This was mirrored on the lecture weeks, a splendid institution! *The* highlight was of course the detection of the first gravitational-wave signal in 2015. When I started here, I hoped for that to happen during my time at the institute, but that it actually happened is still hard to fathom. The institute's infrastructure has been much appreciated, especially the electronics workshop and the mechanics workshop. You guys really made life easier.

Thank you, Michèle, that you took me as your student. You gave me a lot of freedom which directions to pursue and what problem to tackle next. You always had an ear for me, were open for travel suggestions, and gave valuable feedback, especially when writing up. That was *extremely* helpful.

Thank you, Klemens, for always shedding new light on something, for making me curious about quantum optics theory, and for your razor-sharp view on problems and physics. There's a lot to learn from you for everybody.

Here's to a couple of others ... For good start into the group to: Timo, Max, Dirk. Also for the electronics you left us and I did not have to build myself. For a fresh breeze and many interesting discussions to: Jonas and Dennis. Also for even more electronics I did not have to build myself. For more discussions to: Moritz, Stefan, Henning, Vitus. For travel money and valuable lessons learnt for life to: the RTG1991. For proofreading to: Bernd, Jonas, Dennis, Margot, Dirk, Chris. For carrying me through the thesis and being the best office mate one could wish for. For night shifts and for beer to: Bernd. I probably would not have made it without you #bromance. For making me smile when I came home late at night from the institute to: my WG.

An dieser Stelle möchte ich noch meine Mama grüßen. Hallo Mama :) Und meinen Papa. Hallo Papa :)

Curriculum vitæ

Daniel Steinmeyer

daniel.steinmeyer@aei.mpg.de

Education

Max Planck Institute for Gravitational Physics (Albert Einstein Institute) and Institute for Gravitational Physics, Leibniz Universität Hannover, Hanover, Germany

PhD student within the International Max Planck Research School on Gravitational Wave Astronomy, and within the Research Training Group 1991 – Quantum Mechanical Noise in Complex Systems	since 10/2014

Leibniz Universität Hannover, Hanover, Germany

MSc in Physics, Minor Computer Science	10/2011 – 04/2014
MA in New German Literature Studies (no degree)	10/2011 – 04/2014
BSc in Physics, Minor Business Administration	04/2009 – 11/2011
Interdisciplinary Bachelor's Degree Course, Major Physics, Minor German Studies (for teaching certificate)	10/2007 – 11/2011

Università di Bologna, Bologna, Italy

Courses in Italian Language Studies, Literature Studies, and Intercultural Mediation	09/2012 – 03/2013

California Institute of Technology, Pasadena, USA

Research Internship in the LIGO group	07 – 09/2011

Gymnasium Andreanum, Hildesheim, Germany

Abitur	29/06/2007

List of Publications

Publications with short author-list

Wimmer, M. H., D. Steinmeyer, K. Hammerer and M. Heurs, 'Coherent cancellation of backaction noise in optomechanical force measurements', *Phys. Rev. A* **89** (2014), 053836, DOI: 10.1103/PhysRevA.89.053836, arXiv: 1403.2992.

Publications as a member of the LSC

Publications by the LIGO Scientific Collaboration (LSC) with myself as co-author, sorted by arXiv identifier from most to least recent.

Abbott, B. P. et al., 'Search for Transient Gravitational-wave Signals Associated with Magnetar Bursts during Advanced LIGO's Second Observing Run', *Astrophys. J.* **874** (2019), 163, DOI: 10.3847/1538-4357/ab0e15, arXiv: 1902.01557.

Abbott, B. P. et al., 'Low-latency Gravitational-wave Alerts for Multimessenger Astronomy during the Second Advanced LIGO and Virgo Observing Run', *Astrophys. J.* **875** (2019), 161, DOI: 10.3847/1538-4357/ab0c8f, arXiv: 1901.03310.

Soares-Santos, M. et al., 'First Measurement of the Hubble Constant from a Dark Standard Siren using the Dark Energy Survey Galaxies and the LIGO/Virgo Binary–Blackhole Merger GW170814', *Astrophys. J.* **876** (2019), L7, DOI: 10.3847/2041-8213/ab14f1, arXiv: 1901.01540.

Abbott, B. P. et al., 'Searches for Continuous Gravitational Waves from 15 Supernova Remnants and Fomalhaut b with Advanced LIGO', *Astrophys. J.* **875** (2019), 122, DOI: 10.3847/1538-4357/ab113b, arXiv: 1812.11656.

Albert, A. et al., 'Search for Multimessenger Sources of Gravitational Waves and High-energy Neutrinos with Advanced LIGO during Its First Observing Run, ANTARES, and IceCube', *Astrophys. J.* **870** (2019), 134, DOI: 10.3847/1538-4357/aaf21d, arXiv: 1810.10693.

Burns, E. et al., 'A Fermi Gamma-Ray Burst Monitor Search for Electromagnetic Signals Coincident with Gravitational-wave Candidates in Advanced LIGO's First Observing Run', *Astrophys. J.* **871** (2019), 90, DOI: 10.3847/1538-4357/aaf726, arXiv: 1810.02764.

Abbott, B. P. et al., 'Search for Gravitational Waves from a Long-lived Remnant of the Binary Neutron Star Merger GW170817', *Astrophys. J.* **875** (2019), 160, DOI: 10.3847/1538-4357/ab0f3d, arXiv: 1810.02581.

Abbott, B. P. et al., 'Constraining the p-Mode–g-Mode Tidal Instability with GW170817', *Phys. Rev. Lett.* **122** (2019), 061104, DOI: 10.1103/PhysRevLett.122.061104, arXiv: 1808.08676.

Abbott, B. P. et al., 'Search for Subsolar-Mass Ultracompact Binaries in Advanced LIGO's First Observing Run', *Phys. Rev. Lett.* **121** (2018), 231103, DOI: 10.1103/PhysRevLett.121.231103, arXiv: 1808.04771.

Abbott, B. P. et al., 'GW170817: Measurements of Neutron Star Radii and Equation of State', *Phys. Rev. Lett.* **121** (2018), 161101, DOI: 10.1103/PhysRevLett.121.161101, arXiv: 1805.11581.

Abbott, B. P. et al., 'Properties of the Binary Neutron Star Merger GW170817', *Phys. Rev. X* **9** (2019), 011001, DOI: 10.1103/PhysRevX.9.011001, arXiv: 1805.11579.

Abbott, B. P. et al., 'Search for Tensor, Vector, and Scalar Polarizations in the Stochastic Gravitational-Wave Background', *Phys. Rev. Lett.* **120** (2018), 201102, DOI: 10.1103/PhysRevLett.120.201102, arXiv: 1802.10194.

Abbott, B. P. et al., 'Full band all-sky search for periodic gravitational waves in the O1 LIGO data', *Phys. Rev. D* **97** (2018), 102003, DOI: 10.1103/PhysRevD.97.102003, arXiv: 1802.05241.

Abbott, B. P. et al., 'Constraints on cosmic strings using data from the first Advanced LIGO observing run', *Phys. Rev. D* **97** (2018), 102002, DOI: 10.1103/PhysRevD.97.102002, arXiv: 1712.01168.

Abbott, B. P. et al., 'All-sky search for long-duration gravitational wave transients in the first Advanced LIGO observing run', *Class. Quantum Gravity* **35** (2018), 065009, DOI: 10.1088/1361-6382/aaab76, arXiv: 1711.06843.

Abbott, B. P. et al., 'GW170608: Observation of a 19 Solar-mass Binary Black Hole Coalescence', *Astrophys. J. Lett.* **851** (2017), L35, DOI: 10.3847/2041-8213/aa9f0c, arXiv: 1711.05578.

Abbott, B. P. et al., 'Search for Post-merger Gravitational Waves from the Remnant of the Binary Neutron Star Merger GW170817', *Astrophys. J. Lett.* **851** (2017), L16, DOI: 10.3847/2041-8213/aa9a35, arXiv: 1710.09320.

Albert, A. et al., 'Search for High-energy Neutrinos from Binary Neutron Star Merger GW170817 with ANTARES, IceCube, and the Pierre Auger Observatory', *Astrophys. J. Lett.* **850** (2017), L35, DOI: 10.3847/2041-8213/aa9aed, arXiv: 1710.05839.

Abbott, B. P. et al., 'On the Progenitor of Binary Neutron Star Merger GW170817', *Astrophys. J. Lett.* **850** (2017), L40, DOI: 10.3847/2041-8213/aa93fc, arXiv: 1710.05838.

Abbott, B. P. et al., 'GW170817: Implications for the Stochastic Gravitational-Wave Background from Compact Binary Coalescences', *Phys. Rev. Lett.* **120** (2018), 091101, DOI: 10.1103/PhysRevLett.120.091101, arXiv: 1710.05837.

Abbott, B. P. et al., 'Estimating the Contribution of Dynamical Ejecta in the Kilonova Associated with GW170817', *Astrophys. J. Lett.* **850** (2017), L39, DOI: 10.3847/2041-8213/aa9478, arXiv: 1710.05836.

Abbott, B. P. et al., 'A gravitational-wave standard siren measurement of the Hubble constant', *Nature* **551** (2017), 85–88, DOI: 10.1038/nature24471, arXiv: 1710.05835.

Abbott, B. P. et al., 'Gravitational Waves and Gamma-Rays from a Binary Neutron Star Merger: GW170817 and GRB 170817A', *Astrophys. J. Lett.* **848** (2017), L13, DOI: 10.3847/2041-8213/aa920c, arXiv: 1710.05834.

Abbott, B. P. et al., 'Multi-messenger Observations of a Binary Neutron Star Merger', *Astrophys. J. Lett.* **848** (2017), DOI: 10.3847/2041-8213/aa91c9, arXiv: 1710.05833.

Abbott, B. P. et al., 'GW170817: Observation of Gravitational Waves from a Binary Neutron Star Inspiral', *Phys. Rev. Lett.* **119** (2017), 161101, DOI: 10.1103/PhysRevLett.119.161101, arXiv: 1710.05832.

Abbott, B. P. et al., 'First narrow-band search for continuous gravitational waves from known pulsars in advanced detector data', *Phys. Rev. D* **96** (2017), 122006, DOI: 10.1103/PhysRevD.96.122006, arXiv: 1710.02327.

Abbott, B. P. et al., 'Effects of data quality vetoes on a search for compact binary coalescences in Advanced LIGO's first observing run', *Class. Quantum Gravity* **35** (2018), 065010, DOI: 10.1088/1361-6382/aaaafa, arXiv: 1710.02185.

Abbott, B. P. et al., 'GW170814: A Three-Detector Observation of Gravitational Waves from a Binary Black Hole Coalescence', *Phys. Rev. Lett.* **119** (2017), 141101, DOI: 10.1103/PhysRevLett.119.141101, arXiv: 1709.09660.

Abbott, B. P. et al., 'First Search for Nontensorial Gravitational Waves from Known Pulsars', *Phys. Rev. Lett.* **120** (2018), 031104, DOI: 10.1103/PhysRevLett.120.031104, arXiv: 1709.09203.

Abbott, B. P. et al., 'First low-frequency Einstein@Home all-sky search for continuous gravitational waves in Advanced LIGO data', *Phys. Rev. D* **96** (2017), 122004, DOI: 10.1103/PhysRevD.96.122004, arXiv: 1707.02669.

Abbott, B. P. et al., 'All-sky search for periodic gravitational waves in the O1 LIGO data', *Phys. Rev. D* **96** (2017), 062002, DOI: 10.1103/PhysRevD.96.062002, arXiv: 1707.02667.

Abbott, B. P. et al., 'Upper Limits on Gravitational Waves from Scorpius X-1 from a Model-based Cross-correlation Search in Advanced LIGO Data', *Astrophys. J. Lett.* **847** (2017), 47, DOI: 10.3847/1538-4357/aa86f0, arXiv: 1706.03119.

Abbott, B. P. et al., 'GW170104: Observation of a 50-Solar-Mass Binary Black Hole Coalescence at Redshift 0.2', *Phys. Rev. Lett.* **118** (2017), 221101, DOI: 10.1103/PhysRevLett.118.221101, arXiv: 1706.01812.

Abbott, B. P. et al., 'Search for intermediate mass black hole binaries in the first observing run of Advanced LIGO', *Phys. Rev. D* **96** (2017), 022001, DOI: 10.1103/PhysRevD.96.022001, arXiv: 1704.04628.

Abbott, B. P. et al., 'Search for gravitational waves from Scorpius X-1 in the first Advanced LIGO observing run with a hidden Markov model', *Phys. Rev. D* **95** (2017), 122003, DOI: 10.1103/PhysRevD.95.122003, arXiv: 1704.03719.

Albert, A. et al., 'Search for high-energy neutrinos from gravitational wave event GW151226 and candidate LVT151012 with ANTARES and IceCube', *Phys. Rev. D* **96** (2017), 022005, DOI: 10.1103/PhysRevD.96.022005, arXiv: 1703.06298.

Abbott, B. P. et al., 'First Search for Gravitational Waves from Known Pulsars with Advanced LIGO', *Astrophys. J.* **839** (2017), 12, DOI: 10.3847/1538-4357/aa677f, arXiv: 1701.07709.

Abbott, B. P. et al., 'Directional Limits on Persistent Gravitational Waves from Advanced LIGO's First Observing Run', *Phys. Rev. Lett.* **118** (2017), 121102, DOI: 10.1103/PhysRevLett.118.121102, arXiv: 1612.02030.

Abbott, B. P. et al., 'Upper Limits on the Stochastic Gravitational-Wave Background from Advanced LIGO's First Observing Run', *Phys. Rev. Lett.* **118** (2017), 121101, DOI: 10.1103/PhysRevLett.118.121101, arXiv: 1612.02029.

Abbott, B. P. et al., 'Search for Gravitational Waves Associated with Gamma-Ray Bursts during the First Advanced LIGO Observing Run and Implications for the Origin of GRB 150906B', *Astrophys. J.* **841** (2017), 89, DOI: 10.3847/1538-4357/aa6c47, arXiv: 1611.07947.

Abbott, B. P. et al., 'Effects of waveform model systematics on the interpretation of GW150914', *Class. Quantum Gravity* **34** (2017), 104002, DOI: 10.1088/1361-6382/aa6854, arXiv: 1611.07531.

Abbott, B. P. et al., 'All-sky search for short gravitational-wave bursts in the first Advanced LIGO run', *Phys. Rev. D* **95** (2017), 042003, DOI: 10.1103/PhysRevD.95.042003, arXiv: 1611.02972.

Abbott, B. P. et al., 'The basic physics of the binary black hole merger GW150914', *Ann. Phys.* **529** (2017), 1600209, DOI: 10.1002/andp.201600209, arXiv: 1608.01940.

Abbott, B. P. et al., 'Exploring the sensitivity of next generation gravitational wave detectors', *Class. Quantum Gravity* **34** (2017), 044001, DOI: 10.1088/1361-6382/aa51f4, arXiv: 1607.08697.

Abbott, B. P. et al., 'Upper limits on the rates of binary neutron star and neutron-star–black-hole mergers from Advanced LIGO's first observing run', *Astrophys. J.* **832** (2016), L21, DOI: 10.3847/2041-8205/832/2/L21, arXiv: 1607.07456.

Abbott, B. P. et al., 'Search for continuous gravitational waves from neutron stars in globular cluster NGC 6544', *Phys. Rev. D* **95** (2017), 082005, DOI: 10.1103/PhysRevD.95.082005, arXiv: 1607.02216.

Abbott, B. P. et al., 'Results of the deepest all-sky survey for continuous gravitational waves on LIGO S6 data running on the Einstein@Home volunteer distributed computing project', *Phys. Rev. D* **94** (2016), 102002, DOI: 10.1103/PhysRevD.94.102002, arXiv: 1606.09619.

Abbott, B. P. et al., 'Binary Black Hole Mergers in the First Advanced LIGO Observing Run', *Phys. Rev. X* **6** (2016), 041015, DOI: 10.1103/PhysRevX.6.041015, arXiv: 1606.04856.

Abbott, B. P. et al., 'GW151226: Observation of Gravitational Waves from a 22-Solar-Mass Binary Black Hole Coalescence', *Phys. Rev. Lett.* **116** (2016), 241103, DOI: 10.1103/PhysRevLett.116.241103, arXiv: 1606.04855.

Abbott, B. P. et al., 'Directly comparing GW150914 with numerical solutions of Einstein's equations for binary black hole coalescence', *Phys. Rev. D* **94** (2016), 064035, DOI: 10.1103/PhysRevD.94.064035, arXiv: 1606.01262.

Abbott, B. P. et al., 'Improved Analysis of GW150914 Using a Fully Spin-Precessing Waveform Model', *Phys. Rev. X* **6** (2016), 041014, DOI: 10.1103/PhysRevX.6.041014, arXiv: 1606.01210.

Abbott, B. P. et al., 'Comprehensive all-sky search for periodic gravitational waves in the sixth science run LIGO data', *Phys. Rev. D* **94** (2016), 042002, DOI: 10.1103/PhysRevD.94.042002, arXiv: 1605.03233.

Abbott, B. P. et al., 'First targeted search for gravitational-wave bursts from core-collapse supernovae in data of first-generation laser interferometer detectors', *Phys. Rev. D* **94** (2016), 102001, DOI: 10.1103/PhysRevD.94.102001, arXiv: 1605.01785.

Abbott, B. P. et al., 'Search for transient gravitational waves in coincidence with short-duration radio transients during 2007–2013', *Phys. Rev. D* **93** (2016), 122008, DOI: 10.1103/PhysRevD.93.122008, arXiv: 1605.01707.

Abbott, B. P. et al., 'Localization and broadband follow-up of the gravitational-wave transient GW150914', *Astrophys. J. Lett.* **826** (2016), L13, DOI: 10.3847/2041-8205/826/1/L13, arXiv: 1602.08492.

Adrián-Martínez, S. et al., 'High-energy neutrino follow-up search of gravitational wave event GW150914 with ANTARES and IceCube', *Phys. Rev. D* **93** (2016), 122010, DOI: 10.1103/PhysRevD.93.122010, arXiv: 1602.05411, URL: http://arxiv.org/abs/1602.05411.

Abbott, B. P. et al., 'GW150914: Implications for the Stochastic Gravitational-Wave Background from Binary Black Holes', *Phys. Rev. Lett.* **116** (2016), 131102, DOI: 10.1103/PhysRevLett.116.131102, arXiv: 1602.03847.

Abbott, B. P. et al., 'Astrophysical Implications of the Binary Black-Hole Merger GW150914', *Astrophys. J. Lett.* **818** (2016), L22, DOI: 10.3847/2041-8205/818/2/L22, arXiv: 1602.03846.

Abbott, B. P. et al., 'Calibration of the Advanced LIGO detectors for the discovery of the binary black-hole merger GW150914', *Phys. Rev. D* **95** (2017), 062003, DOI: 10.1103/PhysRevD.95.062003, arXiv: 1602.03845.

Abbott, B. P. et al., 'Characterization of transient noise in Advanced LIGO relevant to gravitational wave signal GW150914', *Class. Quantum Gravity* **33** (2016), 134001, DOI: 10.1088/0264-9381/33/13/134001, arXiv: 1602.03844.

Abbott, B. P. et al., 'Observing gravitational-wave transient GW150914 with minimal assumptions', *Phys. Rev. D* **93** (2016), 122004, DOI: 10.1103/PhysRevD.93.122004, arXiv: 1602.03843.

Abbott, B. P. et al., 'The Rate of Binary Black Hole Mergers Inferred from Advanced LIGO Observations Surrounding GW150914', *Astrophys. J. Lett.* **833** (2016), L1, DOI: 10.3847/2041-8205/833/1/L1, arXiv: 1602.03842.

Abbott, B. P. et al., 'Tests of General Relativity with GW150914', *Phys. Rev. Lett.* **116** (2016), 221101, DOI: 10.1103/PhysRevLett.116.221101, arXiv: 1602.03841.

Abbott, B. P. et al., 'Properties of the Binary Black Hole Merger GW150914', *Phys. Rev. Lett.* **116** (2016), 241102, DOI: 10.1103/PhysRevLett.116.241102, arXiv: 1602.03840.

Abbott, B. P. et al., 'GW150914: First results from the search for binary black hole coalescence with Advanced LIGO', *Phys. Rev. D* **93** (2016), 122003, DOI: 10.1103/PhysRevD.93.122003, arXiv: 1602.03839.

Abbott, B. P. et al., 'GW150914: The Advanced LIGO Detectors in the Era of First Discoveries', *Phys. Rev. Lett.* **116** (2016), 131103, DOI: 10.1103/PhysRevLett.116.131103, arXiv: 1602.03838.

Abbott, B. P. et al., 'Observation of Gravitational Waves from a Binary Black Hole Merger', *Phys. Rev. Lett.* **116** (2016), 061102, DOI: 10.1103/PhysRevLett.116.061102, arXiv: 1602.03837.

Abbott, B. P. et al., 'All-sky search for long-duration gravitational wave transients with initial LIGO', *Phys. Rev. D* **93** (2016), 042005, DOI: 10.1103/PhysRevD.93.042005, arXiv: 1511.04398.

Aasi, J. et al., 'First low frequency all-sky search for continuous gravitational wave signals', *Phys. Rev. D* **93** (2016), 042007, DOI: 10.1103/PhysRevD.93.042007, arXiv: 1510.03621.

Aasi, J. et al., 'Search of the Orion spur for continuous gravitational waves using a loosely coherent algorithm on data from LIGO interferometers', *Phys. Rev. D* **93** (2016), 042006, DOI: 10.1103/PhysRevD.93.042006, arXiv: 1510.03474.

Aasi, J. et al., 'Searches for continuous gravitational waves from nine young supernova remnants', *Astrophys. J.* **813** (2014), 39, DOI: 10.1088/0004-637X/813/1/39, arXiv: 1412.5942.

Aasi, J. et al., 'Directed search for gravitational waves from Scorpius X-1 with initial LIGO data', *Phys. Rev. D* **91** (2015), 062008, DOI: 10.1103/PhysRevD.91.062008, arXiv: 1412.0605.

Aasi, J. et al., 'Advanced LIGO', *Class. Quantum Gravity* **32** (2015), 074001, DOI: 10.1088/0264-9381/32/7/074001, arXiv: 1411.4547.

Aasi, J. et al., 'Narrow-band search of continuous gravitational-wave signals from Crab and Vela pulsars in Virgo VSR4 data', *Phys. Rev. D* **91** (2014), 022004, DOI: 10.1103/PhysRevD.91.022004, arXiv: 1410.8310.

Abbott, B. P. et al., 'Prospects for observing and localizing gravitational-wave transients with Advanced LIGO, Advanced Virgo and KAGRA', *Living Rev. Relativ.* **21** (2018), 3, DOI: 10.1007/s41114-018-0012-9, arXiv: 1304.0670.